Modeling the Emission of the Galactic Very High Energy γ-Ray Sources G 1.9+0.3, G 330.2+1.0, HESS J1303−631 and PSR B1259−63/LS 2883 Observed with H.E.S.S.

D I S S E R T A T I O N

zur Erlangung des akademischen Grades

doctor rerum naturalium (Dr. rer. nat.)
im Fach Physik

eingereicht an der
Mathematisch-Naturwissenschaftlichen Fakultät I
Humboldt-Universität zu Berlin

von
M.Sc. Iurii Sushch

Präsident der Humboldt-Universität zu Berlin:
Prof. Dr. Jan-Hendrik Olbertz

Dekan der Mathematisch-Naturwissenschaftlichen Fakultät I:
Prof. Stefan Hecht, Ph.D.

Gutachter:
1. Prof. Dr. rer. nat. habil. Thomas Lohse
2. Dr. rer. nat. Gernot Maier
3. Prof. Dr. Felix Aharonian

Tag der mündlichen Prüfung: 19 Oktober 2012

Dedication

I would like to thank Erasmus Mundus "External Cooperation Window" fellowship for the financial support without which this work would not be possible.

I would like to thank my thesis supervisor Thomas Lohse for the chance to work in a fantastic scientific group with a great working environment. I also greatly appreciate the financial support which allowed me to finish my thesis after the end of my Erasmus Mundus grant.

Lots of thanks to Ulli Schwanke for the supervision of the work presented in this thesis, lots of scientific discussions and proofreading which considerably improved the thesis.

Many thanks to Manuel Paz Arribas for the collaboration and analysis crosschecks in work on SNRs G 1.9+0.3 and G 330.2+1.0. I am also very grateful for his translation of the abstract of this thesis into German!

I would like to thank Matt Dalton for the joint work on HESS J1303−631 and for being my officemate for 2 years. It was a great time, Matt!

I would also like to thank Ryan Chaves, Mathieu de Naurois, Bruno Khelifi, Matthieu Renauld, Pol Bordas and Felix Aharonian for our joint work and their internal refereeing of papers.

I would like to thank all my collegues and all of the members of the group for a great atmosphere. Extra thanks to Veronika Fetting for helping with all burocratic stuff and Arne Schönwald who helped a lot in the process of getting a visa for my wife.

Finally, thanks to my beloved neighbours Michelangelo Giorgi and Ena Bech for cooking lasagna every time I felt a lack of inspiration.

Величезна подяка Кузик Раїсі Григорівні за всі ті знання які я отримав, за те, що виплекала в мені любов до фізики, що побачила в мені потенціал і не дозволила його розгубити.

Велике дякую Гнатику Богдану Івановичу за знання які він мені передав, за постійну підтримку і співпрацю, і за ту любов до астрофізики і, особливо, до залишків Наднових, яку він мені прищепив.

Дякую своїй коханій дружині Дарусі за те, що поїхала зі мною на чужину і терпіла мене всі ці роки.

Дякую батькам за підтримку, щоденні дзвінки і машину, завдяки якій дорога до роботи стала в декілька разів швидшою. А ще за те, що свого часу віддали мене до фізико-математичного ліцею, не зважаючи ні на що.

Дякую бабі за вареники, які чекали мене щоразу як приїжджав до Львова і цьоці Світлані за готовність приїхати мене підстригти навіть до Берліну!

Дякую сімейству Гуль-Орищин просто за те, що вони кльові і завжди вміли підняти настрій. А також Рості, за те, що не минав можливості нагадати мені, для чого саме я поїхав до Німеччини. І всім друзям, родичам і знайомим, що не забували і підтримували, а також й тим, що забули і не підтримували!

Thanks everybody! If anybody didn't find his or her name here it means that you are in the category of everybody and I thank you too!

Abstract

Recently, imaging atmospheric Cherenkov telescopes (IACTs) have discovered numerous new sources representing various source classes in the very high energy (VHE; $E > 100$ GeV) sky. This work presents studies of representatives of three types of Galactic VHE emitters: the Supernova remnants (SNRs) G 1.9+0.3 and G 330.2+1.0, the pulsar wind nebula (PWN) HESS J1303−631 and the binary system PSR B1259−63/LS 2883. The analysis of the H.E.S.S. data and the broadband emission modeling are presented.

G 1.9+0.3 and G 330.2+1.0 are synchrotron-dominated SNRs whose non-thermal X-ray emission implies that intensive particle acceleration occurs at their shock fronts. This makes them promising candidates for the detection at VHEs. They were observed by the High Energy Stereoscopic System (H.E.S.S.) yielding no signs of significant VHE γ-ray emission from either SNR. The 99% confidence level upper limits on the TeV flux were determined. For an assumed spectral index of 2.5 the obtained upper limits are $F_{\mathrm{G1.9}}(> 260\,\mathrm{GeV}) < 4.6 \times 10^{-13}$ cm^{-2}s^{-1} for G 1.9+0.3 and $F_{\mathrm{G330}}(> 380\,\mathrm{GeV}) < 1.6 \times 10^{-12}$ cm^{-2}s^{-1} for G 330.2+1.0. Upper limits on the VHE emission provide constraints on the interior magnetic field in the context of a leptonic scenario and on the interstellar medium (ISM) density and cosmic-ray (CR) efficiency in a hadronic scenario. Lower limits on the interior magnetic fields were estimated at 15 μG for G 1.9+0.3 and 14 μG for G 330.2+1.0. In the case of the hadronic scenario, the H.E.S.S. upper limits are two orders of magnitude greater than the flux prediction. Obtained upper limits on the ISM densities are compatible with other estimates of the densities (from the thermal X-ray emission for G 330.2+1.0 and from the expansion rate for G 1.9+0.3). The CR efficiency cannot be constrained with the current H.E.S.S. upper limits.

HESS J1303−631 is an initially unidentified H.E.S.S. source which was recently identified as a PWN associated with the pulsar PSR J1301−6305. The broadband emission of the source was modeled within a one-zone 1D stationary model yielding a magnetic field of 1.4 ± 0.2 μG and a total energy in electrons above 1 GeV of 2×10^{48} erg. This estimate of the magnetic field is of the same magnitude as the averaged line-of-sight magnetic field of ~ 2 μG provided by the measurement of the pulsar's rotation measure. A magnetic field in a PWN much lower than the averaged ISM magnetic field would be difficult to explain. A low magnetic field is also expected for evolved PWNe for which the magnetic field is believed to have decreased with time. The obtained total energy in electrons yields an estimate for the pulsar birth period between 51 and 75 ms, which is in good agreement with estimations of birth periods for pulsars associated with composite SNRs. Possible extensions of the modeling towards more realistic scenarios which would take into account the time evolution and spatial distribution of the source emission are also discussed.

The binary system **PSR B1259−63/LS 2883** is the only TeV binary for which the compact companion is unambiguously identified as a pulsar. It consists of a 48 ms pulsar orbiting around a massive Be star. PSR B1259−63/LS 2883 was monitored by H.E.S.S. around the periastron passage on 15th of December 2010. The source was observed by H.E.S.S. in the period from 26 to 32 days after the periastron passage. A firm detection of the source was obtained. The observed

flux $F(> 1\,\mathrm{TeV}) = (1.61 \pm 0.22_{\mathrm{stat}} \pm 0.32_{\mathrm{syst}}) \times 10^{-12}\ \mathrm{cm}^{-2}\mathrm{s}^{-1}$ and spectral index $\Gamma = 2.82 \pm 0.25_{\mathrm{stat}} \pm 0.2_{\mathrm{syst}}$ are in good agreement with results obtained during previous periastron passages. The observations were performed at similar orbital phases as around the 2004 periastron, for the first time directly confirming the repetitive behavior of the source at VHEs. H.E.S.S. observations were part of a joint multiwavelength (MWL) campaign including also radio, optical, X-ray and, for the first time, high energy (HE; $E > 100$ MeV) observations. Fermi LAT detected a spectacular flare which had started within the period of H.E.S.S. observations. A statistical study shows that the HE flare does not have a counterpart at VHEs indicating that the HE and VHE emissions are produced in different physical processes. The modeling of the VHE emission with the model of emission generated via inverse Compton (IC) scattering of shock-accelerated electrons on the stellar photon field is done considering the HE flux as an upper limit for this emission. The modeling yields upper limits on the electron spectral parameters and the total energy in electrons depending on the assumed electron spectral index. It was shown that for indices in the range from 1.7 to 1.9 the time needed to accumulate the required total energy in electrons is smaller than the orbital period of the pulsar.

Zusammenfassung

Abbildende Cherenkov-Teleskope haben in den letzten Jahren eine große Anzahl neuer Gammastrahlungsquellen im Bereich sehr hoher Energien (VHE, *very high energy*, $E > 100\,\mathrm{GeV}$) entdeckt. Diese Studie behandelt Vertreter von drei unterschiedlichen Klassen von galaktischen Gammastrahlungsquellen: die Supernova-Überreste G 1.9+0.3 und G 330.2+1.0, den Pulsarwind-Nebel HESS J1303−631 und das Binärsystem PSR B1259−63/LS 2883. Für alle Objekte werden die Analyse der H.E.S.S.-Daten und die Modellierung der Emission unter Einbeziehung von Daten aus anderen Wellenlängenbereichen dargestellt.

G 1.9+0.3 und G 330.2+1.0 sind Supernova-Überreste, deren nicht-thermische Emission durch Synchrotron-Strahlung dominiert wird und so nahelegt, dass es in den Supernova-Schockfronten zur Beschleunigung von Teilchen auf sehr hohe Energien kommt. Daher sind beide Objekte für Beobachtungen im VHE-Bereich von Interesse. Beobachtungen mit dem High Energy Stereoscopic System (H.E.S.S.) ergaben jedoch keine Hinweise auf signifikante Emission und es wurden daher obere Grenzen auf den Teilchenfluss berechnet. Die oberen Grenzen für ein Konfidenzniveau von 99% und eine angenommen Photon-Index von 2,5 sind $F_{\mathrm{G1.9}}(> 260\,\mathrm{GeV}) < 4.6 \times 10^{-13}\ \mathrm{cm}^{-2}\mathrm{s}^{-1}$ für G 1.9+0.3 und $F_{\mathrm{G330}}(> 380\,\mathrm{GeV}) < 1.6 \times 10^{-12}\ \mathrm{cm}^{-2}\mathrm{s}^{-1}$ für G 330.2+1.0. Die Flussgrenzen auf die Emission im VHE-Bereich schränken die möglichen Werte für das Magnetfeld in einem leptonischen Szenario bzw. die Dichte des interstellares Mediums im Fall eines hadronischen Szenarios ein. Die unteren Grenzen für das Magnetfeld in der Emissionsregion sind 15 μG für G 1.9+0.3 und 14 μG für G 330.2+1.0. Im Rahmen eines hadronischen Modells liegen die H.E.S.S.-Grenzen zwei Größenordnungen oberhalb des vorausgesagten Flusses. Die abgeleiteten oberen Grenze auf die Dichte des interstellaren Mediums sind kompatibel mit anderen Abschätzungen (aus der thermischen Röntgen-Emission für G 330.2+1.0 und aus der Ausdehnungsrate für G 1.9+0.3). Die Effizienz der Umsetzung der Explisionsenergie der Supernova in Energie in Form von Kosmischer Strahlung kann anhand derzeitigen H.E.S.S.-Daten nicht eingeschränkt werden.

HESS J1303−631 ist eine anfangs unidentifizierte H.E.S.S.-Quelle, die vor Kurzem als der Pulsarwind-Nebel des Pulsars PSR J1301−6305 identifiziert wurde. Die Emission der Quelle in verschiedenen Wellenlängenbereichen wurde im Rahmen eines eindimensionalen, stationären Ein-Zonen-Modells beschrieben. Es ergab sich ein Magnetfeld von 1.4 ± 0.2 μG und eine Gesamtenergie in Elektronen über 1 GeV von 2×10^{48} erg. Das ermittelte Magnetfeld liegt in der gleichen Größenordnung wie das mittlere Magnetfeld von $\sim 2\mu$ G entlang der Verbindungslinie zum Pulsar, das aus der Faraday-Rotation der Pulsarstrahlung abgeleitet wird. Ein Magnetfeld des Pulsarwind-Nebels unterhalb dem mittleren Magnetfeld im interstellaren Medium wäre schwer zu verstehen. Andererseits erwartet man in entwickelten Pulsarwind-Nebeln ein schwaches Magnetfeld, da die Stärke des Magnetfeldes im Laufe der Zeit abnimmt. Die berechnete Gesamtenergie übersetzt sich in eine Schätzung der anfänglichen Periode des Pulsars zwischen 51 und 75 ms, was recht gut mit den Erwartungen für Pulsar, die mit Supernova-Überresten assoziiert sind, übereinstimmt. Die Arbeit diskutiert ferner mögliche Erweiterungen der Modellierung im Hinblick

auf realistischere Szenarien, die auch die zeitliche und räumliche Entwicklung der Emission berücksichtigen.

Das TeV-Binärsystem **PSR B1259−63/LS 2883** ist der einzige Vertreter seiner Art, in der der kompakte Begleiter eindeutig als Pulsar identifiziert wurde. Es besteht aus einem Pulsar mit einer Periode von 48 ms, der einen massenreichen Be-Stern umkreist. Um die Jahreswende 2010/11 war PSR B1259−63/LS 2883 um den am 15. Dezember 2010 stattfindenden Periastron-Durchgang das Ziel von Beobachtungen mit H.E.S.S.. Die Beobachtungen deckten den Zeitraum von 26 bis 32 Tage nach dem Periastron-Durchgang ab und erlaubten die eindeutige Detektierung der Quelle. Der gemessene Fluss von $F(> 1\,\mathrm{TeV}) = (1.61 \pm 0.22_{\mathrm{stat}} \pm 0.32_{\mathrm{syst}}) \times 10^{-12}\,\mathrm{cm}^{-2}\mathrm{s}^{-1}$ und Photon-Index von $\Gamma = 2.82 \pm 0.25_{\mathrm{stat}} \pm 0.2_{\mathrm{syst}}$ stimmen gut mit den Resultaten von früheren Periastron-Durchgängen überein. Die Beobachtungen wurden bei ähnlichen Phasen bezüglich der Umlaufperiode wie beim Periastron-Durchgang im Jahr 2004 durchgeführt und stellen daher den ersten direkten Nachweis der Periodizität der Quelle im TeV-Bereich dar. Die H.E.S.S.-Messungen waren Teil einer Beobachtungskampagne mit Instrumenten aus unterschiedlichen Wellenlängenbereichen, darunter optische Teleskope und Radio-Teleskope, sowie Röntgen-Satelliten. Erstmals fanden Beobachtungen auch bei hohen Energien (HE, *high energy*, $E > 100\,\mathrm{MeV}$) statt. Das *Large Area Telescope* des Fermi-Satelliten wies dabei einen spektakulären Strahlungsausbruch nach, der während der Beobachtungen mit H.E.S.S. begann. Eine statistische Auswertung der Daten ergibt, dass der Strahlungsausbruch im MeV-Bereich kein Gegenstück im TeV-Bereich hat. Dies zeigt, dass die MeV- und TeV-Emissionen von unterschiedlichen physikalischen Prozessen stammen. Die Beschreibung der TeV-Emission mittels eines Modells, in dem Gammastrahlung durch inverse Compton-Streuung schockbeschleunigter Elektronen generiert wird, wurde unter die Annahme durchgeführt, dass der MeV-Fluss eine obere Grenze für die Emission darstellt. Die Modellierung ergibt Grenzen auf die Parameter der Elektronenpopulation und die Gesamtenergie in Elektronen in Abhängigkeit vom angenommenen Elektron-Index p. Für p im Bereich von 1.7 bis 1.9 wurde gezeigt, dass die benötigte Zeit zur Akkumulation der Gesamtenergie in Elektronen kleiner als die Umlaufperiode des Pulsars ist.

Contents

1 Introduction

In recent years, high-energy astrophysics has become one of the most popular and quickly developing branches of observational science and a driver of theoretical models. The goal of high-energy astrophysics is to explore the production and propagation of high energy particles in the Universe. The best known example for such non-thermal particle populations are cosmic rays. There are still a lot of uncertainties and open questions about the possible sources and acceleration mechanisms of high energy particles. Among the most plausible accelerators of particles are Supernova Remnants (SNRs) and rapidly rotating neutrons stars (pulsars) surrounded by pulsar wind nebulae (PWNe). The investigation of these objects is necessary in order to progress towards understanding one of the main mysteries of astroparticle physics - the origin of cosmic rays.

Visibility across many energy bands provides an exceptional opportunity to explore different kinds of physical processes inside SNRs and PWNe. Sources of both types can be considered as naturally created laboratories which give us a lot of experimental information confirming or excluding existing models of physical and astrophysical processes. These laboratories combine different fields of physics like magnetohydrodynamics, nuclear and particle physics and allow to build the overall picture of physical processes which take place in the Galaxy. Observations of SNRs and PWNe can provide an insight to the evolution and death of their progenitor stars, give information about the structure of the interstellar gas and magnetic field. These objects allow to observe the interaction of particles with energies which are impossible to reach on the Earth. They are believed to be very efficient natural particle accelerators accelerating paricles at their shocks to very high energies, what makes them good candidates for the origin of cosmic rays.

The field of very high energy (VHE; $E > 100$ GeV) γ-ray astronomy opened a new window for observations of celestial bodies. It provides the opportunity to study emission mechanisms of VHE photons. Currently, more than 100 sources have been detected at VHEs and most of them were discovered with the High Energy Stereoscopic System (H.E.S.S.) – an array of four Imaging Atmospheric Cherenkov Telescopes (IACT). More than half of the detected sources are located in our Galaxy and comprise SNRs, PWNe, binary systems and unidentified sources.

The investigation of the VHE emission from selected Galactic particle accelerators as well as the modeling of their broadband emission is the task of this thesis. Data obtained from H.E.S.S. observations are examined in the multiwavelength (MWL) perspective together with data from radio and X-ray observations. In particular these objects are considered: SNRs G1.9+0.3 and G330.2+1.0, the PWN HESS J1303-631 and a binary system comprising the pulsar PSR B1259-63.

Chapter 2 presents a short introduction into the γ-ray astronomy and a description of H.E.S.S. and the data analysis procedure. In Chapter 3, SNRs are introduced. Mechanisms of SNe explosions, their classification and evolution of SNRs are reviewed. In Chapter 4, a description of pulsars, PWNe and prerionic binaries is presented. Chapter 5 describes possible non-thermal emission mechanisms in SNRs and PWNe. The author's study, analysis of the H.E.S.S. data and broadband emission modeling, on two young synchrotron-dominated SNRs G 1.9+0.3 and G 330.2+1.0 is presented in Chapter 6. In Chapter 7, the evolved PWN HESS J1303−631 is discussed and modeling of the broadband emission of this source performed by the author is presented. The binary system PSR B1259−63/LS 2883 is presented in Chapter 8 together with author's studies of the H.E.S.S. data taken around its 2010/2011 periastron passage. A brief summary of results conclude this thesis in Chapter 9.

2 γ-ray Astronomy

γ-ray astronomy is the branch of astronomy, which studies the radiation from celestial objects at the highest energies ($E \gtrsim 1$ MeV) in the electromagnetic spectrum. In 1961, the first γ-ray telescope was flown in orbit on the Explorer 11 satellite to examine theoretical predictions of the production of high-energy photons in the Universe. It detected 22 cosmic γ-ray photons which were coming isotropically. First γ-rays from an identified source were detected by the OSO-3 satellite from solar flares. A huge step forward was made possible by the SAS-2 (1972) and the COS-B (1975–1982) satellites which provided the first detailed map of the γ-ray sky detecting a number of point-like sources.

Subsequent observations with satellites and with ground-based telescopes discovered many different γ-ray sources inside and outside our Galaxy. Among the most prominent types of γ-ray sources are **Supernova remnants (SNRs)**, massive structures created from the ejecta of stellar explosions, **pulsars**, fast-rotating and highly magnetized neutron stars, left over from the core of the massive star exploded as a Supernova, **pulsar wind nebulae (PWNe) or "plerions"**, nebulae powered by the energy released by pulsars, **active galactic nuclei (AGN)**, compact regions at the center of some galaxies with higher than usual luminosities and believed to result from the accretion of mass by supermassive black holes, and **binary systems**, which consist of a massive star and a compact object like a neutron star or a black hole. These discoveries opened a new broad field for investigations and created a great chance to develop a better understanding of physical processes in celestial bodies, mechanisms of particle acceleration and the nature of γ-ray emission.

2.1 Very High Energy γ-ray Astronomy

First observations and discoveries in γ-ray astronomy were made at relatively low energies in the MeV energy band. Further progress towards GeV–TeV energies and especially VHE (> 100 GeV) faced the challenge of very low fluxes comparing to lower energies. For instance, the integral photon flux above 1 TeV from the Crab Nebula is $\sim 10^{-11}$ cm^{-2}s^{-1}, while the X-ray flux in the 1–10 keV energy band is ~ 0.1 cm^{-2}s^{-1}. The detection of such extremely low fluxes requires detectors with very big effective areas (of order 10^4 m^2 for collecting several photons in 1 hour) and makes it very difficult to launch such an instrument into space. Construction of detectors with large effective areas would be, of course, much easier in ground-based experiments, but γ-ray photons are absorbed in the Earth's atmosphere producing showers of secondary particles which is accompanied by the dissipation of the en-

ergy of the primary particle. Although the absorption of VHE cosmic photons is a necessary condition for the existence of life on Earth, it also prevents us from the direct detection of VHE γ-rays using ground-based instruments.

This problem was solved by using the Earth atmosphere as an integral part of the γ-ray detector. Although, ground-based telescopes are not able to directly detect primary photons, they can detect showers of secondary particles, known as extensive air showers (EAS), created in the interaction of primary particles with the Earth atmosphere. Such a shower is created by a primary high-energy photon which enters the atmosphere and dissipates its energy through the creation of an electron–positron pair. In turn, electron and positron produces secondary photons through Bremsstrahlung in the Coloumb field of the air molecules which again leads to the pair production creating an electromagnetic cascade. The charged particles which comprise the EAS are travelling with velocities which exceed the speed of light in the medium and therefore create Cherenkov radiation[1] as they pass through the atmosphere.

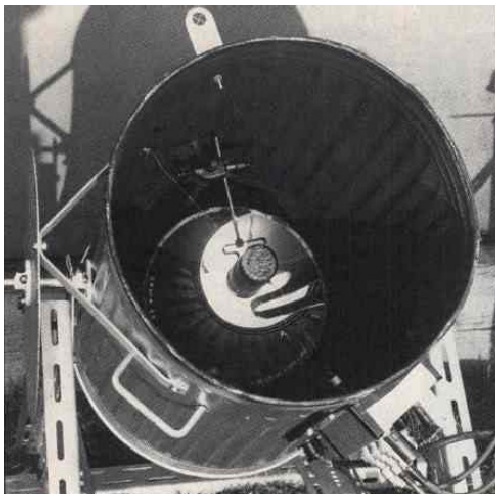

Figure 2.1: The first instrument to detect the Cherenkov light emitted by the cosmic-ray showers was built by Bill Galbraith and John Jelley in 1952.

Up to now, two techniques to detect VHE γ-rays from the ground were successfully applied: atmospheric Cherenkov telescopes (ACT) and EAS arrays. An EAS array directly measures the passage of particles in the shower on the ground. The reconstruction of the direction of the primary particle is made by measuring the difference of the arrival time of the EAS in different detector stations. To effectively implement this technique a set of charged particle detectors spread over a large area is needed in order to contain the core of the EAS (the central portion of the EAS). Individual detectors can be wire chambers, water Cherenkov detectors or scintillation detectors. Major present-day instruments which use this technique are Milagro, Tibet ASγ and ARGO (see e.g. Sinnis [2009] and references therein).

Another technique (atmospheric Cherenkov telescopes) is based on the detection of the Cherenkov light from the EAS. It uses one or more mirrors to focus the Cherenkov radiation onto photon detectors, e.g. photomultiplier tubes (PMTs).

[1] Cherenkov radiation is an electromagnetic radiation emitted by a charged particle (e.g. electron) which is moving in a dielectric medium with a speed higher than the speed of light in this medium. This radiation is named after its discoverer Pavel Cherenkov.

Figure 2.2: First ever ground-based experiment in VHE γ-ray astronomy, which was operating from 1960 to 1965 at Katseveli, Crimea (former USSR, now Ukraine)

The first instrument to detect the Cherenkov light emitted by cosmic-ray showers was built by Bill Galbraith and John Jelley in 1952 following the suggestion of P. M. S. Blackett that a small part of the night-sky background light may come from the Cherenkov radiation. This first experiment consisted of a 5 cm diameter photomultiplier tube mounted in the focal plane of a 25 cm diameter parabolic mirror shielded by a garbage can and coupled to a 5 MHz amplifier and an oscilloscope (Fig. 2.1) [Aharonian et al., 2008b, Weekes, 2007]. B. Galbraith and J. Jelley detected the exceeding of the average noise level of the night-sky light background every two minutes [Galbraith and Jelley, 1953]. The nearby Harwell cosmic ray air shower array (one of the first air shower arrays, consisting of 92 boxes, each containing three Geiger counters and a power supply) confirmed that the detected light was indeed associated with cosmic ray showers.

In 1961, A. Chudakov and G. Zatsepin suggested the atmospheric Cherenkov technique for γ-ray astronomy [Zatsepin and Chudakov, 1961] and led the construction of the experiment at Katseveli, Crimea (former USSR, now Ukraine). It was the first ground-based experiment in TeV γ-ray astronomy. It consisted of twelve 1.5 m ex-World War II searchlight mirrors mounted on railway cars (Fig. 2.2). The experiment was operated from 1960 to 1965 and observed the Crab Nebula and some other sources such as SNRs and radio galaxies which had been recently identified as sources of synchrotron emission. None of observed sources was detected at energies above 5 TeV [Chudakov et al., 1964]. Nevertheless, the obtained upper limit on the Crab Nebula flux led to the conclusion that the synchrotron radiation from the source can not be generated by secondary electrons produced in the decays of pions

created in hadronic collisions as proposed by Cocconi [1960], but rather by electrons directly accelerated in the source [Chudakov et al., 1964].

The development in the field of atmospheric Cherenkov telescopes led to the idea of an imaging ACT (IACT) which has a camera consisting of an array of PMTs in the focal plane of the mirror and can resolve the Cherenkov image of the EAS. The first IACT was the Whipple observatory 10 m γ-ray telescope constructed in 1968 by Giovanni Fazio (see Fig. 2.3). This was the first instrument, which finally detected the first Galactic source, the Crab Nebula, in 1989 and the first extragalactic source, Markarian 421, in 1992 (see Aharonian et al. [2008b] and references therein). Subsequent exploitation of IACT technique in the 90s by Whipple, Durham, Crimea, HEGRA, CAT, CANGAROO and other groups led to important results and discoveries, but did not succeed in expanding the VHE source catalogue, detecting not more than 10 sources (Aharonian et al. [2008b] and references therein). These observations convinced the astrophysical community of the necessity of the next (second) generation instruments, which would combine the strong points of Whipple (a large aperture telescope) and HEGRA (an array of small aperture telescopes). This principle was adopted by the H.E.S.S., CANGAROO and VERITAS collaborations. The MAGIC collaboration went another way constructing a single, but very big 17 m diameter telescope. The second generation of IACTs made a grandiose improvement detecting more than 100 VHE sources in total.

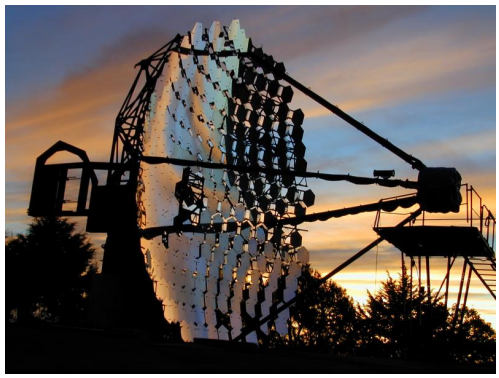

Figure 2.3: The Whipple observatory 10 m γ-ray telescope, which detected the first VHE γ-ray source Crab Nebula in 1989

Nowadays, four major IACT experiments are in operation: H.E.S.S., located in the Khomas Highland in Namibia, VERITAS, situated in Arizona, USA, MAGIC[2] on La Palma, one of the Canary islands, and CANGAROO III in Australia. In the next subsection, more details on the H.E.S.S. telescopes are presented since this thesis is based on H.E.S.S. data.

2.2 The High Energy Stereoscopic System

The High Energy Stereoscopic System (H.E.S.S.) experiment became the first representative of the class of the so called second generation of ground-based detectors. Together with the subsequent MAGIC and VERITAS experiments, H.E.S.S. dramatically changed the situation in VHE γ-ray astronomy filling the TeV sky with dozens

[2]Since the time of construction the second 17 m telescope was build and started to operate in 2009.

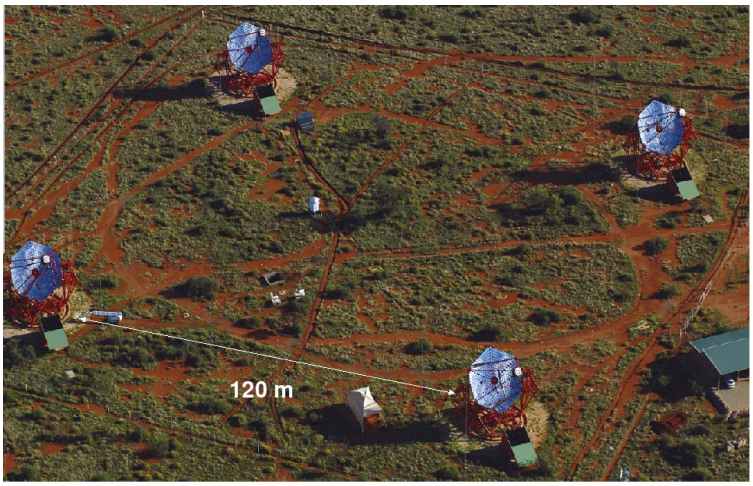

Figure 2.4: The aerial view of the H.E.S.S. telescope array. Four telescopes are arranged on a square with 120 m side length.

of new sources inside and outside the Galaxy, including TeV sources, which do not have counterparts in other energy bands.

2.2.1 General Characteristics

H.E.S.S. (phase I) is an array of four IACTs located in the Khomas Highland in Namibia (23°16′18″ South, 16°30′00″ East) at an altitude of 1800 m above sea level [Funk et al., 2004, Bernloehr et al., 2003]. The telescopes are arranged in a square with a side length of 120 m (Fig. 2.4). The distance between telescopes was chosen in order to find a compromise between a large length needed for good stereoscopic observations of an EAS (precise reconstruction of the shower geometry, i.e. the direction of a primary particle) and the requirement that at least two telescopes are hit by the Cherenkov light generated by an EAS.

Each telescope (Fig. 2.5) has a spherical 13 m dish, consisting of 380 individual mirrors resulting in 107 m^2 of reflective area. A camera located in the focal plane of the mirror consists of 960 pixels with a size of 0.16° giving the overall field of view (FOV) of about 5°. Each pixel uses a 29 mm PMT. For the trigger system, the camera is divided into overlapping sectors, each containing 64 pixels. A camera trigger occurs if the signals in at least 3 pixels within a sector (*sector threshold*) exceed a threshold

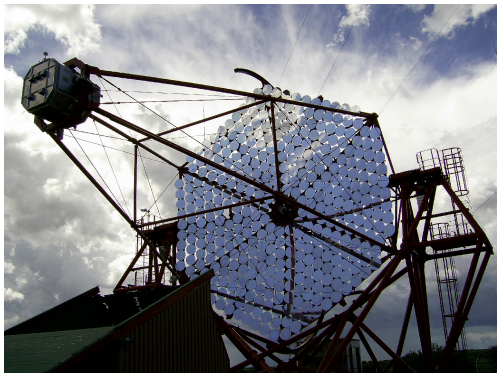

Figure 2.5: A H.E.S.S. telescope.

of 5.3 photoelectrons (*pixel threshold*) within a time-window of ~ 1 ns[3]. The shower image is recorded if at least 2 cameras are triggered in order to fulfill the stereoscopic observation requirement [Funk et al., 2004]. The data from the telescopes are collected and combined by the data acquisition system (DAQ). The DAQ is also responsible for a first online analysis.

The telescopes are optimized for detection of very high energy γ-rays in the range of 100 GeV to 20 TeV. The angular resolution of the system is $\lesssim 0.1^\circ$ and the average energy resolution is about 15% [Aharonian et al., 2006a]. The H.E.S.S. array is capable to detect point sources with a flux of 1% of the Crab nebula flux at the significance level of 5σ in 25 hours at low zenith angles [Aharonian et al., 2006a].

The H.E.S.S. telescope array is about to enter the H.E.S.S. II phase in which a single large telescope with ~ 600 m^2 mirror area is added in the center of the square. It will increase the energy coverage and sensitivity of the array. The inauguration of the new telescope is planned for the autumn of 2012 and first observations are planned to start in the summer of 2012.

For more information on the structure and operation of the H.E.S.S. telescope array please consult e.g. Schlenker [2005], Kerschhaggl [2010].

2.2.2 Data Analysis

The analysis of data obtained from observations with the H.E.S.S. telescope array is a complex process which consists of several key steps:

- data calibration
- data quality selection
- image cleaning and shower reconstruction
- γ/hadron separation
- background modeling

Data Calibration

The pulse generated by a photon in a single pixel, i.e. PMT, is stored by an analog to digital converter (ADC) in counts. In order to convert this value into an intensity of the Cherenkov radiation measured in photo electrons (p.e.), the **calibration of data** is required. For this purpose a set of calibration runs are performed:

- An **electronic pedestal run** is used to estimate the noise in the single pixels, i.e. the ADC counts recorded in the absence of Cherenkov light. It is performed with closed lid of the camera and with the high voltage (HV) turned on. Since the noise in a PMT is a function of temperature and cameras become hotter

[3]The trigger system is changing over time and, thus, presented values should be understood as typical.

during the operation, pedestals are taken also during observation runs. As the lid is opened during the observation runs, these pedestals give also a measure of night-sky background (NSB).

- A **single photo electron run** gives the estimation of conversion coefficients from 1 p.e. to ADC counts. It uses light-emitting diode (LED) pulses into the camera at 70 Hz with an intensity such that on average there is 1 p.e. per pixel, i.e. PMT, per event. It is performed with the camera lid open and HV on. In order to avoid contamination from NSB single photo electron runs are performed inside the camera hut. On average 1 p.e. corresponds to ~ 80 ADC counts.

- A **flatfielding run** is performed to correct for differences in single PMT efficiencies which appear due to the different efficiencies of photo cathodes and Winston cones[4]. The LED mounted in the center of the dish uniformly illuminates the whole camera with short light pulses with a FWHM of 5 ns. LED pulses lie within a wavelength range of $390 - 420$ nm which simulates the Cherenkov light very well. The mean ADC count of all pixels is calculated and a flatfield correction coefficient, i.e. the inverse of the deviation of one pixel ADC count from the mean, for each single pixel is obtained.

- **Muon rings**[5] are recorded to estimate changes in the mirrors reflectivity, which occur with time due to the pollution and degradation of the mirror coating. The Cherenkov light from muons is well understood and modeled. The mirror efficiency can be estimated as the ratio of measured pixel intenisities to simulated Cherenkov photons from a muon. The image intensities are then scaled according to this ratio.

The difference between the raw and calibrated data is well illustrated by the left and middle images in Fig. 2.6. The right panel of the same Figure shows the image after the image cleaning procedure which is discussed below.

Data Quality Selection

Not all of the collected data are used for the analysis. Rejecting data recorded in non-optimal conditions is very important for minimizing the systematic effects on the measured flux and energy spectrum. H.E.S.S. standard quality criteria require a constant trigger rate, a stable tracking and a low number of problematic pixels [Aharonian et al., 2006a]. A constant trigger rate shows that observations are taken in good atmosphere conditions. The presence of clouds or excessive dust in the atmosphere may lead to the absorption of the Cherenkov radiation and provokes fluctuations in the system trigger efficiency, causing systematic uncertainties in the

[4]The Winston cone is a light collector with a prabolic shape and a reflective inner surface mounted on the entrance window of the PMT.

[5]The Cherenkov light from muons produced in hadronic air showers forms rings in the camera image of a single telescope.

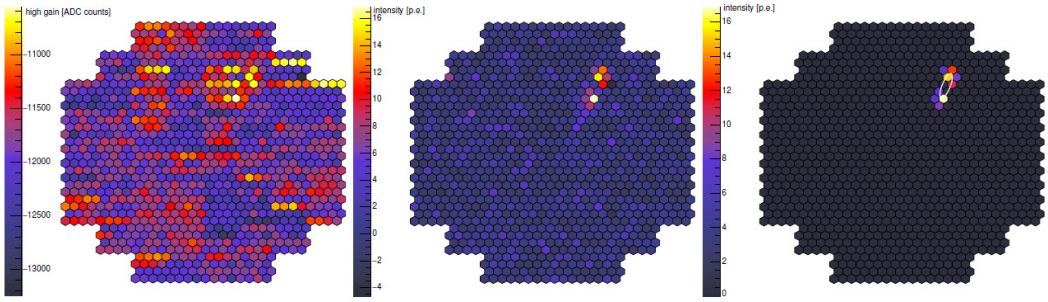

Figure 2.6: Camera images: the raw camera image (before calibration) where the color bar denotes ADC counts (left panel), the calibrated image with the color bar in p.e. (middle panel) and the image after image cleaning (right panel). In the raw data the shower ellipse is hardly recognised while after calibration and cleaning it is well resolved. In the cleaned image the Hillas ellipse is indicated by the white line. The shower image is split into two parts which is probably due to some problematic pixels. The image is taken from the PhD thesis of Nukri Komin [Komin, 2005].

reconstructed photon energies and thus the measured flux. The stable tracking is required to exclude observations with non-functional tracking system, which leads to uncertainties in the source position reconstruction. Unexpected transient light sources like meteorites, lightnings, airplanes, trigger the over-current protection of PMTs and switch them off till the source has left the pixel. Runs which have more than 10% of the pixels switched off are excluded from the analysis.

Shower Reconstruction and γ/Hadron Separation

For the analysis of the observation data of the sources investigated in this thesis two different techniques of the shower reconstruction and γ/hadron separation were used: the *H.E.S.S. standard Hillas reconstruction* [Aharonian et al., 2006a] and the *model analysis* [de Naurois and Rolland, 2009].

- *H.E.S.S. Standard Hillas Reconstruction*

  The prior step to the Hillas analysis procedure is the image cleaning which is necessary in order to remove pixels which do not contain Cherenkov light, i.e. noisy pixels due to the NSB and electronic noise. Images are cleaned using a two-level filter which requires an image pixel to have at least 5 p.e. and to have a neighbour with at least 10 p.e., and vice verse[6]. This allows to select only spatially correlated features which correspond to the EAS Cherenkov light. The camera image after cleaning is shown on the right panel of Fig. 2.6.

  In the Hillas reconstruction method each EAS is characterised by the Hillas parameters based on the second moments of the image [Hillas, 1985]. These parameters are used then for the event selection and shower reconstruction.

[6]This is just one of different configurations used for the two level filter

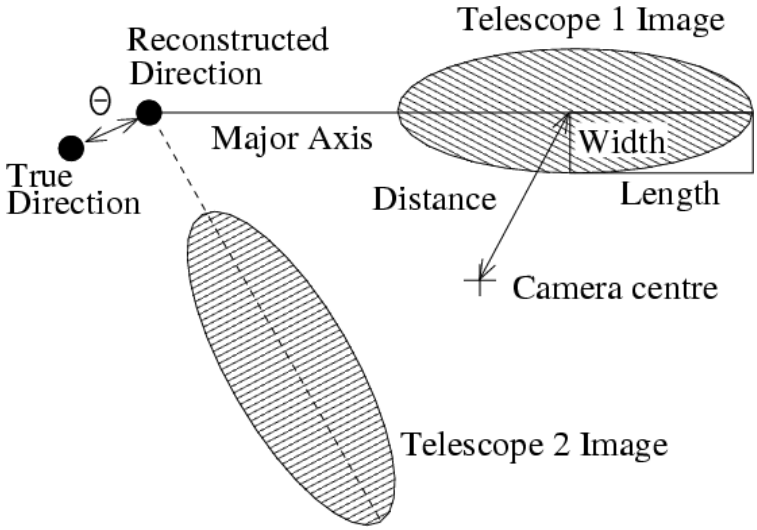

Figure 2.7: Paramterisation of shower images according to Hillas [1985]. The shower image is approximated as a narrow ellipse. Important parameters for the analysis are the length, width, distance and orientation of the ellipse. An image from a second telescope is superimposed to demonstrate the geometrical technique for position reconstruction. The angular separation θ is also shown. The figure is taken from Aharonian et al. [2006a].

According to the Hillas approach each shower image can be approximated as an ellipse and characterised by the following parameters (Fig. 2.7):

- length l – the semi-major axis,
- width w – the semi-minor axis,
- center of gravity c_{g},
- image amplitude s – accumulated pixel intensity,
- pixel number n_{p} – total pixel number in the image.

Another important parameter used for the H.E.S.S. analysis is the angular distance between the reconstructed and true shower direction θ.

In order to filter γ-ray events and to reduce the background the following cuts on the defined above parameters are required:

- A minimum value of the image amplitude s should be set since too dim events are difficult to reconstruct.
- A maximum value of the distance d should be set in order to avoid truncated images close to the camera edge, which often lead to misreconstruction of the shower direction and the energy of the primary photon.
- Only events with images from at least 2 telescopes should be taken into account to ensure a stereoscopic reconstruction of the shower direction.

There are images which do not contain any information after the image cleaning.

- θ^2 cut depends on the size of the source. For extended sources a higher value of θ^2 is used.

The reconstruction of the shower direction is performed by tracing the projected direction of the shower in the field of view, i.e. the major axis of the shower ellipse, to the origin point of the particle. If two or more telescopes are used it is possible to reconstruct the direction with a simple geometric method intersecting the major axis of multiple EAS images [Hofmann et al., 1999].

For the effective analysis of the data the reduction of the hadronic background is indispensable. Hadronic atmospheric showers recorded by H.E.S.S. constitute the bulk of all detected events. Hadronic showers show a broader and more diffuse morphology, which allows their discrimination from electromagnetic showers by analysing the shape of the shower image. For this purpose the *mean scaled parameter* method is used, similar to the one used by the HEGRA collaboration [Daum et al., 1997]. In this method the measured value of a parameter p (either the width w or the length l of the shower image) is compared to the expected value for a γ-ray event $\langle p \rangle$ using the scaled parameter

$$p_{\mathrm{sc}} = \frac{p - \langle p \rangle}{\sigma_{\mathrm{p}}}, \tag{2.1}$$

where σ_{p} is a scatter. The parameters $\langle p \rangle$ and σ_{p} are obtained from lookup tables generated based on Monte Carlo (MC) simulations depepending on the reconstructed impact parameter and image amplitude and the observation zenith angle (ZA). The *mean reduced scaled width* (MRSW) and *mean reduced scaled length* (MRSL) which are finally used to filter out hadronic events are then calculated for each event by averaging over the telescope images which passed the amplitude selection cut:

$$MSRP = \frac{\sum_{\mathrm{tel}}^{N_{\mathrm{tel}}} p_{\mathrm{sc}}}{N_{\mathrm{tel}}}, \tag{2.2}$$

where MSRP is the *mean reduced scaled parameter*, i.e. either MRSW or MRSL.

In Fig. 2.8(a) a comparison between the MRSW distributions for MC γ-ray simulations, MC proton simulations and real OFF data at a ZA of 50° before selection cuts are shown. As expected, the OFF data before cuts corresponds well to simulated protons, but there is an obvious discrepancy with simulated γ-rays. Figure 2.8(b) shows MSRW distributions for MC γ-ray simulations and real data after selection cuts and background subtraction.

The reconstructed energy of the primary particle of a shower depends on image amplitude, impact parameter and zenith angle. Similarly to scaled param-

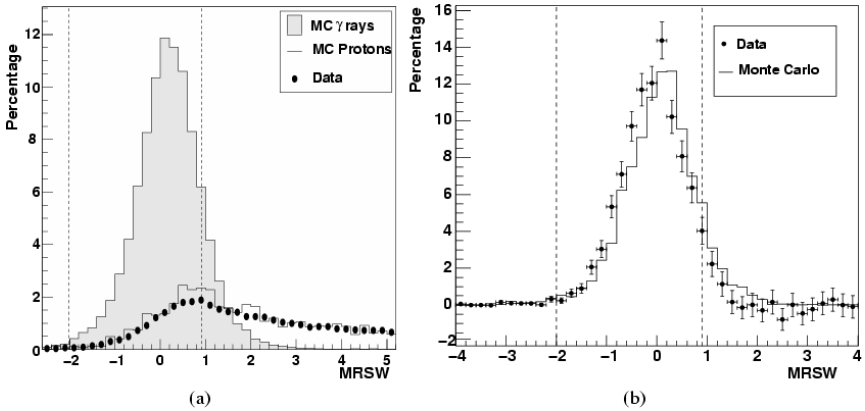

Figure 2.8: **a)** The MRSW distributions for MC γ-ray simulations (spectral index $\Gamma = 2.59$), MC proton simulations ($\Gamma = 2.70$) and real OFF data before selection cuts. **b)** The MRSW distributions for MC γ-ray simulations ($\Gamma = 2.59$) and real data from the direction of the Crab nebula after selection cuts and background subtraction. All distributions are for $ZA = 50°$. Vertical lines denote the H.E.S.S. standard cuts, which are optimised to give the maximum significance for a source with a flux of 10% of Crab nebula flux and with a similar spectrum. The figure is taken from Aharonian et al. [2006a].

eters, the primary particle energy is estimated using a lookup table which contains the mean energy for MC γ-ray simulations as a function of total image amplitude and the simulated true impact parameter. The final reconstructed energy is averaged over the telescopes for each event. H.E.S.S. is capable to reconstruct the photon energy with the resolution of $\Delta E/E < 20\%$.

- *Model Analysis*

  The *model analysis* is a γ-ray likelihood reconstruction technique which is based on the comparison of the raw Cherenkov pixel images of an EAS photon with the predictions from a semi-analytical model for a γ-ray. The semi-analytical description of the shower development determined by the longitudinal, lateral and angular distributions of charged particles in the shower is used to generate a *shower image model* (see Fig. 2.9) for given primary particle energy, direction, impact parameter and a new parameter in the parametrisation – depth of the first interaction. These *shower image models* are then compared to the measured event using a maximum likelihood approach and the parameters of the calculated shower which best fits the measured shower image are determined in the minimisation procedure which yields a selection criteria for the γ/hadron discrimination.

  Similar to the *Hillas reconstruction*, this technique requires event selection cuts (shape cuts) on image amplitude, distance to the center of the camera, tele-

scope multiplicity and θ^2. But in contrast to the *Hillas* technique it does not need any image cleaning procedure, since the contribution of the NSB to every pixel is well modelled based on a detailed statistical analysis.

The hadron discrimination is implemented using the *goodness-of-fit* approach for the comparison of the model prediction to the actual shower images, where the *goodness-of-fit* is defined as a normalised sum over all pixels of the difference between the actual pixel log-likelihood and its expectation value i.e. averaged value of the pixel log-likelihood. For the γ/hadron separation in order to use all differences between γ and hadron showers two kinds of the *goodness-of-fit* variable are defined: *ShowerGoodness* (SG), constructed from the pixels of the *shower core*, i.e. pixels whose predicted intensity is above 0.1 p.e., grouped together with three rows of neighbouring pixels around them, and *Background-Goodness* (BG), constructed from all remaining pixels. SG is more sensitive to discrepancies between the model prediction and the actual shower images due to the large reduction of the number of freedom degrees. BG is sensitive to irregularities outside the main image like hadronic clusters initiated by electromagnetic subshowers. A full description of the *model analysis* can be found in de Naurois and Rolland [2009].

Background Modeling

The modeling of the background is necessary to subtract γ-like proton events which were not reducted in the events selection process. In order to estimate the background a typically larger integration region (OFF region) is taken outside the signal integration region (ON region). The number of excess photons N_γ from the source is calculated as $N_\gamma = N_{\mathrm{ON}} - \alpha N_{\mathrm{OFF}}$, where N_{ON} and N_{OFF} are, respectively, numbers of ON (signal) and OFF (background) events, and α is the normalisation factor between ON and OFF regions. The background modeling can be done in different ways depending on the main task of the analysis (to generate spectrum, sky maps, etc.). In the work presented in this thesis two methods of background estimation were used [Berge et al., 2007]:

- *Ring Background* Model

  In this model, a ring around a test source position is used for the background estimation (Fig. 2.10 (left)). This approach is applied to every point in the FOV, therefore, the resulting map of the excess counts of γ-rays is correlated, since every bin is used as ON and OFF region at the same time. The normalisation α is given by the area ratio of ON and OFF regions modified by a weight factor to account for the radial background acceptance in the camera. Typically α is equal $\sim 1/7$. In this method the camera acceptance can not be assumed as constant within the ring, since the ring covers areas with different offsets from the observation position, i.e. ring pixels are at different distances from the center of the camera, and the camera acceptance is decreasing with increasing distance from the center. Therefore, the acceptance correction function has to

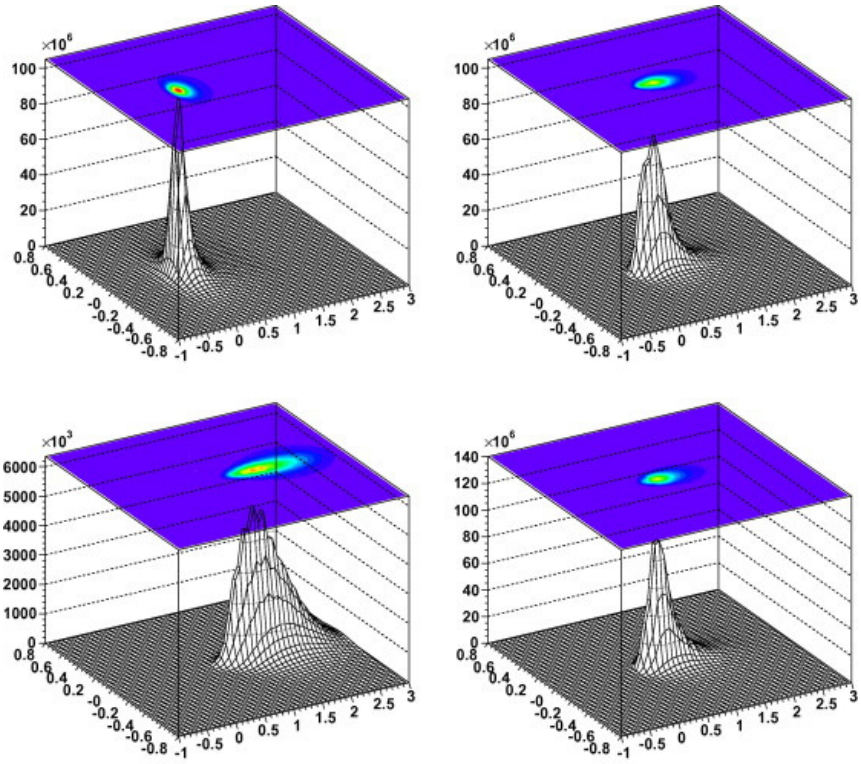

Figure 2.9: Model images of a 1 TeV shower started at one radiation length and falling 20 m (top-left), 100 m (top-right) and 250 m (bottom-left) away from the telescope. Bottom-right: same as top-right but with a higher first interaction depth of 3 radiation lengths. X and Y axes are in units of degrees in the camera frame. The vertical scale denotes the image amplitude. The figure is taken from de Naurois and Rolland [2009].

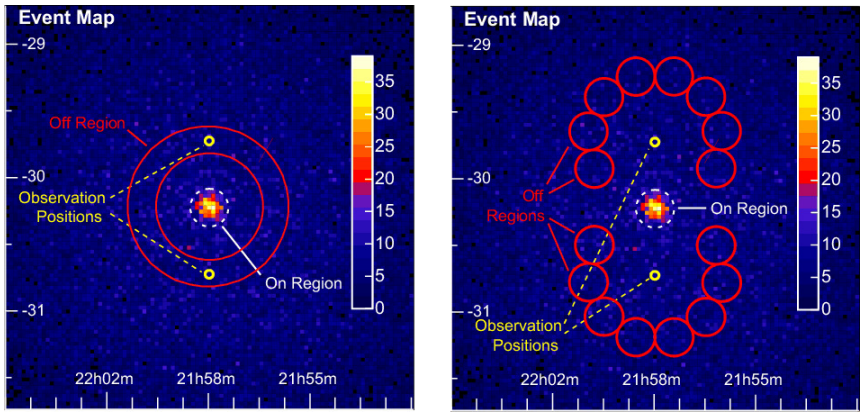

Figure 2.10: **Left:** *Ring Background* model where the background is taken from the ring shaped OFF region around the ON region. **Right:** *Reflected Region Background* model where a number of circular OFF regions at the same distance from the camera center as the ON region are taken. The horizontal axis of each map is Right Ascension and the vertical axis is Declination in J2000 coordinates. The figure is taken from Berge et al. [2007].

be applied for the estimation of α for each position on the ring. This background model is used for extracting skymaps of the observed region, but is disfavoured for the determination of the energy spectrum since it leads to systematical uncertainties due to different offsets of OFF events and dependence of the acceptance function on energy.

- *Reflected Region Background* Model

  In this model, for each test source position a number of OFF regions is used (Fig. 2.10 (right)). Every OFF region has the same shape, size and offset to the observation position like the ON region. The method is called *reflected region* because to get an OFF region one has to reflect the ON region with respect to the observation position. It can be applied to any part of the FoV displaced from the observation position, i.e. FoV center, by the distance larger than the radius of the ON region. Since the offsets of ON and OFF regions are equal, no radial acceptance correction is required and the parameter α is just the ratio of number of ON regions, i.e. one, to the number of OFF regions. The *reflected region background* is mainly used for the spectral analysis since no radial acceptance correction is needed.

3 Supernova Remnants

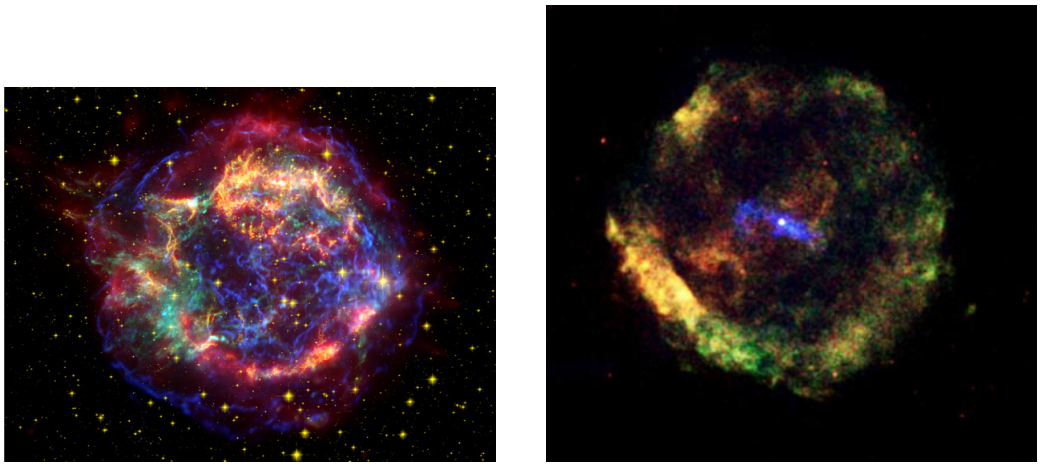

(a) Cas A (b) G11.2-0.3

Figure 3.1: Supernova remnants: a) a composite image of the infrared, optical and X-ray data of Cassiopeia A, one of the most famous shell-like SNRs, b) a composite image of radio and X-ray data of the G11.2-0.3 SNR, a so called "textbook supernova remnant", for its ideal composite morphology, a well resolved shell with a pulsar in the center.

Supernova remnants (SNRs) is one of the best established classes of sources in the VHE sky. Formed in very powerful ($E_0 \simeq 10^{51}$ erg energy) Supernova (SN) explosions at the end of the life cycle of massive stars, they are characterized by fast shock waves expanding into the surrounding circumstellar (gas blown by the progenitor star) or interstellar medium. These shocks are believed to accelerate particles, electrons and protons, to very high energies making SNRs the most plausible candidates for the origin of cosmic rays. Although it is impossible to directly track back the direction of where cosmic ray particles are coming from since they are deflected by magnetic fields and get isotropised, one can indirectly determine the origin by detection of the VHE γ-ray photons produced by electrons and protons through inverse Compton scattering on ambient photon fields and hadronic collisions, respectively (see Chapter 5 for the description of the nonthermal emission mechanisms). Moreover, emitting in all ranges of energies SNRs can be considered as natural laboratories which can be used for the investigation of various physical processes. Physical properties of SNRs strongly depend on the nature of their pro-

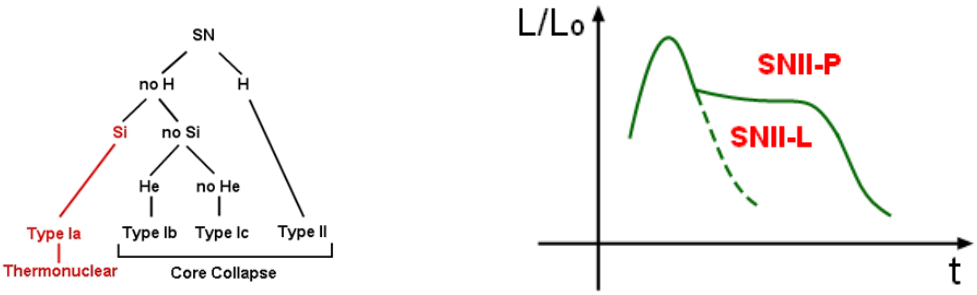

(a) (b)

Figure 3.2: (a) The classification of Supernovae. (b) Typical lightcurve of Type II SNe. A lighcurve with a plateau is typical for Type IIP SNe and a lightcurve with a more linear decline after the maximum intensity is typical for Type IIL SNe.

genitors and on their evolution in the ambient medium. In the following sections, the main properties of different kinds of SN explosions (Section 3.1) and the evolution of SNRs (Section 3.2) are briefly discussed.

3.1 Classification of Supernovae and of Their Remnants

SNRs are basically divided into three main classes according to their morphology:

- *shell-like*, such as Cassiopeia A (Fig. 3.1a)
- *composite*, the shell-like SNR with the compact object (e.g. pulsar) in the center of the remnant, which can be surrounded by an extended nebula (Fig. 3.1b).
- *mixed-morphology* or *thermal composite*, in which thermal X-ray emission from the interior is seen, coming mainly from the swept-up ambient gas and not from the ejecta.

The morphology of an SNR depends on its progenitor (see below) and on the ambient medium. Nevertheless, this classification is very vague and sometimes one SNR can combine properties of two or even all three types at the same time. For instance, the Vela SNR has a strong X-ray interior emission but also contains the Vela pulsar with its pulsar wind nebula Vela X.

The classification of SNe[1] (see Fig. 3.2a) is based on optical spectroscopy, i.e. on the presence or absence of particular features in the optical spectra. SNe were divided into subclasses for the first time in 1941 by Rudolph Minkowski based on the Hydrogen (H) line in their spectra. SNe which show H in their optical spectra were

[1]The classification of SNe is discussed basing on the reviews Reynolds [2008] and Vink [2004].

considered as Type II and those that did not as Type I. The following classification of Type I SNe is based on the presence of Silicon (Si) and Helium (He) lines in the spectra. Type Ia SNe have Si in their spectra, Type Ib SNe do not have Si but have He and, finally, Type Ic SNe have neither Si nor He. According to the underlying explosion mechanism two broad classes can be distinguished: core-collapse SNe (all types except Type Ia) and thermonuclear SNe (Type Ia).

Type Ia SNe are believed to result from the thermonuclear disruption of carbon-oxygen (C-O) white dwarfs, caused by the increasing of the mass. It is, however, still not known what causes the increase of the mass (accretion of the mass from the companion star, collision of two white dwarfs, etc.) and what is the disruption mechanism (detonation, deflagration, delayed detonation). Nevertheless, the most plausible mechanism of the Type Ia SN explosion is discussed in the following. White dwarfs accrete the material from the companion star increasing their density and temperature. When their mass is close to the Chandrasekhar upper limit of $1.38 M_{\odot}$ the temperature in the core reaches the ignition temperature for C-O fusion. The deflagration burning front slowly spreads towards outer layers leaving iron-peak elements created as a result of the burning behind. Due to different kinds of instabilities large-scale convective processes start which lead to the strengthening of thermonuclear synthesis and the production of an energy of about 10^{51} erg which is needed for the explosion. Due to the known and the same for all Type Ia SNe mass before the explosion the luminosity is known and the SNe can be used for distance estimation, i.e. as standard candles in cosmology.

All other SNe are the explosions of massive stars caused by the core-collapse. The thermonuclear fusion of H and He creates heavier elements in a star. In the process of the nuclear synthesis a star is being compressed and the fusion of heavier elements is starting. If the mass of the star is big enough ($\gtrsim 8 M_{\odot}$) the process of the thermonuclear synthesis ends with the creation of an iron (Fe) core and the star obtained the onion-like shape consisting of layers of different elements (Fig. 3.3, Fig. 3.4a). The nuclear synthesis continues in the outer layers but not in the Fe core. The star continues to contract and when the mass of the Fe core reaches the Chandrasekhar limit the core starts to collapse (Fig. 3.4b), the inner core converts into neutrons (Fig. 3.4c) and a large part of the gravitational energy converts into neutrinos. After that the outer shell falls onto the core and bouncing back creates a shock wave (Fig. 3.4d) expanding from the core and initiating thermonuclear processes (Fig. 3.4e). During this process, a large amount of energy is being released which suffices to eject the shell (Fig. 3.4f).

According to the shape of the lightcurve Type II SNe can be divided into two subclasses (Fig 3.2b). The lightcurve for the Type IIL SN shows a stable linear decline after the maximum light emission while in the lightcurve for the Type IIP SN a "plateau" appears. This is explained by the different depth of the H layer. The propagating shock wave ionises H atoms in the outer H envelope creating the layer of ionised H^+ which has a high opacity and prevents photons from the inner parts from escape. After some time the outer parts of the star get cooled enough for

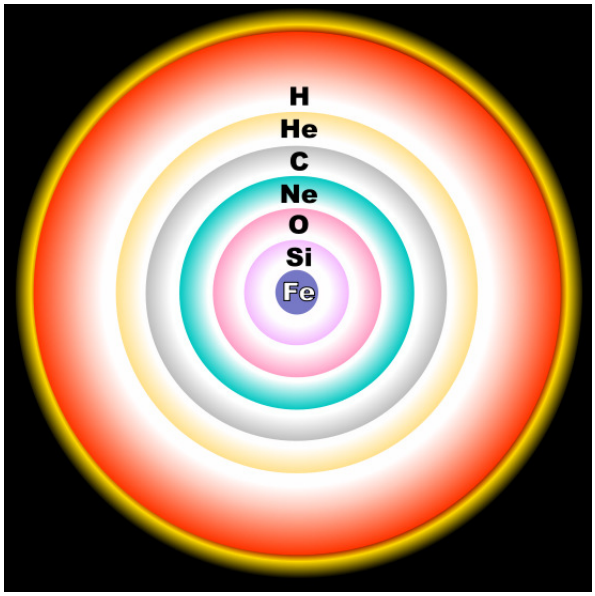

Figure 3.3: A simplified onion-like structure of a massive ($\gtrsim 8M_{\odot}$) star which consists of concentric shells of Hydrogen (H), Helium (He), Carbon (C), Neon/Magnesium (Ne), Oxygen (O) and Silicon (Si). Burning of Si creates an iron (Fe) core.

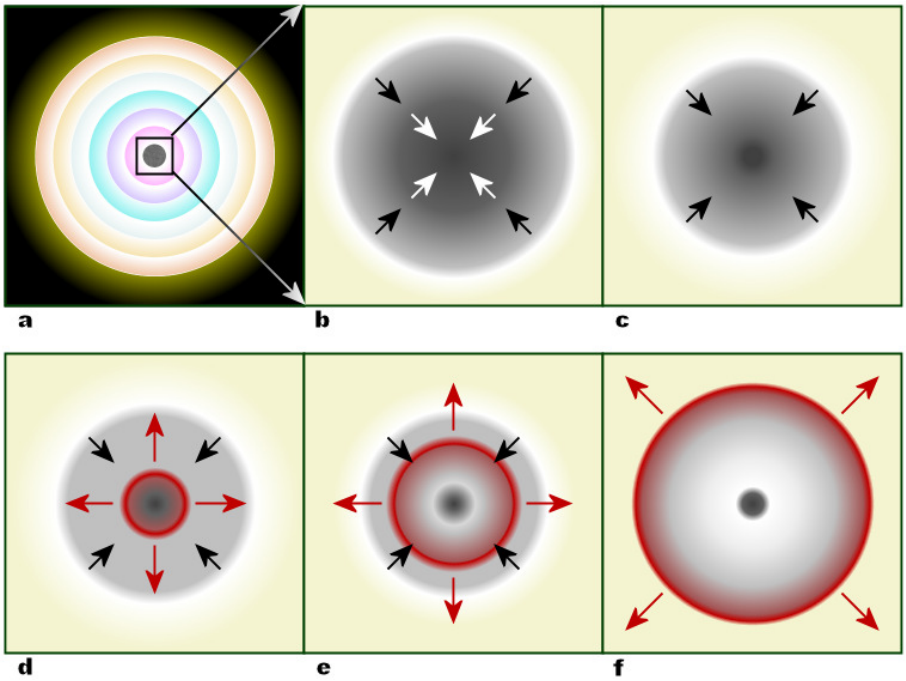

Figure 3.4: Schematic stages of the mechanism of the core-colapse explosion. See description in the text.

ionised H^+ to recombine and form neutral H which is more transparent and allows to see deeper into the star. With the expansion of the star and propagation of the neutral H layer (photosphere) deeper into the star the plateau is created in the lightcurve. Type IIP SNe are expected to result from the explosion of H rich red supergiants (RSGs) and Type IIL SNe from the explosion of supergiants with lower-mass H envelopes.

The Type IIn subclass is defined on the basis of the narrow H emission lines in the spectra of SNe. The light observed from these SNe is believed to originate not from the SN itself but from the interaction with the circumstellar medium. It is not clear if SNe of this subclass originate from a core-collapse of a massive star or from the thermonuclear burning of white dwarfs.

The SNIIb subclass is distinguished according to a very weak emission of H and is very similar to Type Ib and Type Ic SNe. All of them are believed to result from the explosion of very massive stars in binary systems where much of the star's mass is lost due to the transfer to a companion star and due to a stellar wind. Due to this a large fraction (Type IIb) or the whole (Type Ib) H envelope can be lost or even both H and He envelopes can be lost (Type Ic). Type Ib and Type Ic presumably result from the explosion of Wolf-Rayet stars which also lack H in their spectra.

Although the explosion mechanism is different, the explosion energy is similar for all types of SNe. Therefore, the determination of the SN type for a particular SNR is usually a difficult task. Nevertheless, if an SNR is accompanied by a compact object it is clear that it is a core-collapse remnant. Otherwise, to identify a SN type one should use abundance measurements.

3.2 Evolution of Supernova Remnants

The Supernova explosion is followed by the ejection of the star's material into the ambient medium, a gas lost by the progenitor star in previous stages of its evolution. The structure formed by the SN explosion is called Supernova remnant. The expansion of the SNR is accompanied by the creation of two shocks: one of them expands into the interstellar medium and another one (reverse shock) inside the remnant. The spatial evolution of an SNR with time can be divided into three stages: **free expansion** (blast wave), **adiabatic** (Sedov) stage and **radiative cooling** or so called snow plough stage. After this an SNR is slowly merging with the interstellar medium (see Fig. 3.5). In this section, a short review of each stage with analytical models of the hydrodynamical expansion is presented. For more information please consult Lozinskaya [1992], Longair [1994], Padmanabhan [2001].

Free Expansion Stage

Right after explosion the shell consisting of ejecta material is still so thick that it expands without any resistance. The explosion energy of a supernova is transfered almost completely into the kinetic energy of the remnant's expansion, the fraction of the thermal energy is only $2-3\%$ of the total explosion energy. The speed of the shell expansion can reach $(10-20)\times 10^3$ km/s, which exceeds the speed of sound

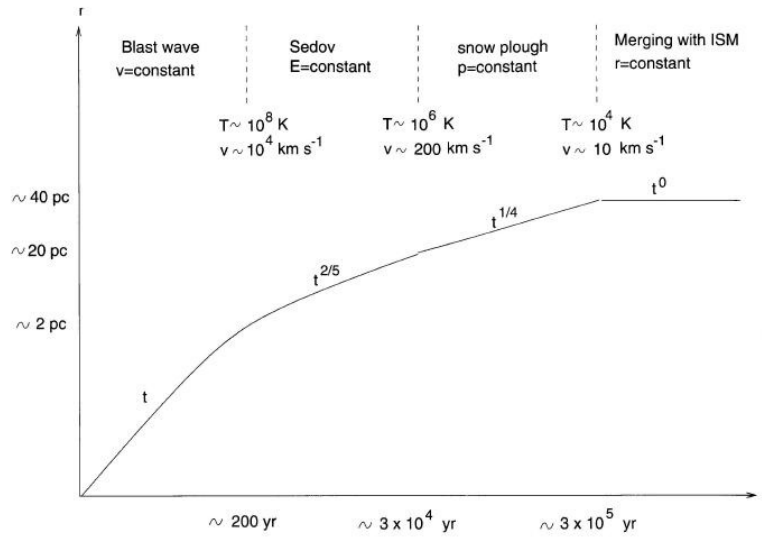

Figure 3.5: The radius of the SNR as a function of time at different evolution stages [Padmanabhan, 2001]

in the ISM by far. The ejected material moving supersonically into the interstellar gas sweeps up the gas up forming a shock front between the swept-up gas and the uncompressed ambient medium. With the movement of the shock front more and more material passes through it and is compressed and heated to extremely high temperatures of $\sim 10^9$ K. As long as the total mass of the swept-up gas is small in comparison to the mass of the ejected material, the shell is expanding freely. This can last for several centuries until the mass of the swept-up ambient gas reaches the mass of the ejected material. This moment corresponds to the radius

$$R_{\text{free}} = \left(\frac{3}{4\pi\rho} M_{\text{ejecta}}\right)^{1/3} = 2\left(\frac{M_{\text{ejecta}}}{1M_{\odot}}\right)^{1/3}\left(\frac{n_{\text{H}}}{1\text{cm}^{-3}}\right)^{-1/3}[\text{pc}] \tag{3.1}$$

and age

$$\begin{aligned} t_{\text{free}} &= \frac{R_{\text{free}}}{v} = R_{\text{free}}\left(\frac{2E_0}{M_{\text{ejecta}}}\right)^{-1/2} \\ &= 190\left(\frac{E_0}{10^{51}\text{erg}}\right)^{-1/2}\left(\frac{M_{\text{ejecta}}}{1M_{\odot}}\right)^{5/6}\left(\frac{n_{\text{H}}}{1\text{cm}^{-3}}\right)^{-1/3}[\text{years}], \end{aligned} \tag{3.2}$$

where M_{ejecta} is the total mass of the ejected material, ρ is the density of the ISM, n_{H} is the hydrogen density of the ISM and v is the speed of the shock front. It is also assumed that the whole explosion energy E_0 was transferred into the kinetic energy of the remnant expansion.

Adiabatic Stage

When the mass of the swept-up gas becomes greater than the ejected mass the effective deceleration starts, i.e. the expansion velocity begins to decrease. On the other hand, energy losses due to radiation processes are still negligible in comparison to the initial explosion energy. It can be assumed that the remnant is expanding almost without energy losses, i.e. adiabatically. The dynamics of the remnant can be well described by the Sedov adiabatic blast-wave similarity solution [Sedov, 1959]:

$$R = \left(\frac{2.4(\gamma+1)}{\pi}\frac{E_0}{\rho}\right)^{1/5} t^{2/5} \simeq 0.3 \left(\frac{E_0}{10^{51}\mathrm{erg}}\right)^{1/5} \left(\frac{n_\mathrm{H}}{1\mathrm{cm}^{-3}}\right)^{-1/5} \left(\frac{t}{1\mathrm{year}}\right)^{2/5} [\mathrm{pc}] \tag{3.3}$$

$$v = \frac{dR}{dt} \simeq 1.2 \times 10^5 \left(\frac{E_0}{10^{51}\mathrm{erg}}\right)^{1/5} \left(\frac{n_\mathrm{H}}{1\mathrm{cm}^{-3}}\right)^{-1/5} \left(\frac{t}{1\mathrm{year}}\right)^{-3/5} [\mathrm{km/s}] \tag{3.4}$$

$$T = \frac{2(\gamma-1)}{(\gamma+1)^2}\frac{\mu m_\mathrm{H}}{k} v^2 \simeq 2 \times 10^{11} \left(\frac{E_0}{10^{51}\mathrm{erg}}\right)^{2/5} \left(\frac{n_\mathrm{H}}{1\mathrm{cm}^{-3}}\right)^{-2/5} \left(\frac{t}{1\mathrm{year}}\right)^{-6/5} [\mathrm{K}] \tag{3.5}$$

where $\gamma = 5/3$ is the adiabatic index, T is the temperature at the shock, k is the Boltzman constant and μ is the average mass per particle in hydrogen mass units[2]. The equations presented above are derived for a homogeneous medium, but for more complicated cases with different inhomogeneities also analytical models exist, e.g. the White&Long solution [White and Long, 1991] for the evolution of the SNR in the cloudy medium, used for instance in the hydrodynamical modeling of the Vela SNR expansion [Sushch et al., 2011].

The significant deceleration of the expansion leads to the formation of the reverse shock. The outer layers of the expanding sphere are decelerated first and thus material inside the sphere begins to catch up with the material in outer layers. Therefore, the density at the boundary of the expanding sphere starts to increase. As the deceleration continues, the flow of the material into the outer layers becomes supersonic relative to the sound speed inside the sphere and therefore a shock wave forms on the inner edge of the compressed outer layers. This results in reheating of the material inside the remnant, which was cooled during the adiabatic stage.

These first two stages are important for this thesis since the SNRs investigated here are in these stages of evolution. G1.9+0.3 is the youngest SNR in the Galaxy whose age could be estimated from direct observation of its expansion. The age of about 100 years suggests the free expansion stage. The age estimate for G330.2+1.0 is higher, at the level of 1000 years, which very likely places it in the second, adiabatic, phase of evolution. Among well-known SNRs, for example for Cassiopeia A, the mass ratio is estimated to be about unity, what makes it intermediate between phases. The adiabatic stage is well presented among supernova remnants – such SNRs as Vela, Tycho, RX J1713-3946 and Puppis A are associated with this stage of

[2]For a helium/hydrogen abundance ratio of 1/10 μ is equal 14/23.

the evolution.

Radiative Cooling Stage

The adiabatic stage lasts until the effective radiative cooling starts, when energy losses are not negligible anymore compared to the initial explosion energy. It starts when the temperature in the region behind the shock front drops below 10^6 K and cooling by line emission of heavy ions becomes important. Radiative cooling of the shell makes it shrink and increases its density in order to preserve the pressure balance with the hot interior. The dense thin shell moves with approximately constant radial momentum piling up interstellar gas like a snow plough piles up snow[3]. The simplest way to describe the dynamics at this stage is the approximation of the momentum conservation:

$$\frac{d}{dt}\left(\frac{4\pi}{3}\rho R^3 \dot{R}\right) \approx 0. \tag{3.6}$$

This leads to the motion equations:

$$R = R_{\mathrm{sf}}\left(1 + \frac{v_{\mathrm{sf}}}{R_{\mathrm{sf}}}(t - t_{\mathrm{sf}})\right)^{1/4} \tag{3.7}$$

$$v = v_{\mathrm{sf}}\left(1 + \frac{v_{\mathrm{sf}}}{R_{\mathrm{sf}}}(t - t_{\mathrm{sf}})\right)^{-3/4} \tag{3.8}$$

where R_{sf}, v_{sf} and t_{sf} are the radius, the expansion speed and the point in time where the dense shell formed. Cioffi et al. [1988] suggest another approach called the *pressure-driven snowplow* (PDS) in which there are no energy losses from radiation for the interior material and the shell is driven by the pressure of the hot interior in addition to its own momentum. This approximation results in a slightly different dependence on time $R \propto (t - t_{\mathrm{PDS}})^{3/10}$, where t_{PDS} denotes the beginning of the PDS stage, which is slightly before t_{sf}[4]. For more details please consult Cioffi et al. [1988] and references therein.

Older remnants, such as the Cygnus Loop (about 50000 years old) are associated with this stage of the evolution. The stage can be identified by the optical line emission of ions (e.g. Oxygen and Sulphur) observed from the filaments of the shell, which are associated with cooling gas.

Eventually, the expansion becomes subsonic and the supernova remnant loses its identity dispersing by random motions in the interstellar medium. The Gum Nebula, a huge ($\sim 15^\circ$ in radius which corresponds to about 100 pc) and old (about 1 Myr) structure, which is believed to be an SNR of the companion of the very hot star ζPuppis [Woermann et al., 2001], can serve a good example of a dispersed SNR.

It has to be mentioned that the evolution of SNRs with central energy sources is somewhat different, mainly because there is a constant supply of energy from the central pulsar.

[3] This comparison was first used by Oort as he described the dynamics of the shell with the solution of the *momentum conserving snowplow* with $R \propto t^{1/4}$ [Oort, 1951].

[4] In Cioffi et al. [1988], it is assumed that $t_{\mathrm{PDS}} \equiv t_{\mathrm{sf}}/e$, where e is the base of the natural logarithm.

4 Pulsars, Pulsar Wind Nebulae and Plerionic Binaries

Pulsar wind nebulae (PWNe) together with SNRs are the most numerous classes of Galactic VHE objects. At the moment, about 30 TeV sources are identified as PWNe which is about 20 % of all TeV sources, galactic and extragalactic. In Fig. 4.1, the whole sky-map of known TeV γ-ray PWNe is shown. As one can see most PWNe are situated in the Galactic plane and in the part of the sky which is best visible to the H.E.S.S. experiment. The most prominent source of this type is the Crab Nebula - the first detected source in TeV γ-ray astronomy.

Recently, pulsed emission from the Crab pulsar was detected by the MAGIC (25–100 GeV) and VERITAS (above 100 GeV) experiments [MAGIC Collaboration et al., 2011, VERITAS Collaboration et al., 2011] which constitutes the first detection of a pulsar at VHEs. This discovery revealed a pulsed VHE flux density higher than expected before, making the Crab pulsar one of the main targets for H.E.S.S. II with its extended energy coverage down to 20 GeV.

Another relatively small class of TeV sources is the class of γ-ray binary systems which consist of a massive star and a compact object like a pulsar or a black hole. Recently, a new representative HESS J0632+057 was added to three well-established members of the class LS 5039 [Aharonian et al., 2005b], LS I +61 303 [Albert et al., 2006] and PSR B1259−63/LS 2883[Aharonian et al., 2005c]. Discovered in 2007 [Aharonian et al., 2007c] HESS J0632+057 was identified as a TeV γ-ray binary in 2011 [Bongiorno et al., 2011] and became the first binary discovered on the basis of TeV observations. This class can be extended by Cygnus X-1 [Albert et al., 2007], a stellar mass black hole binary detected at VHEs at the 4.1 σ significance level, and HESS J1018-589 [HESS Collaboration et al., 2012] which is coincident with the GeV binary 1FGL J1018.6-5856 recently discovered by the Fermi-LAT collaboration [Abdo et al., 2010]. Only for one of these sources, PSR B1259−63/LS 2883, the compact companion is well identified as a pulsar.

The following subsections will present the mentioned source types in more detail. The pulsar and PWNe subsections will mainly follow the book by Aharonian [2004] and the reviews by Gaensler and Slane [2006] and de Jager and Djannati-Ataï [2008]. The review of Be stars mainly follows Tavani and Arons [1997] and Waters et al. [1988]. For more information check also Lamers et al. [1998].

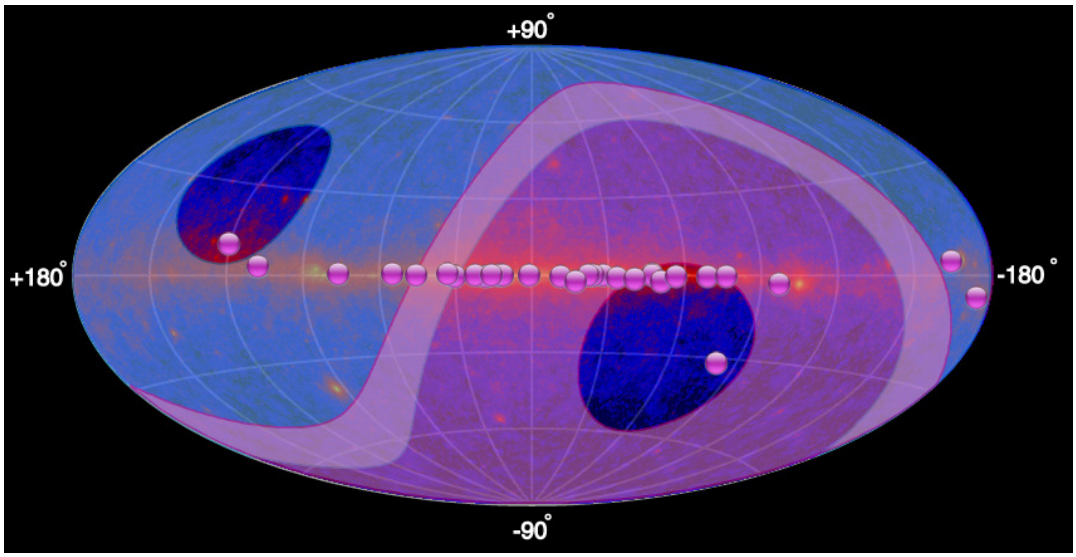

Figure 4.1: The skymap of known TeV γ-ray PWNe in Galactic coordinates superinposed with a Fermi skymap. PWNe are shown as violet filled circles. The violet region indicates the part of the sky best visible to the H.E.S.S. experiment while the blue region shows the part best visible to norther hemisphere experiments, such as VERITAS and MAGIC. The plot is taken from TeVCat: http://tevcat.uchicago.edu/.

4.1 Pulsars and Pulsed Emission

Pulsars are rapidly rotating and highly magnetized neutron stars which are created as a result of a core-collapse SN event. Masses of pulsars vary in the range from 1.38 to 2–3 $M_\odot$ with a corresponding diameter of $\sim$ 12 km. A star with a mass lower than the Chandrasekhar limit of 1.38 $M_\odot$ ends its evolution as a white dwarf. The Chandrasekhar limit denotes the mass above which the electron degeneracy pressure in the core of the star is unsufficient to balance the gravitational self-accretion. Stars with masses greater than this limit undergo further gravitational collapse, electrons are compressed and captured by protons forming neutrons which is followed by the emission of neutrinos. Such a collapse results in the formation of a compact neutron star. The upper limit on the mass of the progenitor star is the Tolman-Oppenheimer-Volkoff (TOV) limit. This limit is an analogous limit to the Chandrasekhar limit but for degenerate neutron matter. Stars with masses which exceed the TOV limit collapse to some denser form like black holes.

The first pulsar (PSR B1919+21) was detected in 1967 by J. Bell and A. Hewish by its pulsating radio signal. A periodic signal on timescales from ms to s in different energy bands is still the main feature of pulsars. Despite the fact that a lot of time has passed since the first detection accompanied by a large amount of observations in various wavebands the mechanisms of the pulsar multiwavelength emission as well as the nature of their lightcurves are not yet fully resolved.

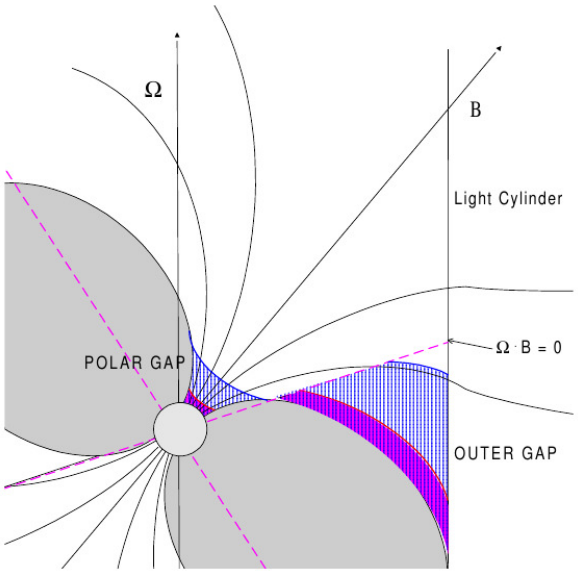

Figure 4.2: A schematical cartoon describing the polar cap and outer gap regions. Pink regions are thin gaps of younger pulsars and hatched regions are thick gaps of older pulsars. The plot is taken from Aharonian [2004].

It is believed, however, that the pulsed emission originates in the powerful co-rotating magnetosphere of the pulsar. Pulsars carry enormous magnetic fields, typically $10^{12} - 10^{13}$ G at the surface, assumed to be simply the field of a dipole, which is not aligned with the pulsar's rotation axis and, therefore, rotates together with the pulsar. The magnetic field lines are frozen into the surrounding electron-positron plasma, which is forced to co-rotate together with the neutron star. This plasma may originate from electrons and positrons ripped out from the neutron star surface by a very high electric field. The primary particles are immediately accelerated and induce pair cascades producing more electrons and positrons. The co-rotating magnetosphere of the pulsar is limited by the light cylinder, a surface where the co-rotating plasma is moving with the speed of light. The radius of the light cylinder is $R_{\rm LC} = c/\omega$, where ω is the angular velocity. Outside the light cylinder the plasma does not co-rotate and, thus, the magnetic field is distorted. Magnetic field lines emerging at the polar caps cross the light cylinder and are not closed. In order to explain the observed pulsed emission up to γ-rays, there should be places where electrons are accelerated to very high energies. This can occur in the regions where the co-rotation condition $\mathbf{E} \cdot \mathbf{B} = 0$ is not maintained, i.e. the parallel electric field is not equal 0. These regions can exist close to the surface of the neutron star in the polar caps or at distances comparable with the light cylinder along the null charge surface defined by the condition $\Omega \cdot \mathbf{B} = 0$ (Ω is the rotation vector), where the co-rotation charge density changes sign in the, so called, outer gaps.

The pulsed radio emission is very bright, reaching brightness temperatures of

$10^{23} - 10^{30}$ K and, therefore, is very likely generated coherently by a beam of relativistic electrons. The radio beam is very narrow and is believed to originate in magnetic polar caps. Since the magnetic dipole vector is not aligned with the rotation axis the radio beam is corotating with the neutron star causing the so called lighthouse effect, i.e. the radio beam is visible only if it crosses the Earth. The emission from optical/IR to γ-rays is not coherent and emission beams are expected to be wider. In the IR/optical and X-rays bands, the emission may have a thermal and/or nonthermal origin. The specific mechanisms for the radio as well as IR/optical and X-ray emission remain highly uncertain. For the γ-ray emission the situation is somewhat clearer. Three γ-ray production mechanisms: curvature radiation, synchrotron radiation and inverse Compton scattering – can effectively contribute to the γ-ray radiation from MeV to TeV.

4.1.1 The Time Evolution of Pulsars

In the absence of accretion of matter (e.g. from a companion star) the rotational energy of the neutron star is the only source of the energy responsible for the emission from the pulsar. The rotational energy of the pulsar, $E_{\rm rot}$, is given by the equation

$$E_{\rm rot} = \frac{1}{2} I \Omega^2 \tag{4.1}$$

where $\Omega = 2\pi/P$ and I is the pulsar's moment of inertia and is usually assumed to have the value 10^{45} g cm^2. The slow down of the pulsar implies a loss of rotational kinetic energy, the pulsar's spin-down luminosity, defined as

$$\dot{E} = -\frac{dE_{\rm rot}}{dt} = 4\pi^2 I \frac{\dot{P}}{P^3}, \tag{4.2}$$

where P is the spin period of the pulsar and $\dot{P}$ is the period time derivative. Values of the spin-down luminosity for the observed pulsars range between $\sim 5 \times 10^{38}$ erg/s for the Crab pulsar down to 3×10^{28} erg/s for the slowest known pulsar PSR J2144−3933.

P and $\dot{P}$ can provide expressions for the age and the surface magnetic field of a neutron star following certain assumptions. Assuming theat the neutron star spins down such that $\dot{\Omega} = -k\Omega^n$, the age of the star is

$$\tau = \frac{P}{(n-1)\dot{P}} \left[1 - \left(\frac{P_0}{P} \right)^{n-1} \right], \tag{4.3}$$

where P_0 is the initial spin period, k is assumed to be a constant and n is the braking index, $n \neq 1$. The braking index has been confidently measured only for five pulsars [Livingstone et al., 2007] for each of them being in the range $2 < n < 3$. A braking index of $n = 3$ corresponds to the spin down of the pulsar due to the magnetic dipole radiation. Assuming $n = 3$ and $P_0 \ll P$, Eq. 4.3 reduces to the expression for

the characteristic age of a pulsar,

$$\tau_c \equiv \frac{P}{2\dot{P}}. \tag{4.4}$$

Note, that the characteristic age can both overestimate (if P_0 is not much smaller than P) and underestimate (if the real braking index is $n < 3$) the true age of the pulsar.

In the case of the dipole magnetic field, the constant k is connected to the magnetic field as $k = 2M_\perp/3Ic^2$, where $M_\perp$ is the component of the magnetic dipole moment orthogonal to the rotation axis. The equatorial surface magnetic field can be then given by

$$B_{eq} \equiv 3.2 \times 10^{19} (P\dot{P})^{1/2} \mathrm{G}. \tag{4.5}$$

Values for B_{eq} range between 10^8 G for millisecond pulsars (pulsars with rotational periods of 1-10 ms) up to $> 10^{15}$ G for magnetars (pulsars with very powerful magnetic fields, whose decay powers the electro-magnetic emission).

For constant n the spin-down luminosity $\dot{E}$ evolves as

$$\dot{E} = \dot{E}_0 \left(1 + \frac{t}{\tau_0}\right)^{-\frac{n+1}{n-1}}, \tag{4.6}$$

where $\dot{E}_0$ is the initial spin-down luminosity and

$$\tau_0 \equiv \frac{P_0}{(n-1)\dot{P}_0} = \frac{2\tau_c}{n-1} - t \tag{4.7}$$

is the initial spin-down time scale of the pulsar. For $t \ll \tau_0$ the pulsar has roughly constant energy loss and for $t \gg \tau_0$ the spin-down luminosity evolves as $\dot{E} \propto t^{-(n+1)/(n-1)}$.

The spin period of the pulsar evolves similarly:

$$P = P_0 \left(1 + \frac{t}{\tau_0}\right)^{\frac{1}{n-1}}, \tag{4.8}$$

so that for $t \ll \tau_0$ spin period is not changing, i.e. $P \approx P_0$ and for $t \gg \tau_0$ the period evolves as $P \propto t^{1/(n-1)}$.

4.2 Pulsar Wind Nebulae and Their Evolution

Rotation powered pulsars are believed to eject an electron-positron plasma in the form of relativistic winds that carry off most of rotational energy of the pulsars. The pulsar wind (PW) escaping from the light cylinder terminates at the standing shock where particles get accelerated to energies of $\sim 10^{15}$ eV randomising their velocities directions. Not being frozen in the magnetic field anymore electrons start to emit synchrotron radiation forming an extended nebula, usually called pulsar wind

nebula (PWN). Inverse Compton scattering of accelerated electrons on CMB photons and other surrounding photon fields and posibly photons created in hadronic interactions expand the broadband emission of PWNe up to multi-TeV energies.

4.2.1 The Wind Zone and Termination Shock

Pulsar winds are characterised by the ratio of the electromagnetic energy flux to the kinetic energy flux of particles in the wind – the magnetization $\sigma \equiv B^2/(4\pi\rho\gamma c^2)$, where B, ρ and γ are the magnetic field, mass density of particles and Lorentz factor in the wind, respectively. At $\sigma \geq 1$ the wind is dominated by the Poynting flux and at $\sigma \leq 1$ the wind is kinetic energy dominated. Observations of PWNe imply a σ parameter which does not exceed 1, in particular for the Crab Nebula it is estimated to be about 10^{-3}. On the other hand, all models of electron-positron pair production in the pulsar magnetosphere predict $\sigma \sim 10^3 - 10^4$, so somewhere between the light cylinder and the termination shock a phase transition of the wind must take place. The mechanism of such a phase transition and the formation of the kinetic energy dominated wind is not yet understood. This transition cannot be directly observed since electrons, although they may reach energies as large as 10^{13} eV, move together with the magnetic field and thus do not emit synchrotron radiation. However, there is a possibility of observing the unshocked kinetic energy dominated PW through its inverse Compton radiation caused by the external photon fields.

The wind termination shock is formed at the radius $R_{\rm TS}$, where the ram pressure of the wind is balanced by the total internal pressure of the PWN $P_{\rm PWN}$ (see Fig. 4.3b):

$$R_{\rm TS} = \sqrt{\frac{\dot{E}}{4\pi c P_{\rm PWN}}}. \tag{4.9}$$

Typical PWN internal pressure and spin-down luminosity values yield termination shock radii of order 0.1 pc.

4.2.2 The Evolution of the PWN

Since the pulsar is the stellar remnant of the SN explosion, it is initially surrounded by an expanding SNR. Obviousely, its PWN is also expanding into the SNR interior. The random space velocity of about ~ 500 km s^{-1} given to the pulsar due to the asymmetry in the SN explosion is considerably lower than the SNR blast wave speed, which can reach $(10 - 20) \times 10^3$ km s^{-1} (see Section 3.5). Therefore, at early phases the pulsar is located near the center of the SNR.

At early stages the pulsar is located in the slowly moving unshocked explosion ejecta. The energy loss is almost constant and the pulsar wind is highly "overpressured" with respect to its environmet, and, therefore, the PWN expands rapidly, moving supersonically into the ejecta. For the spherically symmetric case, the evo-

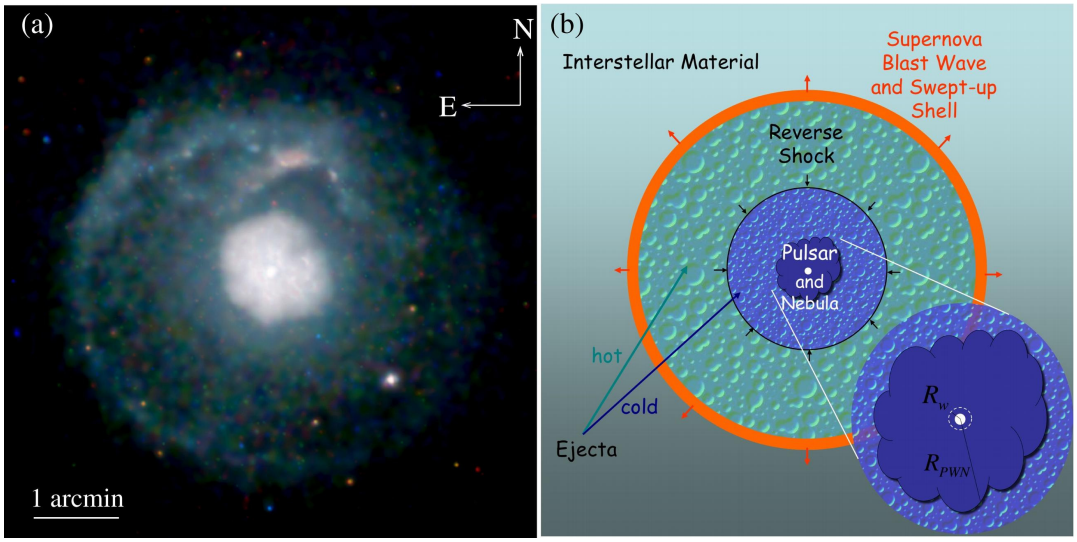

Figure 4.3: a) A deep *Chandra* X-ray image of the composite SNR G21.5-0.9. A spherically symmetric SNR surrounds a ~ 5 times smaller spherical PWN with the young pulsar J1833−1034 at the center. b) A schematic cartoon of a composite SNR, which shows the swept-up ISM shell, hot and cold ejecta separated by the reverse shock and the pulsar in the center surrounded by its nebula. At the expanded PWN view the termination shock can be seen. The figure is taken from Gaensler and Slane [2006].

lution of the PWN radius is given by [Chevalier, 1977]

$$R_{\rm PWN} \approx 1.1 \left(\frac{\dot{E}_0}{10^{38}\,{\rm erg\,s^{-1}}}\right)^{\frac{1}{5}} \left(\frac{E_{\rm SN}}{10^{51}\,{\rm erg}}\right)^{\frac{3}{10}} \left(\frac{M_{\rm ejecta}}{10 M_\odot}\right)^{-\frac{1}{2}} \left(\frac{t}{10^3\,{\rm y}}\right)^{\frac{6}{5}} [{\rm pc}], \qquad (4.10)$$

where $R_{\rm PWN}$ is the radius of the PWN's forward shock at time t, $E_{\rm SN}$ is the total energy produced in the SN explosion and $M_{\rm ejecta}$ is the ejected mass released in the SN explosion. At this early stage the PWN expansion velocity is steadily increasing as $\propto t^{1/5}$ and is typically higher than the pulsar's velocity, the PWN remains centered on the pulsar. A good example of a system at this early stage of evolution is the pulsar J1833−1034, which powers a bright X-ray and radio PWN, which, in turn, is located in the center of the young (~ 1000 y) SNR G21.5-0.9 (Fig. 4.3a).

When the SNR sweeps up a significant amount of the ambient gas and moves into the adiabatic stage of the evolution the reverse shock is formed and moves inside the remnant (see Section 3.5). Assuming that the SNR is expanding into a homogenous medium and that there is no central source, the reverse shock reaches the SNR center in a time [Reynolds and Chevalier, 1984]

$$t_{\rm RS} \approx 7 \left(\frac{M_{\rm ejecta}}{10 M_\odot}\right)^{\frac{5}{6}} \left(\frac{E_{\rm SN}}{10^{51}\,{\rm erg}}\right)^{-\frac{1}{2}} \left(\frac{n_0}{1\,{\rm cm^{-3}}}\right)^{-\frac{1}{3}} [{\rm ky}], \qquad (4.11)$$

where n_0 is the number density of the ambient gas. If the pulsar is located inside the remnant the inward moving reverse shock collides with the outward moving PWN at a time less than t_{RS}, typically a few thousands years. The reverse shock strongly compresses the PWN, which results in the increase of the internal pressure and, thus, a sudden expansion. This can be repeated several times leading to an oscillation of the nebula on the time scale of few thousands years and to the increase of the nebular magnetic field. Eventually, the PWN crushes producing Rayleigh-Taylor instabilities which can result in the filamentary structure. By the time of the collision of the PWN with the reverse shock the pulsar has already moved away from the SNR center due to its space velocity. Moreover, the SNR may expand asymmetrically causing an asymmetrical inward movement of the reverse shock. This results in a very distorted morphology of the PWN which can be significantly displaced from the pulsar position. A good example of such a system is the Vela SNR with the Vela pulsar and its PWN Vela X.

When the oscialltion of the PWN described above subsides, the pulsar can power a steadily expanding nebula again. However, since the SNR interior is shocked, the PWN expands into the hot ejecta at subsonic speeds. The radius of the PWN evolves as $R_{PWN} \propto t^{11/15}$ in the case of a young pulsar and constant spin-down luminosity or as $R_{PWN} \propto t^{3/10}$ ($n = 3$) if the pulsar age is $t > \tau_0$. At this stage, the distance travelled by the pulsar from the SNR center may exceed the size of the PWN. The pulsar may escape the PWN turning it into a so called "relic PWN" and generate a new, smaller one.

The sound speed in the SNR interior gas drops as the pulsar moves from the center to the edge of the remnant. At some point the pulsar's motion becomes supersonic and a bow shock is created. For an SNR at the adiabatic stage, the transition to a bow shock occurs when the pulsar has travelled 68 % of the distance between the center and the shell. Eventually, the pulsar escapes the SNR, which is typically happening at an age of about 40000 years.

4.3 Plerionic TeV γ-ray Binaries

Binary systems are well know non-thermal emitters from radio to VHEs. Although at VHEs it is a relatively young class with just four representatives, in the X-ray waveband about 300 binary systems are detected. These systems consist of a compact object (a neutron star or a black hole) orbiting around a massive star companion. Depending on the mass of the stellar companion binary systems are devided into high mass X-ray binaries (HMXB) with a companion star of a spectral type O or B and low mass X-ray binaries (LMXB) of a spectral type later than B. Another discrimination of binary systems is based on the type of the non-thermal emission mechanism. Non-thermal emission is believed to be created either by particles accelerated during the accretion process of the matter from the massive stellar companion onto the compact object (microquasars) or alternatively by particles accelerated in shocked wind zones between pulsar and stellar winds (plerionic binaries). The

second scenario takes place only for systems with powerful enough pulsars with a high spindown luminosity which prevents the system from being accretion driven.

All four TeV γ-ray binary systems are known to be HMXBs, but only for one of them, PSR B1259−63/LS 2883, the nature of the compact object is well established and the non-thermal emission mechanism can be determined. It is believed to be a plerionic binary system. PSR B1259−63/LS 2883 consists of a powerful pulsar orbiting around a massive companion star of the Be spectral class. Tavani and Arons [1997] demonstrate that the pulsar is powerful enough to produce a magneto-hydrodynamical wind whose pressure would be able to prevent the surface accretion from the companion star.

Be stars are rapidly rotating stars of the late O or early B type. The rapid rotation of the star causes a highly asymmetric mass loss. The wind outflow is basically divided into two wind zones: a dense and low-velocity equatorial wind and a high-velocity but low-density polar wind. The dense equatorial wind forms a circumstellar disk which can be observed in the infrared waveband. It is also responsible for the H_α emission. The polar wind is observed in the ultraviolet resonance lines. From the dependence of the infrared emission on the wavelength the density structure of the equatorial wind and the mass loss rate can be derived. The mass loss rates for Be stars are of the order of $(1-2)\times 10^{-7} M_\odot/\mathrm{y}$.

The density profile of the equatorial disk derived from the infrared excess is of the form

$$\rho(R) = \rho_0 \left(\frac{R}{R_*}\right)^{-n}, \tag{4.12}$$

where R_* is the radius of the star, R is the distance from the star and ρ_0 is the density at the star surface, and n is the so called "outflow exponent", which is estimated to be in the range of $3 < n < 3.75$. Typically, ρ_0 is of the order of 10^{10} to 10^{13} g cm^{-3} and the Be star radius is of order $R_* \sim 10 R_\odot$. Using the equation of continuity of the steady wind in the disk the density distribution can be converted into the velocity profile

$$v(R) = v_0 \left(\frac{R}{R_*}\right)^{n-2}, \tag{4.13}$$

where v_0 is believed to be in the range from 5 to 28 km s^{-1} [Waters et al., 1988].

For the polar wind the velocity profile of the shape

$$v(R) = v_0 + (v_\infty - v_0)\left(1 - \frac{R_*}{R}\right)^\beta \tag{4.14}$$

is adopted, where v_∞ is the terminal velocity, $v_0 \simeq 0.01 v_\infty$ and $\beta \simeq 1$. This velocity law is in agreement with the observed ultraviolet line profiles.

The nonthermal emission from such systems is generated by high energy particles which are accelerated at the termination shock of the pulsar wind, which occurs in the zone where the pulsar wind collides with the outflow from the star. Accelerated particles can then emit photons through various mechanisms like synchrotron emis-

sion, inverse Compton scattering of electrons on the stellar photons, Bremsstrahlung and hadronic interactions. Another mechanism which may be important for the VHE emission from such systems is the Comptonisation of the unshocked cold pulsar electron-positron wind by the stellar photon field (see e.g. Khangulyan et al. [2007]). The pulsar wind is believed to be monoenergetic with a typical bulk motion Lorentz factor of $\sim 10^4 - 10^6$ [Kennel and Coroniti, 1984], thus the interaction of the wind with starlight should lead to the formation of a narrow γ-ray component. The unshocked wind component is not expected to produce also X-ray emission through the synchrotron mechanism because particles are believed to move along magnetic field lines.

Synchrotron emission, inverse Compton scattering and hadronic interactions are described in more detail in Chapter 5 and their role in the PSR B1259−63/LS 2883 system is discussed in Chapter 8.

5 Non-Thermal Radiation Processes in SNRs and PWNe

Particles accelerated to very high energies at the shocks of SNRs and PWNe can produce non-thermal radiation through various mechanisms. Relativistic electrons can emit high energy photons due to bremsstrahlung (scattering on the Columb field of another charged paricle), the synchrotron mechanism (acceleration by the magnetic field) and inverse Compton scattering. VHE photons can also be produced as the result of hadronic interactions of high energy protons (accelerated at SNRs shocks) with the nuclei of the ISM. Synchrotron emission, inverse Compton scattering and hadronic interactions are described in more detail below. The synchrotron and inverse Compton sections basically follow the review by Blumenthal and Gould [1970] and the book by Rybicki and Lightman [1979]. In this context, an approximate analytical solution for the synchrotron spectrum from an electron population with a power-law distribution with exponential cut-off is presented. This solution has been derived by the author. The section about proton-proton interactions follows the paper by Drury et al. [1994].

5.1 Synchrotron Radiation

Synchrotron radiation is a radiation generated by ultrarelativistic charged particles accelerated by a magnetic field B (Fig. 5.1). In astrophysical applications synchrotron radiation generated by ultrarelativistic electrons can contribute to the radio, optical and X-ray flux from the object.

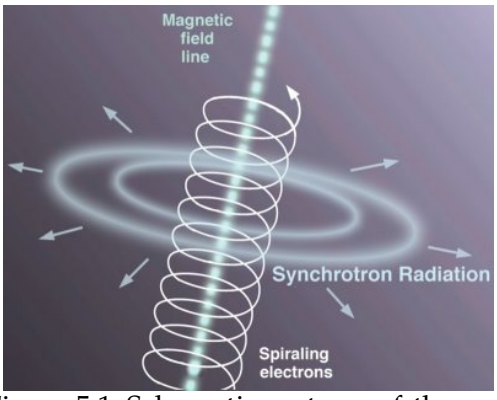

Figure 5.1: Schematic cartoon of the synchrotron mechanism. An electron accelerated in a magnetic field radiates high energy photons.

In the highly relativistic case the power per unit frequency emitted by each electron is

$$P(\omega) = \frac{\sqrt{3}}{2\pi} \frac{q^3 B \sin\alpha}{mc^2} F\left(\frac{\omega}{\omega_C}\right), \quad (5.1)$$

where ω is the frequency of the emitted photon, ω_C is the characteristic frequency of the photons emitted by a sin-

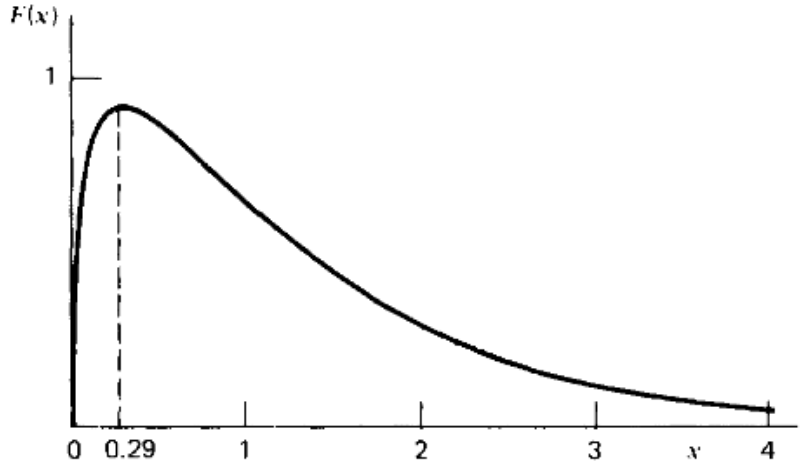

Figure 5.2: The function which describes the total power spectrum of synchrotron emission for a single electron [Rybicki and Lightman, 1979], where x is given by ω/ω_C.

gle electron which can be expressed by Eq. (5.3), q is the electron charge, α is the angle between the magnetic field and the electron velocity, m is the mass of the electron, c is the speed of light and $F(\frac{\omega}{\omega_C})$ is a dimensionless function which can be written as

$$F(x) \equiv x \int_x^\infty K_{3/5}(\xi)\, d\xi, \text{ with} \tag{5.2}$$

$$\omega_C = \frac{3\gamma^2 qB \sin\alpha}{2mc}. \tag{5.3}$$

The function $F(x)$ is plotted in Fig. 5.2.

If the number density of particles with Lorentz factors between γ and $\gamma + d\gamma$ is $N_e(\gamma)d\gamma$ the total power radiated per unit volume per frequency is given by the integral of the product of $N_e(\gamma)d\gamma$ and the single particle power (see Eq. 5.1) over all electron Lorentz factors $\gamma_1 < \gamma < \gamma_2$, i. e.

$$P_{tot}(\omega) = \int_{\gamma_1}^{\gamma_2} P(\omega) N(\gamma) d\gamma. \tag{5.4}$$

Often, the electron density energy distribution $N(\gamma)d\gamma$ can be approximately expressed by a power-law

$$N_e(\gamma)d\gamma = K_e \gamma^{-p} d\gamma,\ \gamma_1 < \gamma < \gamma_2, \tag{5.5}$$

where p is the spectral index and K_e is the normalisation, which denotes the density of electrons with the Lorentz factor $\gamma = 1$. In this case, one can obtain an analytical solution of the integral in Eq. (5.4). For the derivation of this solution it is useful

to change integration variables to $x \equiv \omega/\omega_C$, taking into account that $\omega_C \propto \gamma$. Equation (5.4) can be rewritten as

$$P_{\rm tot}(\omega) = K_e \frac{1}{2\sqrt{3}\pi}\frac{q}{c^2}\left(\frac{3qB\sin\alpha}{2mc}\right)^{\frac{p+1}{2}} \omega^{-\frac{p-1}{2}} \int_{x_2}^{x_1} F(x) x^{\frac{p-3}{2}} dx. \tag{5.6}$$

The limits x_1 and x_2 correspond to the limits γ_1 and γ_2 and actually depend on ω. Nevertheless, if the energy limits are sufficiently wide the integral limits can be approximated as $x_1 \approx \infty$ and $x_2 \approx 0$. Then the integral is independent of ω and can be easily calculated using Eq. 11.4.22 of [Abramowitz and Stegun, 1972]. One can derive the following relation

$$\int_0^\infty x^\mu F(x) dx = \frac{2^{\mu+1}}{\mu+2}\Gamma\left(\frac{\mu}{2}+\frac{7}{3}\right)\Gamma\left(\frac{\mu}{2}+\frac{2}{3}\right), \tag{5.7}$$

where $\Gamma(y)$ is the gamma function. Thus, for a power-law distribution of electrons it can be shown from Eqs. (5.6) and (5.7) that the total photon power per unit volume per unit frequency is

$$P_{\rm tot}(\omega) = K_e \frac{1}{2\sqrt{3}\pi}\frac{q}{c^2}\left(\frac{3qB\sin\alpha}{2mc}\right)^{\frac{p+1}{2}} \frac{2^{\frac{p+1}{2}}}{p+1}\Gamma\left(\frac{p}{4}+\frac{19}{12}\right)\Gamma\left(\frac{p}{4}-\frac{1}{12}\right)\omega^{-\frac{p-1}{2}}. \tag{5.8}$$

5.1.1 Analytical Solution for the Power-Law Electron Spectrum with an Exponential Cut-Off

An analytical solution for the synchrotron spectrum in the case of a power-law electron distribution was presented above. This solution is appropriate if the considered electrons have energies smaller than the cut-off energy, e.g. for synchrotron radio emission. Otherwise, one has to assume a cut-off. In this subsection an exponential cut-off will be considered, i. e. the electron density energy distribution is described by

$$N_e(\gamma) = K_e \gamma^{-p} e^{-\frac{\gamma}{\gamma_{\rm max}}}, \tag{5.9}$$

where $\gamma_{\rm max} mc^2$ is the cut-off energy of the electron spectrum. In this framework, an approximate analytical solution of synchrotron spectrum will be derived.

According to Eqs. 5.4, 5.1 and 5.9 the expression for the total power radiated per unit volume per frequency can be written as

$$P_{\rm tot}(\omega) = K_e \frac{\sqrt{3}}{2\pi}\frac{q^3 B\sin\alpha}{mc^2}\int_{\gamma_1}^{\gamma_2} F\left(\frac{\omega}{\omega_C}\right)\gamma^{-p} e^{-\frac{\gamma}{\gamma_{\rm max}}} d\gamma. \tag{5.10}$$

Using the same change of variables as in Eq. 5.6 it can be rewritten as

$$P_{\rm tot}(\omega) = K_{\rm e}\frac{1}{2\sqrt{3}\pi}\frac{q}{c^2}\left(\frac{3qB\sin\alpha}{2mc}\right)^{\frac{p+1}{2}}\omega^{-\frac{p-1}{2}}\int_{x_2}^{x_1}F(x)x^{\frac{p-3}{2}}e^{-\frac{\omega}{\omega_{\rm Cmax}}^{1/2}x^{-1/2}}dx, \quad (5.11)$$

where $\omega_{\rm Cmax}$ is the characteristic frequency of the photon emitted by an electron with cut-off energy $\gamma_{\rm max}mc^2$.

The integral in Eq. 5.11 can be solved only numerically. Therefore, to get a handy analytical solution some approximations should be made. The approximation proposed here is to assume $\omega = \omega_C$, i. e. $x = 1$, in the argument of the exponential. With this assumption the exponent can be taken out of the integral and the resulting integral is the same as in Eq. 5.6 and can be calculated analytically. Then the total photon power per unit volume per unit frequency is

$$\begin{aligned} P_{\rm tot}(\omega) =& K_{\rm e}\frac{1}{2\sqrt{3}\pi}\frac{q}{c^2}\left(\frac{3qB\sin\alpha}{2mc}\right)^{\frac{p+1}{2}}\frac{2^{\frac{p+1}{2}}}{p+1} \\ & \Gamma\left(\frac{p}{4}+\frac{19}{12}\right)\Gamma\left(\frac{p}{4}-\frac{1}{12}\right)\omega^{-\frac{p-1}{2}}e^{-\frac{\omega}{\omega_{\rm Cmax}}^{1/2}}. \end{aligned} \quad (5.12)$$

In order to investigate how close this approximation is to the real solution the following parameters of the electron distribution were considered:

$$p = 2.5, \quad (5.13)$$

which is a typical spectral index of the spectrum of accelerated particles in SNRs or PWNe,

$$\gamma_{\rm max} = 6\times10^7, \quad (5.14)$$

which corresponds to the cut-off energy $E_{\rm max} = \gamma_{\rm max}mc^2 = 30$ TeV and

$$K_{\rm e} = 1\ {\rm cm}^{-3}, \quad (5.15)$$

which corresponds to a density of relativistic electrons above 1 GeV $n_{\rm e} = 7.7\times10^{-6}$ cm^{-3}. To complete the list of free parameters the magnetic field is assumed to be $B = 10\,\mu$G.

In Fig. 5.3a the comparison of the photon spectrum calculated numerically and the analytical approximation is presented. The difference between the spectra calculated in numerical and analytical modes in units of the exact numerical result is presented in Fig. 5.3b. It can be seen that the approximation is in a good agreement with the exact result up to $\sim 10^{18}$ Hz, which corresponds to a photon energy of 4 keV. The relative difference reaches a value 0.5 at the frequency 3.2×10^{18} Hz, which corresponds to a photon energy of 13 keV. Since the energy range of X-ray instruments is usually 0.2–10 keV and the error of the calculated flux can reach 50% this approximation can be used for a quick modeling of synchrotron emission to explain

the radio and X-ray emission. It should be mentioned, though, that for low electron cut-off energies ($E_{\max} \leq 10$ TeV) the suggested approximation underestimates the flux in the X-ray energy range strongly. For instance, for $E_{\max} = 10$ TeV the difference between analytical approximation and exact result reaches 0.5 already for photons with energy 1.5 keV.

5.2 Inverse Compton scattering

Another mechanism for the production of high energy photons is inverse Compton (IC) scattering. It implies the scattering of ultrarelativistic electrons on low energy photons and boosts the photons to high energies. The process is called "inverse" because it is the opposite of the standard Compton effect where high energy photons are scattered on electrons and electrons gain energy due to this interaction. In astrophysical applications, IC scattering contributes to the γ-ray flux from the object.

IC scattering leads to the change of momentum and energy of the scattered photon. The energy of the photon after scattering in the electron rest system is given by

$$\epsilon_1' = \frac{\epsilon'}{1 + (\epsilon'/m_e c^2)(1 - \cos\theta_1')}, \tag{5.16}$$

where ϵ' is the energy of the photon in the electron rest system before the scattering, θ_1' is the scattering angle and m_e is the electron mass. In the lab system, the energy after scattering is

$$\epsilon_1 = \gamma\epsilon_1'[1 + \beta\cos(\pi - \theta_1')] \approx \gamma\epsilon_1'(1 - \cos\theta_1'), \tag{5.17}$$

where

$$\gamma \equiv \frac{1}{\sqrt{1 - \frac{v^2}{c^2}}} = \frac{1}{\sqrt{1 - \beta^2}} \tag{5.18}$$

and v is the velocity of the electron in the lab frame. Then the maximum possible energy of the scattered photon is $\epsilon_{1\max} \approx 2\gamma\epsilon_1'$. In the classical Thomson limit which involves that the energy of the photon is much smaller than the rest mass of the electron, i. e. $\epsilon' \ll m_e c^2$, according to Eq. 5.16 the energy change in the electron rest frame is then very small $\epsilon_1' \approx \epsilon'$. Then the maximum energy of the scattered photon in the lab frame is

$$\epsilon_{1\max} \approx 2\gamma\epsilon_{1\max}' \approx 4\gamma^2\epsilon. \tag{5.19}$$

The maximum energy corresponds to the head-on collision of the electron and the photon. Although the average energy of the scattered photon in the Thomson regime is quite large ($\sim \gamma^2\epsilon$) it is still much lower than the energy of the electron. So the electron loses only a small fraction of its energy. Another situation takes place in SNRs and PWNe where the energy of the photon before scattering in the electron rest system can be similar or higher than the mass of the electron ($\epsilon' \gtrsim mc^2$). In

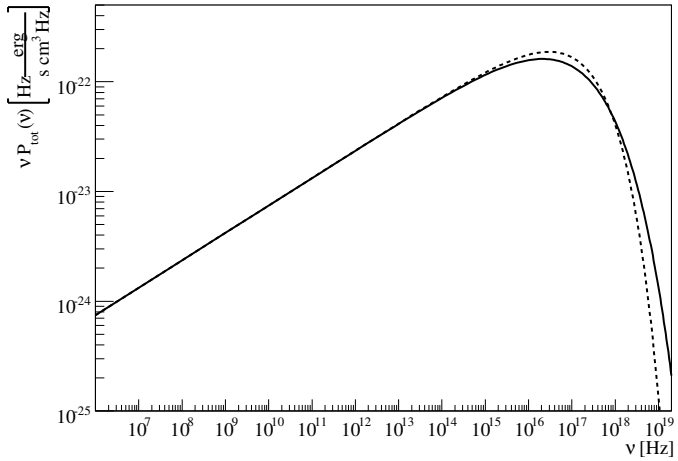

(a)

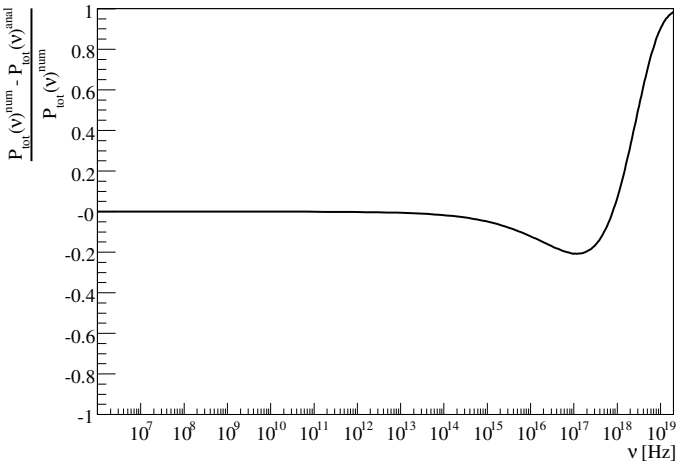

(b)

Figure 5.3: a) Comparison of the analytical approximation (dashed line) and the exact synchrotron spectrum (solid line) produced by an electron population with the exponentially cut-off power-law energy distribution (see the main text for parameters of the distribution). b) The difference between the spectral power calculated numerically and the analytical approximation in units of the exact numerical result.

this case the electron loses a large fraction of its energy and a general Klein-Nishina regime which is used below for the expression for the spectrum of scattered photons is required.

The exact cross section of the Compton scattering is energy dependent and given by the relation

$$\frac{d\sigma_{\rm exact}}{d\Omega_1' d\epsilon_1'} = \frac{1}{2} r_0^2 \left(\frac{\epsilon_1'}{\epsilon'}\right)^2 \left(\frac{\epsilon'}{\epsilon_1'} + \frac{\epsilon_1'}{\epsilon'} - \sin^2\theta_1'\right) \delta\left(\epsilon_1' - \frac{\epsilon'}{1 + \frac{\epsilon'}{mc^2}(1-\cos\theta_1')}\right), \quad (5.20)$$

where $\frac{d\sigma_{\rm exact}}{d\Omega_1' d\epsilon_1'}$ is the differential cross section for scattering into the solid angle $d\Omega_1'$ within the energy interval $d\epsilon_1'$ and r_0 is the classical radius of the electron. This general expression reduces to the classical Thomson cross section for $\epsilon' \ll m_{\rm e}c^2$. The exact differential cross section shows the asymmetric behavior with respect to the scattering angle for high energies with a higher probability for low angles (see Fig. 5.4). With the increase of energy the possibility for photons to be back scattered drops. For low energies the distribution is symmetric as it is expected in the classical Thomson regime.

With the expression for the cross section one can obtain the spectrum of photons scattered by a high-energy electron with Lorentz factor γ from a segment of an isotropic photon gas of differential density $dn = n(\epsilon)\, d\epsilon$ as (for more detail please see the derivation in [Blumenthal and Gould, 1970])

$$\frac{dN_{\gamma,\epsilon}}{dt dE_1 d\epsilon} = \frac{2\pi r_0^2 mc^3}{\gamma} \frac{n(\epsilon)}{\epsilon} \times \left[2\psi \ln\psi + (1+2\psi)(1-\psi) + \frac{1}{2}\frac{(\Gamma_e\psi)^2}{1+\Gamma_e\psi}(1-\psi)\right], \quad (5.21)$$

where $E_1 = \epsilon_1/\gamma mc^2$ is the scattered photon energy normalized to the initial electron energy and

$$\Gamma_e = \frac{4\epsilon\gamma}{mc^2},\ \psi = \frac{E_1}{\Gamma_e(1-E_1)}. \quad (5.22)$$

Clearly, the total IC spectrum results then from an integration over all electron and target photons energies. So, if the differential number of electrons is $N_{\rm e}(\gamma)\, d\gamma$, the total IC spectrum would be

$$\frac{dN_{\rm tot}}{dt d\epsilon_1} = \int\int \frac{dN_{\gamma,\epsilon}}{dt d\epsilon_1 d\epsilon} N_{\rm e}(\gamma)\, d\gamma d\epsilon, \quad (5.23)$$

where the integration is over γ and ϵ.

Blumenthal and Gould [1970] present a useful analytical solution of the total IC spectrum in the case of the Thomson limit, a power law distribution of electrons, i.e. $N_{\rm e} = K_{\rm e}\gamma^{-p}$, and a blackbody distribution of target photons for which

$$n(\epsilon) = \frac{1}{\pi^2 (\hbar c)^3} \frac{\epsilon^2}{e^{\epsilon/kT} - 1}, \quad (5.24)$$

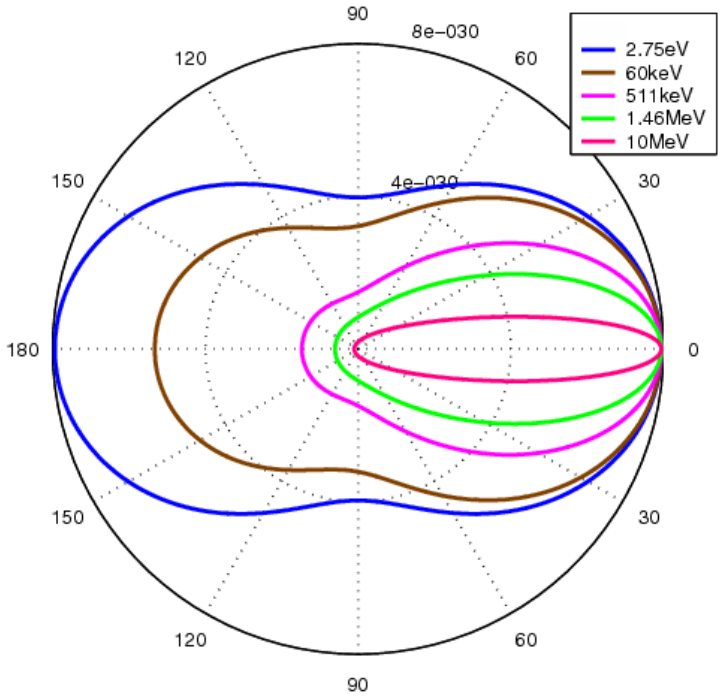

Figure 5.4: The distribution of the Klein-Nishina cross section with the photon scattering angles over a range of energies. The radial distance denotes the cross section in m^2. Two concentric rings indicate cross sections of 4×10^{-30} and 8×10^{-30} m^2. The angular axis denotes the photon scattering angle in degrees. For lower energies the angular distribution is symmetric (Thomson regime), while for higher energies the possibility of back scattering drops.

where $\hbar$ is the reduced Planck constant, k is the Boltzmann constant, and T is the average temperature. With these assumptions the total IC spectrum can be expressed as

$$\frac{dN_{\rm tot}}{dtd\epsilon_1} = \frac{r_0^2}{\pi\hbar^3c^2} K_{\rm e} \left(kT\right)^{\frac{p+5}{2}} C\left(p\right) \epsilon_1^{-\frac{p+1}{2}}, \tag{5.25}$$

where the parameter $C\left(p\right)$ is given by

$$C\left(p\right) = 2^{p+3} \frac{p^2+4p+11}{(p+3)^2(p+1)(p+5)} \Gamma\left(\frac{p+5}{2}\right) \zeta\left(\frac{p+5}{2}\right), \tag{5.26}$$

where $\zeta(y)$ is the Riemann zeta function.

5.3 Proton-Proton Interaction

Finally, high energy photons can be created in SNRs through hadronic interactions. Relativistic protons and nuclei produce π^0-mesons in inelastic collisions with ambient nuclei with a cross section of about 40 mb[1], $pp \rightarrow X\pi^0$. In turn π^0-mesons decay producing γ-rays, $\pi^0 \rightarrow \gamma\gamma$.

Following a simplified model of Drury et al. [1994] the expected γ-ray flux from an SNR can be calculated. The Drury et al. [1994] model assumes a power-law spatially averaged spectrum of protons in the SNR,

$$f(p) = f_0 \left(\frac{p}{2m_{\rm p}c}\right)^{-\alpha_{\rm p}} \tag{5.27}$$

with $4 \leq \alpha_{\rm p} \leq 5$, where $m_{\rm p}$ is the proton mass, f is the phase space density and p is the momentum of the particle.

For an SNR at the distance D from the Earth with an explosion energy $E_{\rm SN}$ the expected γ-ray flux from interactions of relativistic protons with the ambient medium of density n can be expressed as

$$F(E > E_{\rm threshold}) \approx 8.84 \times 10^6 q_\gamma(E > E_{\rm threshold}) \left(\frac{E}{1\ {\rm TeV}}\right)^{3-\alpha_{\rm p}} \theta \left(\frac{E_{\rm SN}}{10^{51}\ {\rm erg}}\right) \left(\frac{d}{1\ {\rm kpc}}\right)^{-2} \left(\frac{n}{1\ {\rm cm}^{-3}}\right)\ {\rm cm}^{-2}\,{\rm s}^{-1}, \tag{5.28}$$

where θ is the CR efficiency, i.e. the fraction of the explosion energy transferred to accelerated particles and q_γ is the γ-ray emissivity normalized to the CR energy density, i.e. the production rate of γ-rays.

[1]The inelastic part of the total cross section of proton-proton interactions can be presented as $\sigma_{\rm inel}(E_{\rm p}) = 34.3 + 1.88L + 0.25L^2$ [mb], where $L = \ln(E_{\rm p}/1\,{\rm TeV})$, and $E_{\rm p}$ is the energy of an incident proton [Kelner et al., 2006]. This approximation is obtained from a fit of the numerical data included in the SIBYLL code [Fletcher et al., 1994].

Table 5.1: The production rates of γ-rays for different spectral indices α_p of the relativistic protons distribution [Drury et al., 1994]. The units are $s^{-1}erg^{-1}cm^3(\text{H-atom})^{-1}$

α_p	$q_\gamma(E \geq 100\text{MeV})$	$q_\gamma(E \geq 1\text{TeV})$
4.1	0.46×10^{-13}	1.02×10^{-17}
4.2	0.58×10^{-13}	4.9×10^{-18}
4.3	0.61×10^{-13}	2.1×10^{-18}
4.4	0.57×10^{-13}	8.1×10^{-19}
4.5	0.51×10^{-13}	3.0×10^{-19}
4.6	0.44×10^{-13}	1.0×10^{-19}
4.7	0.39×10^{-13}	3.7×10^{-20}

The production rate varies with the spectral index of the proton distribution and with energy (see Table 5.1). For low-energy γ-rays ($100\,\text{MeV} \leq E \leq 1\,\text{TeV}$) the production rate is almost independent of α_p, for $4.1 \leq \alpha_p \leq 4.7$ it can be considered a constant within 20% error (see Table 5.1). At higher energies it becomes more sensitive to the spectral index. The production rate of γ-rays with energies above 1 TeV, which are more interesting for observations with H.E.S.S., decreases by more than two orders of magnitude from $\alpha_p = 4.1$ to $\alpha_p = 4.7$ (Table 5.1).

The exact value of the CR efficiency θ is unknown and model dependent. Nevertheless, observations require a lower limit on CR efficiency $\theta \geq 0.1$ in the moment when acceleration stops and CRs diffuse into the ISM in order to maintain the observed level of the CR population. From the definition it is also clear that $\theta < 1$. In the free-expansion stage of the SNR evolution θ is very low ($\theta \ll 1$): almost all the explosion energy is in the form of the kinetic energy of the ejecta and only a very small amount is processed through shocks. Later when the SNR enters the adiabatic stage of evolution (Sedov stage) and swept-up gas forms a dense shell the CR efficiency θ rises and remains then roughly constant.

6 The SNR G 1.9+0.3 and The SNR G 330.2+1.0

6.1 Young Synchrotron-Dominated SNRs at High and Very High Energies

The class of so-called synchrotron-dominated SNRs consists of remnants whose X-ray emission is dominated by a non-thermal component. Synchrotron emission from these SNRs reveals the existence of high-energy electrons which implies that intensive particle acceleration occurs at shock fronts of remnants. It makes them particularly interesting for γ-ray astronomy since high-energy particles accelerated at shock fronts can produce VHE γ-rays through the IC scattering of relativistic electrons on nearby photon fields and/or through proton-proton interactions, and subsequent π^0 decay (see Section 5).

The most prominent members of this class detected at VHEs are RX J1713−3946 [Aharonian et al., 2004b, 2006b, 2007a], RX J0852.0−4622 (Vela Jr.) [Aharonian et al., 2005e, 2007b, Paz Arribas et al., 2012], and the historical supernova remnant SN 1006 [Acero et al., 2010]. All of them are quite young, with an age of around 1000 y. The VHE emission from all of these remnants shows a shell-like morphology confirming the hypothesis that particles are accelerated at shock fronts. It is impossible, however to determine the physical process responsible for the γ-ray emission using only VHE data. In Fig. 6.1 spectral energy distribution (SED) models in leptonic (top), hadronic (middle) and mixed leptonic/hadronic (bottom) scenarios are shown. All of them describe the existing VHE data quite well and it is hard to distinguish between them.

The detection of an SNR at lower, i.e. GeV energies, can be very helpful for the determination of the nature of the γ-ray emission resolving the shape of the spectrum. Currently, only two synchrotron dominated SNRs are detected at HEs with Fermi LAT: RX J0852.0−4622 [Tanaka et al., 2011] and RX J1713−3946 [Abdo et al., 2011a]. For RX J1713−3946 the observed GeV spectrum slightly favours the leptonic model. Although the HE-VHE emission can still be explained within both scenarios, the hadronic model requires a very high total energy in protons of around 10^{52} erg [Yuan et al., 2011] which is larger than the explosion energy of the SN. The leptonic model implies a weak magnetic field of 12 μG and an electron spectrum with a spectral index of 2.15, the cut-off energy of about 50 TeV and a total energy in electrons of 5.5×10^{47} erg [Yuan et al., 2011].

In the case of RX J0852.0−4622 the HE-VHE spectrum can still be described within

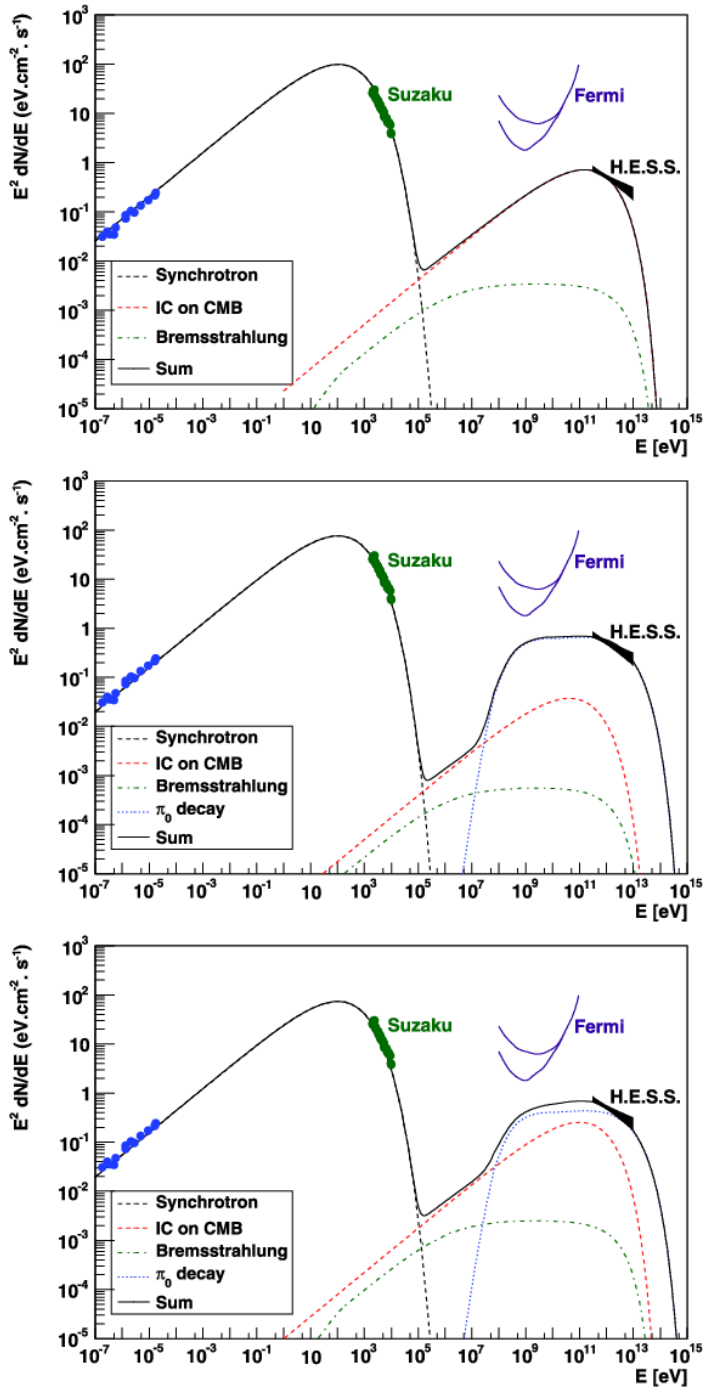

Figure 6.1: Broadband SED models of SN 1006 for leptonic (top), hadronic (centre) and mixed leptonic/hadronic (bottom) scenarios. The figure is taken from Acero et al. [2010].

both leptonic and hadronic scenarios. Both of them, however, face some difficulties. The leptonic model requires a weak magnetic field of 12 μG which is in contradiction with the *Chandra* observations of X-ray filaments, which imply a higher magnetic field of $\sim$ 100 μG. It is, however, possible ro reconcile this high magnetic field with the weaker averaged magnetic field implied by the leptonic model if the HE-VHE emission comes not only from filamentary structures but also from other regions where the magnetic field may be weaker. Parameters for the electron spectrum yielded from the leptonic model are similar to ones for RX J1713−3946: the spectral index is 2.15, cut-off energy is 25 TeV and the total energy in electrons is around 10^{48} erg. The hadronic model, in turn, requires an unrealistically high energy in protons of more than 10^{51} ergs for a small density of ~ 0.01 cm^{-3} suggested by the observations of the thermal X-ray emission (Tanaka et al. [2011] and references therein).

G 1.9+0.3 and G 330.2+1.0 discussed below also belong to the class of synchrotron-dominated SNRs and, thus, are good candidates for the detection at VHEs. Results of H.E.S.S. observations of these two remnants presented below were published in Sushch et al. [2012].

6.2 Multiwavelength Observations of SNR G 1.9+0.3 and SNR G 330.2+1.0

6.2.1 SNR G 1.9+0.3

In 1984, a radio survey using the Very Large Array (VLA) at 4.9 GHz discovered G 1.9+0.3 (also G 1.87+0.33), identifying it as an SNR based on its shell-like morphology and non-thermal radio emission [Green and Gull, 1984]. SNR G 1.9+0.3 had the smallest angular extent ever measured for a Galactic SNR ($\sim$1.2′) suggesting a small age $\lesssim 10^3$ yr and/or a large distance. Further evidence for the small age of SNR G 1.9+0.3 came from VLA observations at 1.5 GHz from 1985 [Green, 2004] which clearly showed a circular symmetry, as observed in other young SNRs.

More recent observations at both X-ray and radio wavelengths (Reynolds et al. [2008] and Green et al. [2008] correspondingly) were able to confirm the small age of G 1.9+0.3 by directly measuring the expansion of the SNR since earlier epochs. A spectral analysis of the *Chandra* X-ray data revealed that the integrated X-ray emission is well described as synchrotron emission from an electron population characterized by a power-law distribution with an exponential cut-off. In the context of the `srcut` model[1] adopted by Reynolds et al. [2008], a roll-off frequency $\nu_{\rm roll} = 1.4 \times 10^{18}$ Hz, one of the highest values ever reported for an SNR, and a spectral index $\alpha = 0.65^{+0.021}_{-0.020}$ (90 % confidence level), were obtained, as well as an absorption column density $N_{\rm H} = 3.48^{+0.87}_{-0.80} \times 10^{22}$ cm^{-2}. The latter suggests a loca-

[1] The `srcut` model describes the synchrotron radiation from an electron population with a power law energy distribution with an exponential cut-off in a homogeneous magnetic field.

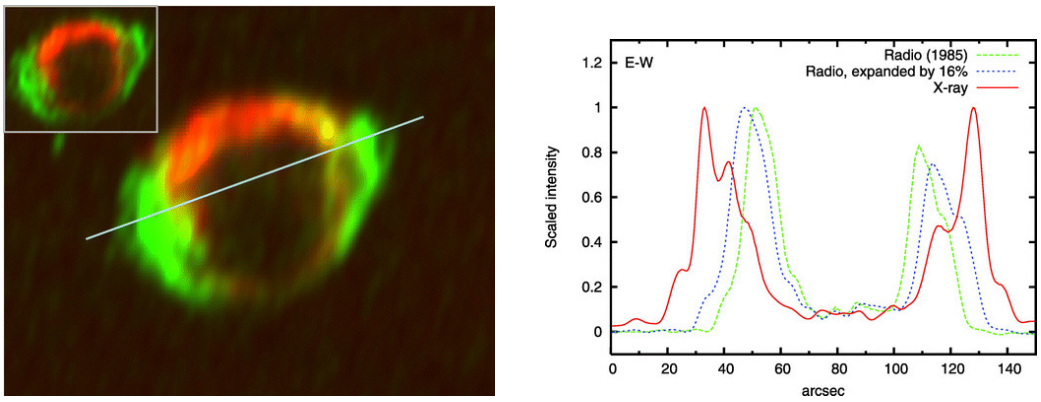

(a) (b)

Figure 6.2: **a)** A composite image of radio (red) and X-ray (green) emission. Inset: original radio image from 1985. Main figure: radio image expanded by 16%. The white line shows the orientation of the profiles. **b)** Profiles of radio and X-ray images. Red line: X-ray emission. Dashed green line: Original radio emission from 1985. Dashed blue line: Radio emission expanded by 16% around the center of the ring, to bring outer inflection points to X-ray maxima. X-ray extensions ("ears") are apparent at about 30% of maximum. Figures are taken from Reynolds et al. [2008].

tion close to the Galactic Center at a distance of $\sim$8.5 kpc which is assumed throughout this thesis. The *Chandra* image further revealed that the shell had significantly expanded (by $\sim$16%) to its present diameter of 1.7′ (Fig. 6.2) [Reynolds et al., 2008]. An age $\lesssim$150 yr was then derived by comparing radio observations from 1985 and *Chandra* observations from 2007 [Reynolds et al., 2008] and later confirmed using only radio observations from the VLA at two different epochs [Green et al., 2008, Murphy et al., 2008]. These new observations also imply a mean physical radius of $\sim$2 pc and a mean expansion velocity of $\gtrsim$12 000 km s^{-1} [Green et al., 2008]. The most recent X-ray measurements by Carlton et al. [2011] are in agreement, finding an age 156 ± 11 yr assuming no deceleration has taken place, with a true age of most likely $\sim$110 yr.

The combined radio/X-ray image (Fig. 6.2a) shows a bright, nearly circular ring with extensions (“ears”) extruding symmetrically from the Eastern and Western rims. However, the radio and X-ray morphologies differ significantly from each other; while the radio emission exhibits its maximum brightness in the North, the X-ray emission has a marked bilateral E-W symmetry. Interaction of the SNR shock front with a roughly uniform magnetic field B could explain the bilateral X-ray morphology, provided that the electron acceleration is dependent on the obliquity angle between the shock normal and B [Fulbright and Reynolds, 1990], but suggests that the large-scale magnetic field B may not be important for the radio emission [Green et al., 2008], which exhibits a markedly different morphology. The feature-

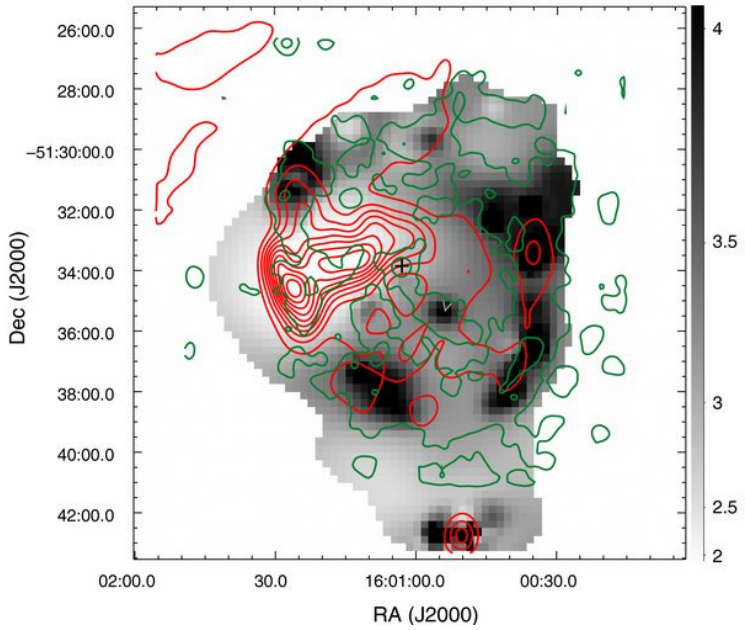

Figure 6.3: 2-8 keV to 1-2 keV hardness ratio map of G330.2+1.0 as obtained by the XMM-Newton satellite. Green image contours are the 1-8 keV image of the SNR. Red contours are the 843 MHz radio image taken from the MOST SNR catalog [Whiteoak and Green, 1996]. The position of the central compact object (CCO) J1601 is marked with a cross. The figure is taken from Park et al. [2009]

less, non-thermal, synchrotron-dominated, X-ray spectrum of the integrated emission [Reynolds et al., 2008] implies that electrons are efficiently accelerated, reaching a maximum energy $E_{\rm max} = 58$ TeV assuming $B = 10\,\mu$G. Recently, thermal X-ray emission was also discovered from the interior of the remnant and the Northern rim [Borkowski et al., 2010].

For a sphere of radius 2.2 pc, a Type Ia SN explosion model with an exponential ejecta profile [Dwarkadas and Chevalier, 1998] predicts an age of 100 yr and an ISM number density of about 0.04 cm^{-3}. Ksenofontov et al. [2010] derive slightly different values of the age (80 yr) and number density ($\sim$0.02 cm^{-3}), assuming an expansion velocity of 14 000 km s^{-1} and radius of 2 pc in their diffusive shock acceleration (DSA) model.

6.2.2 SNR G330.2+1.0

The radio source G 330.2+1.0 was identified as a Galactic SNR by Clark et al. [1973] and Clark et al. [1975] on the basis of its non-thermal spectrum and its proximity to the Galactic plane. Subsequent observations at radio frequencies [Caswell et al., 1983] showed the shell-like structure of the remnant delineated by eight "blobs" of elevated brightness. They also showed the existence of a gradient in the surface

brightness, with higher intensity towards the Galactic plane. Whiteoak and Green [1996] classified SNR G 330.2+1.0 as a possible composite-type SNR. The size of the shell is $\sim$11′ in diameter [Caswell et al., 1983, Whiteoak and Green, 1996].

Based on *ASCA* observations [Tanaka et al., 1994], Torii et al. [2006] discovered a featureless X-ray spectrum with a photon index $\Gamma \simeq 2.8$ and interstellar absorption $N_{\rm H} \simeq 2.6 \times 10^{22}\,{\rm cm}^{-2}$. It was also fit with a power law with exponential cut-off model (`srcut` model), deriving $\nu_{\rm roll} = 4.3 \times 10^{15}\,{\rm Hz}$ and $N_{\rm H} \simeq 5.1 \times 10^{22}\,{\rm cm}^{-2}$ for the fixed $\alpha = 0.3$ and flux density of 5 Jy at 1GHz [Green, 2004]. The general anti-correlation between radio and X-ray intensities was shown (see Fig. 6.3) and explained by the different density of the interstellar medium (ISM) on the eastern and western sides of the remnant. The dense ISM in the eastern shell causes the efficient deceleration of moderately-accelerated (GeV) electrons, while the lower ISM density in the western shell results in the acceleration to the TeV range. As a result, the X-ray emission is stronger in the western part of the shell and radio emission in the eastern part [Torii et al., 2006].

Subsequent *Chandra* and *XMM-Newton* observations [Park et al., 2006, 2009] revealed that the X-ray emission from SNR G 330.2+1.0 is dominated by a power-law continuum ($\Gamma \sim$ 2.1–2.5) and comes primarily from thin filaments along the boundary of the shell. Park et al. [2006] also discovered CXOU J160103.1−513353, a point-like source at the center of the SNR, claiming it to be a candidate central compact object (CCO). Additionally, evidence of pulsations were found with a period of $\sim$7.5 s, although later *XMM-Newton* observations [Park et al., 2009] did not confirm this. *Chandra* and *XMM-Newton* observations also revealed faint thermal X-ray emission in G 330.2+1.0 [Park et al., 2009]. Using the thermal emission, the ISM density was calculated and appears to be low ($0.1\,{\rm cm}^{-3}$). A lower limit on the distance $d_{\rm G\,330} \geq 4.9\,{\rm kpc}$ was calculated by McClure-Griffiths et al. [2001] using the H I absorption measurement. Therefore, the distance to G 330.2+1.0 is assumed to be 5 kpc hereafter. Assumptions on the ISM density and the distance to the SNR presented above lead to the estimation of the age of the remnant $t_{\rm G\,330} \simeq 1000\,{\rm yr}$ using the Sedov [1959] solution for the adiabatic stage of the hydrodynamical expansion of the SNR [Park et al., 2009].

6.3 Observations and Analysis

6.3.1 Data and Analysis Techniques

SNR G 1.9+0.3 is located $\sim$2° from the supermassive black hole Sgr A* at the Galactic Center (GC) and the TeV γ-ray source HESS J1745−290 which is coincident with positions of Sgr A* and the pulsar wind nebula G 359.95−0.04 [Aharonian et al., 2004a]. Analyses of the SNR therefore benefit from the deep H.E.S.S. exposure in the region. More than half of the observations used for the analysis are obtained from Sgr A* observations, while the remainder is from the H.E.S.S. Galactic Plane Survey [Aharonian et al., 2006c, Hoppe, 2008, Chaves et al., 2008, Chaves, 2009]. In

Table 6.1: H.E.S.S. data for SNR G1.9+0.3 and SNR G330.2+1.0

SNR	data-taking period	Livetime, [h]	mean offset angle, [°]	mean zenith angle, [°]	threshold energy, [GeV]
G1.9+0.3	2004-2010	75	1.5	19	260
G330.2+1.0	2005-2009	20	1.3	32	380

order to reduce the large exposure gradient towards the GC, only those observations centered within 2.0° were selected for the analysis. The observations which pass the standard H.E.S.S. data quality selection [Aharonian et al., 2006a] cover a six-year period from 2004 until 2010, have a livetime of 67 h, and a mean offset of $1.2° \pm 0.2°$ from G 1.9+0.3 (see Table 6.1). The selection excludes observations taken during poor or variable weather conditions and includes only those runs where at least three telescopes were in operation. The mean zenith angle (ZA) is relatively low, 19°, leading to a low energy threshold of 0.26 TeV.

SNR G 330.2+1.0 does not benefit from the neighbourhood to any other source in the FoV and does not have an exposure as large as G 1.9+0.3. All available data from June 2005 through May 2009 within 2.5° of the center of the remnant were used for the analysis. The collected data result in ∼20 h of livetime using only data which passed the standard H.E.S.S. quality selection and includes only those observations where not less than three telescopes were in operation. The data were taken at a mean ZA of 32°; the higher ZA results in a higher energy threshold, 0.380 TeV, compared to G 1.9+0.3. The average offset of the observations is ∼ 1.3°. The datasets used for the analyses of both G 1.9+0.3 and G 330.2+1.0 are summarized in Table 6.1.

The H.E.S.S. standard Hillas reconstruction [Aharonian et al., 2006a] (see Section 2.2.2) was used for the data analysis[2]. Standard cuts with the *reflected region background* method [Berge et al., 2007] were used. Results were cross-checked using the alternative *model analysis* technique for the γ-hadron separation as well as an independent calibration of the raw data and independent quality selection criteria [de Naurois and Rolland, 2009] (see Section 2.2.2). Both analysis chains yielded consistent results.

Since G 1.9+0.3 has a diameter of ∼1′ when observed at both radio and X-ray energies, and since the H.E.S.S. PSF (68% containment) is much larger (∼10′ diameter), the test region from which the signal is measured (ON region) was defined *a priori* as a circle with radius 0.10°, the standard size used to search for point-like sources with H.E.S.S. The test region is positioned at the apparent center of SNR G 1.9+0.3 at $\alpha_{\mathrm{J2000}} = 17^{\mathrm{h}}48^{\mathrm{m}}45^{\mathrm{s}}$, $\delta_{\mathrm{J2000}} = -27°10'$ [Green and Gull, 1984]. The size of the SNR G 330.2+1.0 is compatible with the H.E.S.S. PSF. Thus, in order to take into account all the emission from the remnant a bigger ON region comparing to G 1.9+0.3 was

[2]H.E.S.S. Analysis Package (HAP) version 10-06-pl07

chosen, defined as a circle with radius 0.22°. The test region is positioned at the center of the SNR at $\alpha_{J2000} = 16^h01^m3.14^s$, $\delta_{J2000} = -51°33'54''$.

Over the six-year observation period, the optical reflectivity of the H.E.S.S. telescope mirrors varied and the gains of the camera's photomultiplier tubes changed. This time-dependent optical response was taken into account in the spectral reconstructions by calibrating the energy of each event with the ring-like images of single muon passing close to the telescopes [Bolz, 2004].

6.3.2 Upper Limits Calculation

Despite relatively deep exposures with the H.E.S.S. telescopes, no significant VHE γ-ray signal was detected from SNRs G 1.9+0.3 or G 330.2+1.0. The upper limits (ULs; 99% confidence level) [Feldman and Cousins, 1998] on the integral fluxes above the 0.260 TeV (G 1.9+0.3) and 0.380 TeV (G 330.2+1.0) energy thresholds were calculated for three assumed spectral indices, $\Gamma = 2.0$, 2.5 and 3.0. The event statistics and ULs are summarized in Table 6.2. The dependence of the integral flux UL on the energy threshold can be seen in Fig. 6.4. Since the ULs are not strongly dependent on the value of Γ, ULs with the assumed spectral index $\Gamma = 2.5$ are used hereafter in this thesis.

Table 6.2: The 99 % confidence level upper limits on the TeV γ-ray flux from SNRs G 1.9+0.3 and G 330.2+1.0

	N_{ON}	N_{OFF}	α	N_γ	Sign.	F [cm^{-2} s^{-1}]
G 1.9+0.3	2812	35948	0.078	6.5	0.1 σ	$F(> 0.260\,\text{TeV}) < 3.8 \times 10^{-13}$ for $\Gamma = 2.0$ $F(> 0.260\,\text{TeV}) < 4.6 \times 10^{-13}$ for $\Gamma = 2.5$ $F(> 0.260\,\text{TeV}) < 5.3 \times 10^{-13}$ for $\Gamma = 3.0$
G 330.2+1.0	3212	46168	0.067	132.9	2.3 σ	$F(> 0.380\,\text{TeV}) < 1.4 \times 10^{-12}$ for $\Gamma = 2.0$ $F(> 0.380\,\text{TeV}) < 1.6 \times 10^{-12}$ for $\Gamma = 2.5$ $F(> 0.380\,\text{TeV}) < 1.8 \times 10^{-12}$ for $\Gamma = 3.0$

6.4 Interpretation

The synchrotron nature of the X-ray emission indicates that electrons are accelerated to very high energies in both SNRs. For such energies the acceleration process should run very similar for electrons and hadrons with one exception, which is the cut-off in the electron spectrum due to the electron radiation losses. Other processes which can cause the cut-off in the particle spectrum, such as finite age of the shock or the change in the nature of scattering above some energy should affect both electrons and protons identically providing a cut-off at similar energies (see

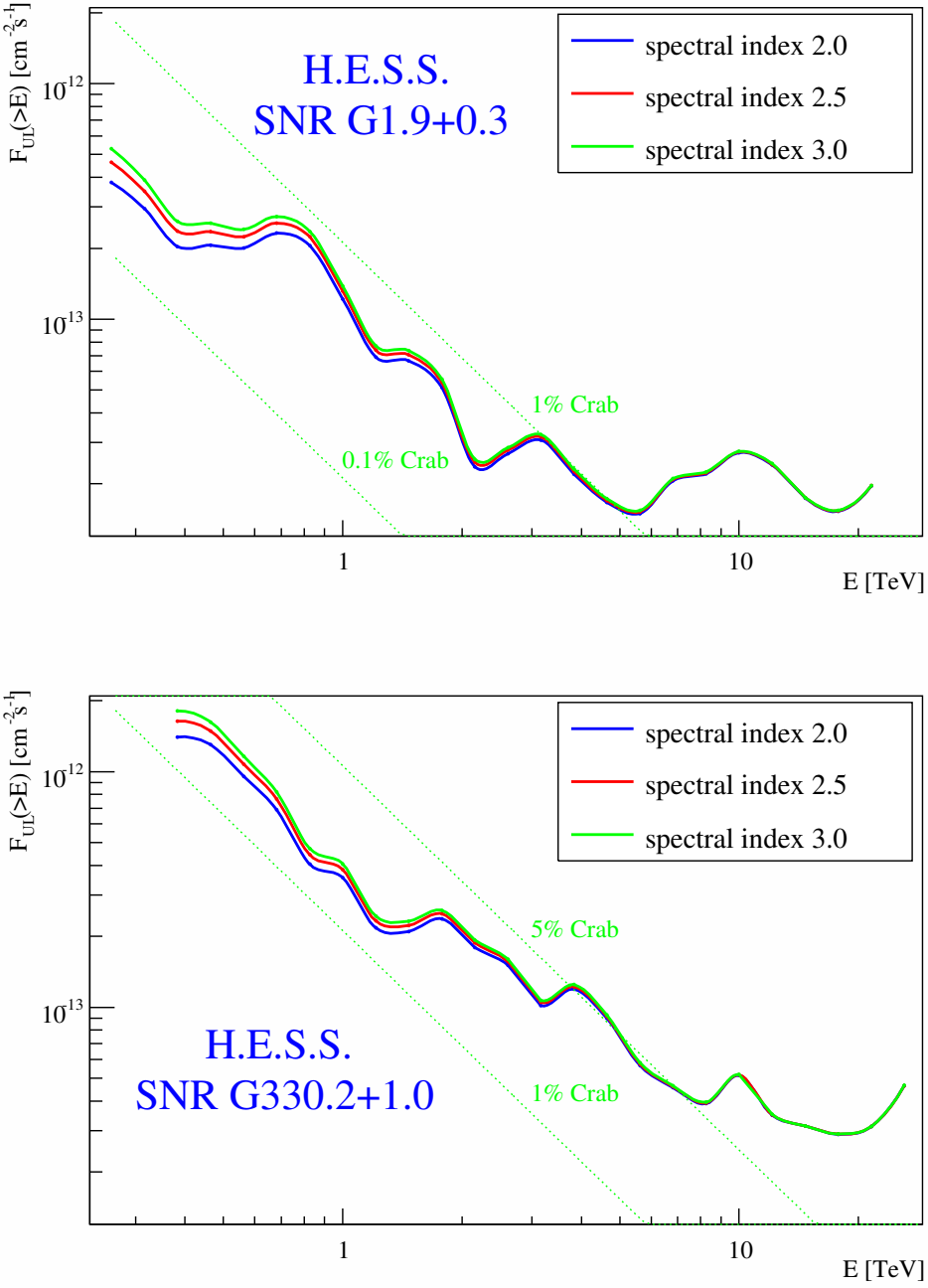

Figure 6.4: The 99% upper limits on the integrated TeV γ-ray flux from SNR G1.9+0.3 (top) and SNR G330.2+1.0 (bottom) presented for three different assumed spectral indices 2.0, 2.5 and 3.0

e.g. Reynolds and Keohane [1999]). Therefore, the existence of high energy electrons directly shows that there should exist hadrons accelerated to energies at least as high.

This leads to the expectation of γ-ray emission from the inverse Compton (IC) scattering of relativistic electrons on photon fields and/or from hadronic (e.g. proton-proton) interactions. The non-detection of this emission allows constraints to be placed on parameters such as the magnetic field strength, the ISM density, the distance and the cosmic-ray efficiency. In the following section, the predicted γ-ray flux in both leptonic (i.e. γ-rays from IC scattering) and hadronic (i.e. γ-rays from p-p interactions) scenarios will be discussed, and limits on the SNR parameters above will be set by comparing the predictions with the γ-ray flux ULs.

6.4.1 Leptonic Scenario

Although the comparison of the X-ray and radio data reveals a general anti-correlation for both SNRs indicating that radio and X-ray emitting electrons may not come from the same population, the "one-zone" leptonic modeling is used to obtain constraints on general parameters of the remnants and ambient media. In the framework of this model, it is assumed that one population of relativistic electrons creates radio and X-ray emission via the synchrotron mechanism and the VHE γ-ray emission via the IC scattering on Cosmic Microwave Background (CMB) photons and other ambient photon fields. Observational radio and X-ray data constrain the electron population for the assumed magnetic field, which can be used then for the prediction of VHE γ-ray emission. In turn, the calculated upper limit on the VHE emission constrains the magnetic field providing a lower limit.

The electron population is assumed to follow a power-law energy distribution with the exponential cut-off

$$N_{\mathrm{e}}(\gamma) = K_{\mathrm{e}}\,\gamma^{-p}\,e^{-\frac{\gamma}{\gamma_{\mathrm{cut}}}}, \tag{6.1}$$

where γ is the Lorentz factor of the electrons, γ_{cut} is the cut-off Lorentz factor, p is the spectral index and K_{e} is the normalisation which denotes the number of electrons with $\gamma = 1$ in the SNR. In the presented model the source is considered as point-like and no spatial distribution is taken into account, i.e. the model is one-dimensional. Moreover, a steady state is assumed in the modeling. According to Eqs. (5.1), (5.4) and (6.1) the total synchrotron SED as it is observed at the Earth is

$$\epsilon_1^2 \frac{dN_{tot,syn}}{d\epsilon_1} = \frac{1}{4\pi D^2} \int_{\gamma_1}^{\gamma_2} \frac{\sqrt{3}}{h} \frac{q^3 B \sin\alpha}{mc^2} F\left(\frac{\epsilon_1}{\epsilon_c}\right) K_{\mathrm{e}}\,\gamma^{-p}\,e^{-\frac{\gamma}{\gamma_{\mathrm{cut}}}}\,d\gamma, \tag{6.2}$$

where D is the distance to the Earth, ϵ_1 is the energy of photons and ϵ_c is the characteristic energy of the photons emitted by a single electron and is a function of the electron Lorentz factor and magnetic field. Electron velocities are assumed to be isotropically distributed, so the spherically averaged value $\sin(\alpha) = \sqrt{2/3}$ (where

Table 6.3: Parameters of optical and IR photon fields

SNR	Optical photons		IR photons	
	$T_{\rm opt}$, [K]	energy density, [eV cm^{-3}]	$T_{\rm IR}$, [K]	energy density, [eV cm^{-3}]
G1.9+0.3	4300	14.6	48	1.5
G330.2+1.0	3500	2.4	39	1.4

α is the angle between the magnetic field and the electron velocity) can be used.

The total IC SED for the electron distribution $N_{\rm e}(\gamma)$ according to Eqs. (5.23) and (6.1) is

$$\epsilon_1^2 \frac{dN_{tot,IC}}{dt d\epsilon_1} = \frac{1}{4\pi D^2} \int\int K_{\rm e}\, \gamma^{-p}\, e^{-\frac{\gamma}{\gamma_{\rm cut}}} \frac{dN_{\gamma,\epsilon}}{dt d\epsilon_1 d\epsilon}\, d\gamma\, d\epsilon, \tag{6.3}$$

where ϵ and ϵ_1 are energies of the target and the scattered photon correspondingly, $\frac{dN_{\gamma,\epsilon}}{dt d\epsilon_1 d\epsilon}$ is the scattered photon spectrum per electron which depends on the target photon distribution $n(\epsilon)$. In the vicinity of the Galactic Center the contribution of the infrared and optical photon fields to the overall IC emission can be comparable or may even exceed the contribution of the CMB photons [Porter et al., 2006]. Therefore, there is a necessity to describe these photon fields in detail. For this purpose the interstellar radiation field (ISRF) model [Porter et al., 2006] was used. Considering the locations of the two SNRs relative to the Galaxy center two ISRF distributions were used: at $R = 0$ kpc, $z = 0$ kpc for G1.9+0.3 and at $R = 4$ kpc, $z = 0$ kpc for G330.2+1.0, where R is the Galactocentric radius and z is the hight from the Galactic plane. To simplify the calculation of the IC emission these distributions were fitted with three Planckian distributions of optical, IR and CMB photons (Fig. 6.5). While CMB photons follow a pure blackbody distribution with the temperature 2.7 K, the IR and optical photons follow a greybody distribution. The fit parameters are energy density ω and temperature T. The ISRF at $R = 0$ kpc, $z = 0$ kpc corresponds to the optical radiation of the temperature $T_{\rm opt} = 4300$ K with the energy density of $\omega_{\rm opt} = 14.6$ eV cm^{-3} and IR radiation of the temperature $T_{\rm IR} = 48$ K with the energy density of $\omega_{\rm IR} = 1.5$ eV cm^{-3}. The ISRF at $R = 4$ kpc, $z = 0$ kpc can be fitted with the optical radiation of the temperature $T_{\rm opt} = 3500$ K with the energy density of $\omega_{\rm opt} = 2.4$ eV cm^{-3} and IR radiation of the temperature $T_{\rm IR} = 39$ K with the energy density of $\omega_{\rm IR} = 1.4$ eV cm^{-3} (see Table 6.3). Defining $n(\epsilon_0)$ as the sum of optical, IR and CMB photon distributions one can calculate $\frac{dN_{\gamma,\epsilon}}{dt d\epsilon_1 d\epsilon}$, using Eq. (5.21).

In Fig. 6.6, SED models for SNR G 1.9+0.3 and SNR G 330.2+1.0 are presented. A fit of the synchrotron emission to the radio and X-ray observational data, results in an electron spectral index $p = 2.2$ for both G 1.9+0.3 and G 330.2+1.0. The other two fit parameters are the normalisation of the synchrotron spectrum at 1 eV $\phi_0 =$

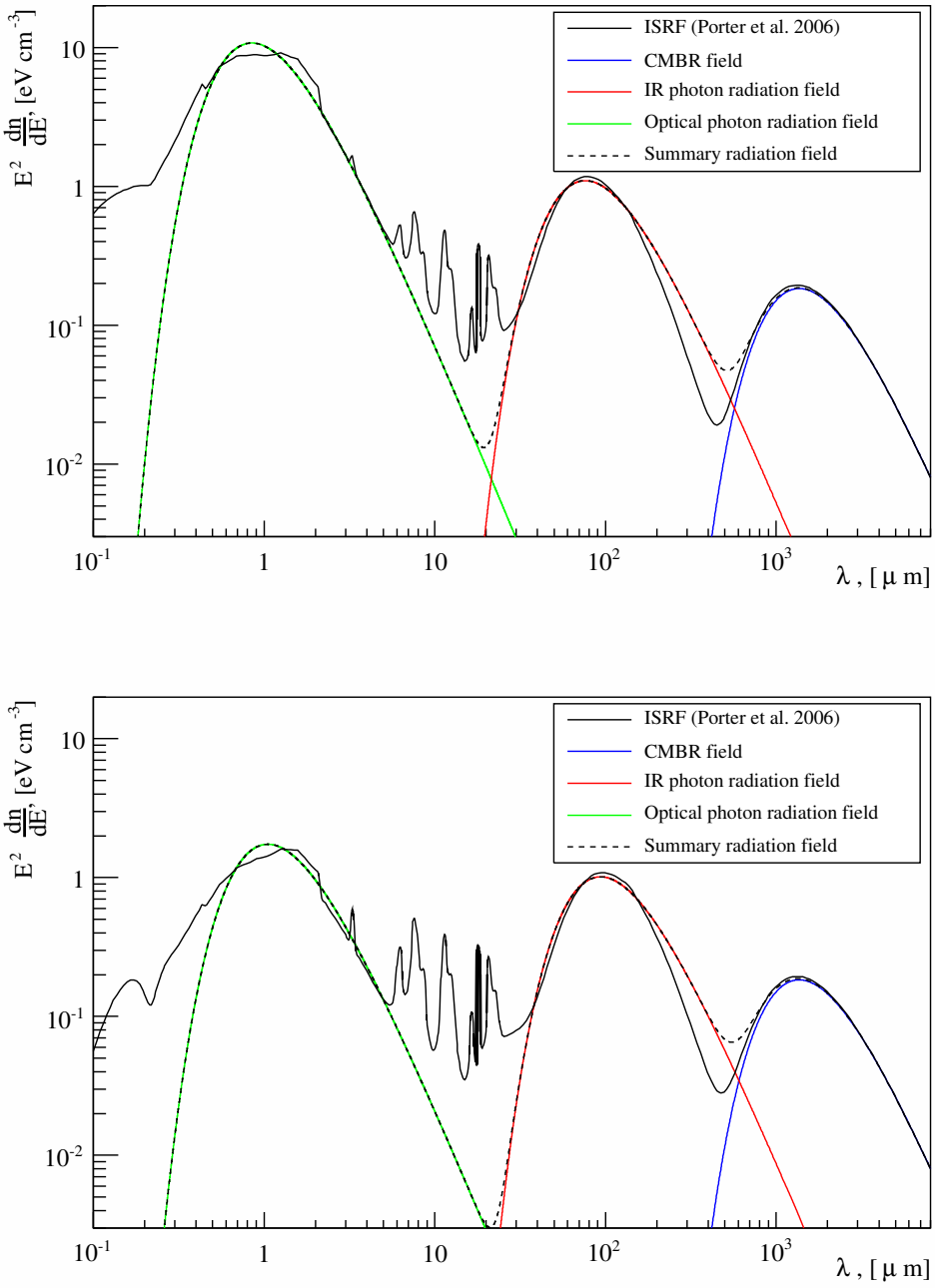

Figure 6.5: Interstellar radiation field (ISRF) model [Porter et al., 2006] at $R = 0$ kpc, $z = 0$ kpc (top) and at at $R = 4$ kpc, $z = 0$ kpc (bottom) fitted with three Planckian distributions of optical, IR and CMB photons

Table 6.4: SED model fitting parameters.

SNR	Γ	ϕ_0 [eV cm^{-2}s^{-1}]	$\epsilon_{\rm roll}$ [eV]	B [μG]	$E_{\rm cut}$ [TeV]	$W_{\rm tot}$ [erg]
G 1.9+0.3	2.20 ± 0.01	0.33 ± 0.1	2005 ± 180	> 15	< 50	$< 3.1 \times 10^{48}$
G 330.2+1.0	2.20 ± 0.01	2.2 ± 0.1	228 ± 1	> 14	< 17	$< 5.7 \times 10^{48}$

$f(K_{\rm e}, B)$ and the roll-off energy $\epsilon_{\rm roll} = f(\gamma_{\rm cut}, B)$ (see Table 6.4). The fit procedure is described in detail in Appendix A. The IC contribution to the SED is presented for two different assumed values of B. Only CMB and IR photon fields are used for the IC modeling, since the contribution of the optical photons to the total IC emission is found to be less than 1% even in the vicinity of the GC.

A magnetic field for both SNRs can be constrained by the UL on the VHE flux. Comparing the H.E.S.S. integral flux ULs to the predicted γ-ray flux in the same energy band, one can calculate lower limits on the interior magnetic field strength B. Synchrotron fit parameters were varied within errors and for each combination of parameters the magnetic field B for which the predicted flux is equal to the H.E.S.S. upper limit was found. 99 % CL lower limit on the magnetic field was then estimated as the 1st percentile of the B variable. The lower limits are found to be 15 μG for G 1.9+0.3 and 14 μG for G 330.2+1.0.

Lower limits on B, in turn, allow to constrain electron energy distribution parameters $K_{\rm e}$ and $\gamma_{\rm cut}$ (see Eq. 6.1) and, thus, the electron cut-off energy

$$E_{\rm cut} = m_{\rm e}c^2\gamma_{\rm cut} \tag{6.4}$$

and the total energy in electrons

$$W_{\rm tot} = m_{\rm e}c^2 \int_1^\infty K_{\rm e}\, \gamma^{-p+1}\, e^{-\frac{\gamma}{\gamma_{\rm cut}}} d\gamma. \tag{6.5}$$

ULs for $E_{\rm cut}$ and $W_{\rm tot}$ are listed in the Table 6.4.

The lower limits on the magnetic field derived for G 1.9+0.3 and G 330.2+1.0 are compatible with estimates for RX J1713.7-3946 and RX J0852.0-4622 obtained in the leptonic scenario. The electron spectral parameters such as spectral index p and cut-off energy $E_{\rm cut}$ are also similar to the ones obtained for the SNRs observed at GeV-TeV energies. However, to explain the synchrotron X-ray emission from G 1.9+0.3 and G 330.2+1.0 a weak magnetic field would require a large total energy in electrons. The obtained upper limits for $W_{\rm tot}$ correspond to 3×10^{-3} and 6×10^{-3} of the typical explosion energy of the SN for G 1.9+0.3 and G 330.2+1.0 respectively. If SNRs are the origins of CRs they have to convert around 10 % of their total energy into relativistic protons and the electrons to protons ratio $K_{\rm ep}$ should be of $\sim 10^{-2}$

as observed for cosmic rays or even smaller (see e.g. Gabici [2008]). This implies a total energy in relativistic electrons of not more than 10^{-3} of the total SNR energy or 10^{48} erg. Obtained upper limits for $W_{\rm tot}$ are somewhat higher than this value. Nevertheless, the higher magnetic field would also reduce the total energy in electrons making the model self-consistent.

For SN 1006 the interpretation of the VHE emission within the leptonic scenario requires a magnetic field of 30 μG what is about twice as high as the lower limits found for G 1.9+0.3 and G 330.2+1.0. An electron spectrum with $p = 2.1$, $E_{\rm cut} = 10$ TeV and $W_{\rm tot} = 3.3 \times 10^{47}$ is needed to explain the broadband emission of the source. These values lie within the limits obtained for G 1.9+0.3 and G 330.2+1.0 and, thus, suggest that further observations of these SNRs can probably lead to a detection. For G 1.9+0.3 further observations with H.E.S.S. are less reasonable because of its already large exposure of about 75 h of livetime and a low flux upper limit, which is almost an order of magnitude lower than the flux observed from SN 1006. But for G 330.2+1.0 with its relatively smaller exposure of 20 h and flux upper limit comparable with the flux from SN 1006 the situation is much more promising.

6.4.2 Hadronic Scenario

The H.E.S.S. ULs on the γ-ray flux from G 1.9+0.3 and G 330.2+1.0 can also be compared to predictions based on a hadronic scenario, where CR ions accelerated in the SN shock wave collide with the ambient thermal gas, producing γ-ray photons during the resulting π^0 decay. Since both SNRs exhibit synchrotron X-ray emission which reveals the existence of electrons with energies $\gtrsim 20$ TeV, the maximal energy of accelerated hadrons should be at least 20 TeV. This suggests that the spectrum of γ-rays produced in proton-proton interactions extends to at least few TeV. The expected flux from an SNR in the hadronic scenario is given by Eq. (5.28) according to Drury et al. [1994] (see Section 5.3). The values $\alpha_{\rm p} = 4.1$ and $q_\gamma = 1.02 \times 10^{-17}$ are adopted to predict the highest possible flux. This is done in order to show that even the highest possible predicted flux is lower than the H.E.S.S. upper limitis for both SNRs (see below). The expression for the predicted flux with assumed values of $\alpha_{\rm p}$ and q_γ can be rewritten as

$$F(>E) \approx 0.9 \times 10^{-12} \left(\frac{E}{1\ \text{TeV}}\right)^{-1.1} \theta \left(\frac{E_{\rm SN}}{10^{51}\ \text{erg}}\right) \left(\frac{d}{1\ \text{kpc}}\right)^{-2} \left(\frac{n}{1\ \text{cm}^{-3}}\right)\ \text{cm}^{-2}\,\text{s}^{-1}. \tag{6.6}$$

After fixing the spectral index and the CR production rate four parameters remain undefined: θ, $E_{\rm SN}$, d and n. Assuming the explosion energy to be 10^{51} erg and taking into account the estimated distance to the SNR one can constrain the product of the ISM density and CR efficiency with the H.E.S.S. upper limit. The resulting γ-ray spectrum should roughly follow the energy spectrum of protons, i.e. the power-law

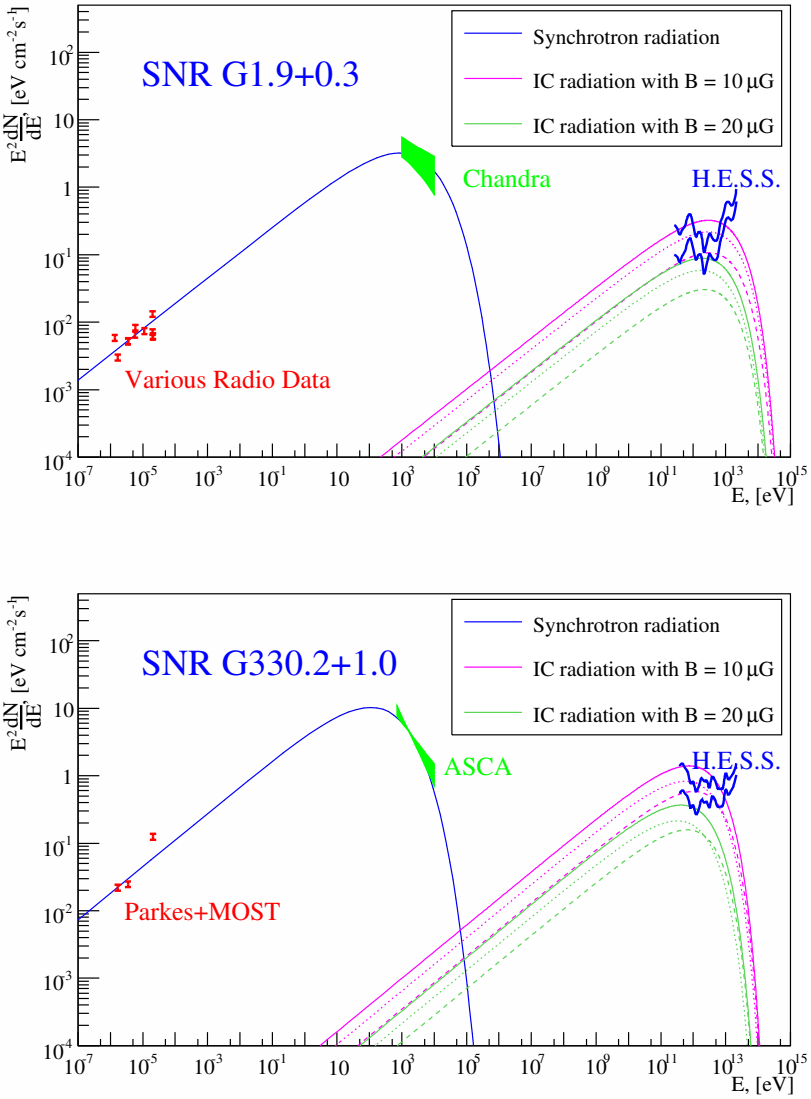

Figure 6.6: Spectral energy distribution of SNR G 1.9+0.3 (*top*) and SNR G 330.2+1.0 (*bottom*) in a leptonic scenario. The H.E.S.S. upper limit is shown assuming two different spectral indices, 2.0 (lower curve) and 3.0 (upper curve). The multi-frequency radio data shown for G 1.9+0.3 was compiled by Green et al. [2008]; additional upper limits in the IR domain [Arendt, 1989] are not shown because they lie outside of the plotted range and are not constraining. For the IC emission, dashed lines correspond to the contribution due to IC scattering on IR photons, dotted lines to IC scattering on CMB photons, and solid lines to the total IC emission.

distribution with the spectral index of $\alpha_p - 2$. Since $\alpha_p = 4.1$ is assumed, the H.E.S.S. upper limit with the assumed index of 2.0 should be used for placing constraints as the closest to the modeled γ-ray spectrum.

Then the expected flux above 260 GeV from G1.9+0.3 assuming a distance of 8.5 kpc is

$$F_{\rm G1.9}(>\ 260\ {\rm GeV}) \approx 5.5 \times 10^{-12} \theta_{\rm G1.9} \left(\frac{n_{\rm G1.9}}{1\ {\rm cm}^{-3}}\right)\ {\rm cm}^{-2}\ {\rm s}^{-1}. \quad (6.7)$$

The H.E.S.S. upper limit on the flux above the same energy 4.6×10^{-13} cm^{-2} s^{-1} corresponds to an upper limit on the product of the density and CR efficiency

$$\theta_{\rm G1.9} \left(\frac{n_{\rm G1.9}}{1\ {\rm cm}^{-3}}\right) < 0.07. \quad (6.8)$$

During the free expansion stage of the SNR evolution, suitable for G1.9+0.3, the fraction of the explosion energy converted into cosmic rays is expected to be very low [Drury et al., 1994]. Ksenofontov et al. [2010] show that at the age of 100 years the CR efficiency for G1.9+0.3 should be about 3×10^{-3}. Here a conservative value $\theta_{\rm G1.9} = 0.02$ is considered in order to obtain the upper limit on the expected γ-ray flux from hadronic interactions. This leads to an upper limit on the ISM density $n_{\rm G1.9} < 3.5$ cm^{-3}. This upper limit is two orders of magnitude higher than the estimate of the density by Reynolds et al. [2008] based on the SNR expansion. On the other side assuming the Reynolds et al. [2008] estimate of the ISM density $n_{\rm G1.9} \approx 0.04$ cm^{-3} the upper limit on the CR efficiency can be obtained which in this case is $\theta_{\rm G1.9} < 1.8$. Per definition $\theta < 1$. Therefore, in the case of G1.9+0.3 H.E.S.S. ULs are not constraining any parameters within the hadronic scenario.

For G330.2+1.0 the expected flux above 380 GeV for a distance of 5 kpc is

$$F_{\rm G330}(>\ 380\ {\rm GeV}) \approx 10^{-11} \theta_{\rm G330} \left(\frac{n_{\rm G330}}{1\ {\rm cm}^{-3}}\right)\ {\rm cm}^{-2}\ {\rm s}^{-1}. \quad (6.9)$$

The H.E.S.S. upper limit on the flux above this energy 1.6×10^{-13} cm^{-2} s^{-1} constrains the product of the density and CR efficiency

$$\theta_{\rm G330} \left(\frac{n_{\rm G330}}{1\ {\rm cm}^{-3}}\right) < 0.14. \quad (6.10)$$

It corresponds to the upper limit on the ISM density $n_{\rm G330} < 1.4$ cm^{-3} assuming the typical value of the cosmic-ray efficiency in the adiabatic stage of the SNR evolution $\theta_{\rm G330} = 0.1$ and to the upper limit on the CR efficiency $\theta_{\rm G330} < 1.4$ assuming the Park et al. [2006] estimate of the ISM density $n_{\rm G330} \approx 0.1$ cm^{-3} (based on the observations of the X-ray thermal emission). In the case of G330.2+1.0 the hadronic scenario constraints are also not significant.

Alternatively, with existing estimates of ISM densities and assumptions on CR efficiencies one can predict fluxes from G1.9+0.3 and G330.2+1.0. Assuming $n_{\rm G1.9} = 0.04$ cm^{-3} and $\theta_{\rm G1.9} = 0.02$ the expected VHE flux from G1.9+0.3 above 260 GeV according to Eq. 6.7 is about 4.4×10^{-14} cm^{-2} s^{-1} which is about 9 times lower

than the H.E.S.S. upper limit. For SNR G330.2+1.0 assuming $n_{G330} = 0.1$ cm^{-3} and $\theta_{G330} = 0.1$ according to Eq. 6.9 one can calculate the expected flux above 380 GeV of 1×10^{-13} cm^{-2} s^{-1}, 14 times lower than the upper limit. These estimates show that if these SNRs would be still detected with current instruments it will be difficult to explain it in the hadronic scenario.

Although the H.E.S.S. ULs for both SNRs do not constrain the predictions of this scenario, it should be noted that there exist non-negligible uncertainties in many of the model parameters. In particular, the expected γ-ray flux is very sensitive to the estimate of the distance to the sources. According to Ksenofontov et al. [2010], the dependence of the γ-ray flux on the distance, taking into account the relations between the distance and the ISM density, SNR radius and shock velocity, is $F_\gamma \propto d^{-11}$. Therefore, even a small decrease in the distance estimate would significantly increase the expected flux and consequently improve the constraints on the ISM density and the CR efficiency. So, if G 1.9+0.3 and G 330.2+1.0 would be located at distances of 7 and 4 kpc respectively, a scaling of the flux estimates obtained above gives fluxes compatible to the H.E.S.S. ULs.

Ksenofontov et al. [2010] also show that the VHE flux in the hadronic scenario from G 1.9+0.3 should strongly depend on time because of its small age and, thus, early evolution stage. The flux is expected to increase with time mainly due to the increase of the overall number of particles accelerated up to energies above 10 TeV. The expected increase could reach up to one order of magnitude in 100 years. At the same time the X-ray flux remains almost constant due to the strong synchrotron cooling of the highest energy electrons. However, this should not be the case for G 330.2+1.0, because it is much older and the VHE flux should follow the constant dependence on time at this stage of evolution.

6.5 Summary

The SNRs G 1.9+0.3 and G 330.2+1.0 can serve as valuable astrophysical laboratories for investigating the MWL properties of young, shell-type SNRs whose emission is dominated by non-thermal synchrotron emission. Observations in different energy regimes can provide insight into the physical properties of this important subclass of SNRs. H.E.S.S. observations of these two SNRs can provide a unique probe at the highest energies, in the TeV γ-ray domain.

Despite relatively deep exposures, the H.E.S.S. data do not show any signs of significant TeV γ-ray emission from either SNR. The 99% confidence level upper limits on the TeV flux from these sources were determined. For the assumed spectral index 2.5 the obtained upper limits are $F_{G1.9}(> 260\ \text{GeV}) < 4.6 \times 10^{-13}$ cm^{-2}s^{-1} for G1.9+0.3 and $F_{G330}(> 380\ \text{GeV}) < 1.6 \times 10^{-12}$ cm^{-2}s^{-1} for G330.2+1.0. The non-detection of G 1.9+0.3 and G 330.2+1.0 in the TeV γ-ray domain can be understood by comparing of their characteristics with characteristics of the other members of the class of synchrotron-dominated SNRs. The only significant difference which sets them apart from the other SNRs of this class is the distance. While most are

situated at relatively small distances from the Sun ($d \lesssim 2kpc$), SNRs G 1.9+0.3 and G 330.2+1.0 are significantly farther away. Their remoteness considerably reduces the γ-ray flux predictions, particularly in hadronic scenarios.

ULs on the TeV γ-ray flux provide an opportunity to place constraints on the interior magnetic field in the context of a leptonic particle acceleration scenario and on the ISM density and CR efficiency in a hadronic scenario. Lower limits on the interior magnetic fields were estimated at 15 μG for G 1.9+0.3 and 14 μG for G 330.2+1.0. In the case of the hadronic scenario, the H.E.S.S. upper limits are two orders of magnitude greater than the flux prediction. Obtained upper limits on the ISM densities are compatible with other estimates of the densities (from the thermal X-ray emission for G 330.2+1.0 and from the expansion rate for G 1.9+0.3). The CR efficiency cannot be constrained with the current H.E.S.S. upper limits.

G 330.2+1.0 and G 1.9+0.3 remain promising targets for γ-ray observations at TeV energies, in particular with the future generation of instruments, namely the Cherenkov Telescope Array (CTA) [Actis et al., 2011]. Significant improvement of the sensitivity would make CTA capable to detect fluxes an order of magnitude lower than H.E.S.S. This may be enough for the detection of the discussed remnants. But even if not detected, observations with CTA would put much stronger constraints on the parameters of the SNRs which is essential for the understanding of the physical processes in synchrotron-dominated SNRs.

7 The Evolved PWN HESS J1303-631

7.1 Evolved PWNe

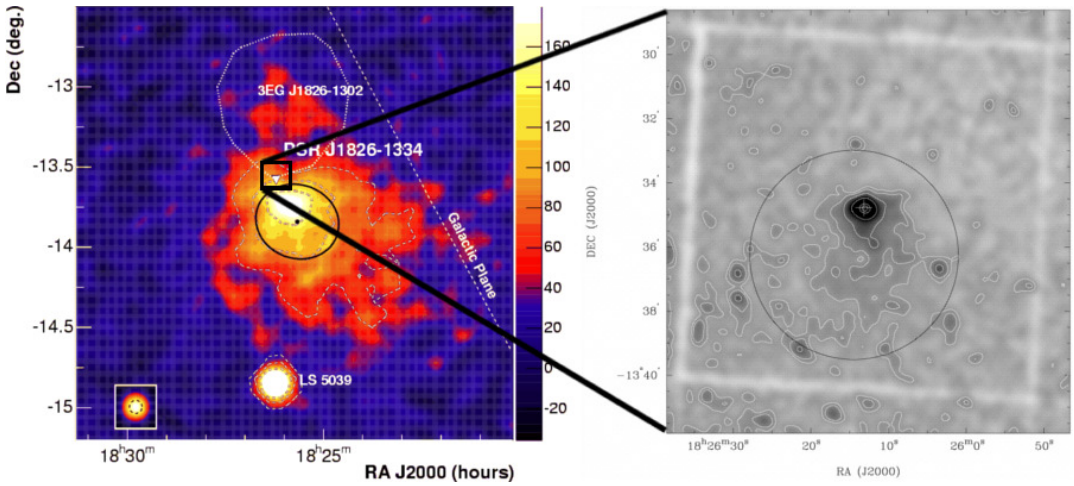

Figure 7.1: **Left:** Acceptance corrected smoothed excess map of the HESS J1825-137 field of view [Aharonian et al., 2006d]. The yellow triangle indicates the position of the pulsar PSR B1823−13. The black square shows the XMM-Newton field of view. **Right:** XMM-Newton image of the field surrounding PSR B1823-13 in the energy range 0.5 − 10 keV [Gaensler et al., 2003].

The class of TeV PWNe can be divided into two subclasses according to the source morphology which appears to be closely related to the age of the pulsar. The first subclass comprises young PWNe for which the pulsar is located close to the center of the TeV emission and the TeV emission region is comparable in size to the emission regions observed at radio and X-ray wavelengths. Usually such PWNe are surrounded by SNRs observed in the radio or/and X-ray energy bands, forming, so called, composite SNRs (see Chapter 3). The best established member of this class is the Crab Nebula [Aharonian et al., 2006a]. Among the other representatives are Kes 75 [H. E. S. S. Collaboration: A. Djannati-Atai et al., 2007], G0.9+0.1 [Aharonian et al., 2005a] and G21.5-0.9 (see Fig. 4.3a).

PWNe evolve with time which also brings changes to the morphology of the TeV emission. Such "evolved" PWNe form the second subclass of TeV PWNe. In such systems the pulsar is not located anymore close to the center of the TeV emission region, but rather close to the edge of it. This feature is responsible for another name for this class of objects - "offset" PWNe, since PWNe are offset from pulsars,

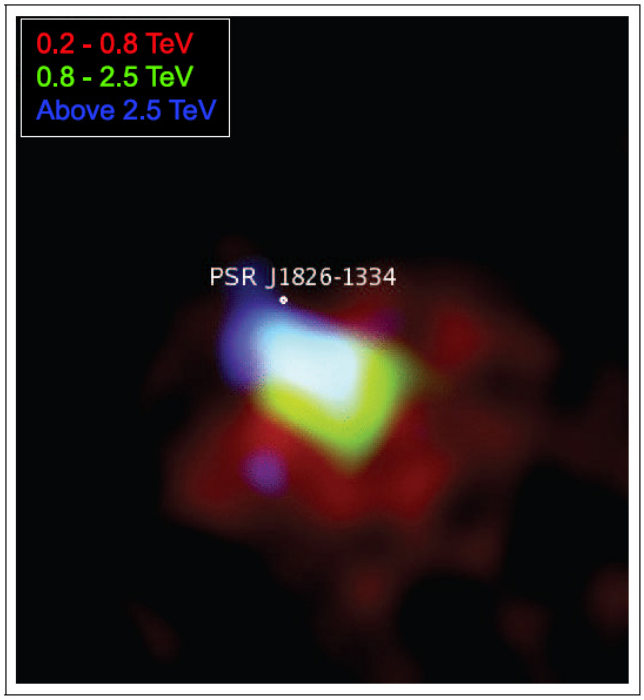

Figure 7.2: Energy dependent mosaic of HESS J1825−137. Red: 0.2 TeV $< E <$ 0.8 TeV, Green: 0.8 TeV $< E <$ 2.5 TeV, Blue: $E >$ 2.5 TeV. The emission region "shrinks" towards the direction of the pulsar PSR B1823−13 with increasing photon energy.

which create them. This is happening mainly for two reasons:

- **The proper motion of a pulsar**, which appears due to the kick a pulsar can gain in an asymmetrical SN explosion. At the early stages of the PWN evolution the distance travelled by a pulsar is negligible and observationally it is still located in the center of a PWN. But at later stages this effect becomes crucial, the pulsar travels a sufficient distance to be resolved in observations, leaving behind accelerated particles, which can still upscatter ambient photons and produce the TeV emission.
- **Collision with the SNR reverse shock** may also result in a similar morphology of the TeV source if for some reason the reverse shock is faster on one side of a PWN. In this case a PWN may be distorted by the reverse shock on one side before it was reached by the reverse shock on the other side, which results in an asymmetrical morphology, placing the pulsar at the edge of the PWN. The possible reason for the spatial discrepancy of the reverse shock velocity can be e.g. an interstellar medium density gradient [Blondin et al., 2001]. This scenario is believed to take place, for instance, in Vela X, the PWN created by the Vela pulsar.

Another feature of an evolved PWN is that the TeV emission region is consider-

ably bigger than the X-ray emission region. In Fig. 7.1, the TeV excess map for the HESS J1825−137 field of view [Aharonian et al., 2006d] is shown together with its X-ray counterpart [Gaensler et al., 2003]. The synchrotron X-ray nebula with a peak of the emission coincident with the pulsar PSR B1823−13 is much smaller than the TeV nebula which expands far away from the pulsar (indicated as a yellow triangle on the TeV excess map). Since VHE-emitting electrons are usually less energetic than X-ray-emitting ones, their population suffers less from radiative losses and the majority of them may survive from early stages of the PWNe evolution. In addition, the magnetic field is believed to decrease with time [de Jager et al., 2009], which in turn supresses the synchrotron emission from a PWN. Thus, it is possible that the TeV emission from the source would not have any counterpart at X-rays.

The idea that more energetic electrons responsible for a synchrotron X-ray emission simply do not survive the cooling while older less energetic TeV-emitting electrons are left from early stages of the evolution is further supported by the energy dependent morphology of the VHE emission. Figure 7.2 shows the energy dependent mosaic of three overlaid excess maps for different energy bands: $0.2\,\mathrm{TeV} < E < 0.8\,\mathrm{TeV}$, $0.8\,\mathrm{TeV} < E < 2.5\,\mathrm{TeV}$ and $E > 2.5\,\mathrm{TeV}$ [Funk et al., 2007]. It clearly indicates that the highest energy photons produced by more energetic electrons originate closest to the pulsar while for the lowest energy photons which can be generated by lower energy electrons the emission region is much more expanded.

It is believed that many, so called, "dark sources" which are observed only at the VHE range may be very old PWNe, and some of them initially classifed as "dark" were later identified as PWNe. A good example for such source is HESS J1303−631 which was found to be associated with the pulsar PSR J1301−6305 benefiting from deep H.E.S.S. observations and a thorough data analysis as well as the analysis of archival X-ray and radio data in search for counterparts [Dalton, 2011, The H.E.S.S. Collaboration: Abramowski, A. et al., 2012]. The pulsar is located at the North-Western edge of the TeV emission region and the energy-dependent morphology of the H.E.S.S. source HESS J1303−631 indicates the "shrinking" of the emission region towards the pulsar position with the increase of the threshold energy (see Section 7.3.3). Analysis results of the H.E.S.S., X-ray and radio data which revealed the association of the H.E.S.S. source with PSR J1301−6305 [Dalton, 2011, The H.E.S.S. Collaboration: Abramowski, A. et al., 2012] are presented in detail in the following sections in order to prepare the ground for the modeling of the broadband emission.

7.2 PSR J1301−6305

PSR J1301−6305 was among the first pulsars discovered in the Parkes multibeam survey [Manchester et al., 2001]. It is characterised by a fast spin period of 185 ms. The characteristic age of the pulsar is $\tau_c = 11$ kyr. It also has a large spin-down luminosity $\dot{E} = 1.7 \times 10^{36}\,\mathrm{erg\,s^{-1}}$ which makes it the most powerful pulsar known within 6° of the H.E.S.S. source HESS J1303−631. These properties place PSR J1301−6305 in

the category of, so called, "Vela-like" pulsars which are characterised by their fast rotation, characteristic ages between 10 to 100 kyr and a spin-down luminosity above 10^{36} erg s^{-1} (see e.g. Crawford and Tiffany [2007] and references therein).

The distance to the pulsar is estimated to be 6.6 kpc based on the model of the Galactic electron distribution NE2001 [Cordes and Lazio, 2002]. It was shown that pulsars with a spin-down flux of $\dot{E}d^{-2} \geq 10^{34}$ erg s^{-1} kpc^{-2}, where d is the distance to the pulsar, are connected to nebulae detectable at VHEs [Carrigan et al., 2008]. The distance of 6.6 kpc yields a spin-down flux from PSR J1301−6305 of $\dot{E}d^{-2} = 3.9 \times 10^{34}$ erg s^{-1} kpc^{-2}, suggesting that a nebula generated by this pulsar can be detected at VHEs.

7.3 VHE Observations with H.E.S.S.

7.3.1 The Discovery of HESS J1303−631

HESS J1303−631 was discovered during observations of the binary system PSR B1259−63/LS 2883 around its 2004 periastron passage [Aharonian et al., 2005d] yielding an extended TeV emission with a Gaussian source size of $\sim 0.16^\circ$ extent. The spectrum can be described with a simple power-law with a photon index $\Gamma = 2.44 \pm 0.05_{\mathrm{stat}} \pm 0.05_{\mathrm{syst}}$ and normalisation at 1 TeV of $N_0 = (4.3 \pm 0.3) \times 10^{-12}$ TeV^{-1}cm^{-2}s^{-1} with a rather low fit probability of 0.1 %. The fit of a curved spectral shape resulted in better χ^2 suggesting a cut-off, but due to the poor understanding of the systematic effects at that time no strong statemants were made. In addition, some of these early observations were performed with telescope pointings coincident with the HESS J1303−631 emission region, making them unsuitable for the spectral analysis since placement of reflected regions for the background estimation is not possible. The integral photon flux above 380 GeV is compatible with a constant emission of (17 ± 3) % of the Crab Nebula flux above the same energy threshold. At the time of discovery, no extended counterparts at other energies were found and, therefore, HESS J1303−631 was classified as a dark source.

7.3.2 Follow-up Observations

The discovery of HESS J1303−631 was followed by deep dedicated observations of its field of view resulting in more than 100 hours of livetime in the period from 2004 to 2008 [Dalton, 2011]. The rich exposure of the source allowed to provide a thorough study of the source morphology and its spectral shape revealing its association with the pulsar PSR J1301−6305.

In Fig. 7.3a the VHE γ-ray excess map of the HESS J1303−631 field of view is presented showing an extended emission to the South-East of PSR J1301-6305. The best-fit position of the source obtained in a fit of a two-dimensional elongated Gaussian is consistent with the one quoted in the discovery paper. Nevertheless, it appears to be slightly shifted towards the direction of the pulsar. This can be explained by

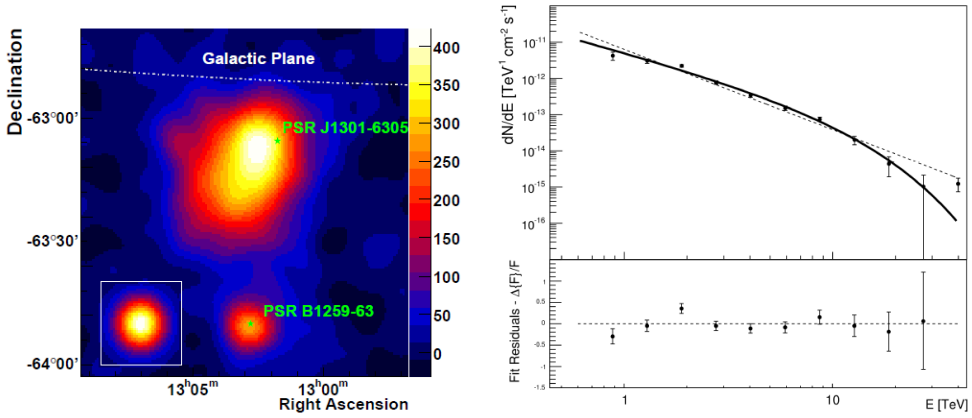

(a) (b)

Figure 7.3: (a) VHE γ-ray excess map of the HESS J1303−631 field of view. The pulsar PSR J1301−6305 is indicated with a green star to the North-West of HESS J1303−631. The point-source located in the bottom of the field of view is associated to the binary system PSR B1259−63/LS 2883. The size of the H.E.S.S. PSF is shown in the white box in the lower left corner. (b) Differential energy spectrum of the VHE emission from HESS J1303−631. The spectrum is well fit with a power-law with exponential cut-off function (solid curve). The last spectrum point deviates $\sim 2\sigma$ from the fit curve and thus is removed from the residuals plot for better visibility. The dashed line indicates a fit with a simple power-law. The figures are taken from The H.E.S.S. Collaboration: Abramowski, A. et al. [2012].

the higher energy threshold of the analysis and the energy dependent morphology of the source (see Section 7.3.3). The fit yields coordinates of the best-fit position of $\alpha_{J2000} = 13^h02^m48^s \pm 3^s_{stat}$, $\delta_{J2000} = -63°10'39'' \pm 24''_{stat}$ with Gaussian widths of $\sigma_x = 0.194° \pm 0.008°$ and $\sigma_y = 0.145° \pm 0.006°$ and a counter clockwise rotation angle (from North) of $\phi = 147° \pm 6°$.

The measured spectrum of the source is shown in Fig. 7.3b. It was fitted with a power-law function resulting in a photon index $\Gamma = 2.44 \pm 0.03_{stat}$ and a normalisation at 1 TeV $N_0 = (5.9 \pm 0.3_{stat}) \times 10^{-12}\text{TeV}^{-1}\text{cm}^{-2}\text{s}^{-1}$. The normalisation is larger than the one measured in the discovery paper due to a larger integration region of radius 0.6°. The fit of a power-law results in a very low χ^2 probability of 7×10^{-8}. A fit of a power-law with an exponential cut-off resulted in a much better χ^2 probability of 0.01 with $N_0 = (5.6 \pm 0.5_{stat}) \times 10^{-12}\text{TeV}^{-1}\text{cm}^{-2}\text{s}^{-1}$, $\Gamma = 1.5 \pm 0.2_{stat}$ and a cut-off energy $E_{cut} = 7.7 \pm 2.2_{stat}$ TeV. The integral energy flux in the $1 - 30$ TeV energy band is $F_{(1-30)\text{TeV}} = (2.5 \pm 0.1) \times 10^{-11}$ erg $\text{cm}^{-2}\text{s}^{-1}$ which is twice the flux obtained in the discovery paper. The VHE luminosity defined as the integral flux in the 0.3 to 30 TeV band (see Wilhelmi [2011]) results in 10.5 % of the pulsar spin-down luminosity, assuming that the distance to the pulsar is 6.6 kpc. This value of the conversion efficiency is comparable to other VHE PWNe (see Table 2 in Wilhelmi [2011]).

7.3.3 Energy Dependent Morphology

The presence of the energy-dependent morphology in the VHE source, which shows that the emission region is shrinking towards the position of the pulsar, became the first strong evidence of the association with PSR J1301−6305.

To study the energy-dependent morphology excess images of HESS J1303−631 were generated in three energy bands: $0.84\,\text{TeV} < E < 2\,\text{TeV}$, $2\,\text{TeV} < E < 10\,\text{TeV}$ and $E > 10\,\text{TeV}$ (Fig. 7.4, left, top to bottom). Slices of the size $1.0° \times 0.1°$ were made on the excess image, centered at the best fit position of the VHE excess and oriented along the fitted rotation angle ϕ. A fit of a Gaussian to each slice shows a significant decrease of the distance between Gaussian mean and a pulsar position as well as the decrease of the Gaussian width with the increase of the threshold energy (see [The H.E.S.S. Collaboration: Abramowski, A. et al., 2012] for details). This indicates that the higher energy photons are generated in the immediate vicinity of the pulsar PSR J1301−6305 while the low energy VHE emission is much more extended with the pulsar located towards the edge of the emission region. It can be very well seen from the mosaic plot (Fig. 7.5) in which smoothed excess images from Fig. 7.4 are overlaid. This kind of energy-dependent morphology is expected to be observed in the evolved PWNe and thus serves as evidence of the association of VHE source with the pulsar.

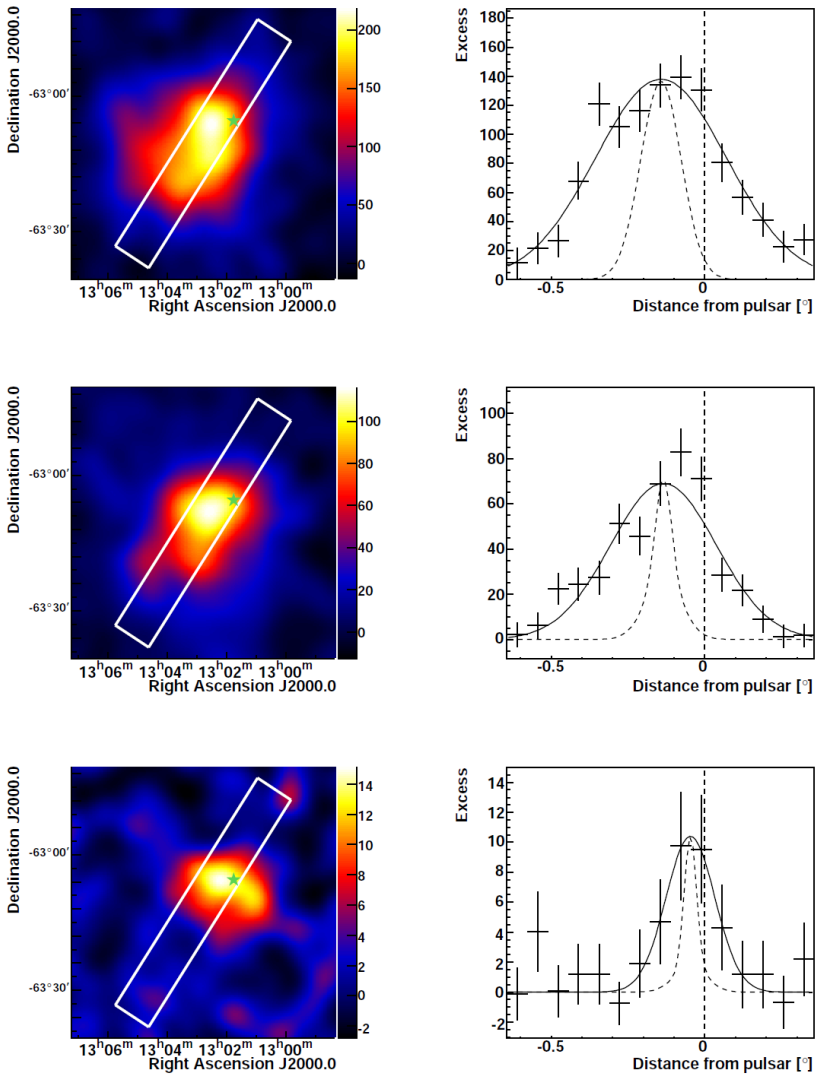

Figure 7.4: Left: excess images of the HESS J1303−631 region in the energy bands 0.84 TeV $< E <$ 2 TeV, 2 TeV $< E <$ 10 TeV and $E >$ 10 TeV (from top to bottom). Slices taken on the images are indicated by white rectangles. The pulsar position is indicated with a green star. Right: a fit of a Gaussian to each slice is shown by the solid curves. The dashed curves show the energy-dependent PSF of the H.E.S.S. instrument. The pulsar position is shown with dashed vertical lines. The figure is taken from The H.E.S.S. Collaboration: Abramowski, A. et al. [2012].

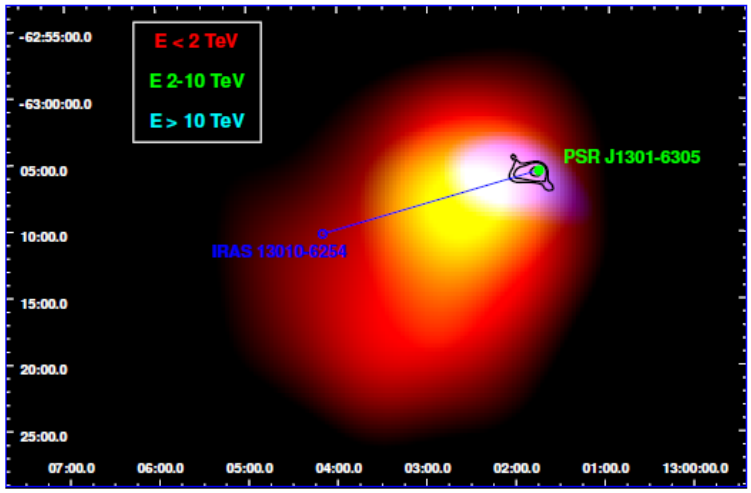

Figure 7.5: Energy mosaic of HESS J1303−631. The horizontal axis is Right Ascension and the vertical axis is declination in J2000 coordinates. Red: 0.84 TeV $< E <$ 2 TeV, Green: 2 TeV $< E <$ 10 TeV and Blue: $E >$ 10 TeV. XMM-Newton X-ray contours are overlaid in black. The pulsar PSR J1301−6305 is indicated by the green dot. The star forming region IRAS 13010−6254, considered as a possible birthplace of the pulsar, is marked by a blue circle. The figure is taken from The H.E.S.S. Collaboration: Abramowski, A. et al. [2012].

7.4 MWL Observations of HESS J1303−631

7.4.1 X-ray Observations

In a search for an X-ray counterpart of the VHE γ-ray source, two XMM-Newton observations were carried out on 12th and 14th of July 2005 with a duration of 30 ksec each. The X-ray source 2XMM J130145.7-630536 asociated to PSR J1301−6305 was detected with a flux of $F_{2-12\mathrm{keV}} = (7.7 \pm 1.0) \times 10^{-14}$ erg cm^{-2}s^{-1}[Watson et al., 2009]. The peak of the emission is located $15'' \pm 1.6''$ to the East of the pulsar with an extension of $6''$. Although no emission corresponding to the full region of the H.E.S.S. source was found, the X-ray source is seen extending roughly towards the center of the TeV emission region. A detailed analysis of this feature presented in [The H.E.S.S. Collaboration: Abramowski, A. et al., 2012] revealed a $145''$ extension at the significance level of 6.5σ. A slice taken in the direction of the extension (see below) reveals a hint of two features (Fig. 7.6a): a "compact" region near the pulsar position extending $\sim 40''$ to the East and corresponding to the 2XMMi catalog source 2XMM J130145.7-630536 and an offset "diffuse" emission region extending from $\sim -40''$ to $\sim -150''$. Figure 7.6a (bottom) shows a fit of two Gaussians to the "compact" and "diffuse" regions. The compact emission region is centered at $-10'' \pm 4''$ with a width of $16'' \pm 4''$ and the diffuse emission region is centered at $-104'' \pm 18''$ with a width of $66'' \pm 19''$. The point-source located to the West from

the pulsar is presumably unrelated to the pulsar due to its soft nature. It is fitted with a King profile, describing the XMM-Newton PSF.

A fit of a power-law to the spectrum yielded a column density $N_{\rm H} = 2.7^{+1.3}_{-1.1} \times 10^{22}$ cm^{-2}, a photon index $\Gamma = 2.0^{+0.6}_{-1.1}$ and a flux normalization at 1 keV of $6.2^{+10}_{-3.8} \times 10^{-5}$ keV^{-1} cm^{-2}s^{-1}. The integrated unabsorbed flux in the $2 - 10$ keV energy band was measured to be $F_{2-12\rm keV} = 1.6^{+0.2}_{-0.4} \times 10^{-13}$ erg cm^{-2}s^{-1}.

In order to determine the direction of the extension an azimuthal projection was taken around the pulsar with an inner radius of 48″ and outer radius 120″ (see Fig. 7.6b top). A fit of the projected counts with a sum of a Gaussian and a flat background provided a direction angle of $101.5^\circ \pm 5.3^\circ$ (starting from North) with a Gaussian width of $30^\circ \pm 7^\circ$. The obtained X-ray extension direction is consistent to within 1σ with the direction from the pulsar to the star froming region IRAS 13010-6254 located within 8σ significance contour of the VHE source (Fig. 7.6b top). If one assumes that the X-ray extension indicates the trail of the pulsar proper motion then the star forming region may be a possible birthplace of the pulsar. This hypothesis is discussed in more detail in Section 7.5.

7.4.2 Radio Observations

The region of HESS J1303−631 was covered by a 4.85 GHz radio survey of the southern sky performed by the Parkes, MIT and NRAO (PMN) telescopes [Condon et al., 1993]. It reveals a radio feature just East of the X-ray nebula and near the peak of the VHE emission region (Fig. 7.7). The peak flux of the feature is 0.03 Jy/beam, which is at the 3σ significance level of the instrument and, thus, should be treated as an upper limit. The peak position is located $\sim 3'$ East of the pulsar. The apparent position of the feature may be slightly shifted to the North-East due to a strong background gradient in the field of view from the nearby strong unidentified radio source. The size of the feature on the North-East to South-West direction is consistent with size of the instrument's PSF, but it is slightly elongated in the North-West to South-East direction. Further radio observations are necessary to precisely determine the morphology and polarization of the feature in order to confirm or discard the possible association with the pulsar.

7.4.3 Fermi LAT observations

Observations at HEs with Fermi LAT revealed a point-like source 2FGL J1303.7-6316c [Nolan et al., 2012] which is coincident with HESS J1303−631. The spectrum of the source follows a power-law with a spectral index 2.1 ± 0.1 and an integral photon flux between 1 and 100 GeV of $(2.46 \pm 0.46) \times 10^{-9}$ cm^{-2}s^{-1}.

Observations of the SNR Kes 17 resulted in a detection of the HE source to the South-West of the remnant (hereafter, SW source) with a peak at $\alpha_{\rm J2000} = 13^{\rm h}04^{\rm m}11^{\rm s}$, $\delta_{\rm J2000} = -63^\circ 14' 52''$ [Wu et al., 2011]. This source is coincident with the catalogued source 2FGL J1303.7−6316c within the 95 % confidence level contours, but the mea-

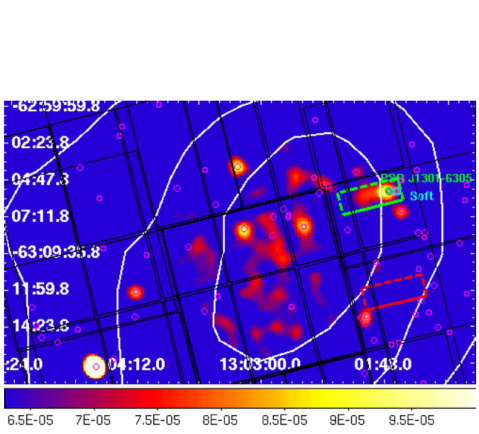

(a) Top: XMM-Newton X-ray flux map in the $2-8$ keV energy band. The horizontal axis is Right Ascension and the vertical axis is declination in J2000 coordinates. XMM catalog sources are shown by magenta circles. The pulsar PSR J1301−6305 is shown as a green circle and a soft point-source presumably unrelated to the pulsar is indicated by a cyan circle. White contours of the VHE source correspond to the 8, 14, 20 σ significance. The green box shows the slice used to create the profile (bottom) and the red box shows the slice used for the background estimation. Bottom: The slice profile fitted with the sum of two Gaussians for the compact and diffuse regions (see text) and a flat background (indicated with a dashed horizontal line). The unrelated soft point source at $\sim 25''$ is fitted with a King profile.

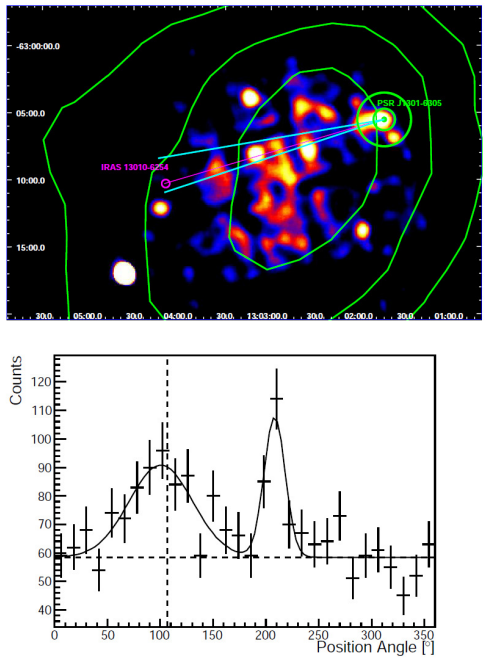

(b) Top: The XMM-Newton X-ray count map of the HESS J1303−631 field of view. The horizontal axis is Right Ascension and the vertical axis is declination in J2000 coordinates. The ring used for the azimuthal profile estimation is shown in green. Green contours of the VHE source correspond to the 8, 14, 20 σ significance. Cyan lines denote 1σ errors of the fitted direction of the X-ray extension. The star forming region IRAS 13010-6254 is indicated by a magenta circle and the direction to it by a magenta line. Bottom: The azimuthal profile in a position angle from the North of the pulsar. The projected on-counts are fitted with a sum of a Gaussian and a constant to account for a flat background. The horizontal dashed line indicates the flat background. The vertical dashed line indicates the direction to the star froming region. The point-source located at $\sim 210^{\circ}$ is an unidentified X-ray source.

Figure 7.6: X-ray observations of the HESS J1303−631 field of view. Figures are taken from The H.E.S.S. Collaboration: Abramowski, A. et al. [2012].

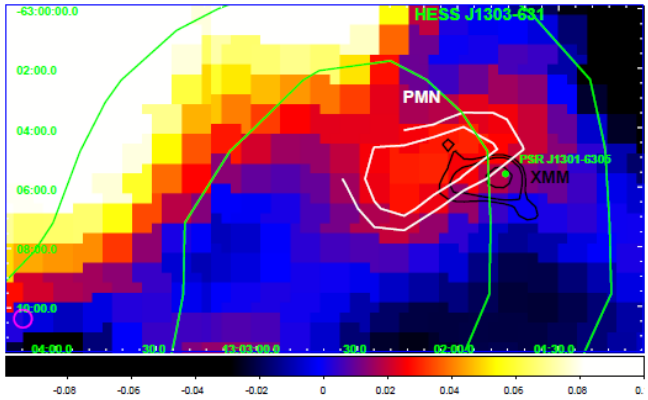

Figure 7.7: 4.85 GHz radio image from the PMN survey of the HESS J1303−631 region. The horizontal axis is Right Ascension and the vertical axis is declination in J2000 coordinates. H.E.S.S. VHE contours are shown in green, XMM-Newton X-ray contours are shown in black and the radio contours are shown in white. The pulsar position is indicated by a green filled circle. The figure is taken from The H.E.S.S. Collaboration: Abramowski, A. et al. [2012].

sured spectrum parameters are quite different. Under the assumption of a point-like source the power-law fit of the SW source spectrum results in a spectral index of 2.57 ± 0.23 with an integral photon flux in the $1 - 20$ GeV energy band of $(3.02 \pm 0.59) \times 10^{-9}$ cm^{-2}s^{-1}. Due to the very steep spectrum Wu et al. [2011] argue that this source cannot be a counterpart of HESS J1303−631 but should rather be the counterpart of the star-forming region IRAS 13010−6254. Nevertheless, the discrepancy of the measured parameters between the SW source and 2FGL J1303.7−6316c needs more investigation and a careful data analysis for this region is required, but this is beyond the scope of this thesis.

7.5 Modeling of the Broadband Emission from HESS J1303−631

7.5.1 One-zone 1D Model

As a first approximation of the broadband modeling of the MWL emission from HESS J1303−631 the simple one dimensional static model was used. In this model, it is assumed that only one population of electrons is responsible for all the observed emission from the source. Similar to the model applied to the MWL emission from the SNRs G 1.9+0.3 and G 330.2+1.0 in the leptonic scenario described in Section 6.4.1, it is assumed that one population of isotropically distributed relativistic electrons generates radio and X-ray emission through the synchrotron mechanism and the VHE γ-ray emission through the IC scattering on CMB photons. In the case of HESS J1303−631 the contribution of other photon fields to the IC emission is neg-

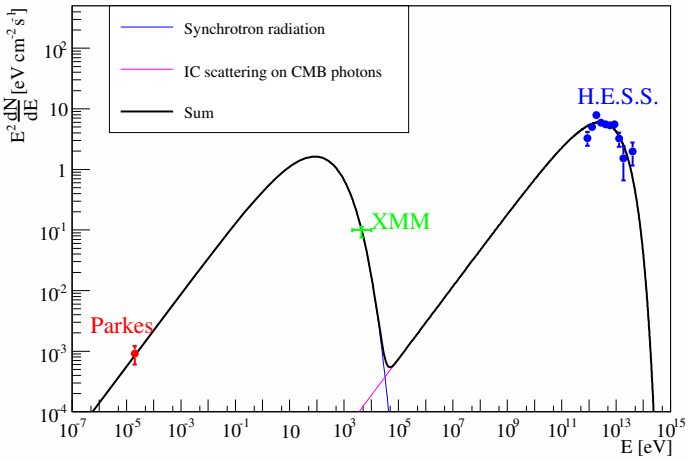

Figure 7.8: Spectral energy distribution of HESS J1303−631 fitted with sum of the synchrotron and IC emission.

ligible. The electron energy distribution is assumed to follow a power-law with an exponential cut-off

$$N_e(\gamma) = K_e \gamma^{-p} e^{-\frac{\gamma}{\gamma_{cut}}}, \tag{7.1}$$

where K_e is the normalisation, γ is the Lorentz factor of the electrons, γ_{cut} is the cut-off Lorentz factor and p is the spectral index.

The sum of the synchrotron and IC emission was fitted to the MWL data including a radio measurement and considering the X-ray data as a single point at $E_{\mathrm{X-ray}} = 4.4^{+5.6}_{-2.4}$ keV (Fig. 7.8). The fit resulted in a χ^2 probability of 2 % and yielded the following values for the free parameters:

$$\begin{aligned} p &= 1.8^{+0.1}_{-0.1}, \\ E_{\mathrm{cut}} &= 31^{+5}_{-4}\ \mathrm{TeV}, \\ K_{\mathrm{e}}/(4\pi D^2) &= 3.7^{+8.1}_{-2.9}\ \mathrm{cm}^{-2}, \\ B &= 1.4^{+0.2}_{-0.2}\ \mu\mathrm{G}, \end{aligned} \tag{7.2}$$

where $E_{\mathrm{cut}} = m_{\mathrm{e}}c^2\gamma_{\mathrm{cut}}$ is the cut-off energy of the electron spectrum, D is the distance to the pulsar and B is the magnetic field.

The obtained electron spectrum yields a total energy in electrons above 1 GeV of $W_{\mathrm{tot}} = 2 \times 10^{48}$ erg. As proposed by de Jager [2008] the total energy in electrons can be used for the estimation of the birth period of the pulsar if one expresses it as the fraction of the total pulsar energy loss, i.e. the difference between the initial and

current rotational energies:

$$W_{\rm tot} = \eta(E_{\rm rot,0} - E_{\rm rot}) = \eta\frac{1}{2}I\left[\left(\frac{2\pi}{P_0}\right)^2 - \left(\frac{2\pi}{P}\right)^2\right], \tag{7.3}$$

where η is the conversion efficiency of the spin-down power into accelerated electrons and is typically assumed to be in the range $0.3 - 0.7$. Then assuming the canonical value of the momentum of inertia $I = 10^{45}$ g cm^2 the estimate for the pulsar birth period varies between 51 and 75 ms, which is in agreement with estimations of birth periods for pulsars associated with composite SNRs [van der Swaluw and Wu, 2001].

The estimate of the magnetic field is of the same magnitude as the averaged line-of-sight magnetic field of $\sim 2\mu$G provided by the measurement of the pulsar's rotation measure [Crawford and Tiffany, 2007]. A magnetic field in a PWN much lower than the averaged ISM magnetic field would be difficult to explain. The low magnetic field is also in agreement with what is expected in evolved PWNe given that the magnetic field is decreasing with time as $\propto t^{-1.3}$ and thus supressing the synchrotron emission at later stages of evolution [de Jager et al., 2009]. Nevertheless, the assumption of a one-zone model may significantly underestimate the magnetic field. The much smaller size of the X-ray emission suggests a more realistic scenario where two populations of electrons should be considered: young electrons in the vicinity of the pulsar responsible for the synchrotron nebula and high energy TeV emission and old electrons, far from the pulsar, responsible for the extended TeV source. In this scenario, the non-detection of the X-ray emission from old electrons can be explained simply by radiative losses which imply a strong energy cut-off, which would suppress the synchrotron emission even for a much stronger magnetic field. Simultaneously, the VHE emission can be still reproduced by the same electron population since it is produced by lower energy electrons. A higher magnetic field is also expected for the population of the young electrons in a much smaller region around the pulsar. Indeed, the VHE flux is obviously lower because of the region size and thus needs less electrons to generate it. In turn the smaller amount of electrons requires a higher value of the magnetic field in order to reproduce the X-ray flux from the region.

Although the assumption of two separate electron populations is better, it is still far from reality. The energy-dependent morphology in VHE γ-rays show a rather continuous gradient-like transition from lower to higher energies, i.e. from older to younger electrons. This morphology requires a continuous spatial change of the electron population. Therefore, a detailed spatial-dependent modeling of the MWL emission is needed. Moreover, the spatial distribution is directly connected to the time evolution of the source, which only increases the number of free parameters and makes the modeling even more complicated. In the following section, possible constrains on the model parameters will be discussed.

7.5.2 Extension Towards More Realistic Models

The natural way of the elaboration of the broadband emission model is the extension towards the two-dimensional case, i.e. taking into account the spatial morphology of the source. The energy-dependent morphology of the VHE source, as well as the much smaller size of the X-ray emitting region clearly show that electrons are distributed not uniformely with more energetic electrons closer to the pulsar. It is not totally clear though, what is the reason for such a distribution and some assumptions should be made for further modeling.

The natural explanation could be that the pulsar is moving leaving a trail of older electrons which lose energy through radiative cooling. If one assumes that the extension of the VHE source is exclusively due to the proper motion of the pulsar neglecting diffusion effects, then for given extension of the source of 0.39° (a double Gaussian width σ_x obtained in a position fit with a two-dimensional Gaussian) and distance to the pulsar of 6.6 kpc the pulsar travelled 45 pc, which can be treated as an upper limit on the travelled distance. It corresponds to the upper limit on the mean velocity of the pulsar of $\sim 4,000$ km/s if the characteristic age is taken as a true age, which would place PSR J1301−6305 among the fastest known pulsars, believed to have velocity of $\gtrsim 1,600$ km/s (see e.g. Cordes and Chernoff [1998]).

The estimates presented above are based on the distance to the pulsar calculated using the model of electron distribution in the Galaxy, a method which is often considered unreliable. Another way to constrain the distance to the pulsar and the distance traveled by pulsar is to assume that the birth place of the pulsar is associated with the star forming region IRAS 13010-6254 as suggested by the direction of the X-ray extension. The absence of the plausible SNR association and the fact that it is the only star forming region within more than a degree of the pulsar support this interpretation. The distance to IRAS 13010-6254 inferred by its kinematic velocity is $\sim 12.4 - 12.9$ kpc [The H.E.S.S. Collaboration: Abramowski, A. et al., 2012]. If the pulsar was born in IRAS 13010−6254 then it would have travelled 0.28° or ~ 62 pc corresponding to a very high velocity of $\sim 5,000$ km/s for the true age assumed to be equal to the characteristic age.

The assumption of the true age of the pulsar being equal to the characteristic age can be very misleading. The characteristic age can both overestimate and underestimate the true age of the pulsar (see Section 4.1.1). The underestimation of the age takes place when the braking index is below 3, which is the case for all pulsars for which the braking index was firmly measured. In the extreme case of the Vela pulsar $n = 1.4 \pm 0.2$ [Lyne et al., 1996] and the true age should be 5 times greater than predicted by τ_c if the assumption of $P_0 \ll P$ holds. If this is also a case for PSR J1301−6305 then the estimated velocity becomes more reasonable. For a birth period $P_0 \sim 60$ ms inferred by the one-zone model described in the previous section, the true age can be given as a function of the braking index

$$\tau = \frac{2.2 \times 10^4 [\mathrm{y}]}{n-1} \left(1 - 0.3^{n-1}\right). \tag{7.4}$$

Then, assuming $n = 1.4$ to be the lower limit on the braking index one can calculate the upper limit on the pulsar true age which will be $\tau \lesssim 21,000$ y, which is twice the characteristic age of the pulsar. This would, in turn, decrease the velocity estimate by a factor of two.

The modeling of the broadband emission would benefit a lot from the separate spectral analysis of different regions of the VHE source. The idea here is to divide the source into fractions of concentric rings centered on the pulsar and with an equal size (onion-like structure) and to derive the spectrum for each region. The study of the cut-off energy as a function of the radius would provide a very important information about the evolution of the PWN and particulary about the electron cooling timescales.

The detection at HEs would be also extremely helpful for modeling because HESS J1303−631 is one of a few PWNe for which the SED peak is observed in VHEs (Fig. 7.8). This means that moving to lower energies will allow to independently estimate the electron spectral index. In this respect the careful analysis of the Fermi data is required as well as future observations with H.E.S.S. II.

Despite of the flexibility of physical parameters HESS J1303−631 is a very interesting and promising object for the study of the evoulutionary processes in PWNe and the detailed modeling would require further observations of the source, particularly at radio and HE wavelengths.

8 PSR B1259−63/LS 2883

8.1 Overview

Four binary systems consisting of a massive star and a compact object have been detected at VHEs (see Chapter 4). Only for one of them, PSR B1259−63/LS 2883, the compact companion is unambiguously identified as a pulsar, making it a unique object for the study of the interaction between pulsar and stellar winds and the emission mechanisms in such systems.

PSR B1259−63/LS 2883 was discovered in a high frequency radio survey devoted to the detection of young, distant and short-period pulsars [Johnston et al., 1992a,b]. It consists of a rapidly rotating pulsar with a spin period of $\simeq$ 48 ms and a spin-down luminosity of $\simeq 8 \times 10^{35}$ erg/s in a highly eccentric ($e = 0.87$) orbit around a massive Be star. The pulsar moves around the companion with the period $P_{\rm orb} = 3.4$ years (1237 days).

Latest optical observations with VLT UT2 [Negueruela et al., 2011] significantly updated the previously known parameters of the companion star LS 2883. The luminosity of the star is $L_* = 2.3 \times 10^{38}$ erg s^{-1}. Because of its fast rotation the star is oblate with an equatorial radius of $R_{\rm eq} = 9.7 R_\odot$ and a polar radius of $R_{\rm pole} = 8.1 R_\odot$. This leads to a strong gradient of the surface temperature from $T_{\rm eq} \approx 27,500$ K at the equator to $T_{\rm pole} \approx 34,000$ K at the poles. The mass function of the system suggests a mass of the star of $M_* \approx 30 M_\odot$ and an orbital inclination angle $i_{\rm orb} \approx 25^\circ$ for the minimal neutron star mass of $1.4 M_\odot$. The optical observations also suggest that the system is located at the same distance as the star association Cen OB1 at $d = 2.3 \pm 0.4$ kpc [Negueruela et al., 2011]. The companion Be star features an equatorial disk which is believed to be inclined with respect to the pulsar's orbital plane [Johnston et al., 1992a, Melatos et al., 1995, Negueruela et al., 2011] in a way that the pulsar crosses the disk twice in each orbit just before ($\sim$ 20 days) and just after ($\sim$ 20 days) the periastron.

Since its discovery in 1992, PSR B1259−63/LS 2883 is constantly monitored by various instruments in all energy bands. The source shows broadband emission and is visible from radio wavelengths and up to VHEs. The properties of the radio emission are very different depending on the distance between the pulsar and the star. Radio observations [Johnston et al., 1999, Connors et al., 2002, Johnston et al., 2005a] show that when the pulsar is far from the periastron the observed radio emission consists only of the pulsed component, whose intensity is almost independent on the orbital position. But closer to the periastron, starting at about $t_{\rm p} - 100$d, where $t_{\rm p}$ is the time of periastron, the intensity starts to decrease and disappears

completely approximately at $t_p - 20$d. This is followed by an eclipse of the pulsed emission for about 35-40 days as the pulsar is behind the disk. In contrast, a transient unpulsed component appears and sharply rises to a level more than 10 times higher than the flux density of the pulsed emission far from the periastron. The unpulsed component is believed to come from synchrotron radiation generated in the shocked wind zone between the relativistic pulsar wind and the stellar disk outflow. After the disk crossing the unpulsed emission shows a slight decrease with another increase around $t_p + 20$d at the second crossing of the disk.

PSR B1259−63/LS 2883 is very well covered by X-ray observations carried out with various instruments like ASCA [Kaspi et al., 1995, Hirayama et al., 1999], ROSAT [Cominsky et al., 1994], XMM-Newton [Chernyakova et al., 2006], INTEGRAL [Shaw et al., 2004]. The periastron passage in 2007 was monitored at the same time by Suzaku, Swift, XMM-Newton and Chandra [Chernyakova et al., 2009]. Observations did not show any pulsed X-ray emission from the pulsar. Unpulsed non-thermal radiation from the source appeared to be variable in flux and spectral index. Similarly to radio measurements the enhancement of the flux occurs shortly before and shortly after the periastron. These time intervals coincide with the enhancement period in radio emission and as it is shown later in this chapter also with the VHE emission. Unambiguously, the enhancement of the non-thermal emission from the system is related to the position of the circumstellar disk and results from the interaction of the pulsar wind with the much denser photon field.

8.2 Summary of 2004 and 2007 Periastron Observations by H.E.S.S.

In 2004, PSR B1259−63 was observed by H.E.S.S. (first detection) shortly before periastron and up to $t_p + 100$d (March 7, 2004). The livetime was 50 h (8 h in the phase prior to the periastron passage and 42 h in the post-periastron phase) [Aharonian et al., 2005c]. The overall time averaged differential energy spectrum of photons followed a simple power law

$$\frac{\mathrm{d}N}{\mathrm{d}E} = N_0 \left(\frac{E}{1\mathrm{TeV}}\right)^{-\Gamma}, \tag{8.1}$$

with a photon index $\Gamma = 2.7 \pm 0.2_{\mathrm{stat}} \pm 0.2_{\mathrm{syst}}$ and flux normalization $N_0 = (1.3 \pm 0.1_{\mathrm{stat}} \pm 0.3_{\mathrm{syst}}) \times 10^{-12}\,\mathrm{TeV}^{-1}\mathrm{cm}^{-2}\mathrm{s}^{-1}$. The integral flux above 380 GeV was $F(> 380\,\mathrm{GeV}) = (4.0 \pm 0.4) \times 10^{-12}\mathrm{cm}^{-2}\mathrm{s}^{-1}$ which is equivalent to $\sim$ 5% of the Crab Nebula flux above this threshold energy.

During the second H.E.S.S. observation campaign around the 2007 periastron passage (July 27, 2007), a livetime of 52 h (49 h before the periastron passage and 3 h after the periastron passage) was obtained [Aharonian et al., 2009a]. The data were taken from April to August 2007. This campaign allowed the extraction of

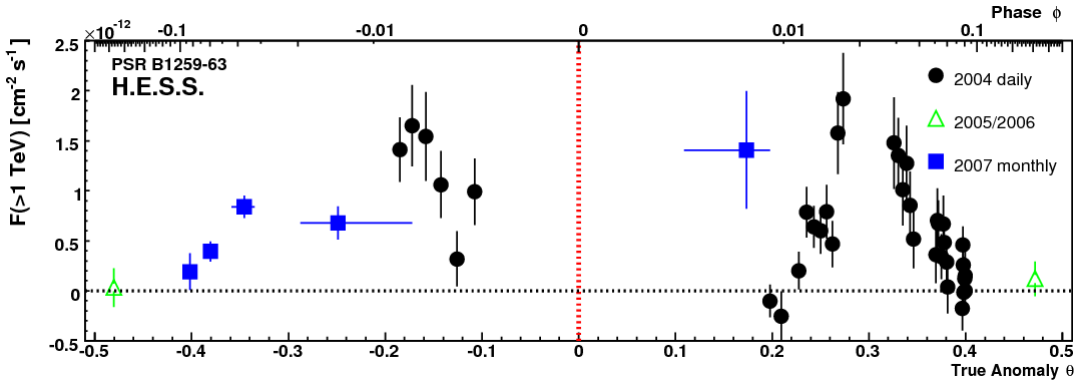

Figure 8.1: The integrated photon flux above 1 TeV as a function of true anomaly θ[1]. The data from 2004 and 2007 periastron passages are shown as well as upper limits for 2005/2006 observations. The periastron position is indicated with the dashed vertical line. The plot is taken from Aharonian et al. [2009a]

the pre-periastron lightcurve, and confirmed the spectral properties of the source obtained from the 2004 data. The spectrum was described by a power law with $\Gamma = 2.8 \pm 0.2_{\rm stat} \pm 0.2_{\rm syst}$ and $N_0 = (1.3 \pm 0.1_{\rm stat} \pm 0.3_{\rm syst}) \times 10^{-12}{\rm TeV}^{-1}{\rm cm}^{-2}{\rm s}^{-1}$. The overall flux level appears to be compatible with the 2004 measurements.

Both observations showed the variable behavior of the source flux with a hint of two asymmetrical peaks around periastron with a significant decrease of the flux at the periastron itself (Fig. 8.1). This shape of the lightcurve can serve as an indication that the TeV emission from PSR B1259−63/LS 2883 is closely connected to the interaction of the pulsar with the disk. This hypothesis is supported by observations in other wavebands which show a similar shape of the flux variability.

The observations around the 2007 periastron confirmed the periodicity of the source only indirectly, since they were performed in different periods of time relative to the periastron passage. In 2004, PSR B1259−63/LS 2883 was observed mostly after the periastron, while in 2007 mostly before it. Therefore it was essential to repeat observations during the next periastron to firmly confirm the periodicity of the source by observations in the same, with respect to periastron, time interval.

PSR B1259−63/LS 2883 was also monitored in 2005 and 2006 far from periastron resulting in 8.9 h and 7.5 h of observations, respectively [Aharonian et al., 2009a]. These measurements showed no significant flux of γ-rays from the source leading to upper limits at the level of 7×10^{-13} cm^{-2}s^{-1} for the integrated flux above 1 TeV.

[1]True anomaly is the angle between the direction of periapsis and the current position of the body moving along a Keplerian orbit as it is seen from the main focus of the ellipse, i.e. the point around which the body is rotating. At this figure and later on true anomaly is scaled as $\theta \in [-0.5, 0.5]$

8.3 2010 Periastron H.E.S.S. Observations

The recent periastron passage which took place on 15th of December 2010 raised a great interest in the astrophysical community. The source was observed by a number of different instruments at different wavelengths. It was also the first periastron with Fermi LAT in orbit. Unfortunately, PSR B1259−63/LS 2883 was not visible for H.E.S.S. before and during the periastron passage, but it could be observed shortly after periastron. Therefore, it was proposed [Sushch et al., 2010] to collect 59 hours of observations after the periastron, but not more than 100 days after periastron. This corresponded to 19 hours in January, 20 hours in February and 20 hours in March. The proposed exposure was fully granted by the H.E.S.S. observation committee.

Unfortunately, the mentioned period (January–March) is the worst time for observations due to the rainy season in Namibia. On top of this there were some technical problems with one of the cameras for a part of observed period. This resulted in a rather modest exposure comparing to the proposed time. The successful observations were performed in the period from 9th to 16th of January, i.e. $(t_\mathrm{p} + 26\mathrm{d}) - (t_\mathrm{p} + 32\mathrm{d}$.

8.3.1 Data and Analysis Techniques

The collected data correspond to 7 h of livetime after the standard quality selection procedure. These data were taken in five nights, namely January 9/10, 10/11, 13/14, 14/15 and 15/16. The data were analysed using two different analysis techniques for the shower reconstruction and γ/hadron separation: the *H.E.S.S. standard Hillas reconstruction*[2] (Iurii Sushch) and the *model analysis*[3] (Mathieu de Naurois) (see Section 2.2.2). For both types of analysis *standard cuts* were used, i.e. 80 p.e. cut for *Hillas reconstruction* and 60 p.e. cut for *model analysis*. Two models of the background subtraction were used depending on the analysis purposes: *Ring Background* was used for the skymaps and *Reflected Region Background* was used for the spectra estimation (see Section 2.2.2).

For the *model analysis* a different procedure of the quality selection was applied which led to a slightly smaller database with 6 hours of livetime. For the spectrum estimation, in order to have the same input information to be able to better compare analysis results, the same database (i.e. the database used for the *model analysis*) was considered.

The observations were performed at a relatively high mean zenith angle of 48° and with a mean offset angle of 0.55° from the test region centered at $\alpha_\mathrm{J2000} = 13^\mathrm{h}02^\mathrm{m}48^\mathrm{s}$, $\delta_\mathrm{J2000} = -63°50'09''$.

The test region was *apriori* defined as a circle with radius 0.11° (i.e. $\theta^2 < 0.0125$, see Section 2.2.2) which is a standard size for point-like sources.

[2] H.E.S.S. Analysis Package (HAP) version 11-02-pl07
[3] ParisAnalysis software version 0-8-18

8.3.2 Analysis Results

A firm detection of the source was obtained in both analysis chains with a significance [Li and Ma, 1983] of 6.6 standard deviations for *Hillas*[4] and 13.5 for *model* (see Table 8.1 for the comparison of *Hillas* and *model* analysis results). This difference in significance is due to the better hadron suppression at low energies for the *model analysis*.

A spectral analysis of the detected excess events shows that the differential energy spectrum of the source follows a simple power law of the form as in Eq. 8.1. Estimates of the flux normalisation at 1 TeV N_0 and the photon spectral index Γ as well as the total photon flux from the source averaged over the whole observation period are collected in the Table 8.1 for *Hillas* and *model* analysis chains. The results obtained within two different analysis techniques are in a very good agreement. Spectra obtained within these two analysis modes are shown in Fig. 8.2. Estimates of the total photon flux are compatible within $\sim 0.1\,\sigma$ (standard deviation).

Table 8.1: The comparison of *Hillas* and *model* analysis results

	Hillas	*model*
Livetime, [h]	7	6.1
excess	113.6	124
significance [σ]	6.6	13.5
Γ	$2.90 \pm 0.34_{\mathrm{stat}} \pm 0.2_{\mathrm{syst}}$	$2.82 \pm 0.25_{\mathrm{stat}} \pm 0.2_{\mathrm{syst}}$
N_0 (1 TeV), [$10^{-12}\mathrm{TeV}^{-1}\mathrm{cm}^{-2}\mathrm{s}^{-1}$]	$2.96 \pm 0.91_{\mathrm{stat}} \pm 0.59_{\mathrm{syst}}$	$2.94 \pm 0.49_{\mathrm{stat}} \pm 0.59_{\mathrm{syst}}$
Fit probaility	0.83	0.63
Flux(>1 TeV), [$10^{-12}\,\mathrm{cm}^{-2}\mathrm{s}^{-1}$]	$1.56 \pm 0.56_{\mathrm{stat}} \pm 0.31_{\mathrm{syst}}$	$1.61 \pm 0.22_{\mathrm{stat}} \pm 0.32_{\mathrm{syst}}$

In order to check for the variability of the source a lightcurve study was performed. The lightcurve is produced on a night-by-night basis assuming the photon spectral index obtained in the spectral fit (Fig. 8.3). The spectral index was fixed because of the low statistics for each individual night. Fitting the lightcurve with a constant leads to a χ^2/NDF of 4.6/4 in the *Hillas* and 6.6/4 in the *model* analysis. These correspond to the null hypothesis probabilities[5] of 0.33 (*Hillas*) and 0.16 (*model*), not showing any significant deviation from the constant, i.e. there is no evidence for a source variability found in the data, which spans a period from $t_{\mathrm{p}} + 26\mathrm{d}$ to $t_{\mathrm{p}} + 32\mathrm{d}$.

The compatibility of the *Hillas* and *model* analysis results was checked by comparing estimated fluxes for each individual night. For this purpose a difference between

[4] In this section analysis results of the PSR B1259−63/LS 2883 observation data are presented for both analysis chains alongside. For simplicity the two different analyses are referred to as *Hillas* (*H.E.S.S. standard Hillas reconstruction*) and *model* (*model analysis*)

[5] The probability of obtaining values for the test statistics at least as extreme as values which were actually observed, assuming that the null hypothesis is true

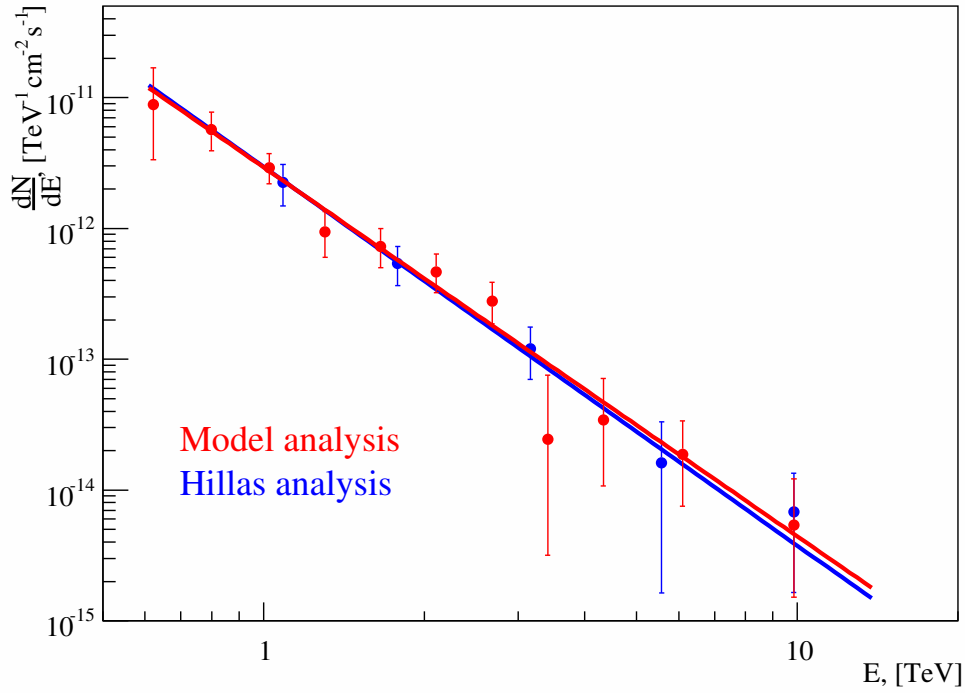

Figure 8.2: The overall differential energy spectrum of the VHE emission from PSR B1259−63 for the whole observation period from 9th to 16th of January 2011 obtained in the *Hillas* (blue) and *model* (red) analysis chains. Solid lines denote spectral fits with a simple power-law.

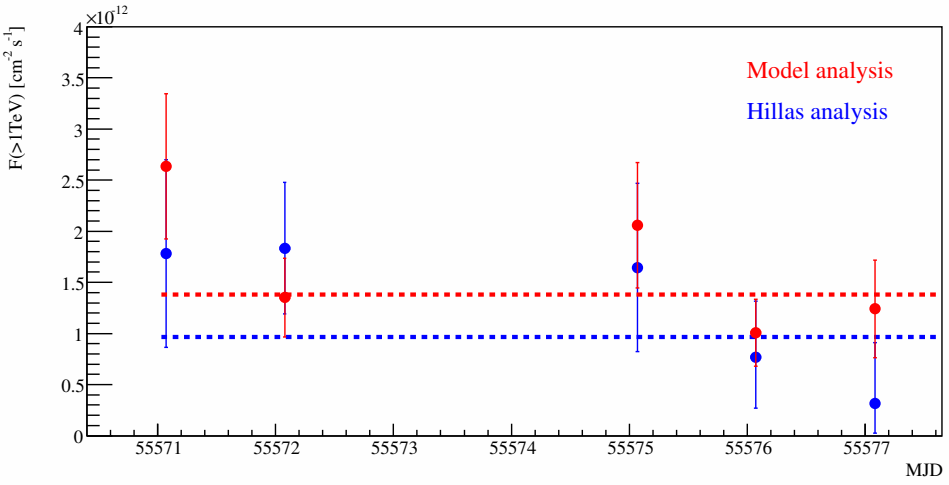

Figure 8.3: Integrated photon flux above 1 TeV for individual observation nights in the *Hillas* (blue) and *model* (red) analysis chains. The dashed lines indicate the result of fitting a constant to the lightcurves.

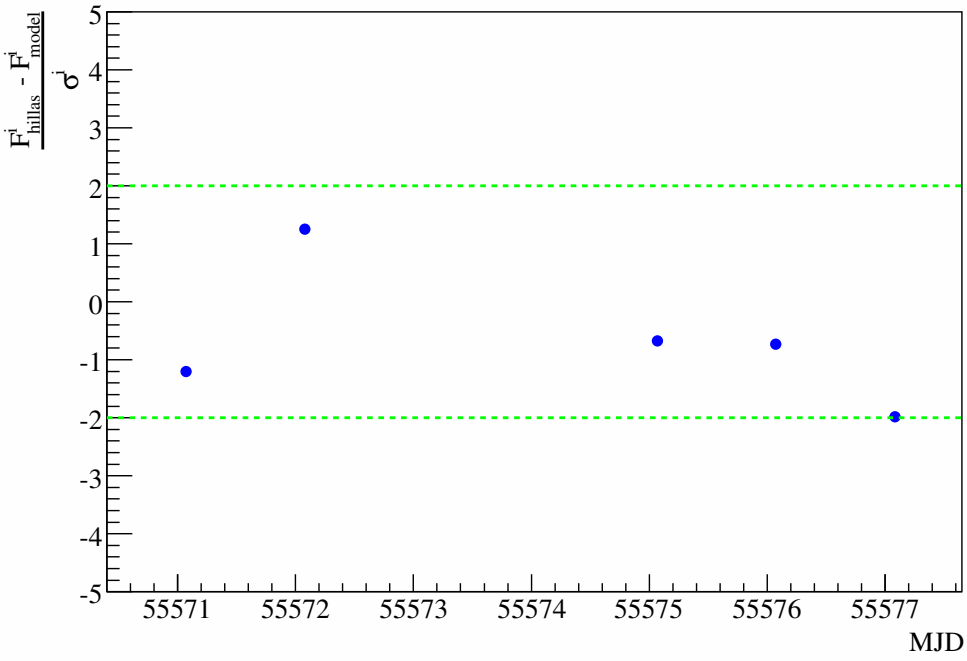

Figure 8.4: The distribution of the difference between integrated fluxes above 1 TeV obtained in the *Hillas* and *model* analysis chains for individual nights in units of standard deviations.

flux estimates $F^i_{Hillas} - F^i_{model}$ was calculated for each night i in units of the standard deviation σ. For each night the standard deviation is defined as minimum from standard deviations of *Hillas* and *model* flux calculations, i.e. $\sigma^i = \min(\sigma^i_{Hillas}, \sigma^i_{model})$ in order to be conservative. From Fig. 8.4 it can be seen that the flux difference is distributed around zero within 2σ deviation which indicates that fluxes estimated in different analysis chains are well compatible.

8.3.3 Comparison with Previous Observations

In order to compare the results of the 2010/2011 observation campaign with previous observations the results obtained with the *model* analysis were used due to the higher sensitivity of the *model* analysis comparing to the *Hillas* analysis and compatibility of analysis results.

In Fig. 8.5 the integrated photon flux above 1 TeV as a function of time with respect to periastron (indicated with the dashed vertical line) is shown. The lightcurve compiles the data from all three periastron observation campaigns spanning from $t_p - 100$d to $t_p + 100$d. The observed flux from the 2010/2011 observation campaign matches the shape of the overall lightcurve very well confirming the periodicity of the source. Observation periods from 2004 and 2007 were separated in time with respect to the periastron position, i.e. observations in 2004 were performed mainly af-

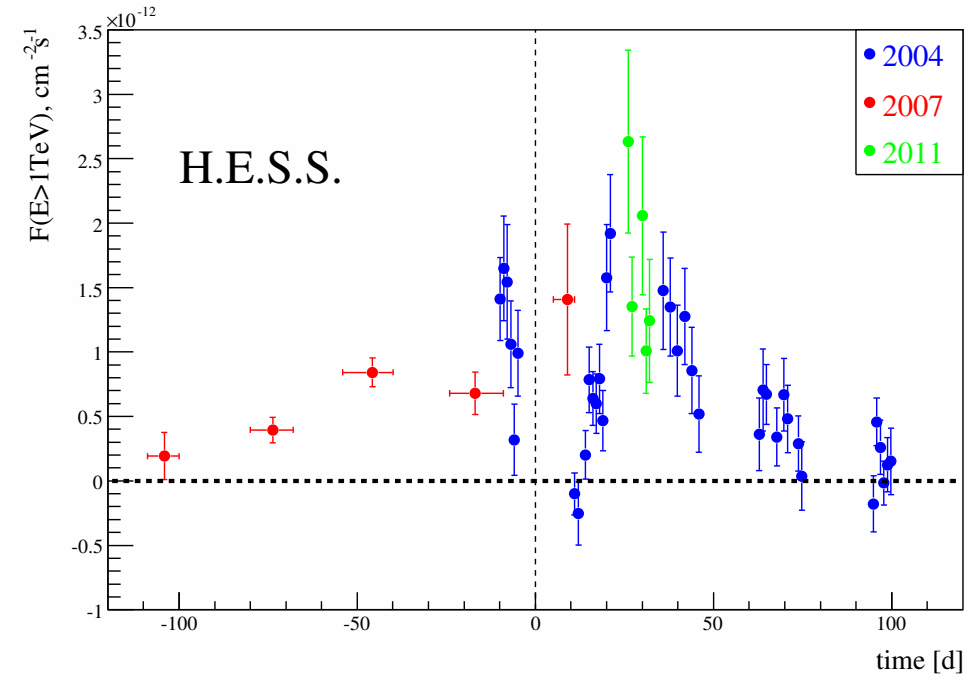

Figure 8.5: The integrated photon flux above 1 TeV as a function of the time with respect to the periastron passage indicated with the dashed vertical line. The data from the 2004 (blue), 2007 (red) and 2011 (green) observation campaigns are shown.

ter and in 2007 mainly before the periastron. Therefore, it was impossible to directly confirm the periodicity of the source by comparing observations of PSR B1259−63 at the same orbital phase. In this perspective, the 2011 observations are very important due to their overlap in time with respect to the periastron with observations from 2004. Although there is no exact overlap, the 2011 observation period fills the gap in the 2004 data post-periastron lightcurve right after the peak position and the integrated flux follows the decreasing shape of the lightcurve in the post-peak phase.

The observations around the 2010 periastron also confirm the permanence of the spectral shape which was found during the previous observations. The 2011 data reveals the spectral index of the differential energy spectrum of $2.82 \pm 0.25_{\mathrm{stat}} \pm 0.2_{\mathrm{syst}}$ which is well compatible with previous results (see Section 8.2).

8.4 Multiwavelength Campaign

The H.E.S.S. observations were a part of an extended multiwavelength (MWL) campaign including also radio, optical, X-ray and high energy (HE; $E > 100$ MeV) observations. In this section, the available MWL data are discussed concentrating on

the Fermi LAT observations in the HE band. The section follows mainly the Fermi LAT discovery paper [Abdo et al., 2011b].

8.4.1 Summary of MWL Observations in the Energy Range from Radio to X-rays

The pulsed radio emission was monitored with the Parkes telescope looking for changes in the dispersion and rotation measure. An eclipse of the pulsed signal lasted from $t_p - 16$d to $t_p + 15$d when pulses appeared again. In the two weeks before the disappearance of the pulsed signal significant changes in the dispersion measure were detected.

Radio emission from PSR B1259−63/LS 2883 at frequencies between 1.1 and 10 GHz was observed using the ATCA array. Twelve observations in the period from $t_p - 31$d to $t_p + 55$d were collected. The detected unpulsed transient radio emission around the periastron passage showed a behavior similar to that seen in previous observations [Johnston et al., 2005b] (see Fig. 8.6d).

The X-ray energy band was sufficiently covered by three instruments: XMM-Newton, Swift and Suzaku. Observations confirmed the 1-10 keV lightcurve shape obtained in previous periastron passages, showing a rapid X-ray brightening starting at about $t_p - 25$d with a subsequent decrease closer to the periastron and a second increase of the X-ray flux after the periastron (Fig. 8.6c).

8.4.2 Fermi LAT Observations

Observations of the binary system PSR B1259−63/LS 2883 at high energies (E>100 MeV) were performed using the Large Area Telescope (LAT) on board of Fermi. The data taken around the periastron passage were analysed by two independent working groups [Abdo et al., 2011b, Tam et al., 2011], revealing similar results. The source was detected close to the periastron passage with a very low energy flux above 100 MeV of about $(1-2)\times10^{-7}$ cm^{-2}s^{-1}. After the initial detection the flux decreased and the source was undetected until 14th of January, $t_p + 30$d, when a spectacular flare was detected with an overall flux ~ 10 times higher than the flux detected close to the periastron. Apart from similarities there are also some discrepancies between the analysis results of the two working groups. For this thesis the analysis results of Abdo et al. [2011b] are considered as the main ones since they are official results provided by the Fermi Collaboration and, thus, may benefit from the usage of more developed analysis tools. The results of Tam et al. [2011] are reviewed and the mentioned discrepancies are discussed in Appendix B.

Abdo et al. [2011b] distinguished two radiation periods: "brightening" and "flare". The brightening period lasted from the typical start of enhanced X-ray and unpulsed radio flux, at $t_p - 28$d on 17th of November, to $t_p + 18$d on 2nd of January. The latter date was chosen using the study of the time evolution of the cumulative test statistic (TS) as the date after which the TS starts to drop monotonically. The spectrum during this period is best described as a power-law with the photon index of

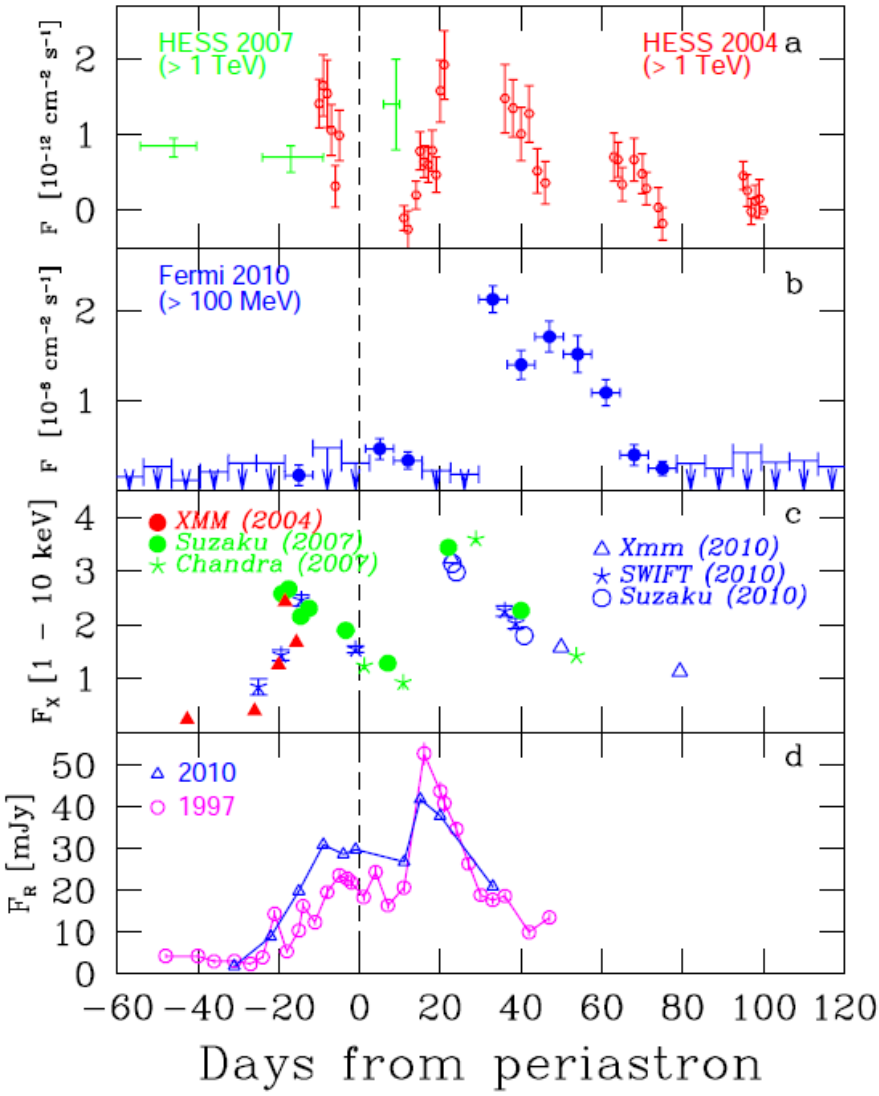

Figure 8.6: Unpulsed fluxes in the radio, X-ray, HE and VHE bands around periastron. Lightcurves are shown in the following order: a) fluxes above 1 TeV obtained with H.E.S.S. around the 2004 and 2007 periastron passages, b) fluxes above 100 MeV obtained with Fermi LAT around the 2010 periastron passage, c) X-ray fluxes from three periastron passages in units of 10^{-11} erg cm^{-2} s^{-1} and d) radio (2.4 GHz) fluxes from the 2010 and 1997 periastron passages measured with the ATCA array. The figure is taken from the Fermi LAT discovery paper [Abdo et al., 2011b].

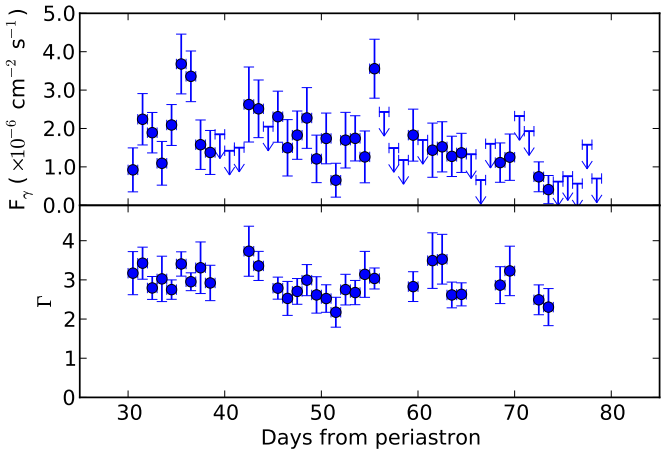

Figure 8.7: Fermi HE photon flux and photon index as a function of time on a daily timescale during the flare period [Abdo et al., 2011b]. Top: the flux above 0.1 GeV is shown as it is reported, 2σ upper limits are drawn for points with TS<5. Bottom: spectral index of a power law spectrum. The figure is taken from Abdo et al. [2011b].

$\Gamma = 2.4 \pm 0.2_{\rm stat} \pm 0.5_{\rm syst}$ and an average flux in the energy range of $0.1 - 1$ GeV of $(2.5 \pm 0.8_{\rm stat} \pm 0.8_{\rm syst}) \times 10^{-7}$ cm^{-2}s^{-1}. There was no significant emission detected above 1 GeV.

The flare period started on 14th of January at $t_{\rm p} + 30$d with a sudden increase of the flux level. An abrupt increase of the flux was followed by a rather smooth decrease over seven weeks up to 4th of March. The flare peaked at $t_{\rm p} + 35$d reaching the flux level of about 3.5×10^{-6} cm^{-2}s^{-1} above 0.1 GeV (see Fig. 8.7). The highest day-averaged flux during the flare almost reached the estimate of the spin-down luminosity of the pulsar, which indicates a close to 100% efficiency of the conversion of the pulsar rotational energy into the γ-rays. The spectrum during this period is best described by a power-law with an exponential cut-off with a photon index $\Gamma = 1.4 \pm 0.6_{\rm stat} \pm 0.2_{\rm syst}$ and a cut-off energy $E_{\rm cutoff} = 0.3 \pm 0.1_{\rm stat} \pm 0.1_{\rm syst}$ GeV. The average flux above 100 MeV is $(1.3 \pm 0.1_{\rm stat} \pm 0.3_{\rm syst}) \times 10^{-6}$ cm^{-2}s^{-1}. Estimation of spectral indices on weekly time scales shows for the power-law fit a clear evidence of a softening of the spectrum from 2.0 to 2.5 during the brightening period to 3.5 around the peak of the flare. After that the spectrum is hardening again up to spectral index values observed during the brightening (see Fig. 8.8). In the period between brightening and flare no significant emission was detected.

Analysing lightcurves around the periastron in different energy bands (Fig. 8.6) one can see an obvious anticorrelation of the HE data comparing to the data in all other energy bands. Lightcurves in radio, X-ray and VHE bands show the two peak structure, one of which occurs shortly before the periastron and the other at about $t_{\rm p} + 20$d. In the HE lightcurve also two structures can be pointed out, but there are two important differences:

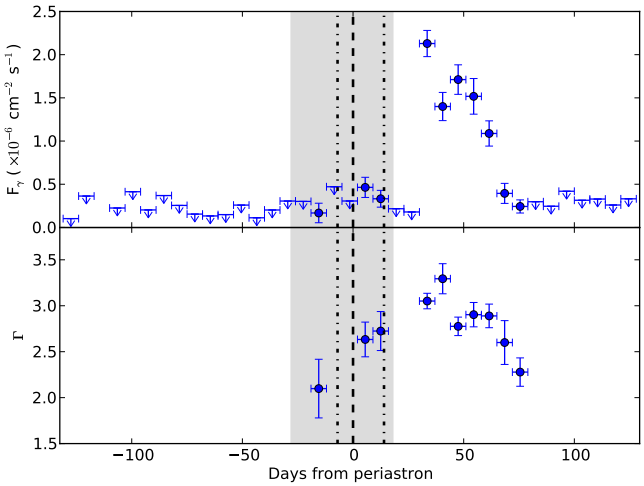

Figure 8.8: HE photon flux (top) and photon index (bottom) obtained with Fermi around the 2010 periastron passage as a function of time [Abdo et al., 2011b]. Top: the flux above 0.1 GeV is shown on a weekly scale, 2σ upper limits are drawn for points with TS<5. Bottom: spectral index of a power law fit. The shaded area shows the brightening period. The dashed-dotted lines mark the orbital phase during which EGRET observed this source in 1994 (see Abdo et al. [2011b]). The figure is taken from Abdo et al. [2011b]

- In the HE band, the flux during the post-periastron flare is much higher (by an order of magnitude) than the flux during the initial detection around the periastron, conversely, in all other energy bands pre- and post-periastron peaks are compatible.
- Although it is difficult to determine the position of the peak during the primary detection period at HEs, it can be said that the post-periastron flare at HEs is shifted in time comparing to post-periastron peak at other energies.

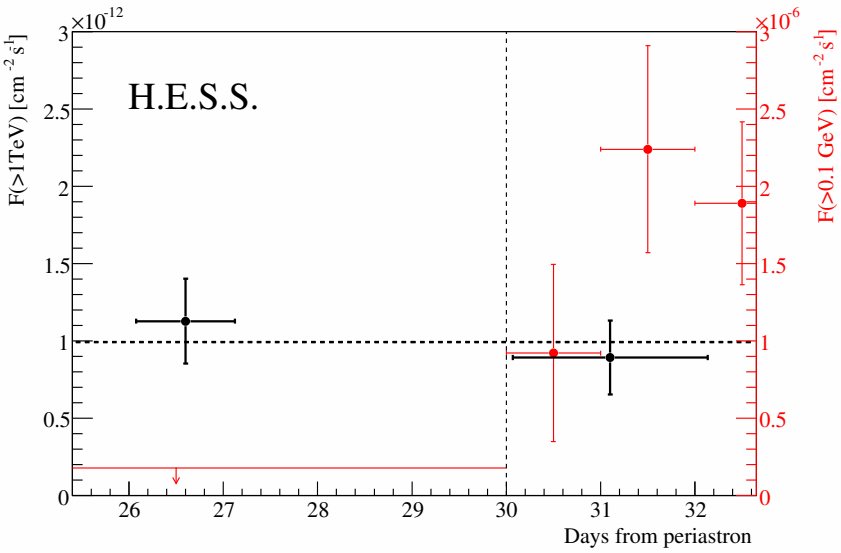

Figure 8.9: The overall photon fluxes above 1 TeV for the pre-flare and flare periods (see text) are shown as black filled circles. The dashed horizontal line shows the best fit with a constant. The HE data points above 0.1 GeV as reported by Abdo et al. [2011b] are shown as red filled circles. The flare start date is indicated by the dashed vertical line. The left axis indicates the units for the VHE flux and the right (red) axis denotes the units for the HE flux.

8.4.3 Search for a VHE Flux Enhancement during the HE Flare in the H.E.S.S. data

In the previous section, the 2011 flare in the HE band was compared to the VHE post-periastron data obtained with H.E.S.S. around the 2004 periastron passage. It is important to check if this phenomenon is seen only at HEs or whether it is a result of the overall behavior of the source and can also be seen at VHEs.

Although the H.E.S.S. exposure around the 2010 periastron passage was limited, the time period of the observations was perfect. The source was observed from 9th to 16th of January providing a three-day overlap with the HE flare. Therefore, it is possible to investigate in detail the level of the flux enhancement in the VHE band on the timescale of the HE flare. In order to optimize the sensitivity of the variability search the whole period of the H.E.S.S observations was divided into two almost equal periods: before and after the HE flare start date. Hereafter these two periods are referred as "pre-flare" and "flare". The pre-flare and flare datasets were analysed using the *model* analysis chain with the *Reflected Background* model for the background subtraction revealing very similar flux levels for both periods (see Table 8.2).

In order to search for a variability, the flux as function of time was fitted with a constant resulting in a mean flux of 0.99×10^{-12} cm^{-2}s^{-1} (horizontal dashed line

Table 8.2: Comparison of the H.E.S.S. data in the pre-flare and flare periods

	Pre-flare	Flare
Livetime [h]	2.4	3.5
excess	34.4	50.5
significance	7.5σ	7.3σ
Flux(> 1 TeV) [10^{-12} cm^{-2}s^{-1}]	$1.13 \pm 0.28_{\mathrm{stat}} \pm 0.23_{\mathrm{syst}}$	$0.89 \pm 0.24_{\mathrm{stat}} \pm 0.18_{\mathrm{syst}}$

in Fig. 8.9). The test of the constant null hypothesis revealed a χ^2 to NDF ratio of 0.42/1 which corresponds to a probability of 0.52, showing no indication for a flux change.

If one assumes that HE and VHE emission are created via the same mechanism then a flux enhancement of the same magnitude as observed at HEs should also be seen at VHEs. In order to investigate this hypothesis, the flare coefficient κ is introduced as the ratio of the fluxes during the flare period and the pre-flare period. The ratio of the $(t_{\mathrm{p}} + 30\mathrm{d}) - (t_{\mathrm{p}} + 32\mathrm{d})$ HE ($E > 0.1$GeV) flux averaged over three days to the upper limit on the HE pre-flare emission (see Fig. 8.9) yields a lower limit on the HE emission flare coefficient $\kappa_{\mathrm{HE}} \geq 9.2$. An upper limit on the VHE flare coefficient can be estimated using the profile likelihood method. The likelihood function is defined as the product of two Gaussian distributions of the pre-flare and flare measurements ϕ_1 and ϕ_2 correspondingly, stating that the flare measurement ϕ_2 varies around $\tilde{\kappa}\tilde{\phi_1}$, where the tilde denotes the true value for a parameter. The profile likelihood λ is then built as a function of κ:

$$\lambda(\kappa) = \frac{L(\hat{\phi}_1, \kappa | \phi_1, \phi_2)}{L(\hat{\phi}_1, \hat{\kappa} | \phi_1, \phi_2)}, \tag{8.2}$$

where the hat denotes the maximum likelihood estimate for a parameter. The variable $-2\log\lambda$ (Fig. 8.10) follows a χ^2 distribution with 1 degree of freedom, which can be used to extract limits. A $100(1-\alpha)\%$ confidence interval is limited by points where the function increases by the α percentile of a χ^2 distribution with 1 degree of freedom comparing to the function minimum, which corresponds to the maximum likelihood. To calculate the 99.7 % confidence level (equivalent of 3 σ) upper limit on κ one should calculate an increase of the function by 0.003 percentile, which is equal 8.8 (see horizontal line in Fig. 8.10). This corresponds to an upper limit on $\kappa_{99.7\%} < 3.3$. The obtained upper limit is lower than the observed lower limit on $\kappa_{\mathrm{HE}} \geq 9.2$.

The statistical tests presented above can be summarised in two main results:

- A flare of similar magnitude as observed in the HE band can be firmly rejected in the VHE band.
- There is no evidence for any significant difference between the pre-flare and

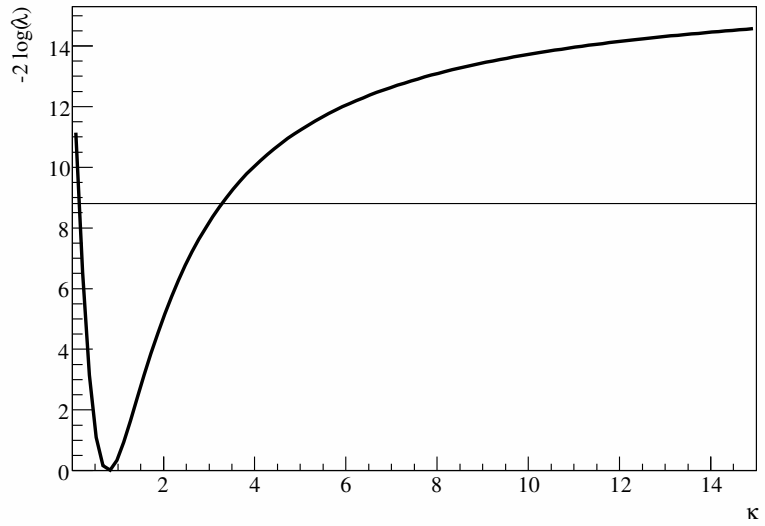

Figure 8.10: The likelihood profile as a function of κ. The horizontal line indicates the increase of the function comparing to the minimum by 0.003 percentile of χ^2 distribution with 1 degree of freedom. The function point with such increase corresponds to the 99.7 % confidence interval.

the flare flux in the VHE band.

These two results lead to the conclusion that either the HE flare emission is of the different nature than the VHE emission in the same period of time or the HE pre-flare emission is somehow concealed from the observer. Although the second possibility is disfavored by the fact that there is no such a "shield" observed at other energies it can not be completely excluded. Nevertheless, it is not understood what can be an origin of such a HE filter.

8.5 Discussion

8.5.1 The Nature of the HE Emission

The HE flare observed by Fermi LAT [Abdo et al., 2011b] is much brighter in comparison to the faint emission during the brightening period, i.e. during the periastron passage. Also, it does not coincide with the post-periastron peak at radio, X-ray or VHEs. The lack of evidence of a flare in other wavebands naturally suggests that the HE flare emission is produced by a different mechanism.

Khangulyan et al. [2012] suggested that the HE emission is produced through the inverse Compton scattering of unshocked relativistic electrons of the pulsar wind on the photons of the companion star. The observed flare can be explained by a pulsar wind with a bulk Lorentz factor $\Gamma_0 \approx 10^4$ (Fig. 8.11). To reach the level of the detected GeV flare through the formation of IC γ-rays the optical luminosity of the

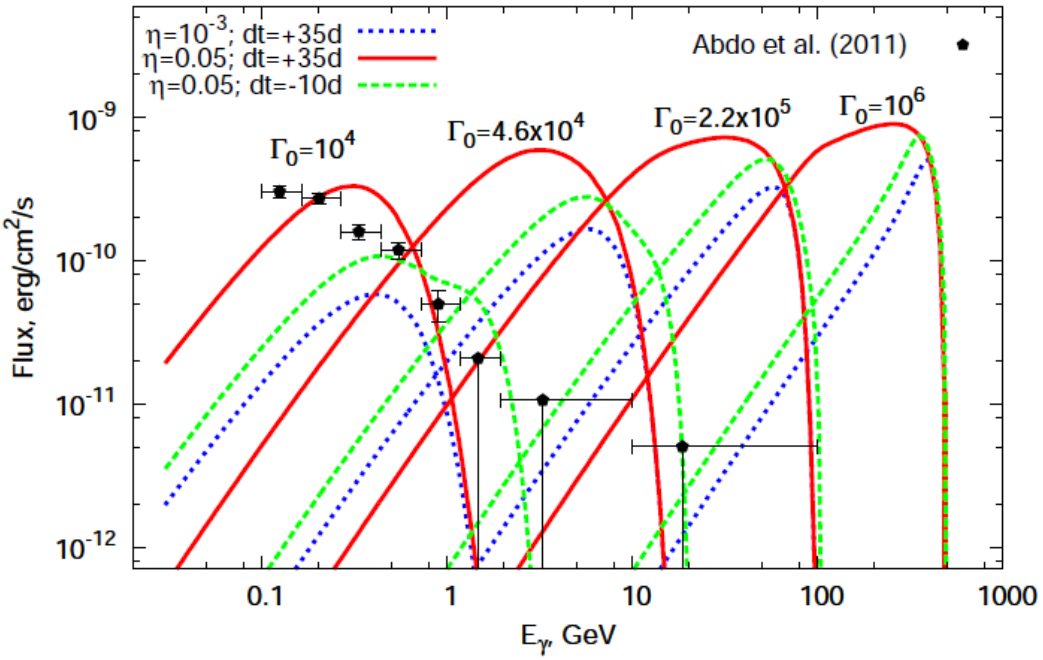

Figure 8.11: Models by Khangulyan et al. [2012] for varios values of Γ_0 and parameter η which is the ratio of the pulsar wind ram pressure to the star wind ram pressure and has an impact on the location of the termination shock for two epochs $t_\mathrm{p} + 35\mathrm{d}$ and $t_\mathrm{p} - 10\mathrm{d}$. The calculations were performed for a photon field with two contributions: the radiation of a spherical star with radius $R_* = 6.2 \times 10^{11}$ cm and surface temperature $T_* = 3 \times 10^4$ K and the stellar disk emission which was assumed to be isotropic grey body with the temperature $T_\mathrm{disk} = 10^4$ K and energy density of 2.8 erg cm^{-3}. Filled pentagons denote the observational data from the flaring period as reported by Abdo et al. [2011b]. The figure was taken from Khangulyan et al. [2012].

star is not large enough and, thus, an additional target photon field is required. This additional radiation component can be the infrared radiation of the circumstellar disk.

Khangulyan et al. [2012] argue that the effective Comptonisation of the cold relativistic wind of the pulsar occurs in the immediate vicinity of the disk where the density of IR photons is still very high but the pressure is low enough for the wind to terminate quite far from the pulsar. In this case the optical depth for the inverse Compton scattering may be as high as 1, and, therefore, a very effective (close to 100 % efficiency) transformation of the rotational energy of the pulsar into the HE γ-rays is expected. This is not possible when the pulsar passes the disk since the pulsar wind is suppressed due to the high pressure and there is not enough time to upscatter a sufficient number of optical and IR photons. The departure of the pulsar from the disk leads to the gradual decrease of the density of IR photons emitted by

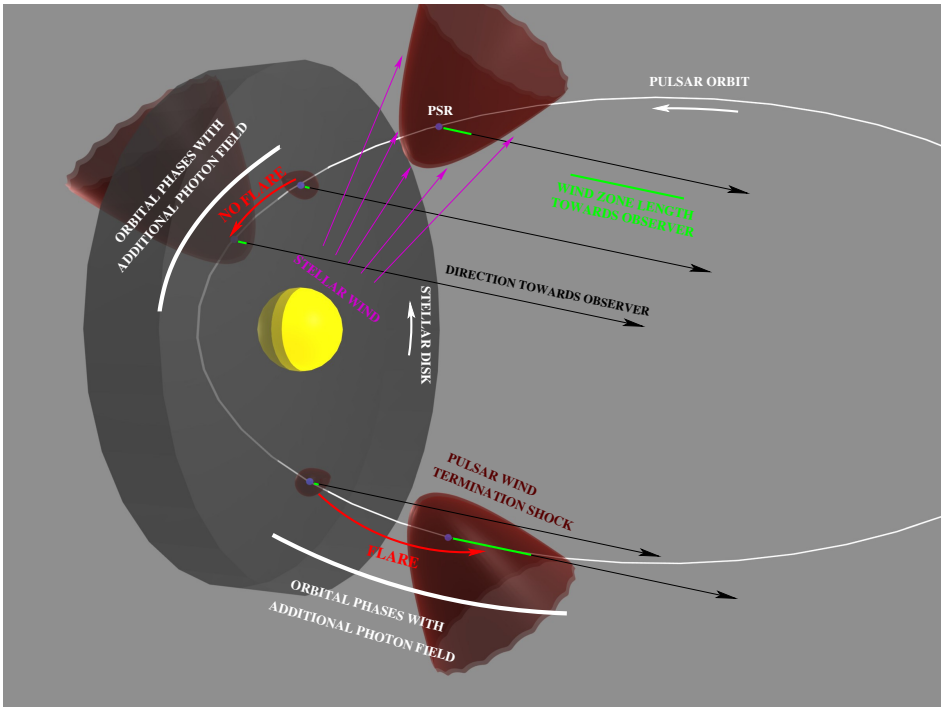

Figure 8.12: Sketch of the unshocked pulsar wind scenario. The figure was taken from Khangulyan et al. [2012].

the disk which, in turn, causes the decrease of the γ-ray flux.

The non-detection of a similar flare during the first crossing of the disk before the periastron may be the result of the strong dependence of the γ-ray flux on the orientation of the terminated shock. At the first passage of the disk the termination shock is expected to expand towards the direction opposite to the observer, while at the second exit from the disk the termination shock expands towards the observer, which leads to a significant enhancement of the wind signal in this direction (see Fig. 8.12).

The time delay between the HE flare and the appearance of the pulsed radio emission as well as peaks of the radio, X-ray and VHE unpulsed emission indicates that the HE flux enhancement starts rather far away from the disk center. This can be explained by the high pressure in the disk which causes a "closed" shape of the termination shock, and, thus, lowers the possibility of the upscattering of target photons by the pulsar wind. The transformation from "closed" shape to the "open" one occurs for the pulsar wind ram pressure to the star wind ram pressure ratio $\eta \approx 10^{-2}$, which exceeds the value which is expected in the disk by an order of magnitude.

The HE emission detected at the periastron passage can be created by the inverse Compton scattering of the shock-accelerated electrons on the stellar photons. This hypothesis explains the difference in the spectral shape of the periastron emission (generated by shocked particles) and flare emission (generated by unshocked wind). The possible detection of the emission far away from periastron with a spectral

shape similar to the periastron emission would support such a scenario, since the emission close to the periastron should have no contribution from disk IR photons.

There are few other possible explanations for the nature of the HE flare discussed in the literature. One of them suggests that the HE flare can be the Doppler boosting of the radiation created by the shocked pulsar wind [Bogovalov et al., 2008, Dubus et al., 2010]. It is unclear though why the flare is not detected at other wavebands, since the Doppler boosting should enhance also X-ray and VHE γ-ray fluxes. The flare can also be explained by an anisotropy of the pulsar wind and/or stellar material [Abdo et al., 2011b]. The anisotropy of electrons with highest energies would cause the anisotropy of the synchrotron spectrum at its high-energy end. In this interpretation, the HE emission is produced by the synchrotron mechanism. The local increase of the stellar wind density would increase the Bremsstrahlung component which may also cause the HE flare. Regardless of which mechanism is responsible for the HE flare the fact that it is observed only after the periastron indicates either the strong dependancy of the HE emission on the geometry of the system, i.e. its configuration with respect to the direction to the observer, or some local perturbation of the stellar material.

8.5.2 VHE Emission Modeling

The non-detection of a similar flare at a VHEs indicates that HE emission and VHE emission originate from different physical processes. Several models have been proposed to explain the VHE emission from the source. In a hadronic scenario, the VHE emission could be produced in the interaction of the ultrarelativistic pulsar wind particles with the dense equatorial disk outflow with subsequent production of π^0 pions and hence VHE γ-rays [Kawachi et al., 2004, Neronov and Chernyakova, 2007]. However, the detection of the source before the expected disk location in 2007 put the hadronic scenario under doubt suggesting that at least partly VHE emission should be created in the leptonic scenario [Aharonian et al., 2009a]. Within the leptonic scenario, VHE emission from PSR B1259−63/LS 2883 is explained by the inverse Compton scattering of shock-accelerated electrons on stellar photon fields [Tavani and Arons, 1997, Kirk et al., 1999, Dubus, 2006, Khangulyan et al., 2007]. Moreover, the HE flare flux can serve as an upper limit for the IC emission of shocked particles, imposing constraints on the electron population responsible for the VHE emission. A very simple model of the VHE emission within the leptonic scenario is considered in the following. Since at VHE the system was observed for a short period and the lightcurve does not show any variability on this time scale, the time dependence can be neglected, and thus, one population of electrons can be assumed. The energy distribution of the electron density is assumed to follow a power-law with an exponential cut-off

$$\frac{dN_{\rm e}}{d\gamma} = K_{\rm e}\gamma^{-p}e^{-\frac{\gamma}{\gamma_{\rm max}}}. \tag{8.3}$$

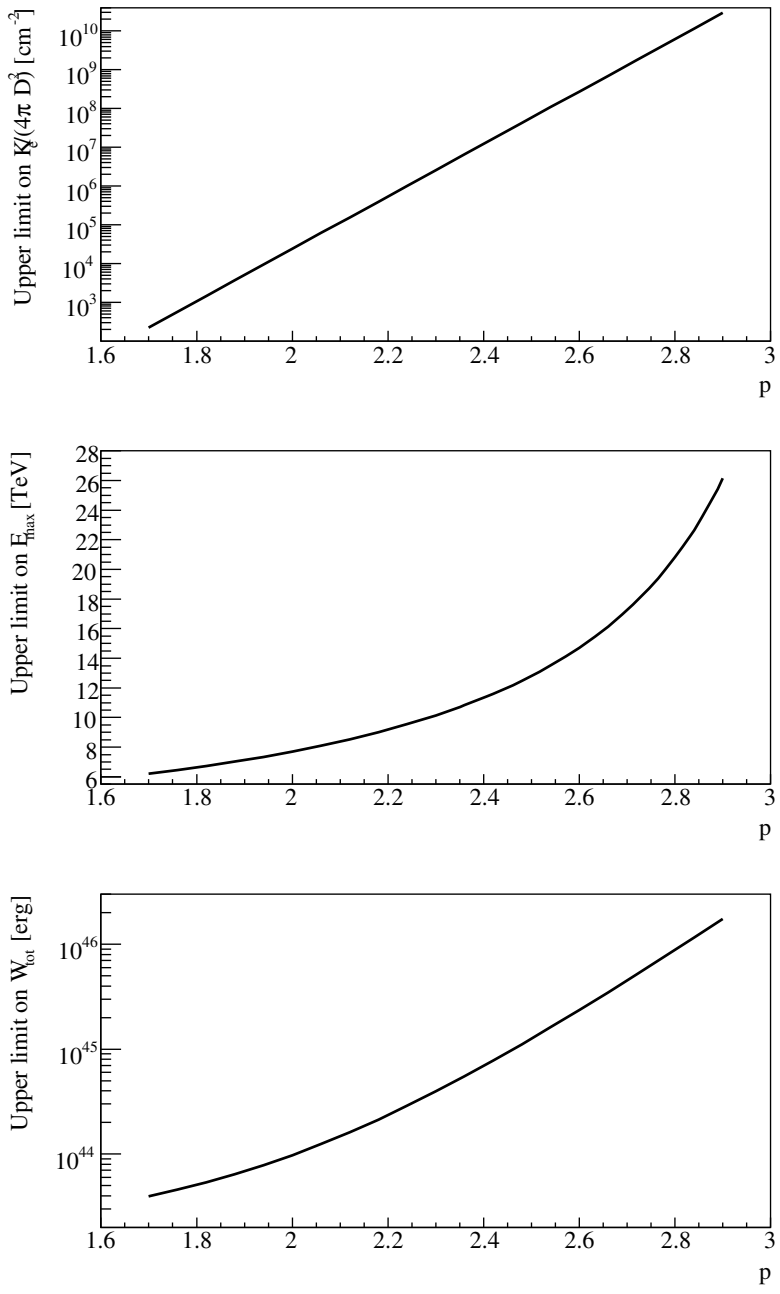

Figure 8.13: The upper limits on K_e (top), E_{max} (middle) and W_{tot} (bottom) as a function of the electron distribution spectral index p. See the explanation for the derivation of the upper limit in the text.

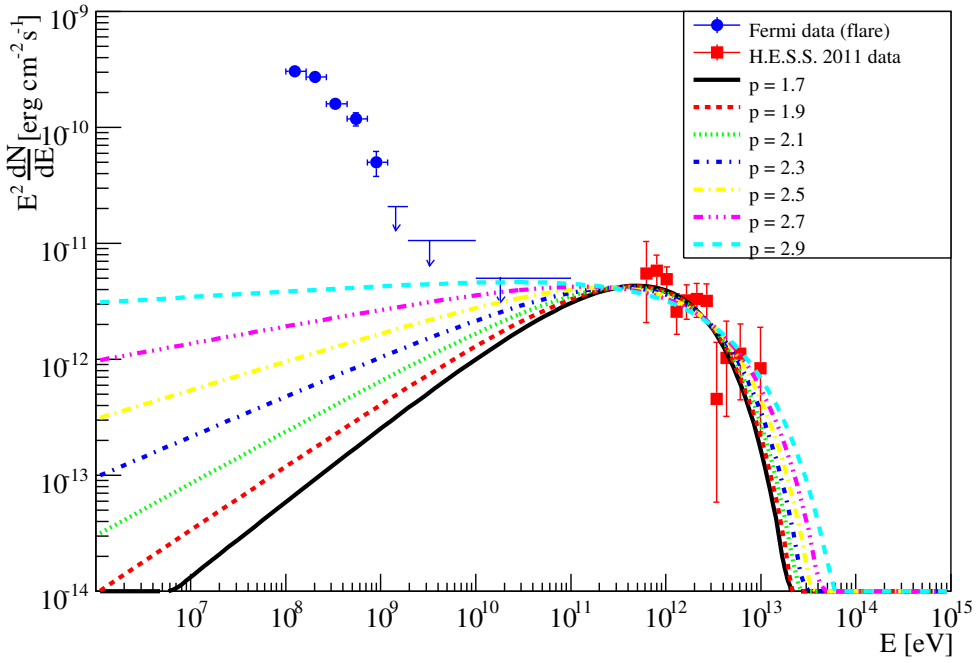

Figure 8.14: Inverse Compton emission models for different spectral indices of the electron energy distribution. H.E.S.S. data are shown with red squares and Fermi LAT data are shown with blue circles.

It is further assumed that this distribution of electrons already accounts for all kinds of energy losses and that these losses are not important on the considered time scale. The absorption due to the pair production of the individual γ-rays is not taken into account in the calculation of the resulting γ-ray flux. The electrons are assumed to be distributed isotropically at the "closed" spherical termination shock. The stellar radiation at the location of the pulsar wind termination shock plays the role of target photons, assuming that the distance from the pulsar to the shock is much smaller than the distance from the star to the shock. The target photon field has then a Planckian distribution with a temperature $T_* = 30000K$ and an energy density of 1 erg cm^{-1}. Although the model is rather simple and does not account for a number of different processes which take place in the system in the vicinity of the emission region, it can still give an understanding of the population of electrons required to produce the observed VHE γ-ray flux.

The model has three free parameters: the electron spectral index p, the normalisation

parameter K_e, which physically corresponds to the number of electrons with $\gamma = 1$, and the electron cut-off energy $E_{max} = mc^2\gamma_{max}$. The Fermi upper limit extends to 100 GeV, so to constrain the IC flux the upper limit value at 100 GeV is used. If one assumes then that $E_{UL} = 100$ GeV is far from the cut-off energy, the IC emission at this energy would depend only on two parameters, K_e and p. Therefore, it is possible to obtain an upper limit on K_e as a function of p (Fig. 8.13 (top)). Then, for each pair of p and K_e one can estimate E_{max} by fitting the IC emission to the H.E.S.S. data (Fig. 8.14). In Table 8.3, upper limits on K_e and corresponding E_{max} obtained from the fit of the H.E.S.S. data are shown for different values of the spectral index. The fit probability is also presented and it is $\gtrsim 0.5$ for all studied spectral indices. Based on the obtained parameters of the electron distribution an upper limit on the total energy in electrons W_{tot} which is needed to produce the VHE emission not exceeding the HE emission upper limit can be calculated. It is calculated assuming the minimum energy of the electron $E_{e,min} = 1$ GeV. Depending on the assumed spectral index it varies from 4.0×10^{43} erg for $p = 1.7$ to 1.7×10^{46} erg for $p = 2.9$. The dependencies of E_{max} and W_{tot} on the assumed p are shown graphically in Fig. 8.13 (middle, bottom).

Table 8.3: Fit parameters for fixed values of the spectral index p

p	$K_e/(4\pi D^2)$, cm^{-2}	E_{max}, TeV	Fit probability	W_{tot}, erg
1.7	2.2×10^2	6.2	0.72	4.0×10^{43}
1.9	5.0×10^3	7.1	0.70	6.9×10^{43}
2.1	1.1×10^5	8.4	0.68	1.5×10^{44}
2.3	2.6×10^6	10.1	0.65	4.0×10^{44}
2.5	5.8×10^7	12.8	0.61	1.3×10^{45}
2.7	1.3×10^9	17.3	0.56	4.5×10^{45}
2.9	2.9×10^{10}	26.1	0.50	1.7×10^{46}

Assuming that the spin-down luminosity of the pulsar is transferred to the electron acceleration with the 100% efficiency a lower limit on time required to accumulate W_{tot} can be derived. The lower limit on time ranges between 1.5 y for $p = 1.7$ to 674 y for $p = 2.9$. For the range of spectral indices from 1.7 to 1.9 the lower limit on time is less than 3.4 y, i.e. the orbital period of the pulsar. This would mean that electrons accelerated at the shock during one orbital period lose all their energy producing IC emission close to periastron and this process repeats every 3.4 y.

8.5.3 Outlook

Future Fermi LAT and H.E.S.S. observations around 2014 periastron passage are required in order to obtain a bigger time overlap of the HE/VHE observations for better understanding of the emission mechanisms. The next periastron passage will be also the first one with H.E.S.S. II in operation. With a higher than Fermi LAT sensitivity at energies $\gtrsim 50$ GeV H.E.S.S. II would fill the gap in the spectrum be-

tween Fermi LAT and H.E.S.S. I. This may lead to several very important results, like detection of the HE emission cut-off and/or IC peak of the VHE emission, which would help to resolve the nature of the HE/VHE emission. Observations far away from periastron would also be very interesting and important for understanding the physical processes in PSR B1259−63/LS 2883. The emission produced far away from periastron does not depend on stellar disk photons and, therefore, the possible detection or improved upper limits would lead to the better understanding of the stellar–pulsar winds interaction.

9 Summary

The SNRs G 1.9+0.3 and G 330.2+1.0 belong to the class of synchrotron-dominated SNRs whose non-thermal X-ray emission implies that intensive particle acceleration occurs at their shock fronts. It makes them particularly interesting for γ-ray astronomy since high-energy particles can produce VHE γ-rays. H.E.S.S. observations of these remnants do not show any signs of significant TeV γ-ray emission from either SNR. The non-detection of G 1.9+0.3 and G 330.2+1.0 in the TeV γ-ray domain is probably due to very large distances to these remnants comparing to synchrotron-dominated SNRs already detected at VHEs. The 99% confidence level upper limits on the TeV flux were determined. For the assumed spectral index 2.5 the obtained upper limits are $F_{\mathrm{G1.9}}(> 260\,\mathrm{GeV}) < 4.6 \times 10^{-13}\ \mathrm{cm}^{-2}\mathrm{s}^{-1}$ for G1.9+0.3 and $F_{\mathrm{G330}}(> 380\,\mathrm{GeV}) < 1.6 \times 10^{-12}\ \mathrm{cm}^{-2}\mathrm{s}^{-1}$ for G330.2+1.0. ULs on the TeV γ-ray flux provide an opportunity to set constraints on the interior magnetic field in the context of a leptonic scenario and on the ISM density and CR efficiency in a hadronic scenario. Lower limits on the interior magnetic fields were estimated at 15 μG for G 1.9+0.3 and 14 μG for G 330.2+1.0. In the case of the hadronic scenario, the H.E.S.S. upper limits are two orders of magnitude greater than the flux prediction. Obtained upper limits on the ISM densities are compatible with other estimates of the densities (from the thermal X-ray emission for G 330.2+1.0 and from the expansion rate for G 1.9+0.3). The CR efficiency cannot be constrained with the current H.E.S.S. upper limits. G 330.2+1.0 and G 1.9+0.3 remain promising targets for γ-ray observations at TeV energies, in particular with the future generation of instruments like the Cherenkov Teleskope Array (CTA).

Evolved PWNe are characterised by a considerably bigger TeV emission region comparing to the X-ray emission region. Additionally, the X-ray emission can be so weak that it may be below the sensitivity of current X-ray instruments. Therefore, it is believed that many TeV "dark sources" may be very old PWNe. One example of an initially "dark source" which was later identified as evolved PWNe is HESS J1303−631. It features an energy-dependent morphology with the "shrinking" towards the pulsar PSR J1301−6305 position emission region with the increase of the threshold energy. The association with the pulsar is also supported by the detection of the X-ray PWN and a hint of the counterpart at radio waveband. The broadband emission of the source was modeled within a one-zone 1D stationary model yielding a magnetic field of 1.4 ± 0.2 μG and a total energy in electrons above 1 GeV of 2×10^{48} erg. The estimate of the magnetic field is consistent with an averaged line-of-sight magnetic field of $\sim$ 2 μG provided by the measurement of the pulsar's rotation measure. A low magnetic field is also expected for evolved PWNe for which the magnetic field is believed to decrease with time. The obtained total

energy in electrons yields the estimate for the pulsar birth period between 51 and 75 ms, which is in good agreement with estimations of birth periods for pulsar associated with composite SNRs. The possible extension of the model by inclusion of the spatial distribution is suggested. The idea is based on the assumption that the source extension is due to the proper motion of the pulsar from its possible birth place in the star formation region IRAS 13010−6254. It is suggested that the division of the source into fractions of concentric rings centered on the pulsar and subsequent data analysis for each region would provide a very important information about the evolution of the PWN and particularly about the electron cooling timescales. The modeling would also benefit from the careful analysis of the Fermi data and future observations with H.E.S.S. II. The detection of the source at HEs would allow to independently estimate the electron spectral index.

The binary system PSR B1259−63/LS 2883 is the only TeV binary for which the compact companion is unambiguously identified as a pulsar, making it a unique object for the study of the interaction between pulsar and stellar winds and the emission mechanisms in binary systems. PSR B1259−63/LS 2883 was monitored by H.E.S.S. around the periastron passage on 15th of December 2010. Due to the unsatisfactory weather conditions the performed observations resulted in a rather small dataset with a livetime of about 6 h. Nevertheless, this was enough to obtain a firm detection of the source. The observed flux and spectral shape are in good agreement with what was measured during previous periastron passages. The observations were performed at similar orbital phases as around the 2004 periastron, for the first time directly confirming the repetitive behavior of the source at VHEs. H.E.S.S. observations were part of a joint MWL campaign including also radio, optical, X-ray and HE observations. A spectacular flare observed at HEs with Fermi LAT overlapped in time with the H.E.S.S. observations. A careful statistical study showed that the HE flare does not have a counterpart at VHEs indicating that the HE and VHE emissions are produced by different physical processes. Due to the different nature of the HE and VHE emission the HE flux can be considered as an upper limit for the IC emission (generated by shock-accelerated electrons), which is believed to be responsible for the VHE emission from the source. According to this, the modeling of the IC emission was done yielding upper limits on electron spectral parameters and the total energy in electrons depending on the assumed electron spectral index. It was shown that for indices in the range from 1.7 to 1.9 the time needed to accumulate the required total energy in electrons is less than the orbital period of the pulsar. This means that electrons accelerated at the shock during one orbital period lose all their energy producing IC emission close to periastron and this process repeats every orbital cycle.

Appendix A: Description of the SED Modeling Software

The presented numerical code is dedicated to the calculation of a broadband emission created by the population of relativistic electrons via synchrotron and inverse Compton scattering on target photons. It can be used for the modeling of the MWL emission from such sources as Supernova remnants and pulsar wind nebulae. Based on the radio and X-ray observation data from the source the code produces the calculation of the synchrotron emission which fit the data the best. Then, basing on the synchrotron fit and the assumption of the magnetic field, the emission created through the IC scattering of electrons on ambient photon fields is calculated.

Physical assumptions used in the code:

- synchrotron and IC emission are created by the same electron population (one-zone model);
- electrons are distributed over energies in a form of a power-law with the exponential cut-off
$$\frac{dN}{d\gamma} = K_{\rm e}\gamma^{-p}e^{-\gamma/\gamma_{\rm cutoff}}; \tag{A.1}$$
- electron velocities directions are uniformly distributed;
- the spatial distribution is not taken into account (1D model);
- the steady state is considered.

On a first step, the input radio and X-ray data of the source are converted into the SED format, i.e. with units [eV cm^{-2}s^{-1}], and are fit with the synchrotron emission function[1]

$$f_{\rm syn}(\phi_0, \alpha_{\rm s}, \epsilon_{\rm roll}) = \phi_0 \left(\frac{E}{1\,{\rm eV}}\right)^{-\alpha_{\rm s}+1} \int_0^\infty F(x) x^{\alpha_{\rm s}-1} e^{-\left(\frac{E}{\epsilon_{\rm roll}}\frac{1}{x}\right)^{1/2}} dx \tag{A.2}$$

with three free parameters: the synchrotron spectral index $\alpha_{\rm s}$ which is connected to the electron spectral index p as

$$\alpha_{\rm s} = \frac{p-1}{2}, \tag{A.3}$$

[1] See Chapter 5 for the description of emission mechanisms.

the synchrotron normalisation ϕ_0 which is a function of K_e and B

$$\phi_0 = \frac{K_e}{4\pi D^2} \left(\frac{h}{2\pi}\right)^{\alpha_s - 1} \frac{\sqrt{3}}{6\pi} \frac{q^2}{c} \left(\frac{3qB\sqrt{2/3}}{2mc}\right)^{\alpha_s + 1} \tag{A.4}$$

and the roll-off energy ϵ_{roll} which is a function of γ_{cut} and B

$$\epsilon_{roll} = \frac{h}{2\pi} \frac{3qB\sqrt{2/3}}{2mc} \gamma_{cut}^2. \tag{A.5}$$

Published X-ray data are usually given in the form of a spectral fit, e.g. power-law spectrum, without separate spectral points. This form is inconvenient for the fit procedure. Thus, in order to be able to fit the data, the X-ray spectrum is divided in a set of points which follow the spectrum within errors on the spectral parameters. The choice of the number of such points is, however, quite arbitrary and one should take care not to become too much biased towards the X-ray data. Nevertheless, this should not be a big issue since α_s and ϕ_0 are constrained mainly by the radio data and ϵ_{roll} mainly by the X-ray data. Therefore, the increase of X-ray points simply provides a better estimate of the synchrotron cut-off not affecting the estimates of α_s and ϕ_0.

The obtained fit parameters are then used to calculate the electron spectral parameters as functions of B. Then for the assumed B one can calculate the IC spectrum using Eq. 6.3 for the pre-defined distribution of target photons, i.e. CMB, IR and optical photon fields.

A.1 Usage of the Software

The software consists of two scripts *fit_synchrotron.C* and *ic_modeling.C*.

The first one provides a fit of the radio and X-ray data with the synchrotron emission model. The radio and X-ray data are input using an ASCII file. In Fig. A.1 an example of the input file for G 330.2+1.0 is shown. Radio data are input in the form of flux density points in [Jy] at a frequencies provided in [Hz]. The X-ray data are input in the form of the power-law fit with an energy range in [keV], an integral flux in [erg $cm^{-2}s^{-1}$] and a spectral index. The script *fit_synchrotron.C* converts the input data into the form appropriate for the fit procedure and fits them with the synchrotron model. As discussed above, the input X-ray data are converted into a set of points. The number of X-ray points is controlled by a variable *Xray_points_num* in the script and can be changed if necessary. The default value is 10.

The script *fit_synchrotron.C* returns two output files *synchrotron_fit_parameters.dat* and *synchrotron_fit.root* which can be used afterwards for the modeling of the IC emission with the *ic_modeling.C* script. The first one contains values of the fit parameters and the second one contains the radio data, the X-ray data and the synchrotron fit curve in the form of TObjects.

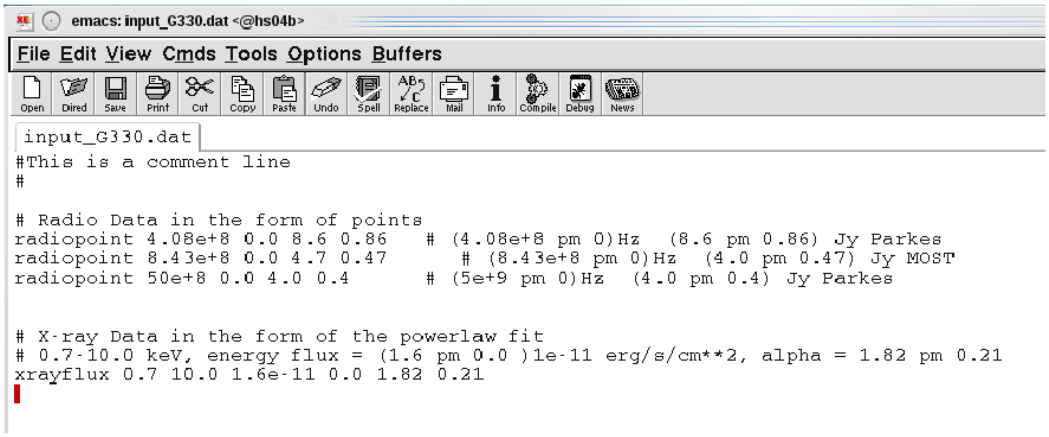

Figure A.1: Example of the data input file for the *fit_synchrotron.C* script. This file was used for the modeling of the synchrotron emission from G 330.2+1.0.

The script *ic_modeling.C* provides the calculation of the IC spectum and plots the overall SED. Besides two output files from the *fit_synchrotron.C* it needs a configuration file *ic_config.dat* as an input. The example of the configuration file used for the modeling of the G 330.2+1.0 emission is shown in Fig. A.2. The configuration file provides the information on the optical and IR photon fields and on the assumed magnetic field values. The user has to choose "YES" or "NO" for the inclusion of the optical and/or IR photon fields in the modeling of the IC emission. CMB photons are included by default. If the user chooses "YES" the corresponding parameters, i.e. the energy density and the temperature should be provided. The script is written in a way that several values of the magnetic field can be tested. In the configuration file the user should indicate the number of tested B values and provide values in [G].

Optionally the H.E.S.S. data can be input (if exists). For this the file *hess_data.root* containing TGraphAsymmErrors object with the name "hess_data" has to be created and placed into the same folder where the script is located. The H.E.S.S. data should be in units of [eV cm^{-2}s^{-1}] for energies with units of [eV]. The script will look for the file and if it exists will read the data. Then the H.E.S.S. data will be overlaid on the overall SED plot.

The modeling results are saved into two files. The parameters of the electron spectrum for each assumed value of B are saved into the file *modeling_results.dat*. All data and model curves are saved into the *ic_modeling.root* as TObjects.

The software is put on the CVS and is available for usage. The package name is *BroadbandModeling*.

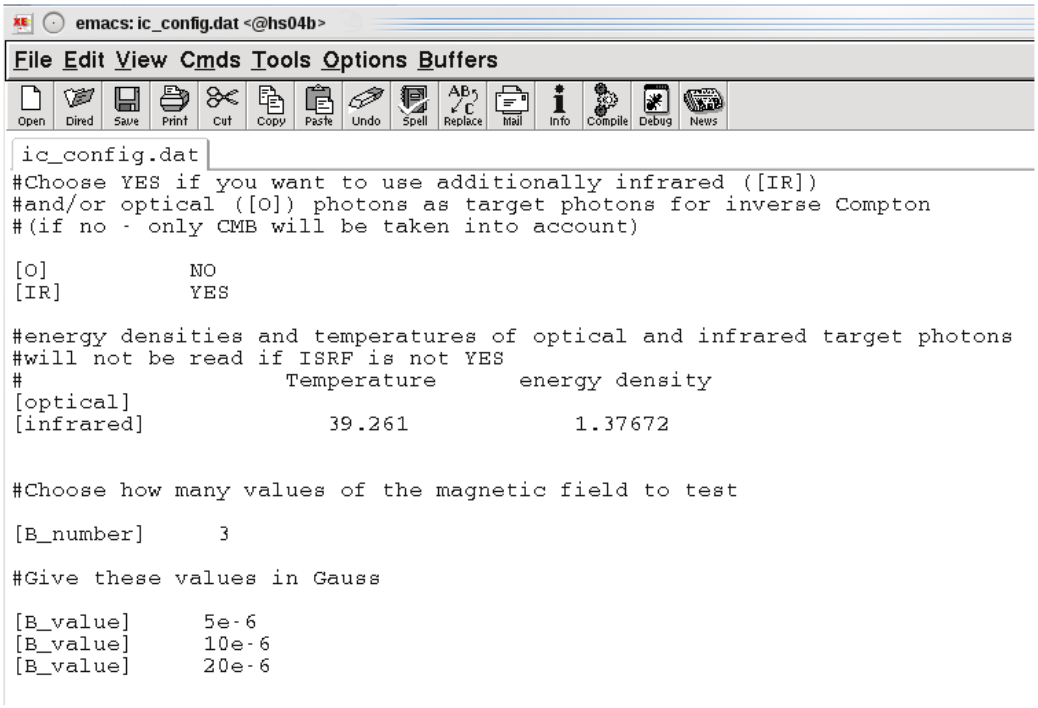

Figure A.2: Example of the configuration file for the *ic_modeling.C* script. This file is used for the modeling of the IC emission from G 330.2+1.0.

Appendix B: Comparison of Analysis Results of Two Different Groups for the Fermi Observations of PSR B1259−63/LS 2883

Tam et al. [2011] divided the whole observation period into four subperiods[2]:

- a period of the primary detection which lasted from about a month before the periastron passage to the periastron passage on December 15 (P1) (see Fig. B.1);
- a period of non-detection from mid-December to mid-January (Q1);
- a first flare, which lasted for 7 days since January 14, with a peak at 35 days after periastron (P2) (see Fig. B.2);
- a second flare that peaks at 46 days after periastron and lasted until the end of February (P3 and P4) (see Fig. B.2).

All spectral properties and integrated photon fluxes for these periods can be found in Table B.1 together with properties for the brightening and flare periods denoted in Abdo et al. [2011b]. Similar to Abdo et al. [2011b], Tam et al. [2011] observed the indication of the spectral index - flux correlation. The HE emission was studied at two timescales: 3-day bins for the whole period (in Fig. B.1 photon fluxes during P1 and Q periods are shown) and 1-day bins for flaring periods P2 and P3 (Fig. B.2).

The lightcurves by Abdo et al. [2011b] and Tam et al. [2011] during the flare period are in very good agreement (Fig. B.2). The overall photon fluxes as well as spectral shapes are also compatible for both analyses, i.e. for the flare period in Abdo et al. [2011b] and P2-P4 periods in Tam et al. [2011]. The only difference of the two analyses of the flaring period is that Abdo et al. [2011b] consider it as a one, but variable flare and Tam et al. [2011] discriminate two flares, a short one-week long P3 flare and long P3-P4 flare which lasted for about four weeks. Nevertheless, this is more a question of the interpretation than the analysis.

The difference for the first detection period is more important. It can be seen from the lightcurve (Fig. B.1) that in the case of Abdo et al. [2011b] the source is almost undetected before the periastron, but it is detected right after the periastron.

[2]The denotation of periods in Tam et al. [2011] are shown in brackets.

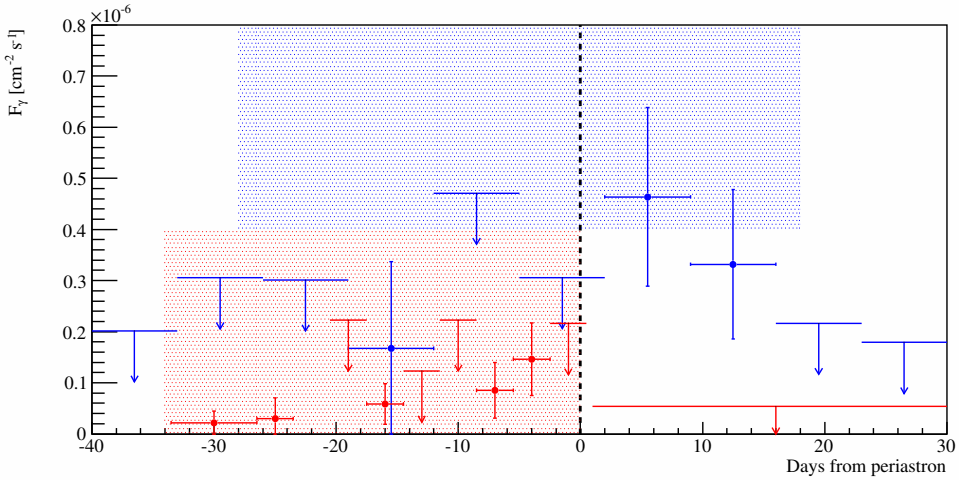

Figure B.1: HE photon flux obtained with Fermi as a function of time around the 2010 periastron passage. With blue points the weekly flux above 0.1 GeV is shown as it is reported in Abdo et al. [2011b], 2σ upper limits are drawn for points with TS<5. With red points the $0.2 - 1$ GeV flux is shown as it is reported in Tam et al. [2011], for points with TS<5 2σ upper limits are shown assuming a spectral index of 2.1. Three-day bins are used for all points except the first point (seven-day bin) and the non-detection period after the periastron (30-day bin). The time interval marked in blue shows the brightening period denoted in Abdo et al. [2011b] and the time interval marked in red shows the P1 period denoted in Tam et al. [2011]. The dashed line shows the position of the periastron.

Conversely, Tam et al. [2011] show the detection of the source before the periastron, but no detection in the period from the periastron and up to the flare period.

Another important difference is the shape of the spectrum for the first detection period for Abdo et al. [2011b] and Tam et al. [2011]. In Fig. B.3, spectral energy distributions (SEDs) are shown for the brightening period in Abdo et al. [2011b] and the P1 period in Tam et al. [2011]. The discrepancy which can be seen for data points obtained by the different groups can be a result of the slightly different selection of the time periods, supported by the fact that the maximum of the flux in Abdo et al. [2011b] is obtained after the periastron passage, it means after the P1 period.

Discrepancies discussed above are not resolved yet and can indicate the misinterpretation of such low fluxes by one of the groups or even both of them.

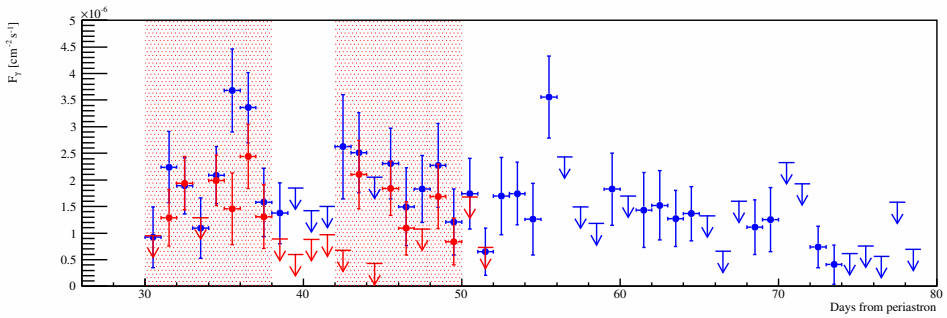

Figure B.2: Fermi HE photon flux as a function of time on a daily timescale during the flare period. With blue points the flux above 0.1 GeV is shown as it is reported in Abdo et al. [2011b], 2σ upper limits are drawn for points with TS<5. With red points a the $0.1 - 1$ GeV flux is shown as it is reported in Tam et al. [2011], for points with TS<5 2σ upper limits are shown assuming spectral index of 2.8. Time intervals marked in red show the P2 and P3 periods as denoted in Tam et al. [2011].

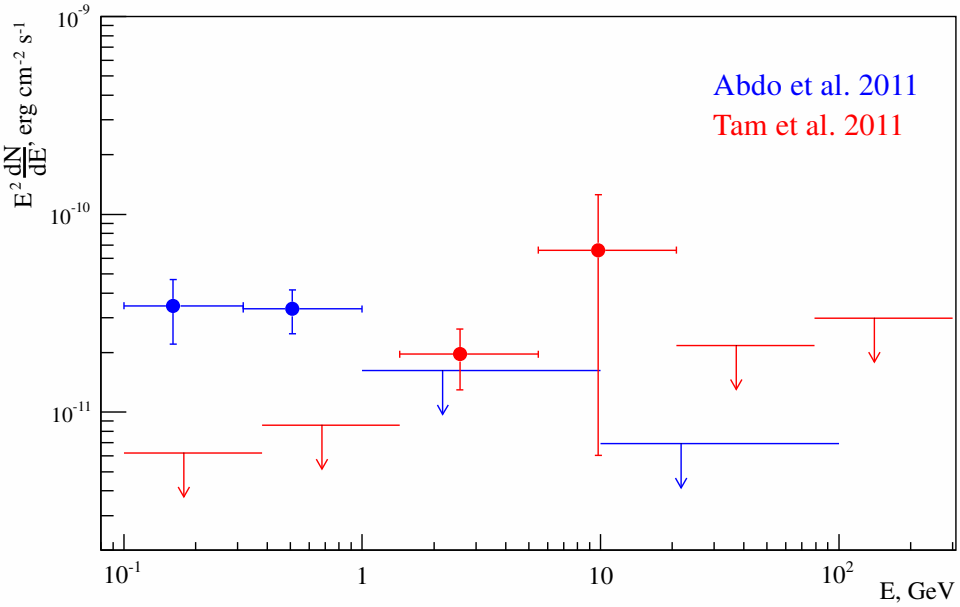

Figure B.3: Spectral energy distribution of the HE emission from PSR B1259−63/LS 2883 detected by Fermi LAT in the following periods: the period from -28 to +18 days with respect to periastron as reported by Abdo et al. [2011b] (blue) and the period from -35 to 0 days with respect to periastron as reported by Tam et al. [2011] (red).

Table B.1: A compilation 0.1-1 GeV γ-ray properties for different periods through the 2010/2011 periastron passage as they were reported by Tam et al. [2011] and Abdo et al. [2011b].

Paper	Period	Year	Date	Model	Photon Flux, $[cm^{-2}s^{-1}]$	Photon Index	Cutoff Energy, [MeV]
Tam et al. [2011]	P1	2010	Nov 11 - Dec 14	PL	$(9.9 \pm 4.1) \times 10^{-8}$	2.1 ± 0.2	
	P2	2011	Jan 14 - Jan 22	PL	$(1.5 \pm 0.2) \times 10^{-6}$	3.0 ± 0.1	
				PLE	$(1.3 \pm 0.2) \times 10^{-6}$	1.8 ± 0.6	310 ± 160
	P3	2011	Jan 26 - Feb 3	PL	$(1.4 \pm 0.2) \times 10^{-6}$	2.8 ± 0.1	
				PLE	$(1.3 \pm 0.2) \times 10^{-6}$	2.0 ± 0.5	550 ± 330
	P4	2011	Feb 4 - Feb 21	PL	$(8.7 \pm 1.1) \times 10^{-7}$	2.8 ± 0.1	
				PLE	$(7.5 \pm 1.1) \times 10^{-7}$	1.1 ± 0.6	250 ± 95
Abdo et al. [2011b]	brightening	2010/2011	Nov 17 - Jan 2	PL	$(2.5 \pm 0.8_{stat} \pm 0.8_{sys}) \times 10^{-7}$	$2.4 \pm 0.2_{stat} \pm 0.5_{sys}$	
	flare	2011	Jan 14 - Mar 4	PLE	$(1.3 \pm 0.1_{stat} \pm 0.3_{sys}) \times 10^{-6}$	$1.4 \pm 0.6_{stat} \pm 0.2_{sys}$	$300 \pm 100_{stat} \pm 100_{sys}$

Bibliography

A. A. Abdo, M. Ackermann, M. Ajello, A. Allafort, E. Antolini, W. B. Atwood, M. Axelsson, L. Baldini, J. Ballet, G. Barbiellini, and et al. Fermi Large Area Telescope First Source Catalog. *ApJS*, 188:405–436, June 2010. doi: 10.1088/0067-0049/188/2/405.

A. A. Abdo, M. Ackermann, M. Ajello, A. Allafort, L. Baldini, J. Ballet, G. Barbiellini, M. G. Baring, D. Bastieri, R. Bellazzini, B. Berenji, R. D. Blandford, E. D. Bloom, E. Bonamente, A. W. Borgland, A. Bouvier, T. J. Brandt, J. Bregeon, M. Brigida, P. Bruel, R. Buehler, S. Buson, G. A. Caliandro, R. A. Cameron, P. A. Caraveo, J. M. Casandjian, C. Cecchi, S. Chaty, A. Chekhtman, C. C. Cheung, J. Chiang, A. N. Cillis, S. Ciprini, R. Claus, J. Cohen-Tanugi, J. Conrad, S. Corbel, S. Cutini, A. de Angelis, F. de Palma, C. D. Dermer, S. W. Digel, E. d. C. e. Silva, P. S. Drell, A. Drlica-Wagner, R. Dubois, D. Dumora, C. Favuzzi, E. C. Ferrara, P. Fortin, M. Frailis, Y. Fukazawa, Y. Fukui, S. Funk, P. Fusco, F. Gargano, D. Gasparrini, N. Gehrels, S. Germani, N. Giglietto, F. Giordano, M. Giroletti, T. Glanzman, G. Godfrey, I. A. Grenier, M.-H. Grondin, S. Guiriec, D. Hadasch, Y. Hanabata, A. K. Harding, M. Hayashida, K. Hayashi, E. Hays, D. Horan, M. S. Jackson, G. Jóhannesson, A. S. Johnson, T. Kamae, H. Katagiri, J. Kataoka, M. Kerr, J. Knödlseder, M. Kuss, J. Lande, L. Latronico, S.-H. Lee, M. Lemoine-Goumard, F. Longo, F. Loparco, M. N. Lovellette, P. Lubrano, G. M. Madejski, A. Makeev, M. N. Mazziotta, J. E. McEnery, P. F. Michelson, R. P. Mignani, W. Mitthumsiri, T. Mizuno, A. A. Moiseev, C. Monte, M. E. Monzani, A. Morselli, I. V. Moskalenko, S. Murgia, M. Naumann-Godo, P. L. Nolan, J. P. Norris, E. Nuss, T. Ohsugi, A. Okumura, E. Orlando, J. F. Ormes, D. Paneque, D. Parent, V. Pelassa, M. Pesce-Rollins, M. Pierbattista, F. Piron, M. Pohl, T. A. Porter, S. Rainò, R. Rando, M. Razzano, O. Reimer, T. Reposeur, S. Ritz, R. W. Romani, M. Roth, H. F.-W. Sadrozinski, P. M. Saz Parkinson, C. Sgrò, D. A. Smith, P. D. Smith, G. Spandre, P. Spinelli, M. S. Strickman, H. Tajima, H. Takahashi, T. Takahashi, T. Tanaka, J. G. Thayer, J. B. Thayer, D. J. Thompson, L. Tibaldo, O. Tibolla, D. F. Torres, G. Tosti, A. Tramacere, E. Troja, Y. Uchiyama, J. Vandenbroucke, V. Vasileiou, G. Vianello, N. Vilchez, V. Vitale, A. P. Waite, P. Wang, B. L. Winer, K. S. Wood, H. Yamamoto, R. Yamazaki, Z. Yang, and M. Ziegler. Observations of the Young Supernova Remnant RX J1713.7-3946 with the Fermi Large Area Telescope. *ApJ*, 734:28, June 2011a. doi: 10.1088/0004-637X/734/1/28.

A. A. Abdo, M. Ackermann, M. Ajello, A. Allafort, J. Ballet, G. Barbiellini, D. Bastieri,

K. Bechtol, R. Bellazzini, B. Berenji, R. D. Blandford, E. Bonamente, A. W. Borgland, J. Bregeon, M. Brigida, P. Bruel, R. Buehler, S. Buson, G. A. Caliandro, R. A. Cameron, F. Camilo, P. A. Caraveo, C. Cecchi, E. Charles, S. Chaty, A. Chekhtman, M. Chernyakova, C. C. Cheung, J. Chiang, S. Ciprini, R. Claus, J. Cohen-Tanugi, L. R. Cominsky, S. Corbel, S. Cutini, F. D'Ammando, A. de Angelis, P. R. den Hartog, F. de Palma, C. D. Dermer, S. W. Digel, E. d. C. e. Silva, M. Dormody, P. S. Drell, A. Drlica-Wagner, R. Dubois, G. Dubus, D. Dumora, T. Enoto, C. M. Espinoza, C. Favuzzi, S. J. Fegan, E. C. Ferrara, W. B. Focke, P. Fortin, Y. Fukazawa, S. Funk, P. Fusco, F. Gargano, D. Gasparrini, N. Gehrels, S. Germani, N. Giglietto, P. Giommi, F. Giordano, M. Giroletti, T. Glanzman, G. Godfrey, I. A. Grenier, M.-H. Grondin, J. E. Grove, E. Grundstrom, S. Guiriec, C. Gwon, D. Hadasch, A. K. Harding, M. Hayashida, E. Hays, G. Jóhannesson, A. S. Johnson, T. J. Johnson, S. Johnston, T. Kamae, H. Katagiri, J. Kataoka, M. Keith, M. Kerr, J. Knödlseder, M. Kramer, M. Kuss, J. Lande, S.-H. Lee, M. Lemoine-Goumard, F. Longo, F. Loparco, M. N. Lovellette, P. Lubrano, R. N. Manchester, M. Marelli, M. N. Mazziotta, P. F. Michelson, W. Mitthumsiri, T. Mizuno, A. A. Moiseev, C. Monte, M. E. Monzani, A. Morselli, I. V. Moskalenko, S. Murgia, T. Nakamori, M. Naumann-Godo, A. Neronov, P. L. Nolan, J. P. Norris, A. Noutsos, E. Nuss, T. Ohsugi, A. Okumura, N. Omodei, E. Orlando, D. Paneque, D. Parent, M. Pesce-Rollins, M. Pierbattista, F. Piron, T. A. Porter, A. Possenti, S. Rainò, R. Rando, P. S. Ray, M. Razzano, S. Razzaque, A. Reimer, O. Reimer, T. Reposeur, S. Ritz, H. F.-W. Sadrozinski, J. D. Scargle, C. Sgrò, R. Shannon, E. J. Siskind, P. D. Smith, G. Spandre, P. Spinelli, M. S. Strickman, D. J. Suson, H. Takahashi, T. Tanaka, J. G. Thayer, J. B. Thayer, D. J. Thompson, S. E. Thorsett, L. Tibaldo, O. Tibolla, D. F. Torres, G. Tosti, E. Troja, Y. Uchiyama, T. L. Usher, J. Vandenbroucke, V. Vasileiou, G. Vianello, V. Vitale, A. P. Waite, P. Wang, B. L. Winer, M. T. Wolff, D. L. Wood, K. S. Wood, Z. Yang, M. Ziegler, and S. Zimmer. Discovery of High-energy Gamma-ray Emission from the Binary System PSR B1259-63/LS 2883 around Periastron with Fermi. *ApJL*, 736:L11, July 2011b. doi: 10.1088/2041-8205/736/1/L11.

M. Abramowitz and I.A. Stegun. *Handbook of Mathematical Functions with Formulas, Graphs, and Mathematical Tables*. U.S. Department of Commerce, 1972. ISBN 978-1-59124-217-8.

F. Acero, F. Aharonian, A. G. Akhperjanian, G. Anton, U. Barres de Almeida, A. R. Bazer-Bachi, Y. Becherini, B. Behera, M. Beilicke, K. Bernlöhr, A. Bochow, C. Boisson, J. Bolmont, V. Borrel, J. Brucker, F. Brun, P. Brun, R. Bühler, T. Bulik, I. Büsching, T. Boutelier, P. M. Chadwick, A. Charbonnier, R. C. G. Chaves, A. Cheesebrough, J. Conrad, L.-M. Chounet, A. C. Clapson, G. Coignet, M. Dalton, M. K. Daniel, I. D. Davids, B. Degrange, C. Deil, H. J. Dickinson, A. Djannati-Ataï, W. Domainko, L. O'C. Drury, F. Dubois, G. Dubus, J. Dyks, M. Dyrda, K. Egberts, P. Eger, P. Espigat, L. Fallon, C. Farnier, S. Fegan, F. Feinstein, A. Fiasson, A. Förster, G. Fontaine, M. Füßling, S. Gabici, Y. A. Gallant, L. Gérard, D. Gerbig, B. Giebels, J. F. Glicenstein, B. Glück, P. Goret, D. Göring,

D. Hauser, M. Hauser, S. Heinz, G. Heinzelmann, G. Henri, G. Hermann, J. A. Hinton, A. Hoffmann, W. Hofmann, P. Hofverberg, M. Holleran, S. Hoppe, D. Horns, A. Jacholkowska, O. C. de Jager, C. Jahn, I. Jung, K. Katarzyński, U. Katz, S. Kaufmann, M. Kerschhaggl, D. Khangulyan, B. Khélifi, D. Keogh, D. Klochkov, W. Kluźniak, T. Kneiske, N. Komin, K. Kosack, R. Kossakowski, G. Lamanna, M. Lemoine-Goumard, J.-P. Lenain, T. Lohse, V. Marandon, A. Marcowith, J. Masbou, D. Maurin, T. J. L. McComb, M. C. Medina, J. Méhault, R. Moderski, E. Moulin, M. Naumann-Godo, M. de Naurois, D. Nedbal, D. Nekrassov, B. Nicholas, J. Niemiec, S. J. Nolan, S. Ohm, J.-F. Olive, E. de Oña Wilhelmi, K. J. Orford, M. Ostrowski, M. Panter, M. Paz Arribas, G. Pedaletti, G. Pelletier, P.-O. Petrucci, S. Pita, G. Pühlhofer, M. Punch, A. Quirrenbach, B. C. Raubenheimer, M. Raue, S. M. Rayner, O. Reimer, M. Renaud, R. de Los Reyes, F. Rieger, J. Ripken, L. Rob, S. Rosier-Lees, G. Rowell, B. Rudak, C. B. Rulten, J. Ruppel, F. Ryde, V. Sahakian, A. Santangelo, R. Schlickeiser, F. M. Schöck, A. Schönwald, U. Schwanke, S. Schwarzburg, S. Schwemmer, A. Shalchi, I. Sushch, M. Sikora, J. L. Skilton, H. Sol, Ł. Stawarz, R. Steenkamp, C. Stegmann, F. Stinzing, G. Superina, A. Szostek, P. H. Tam, J.-P. Tavernet, R. Terrier, O. Tibolla, M. Tluczykont, C. van Eldik, G. Vasileiadis, C. Venter, L. Venter, J. P. Vialle, P. Vincent, J. Vink, M. Vivier, H. J. Völk, F. Volpe, S. Vorobiov, S. J. Wagner, M. Ward, A. A. Zdziarski, A. Zech, and HESS Collaboration. First detection of VHE γ-rays from SN 1006 by HESS. *A&A*, 516:A62+, June 2010. doi: 10.1051/0004-6361/200913916.

M. Actis, G. Agnetta, F. Aharonian, A. Akhperjanian, J. Aleksić, E. Aliu, D. Allan, I. Allekotte, F. Antico, L. A. Antonelli, and et al. Design concepts for the Cherenkov Telescope Array CTA: an advanced facility for ground-based high-energy gamma-ray astronomy. *Experimental Astronomy*, 32:193–316, December 2011. doi: 10.1007/s10686-011-9247-0.

F. Aharonian, A. G. Akhperjanian, K.-M. Aye, A. R. Bazer-Bachi, M. Beilicke, W. Benbow, D. Berge, P. Berghaus, K. Bernlöhr, O. Bolz, C. Boisson, C. Borgmeier, F. Breitling, A. M. Brown, J. Bussons Gordo, P. M. Chadwick, V. R. Chitnis, L.-M. Chounet, R. Cornils, L. Costamante, B. Degrange, A. Djannati-Ataï, L. O'C. Drury, T. Ergin, P. Espigat, F. Feinstein, P. Fleury, G. Fontaine, S. Funk, Y. Gallant, B. Giebels, S. Gillessen, P. Goret, J. Guy, C. Hadjichristidis, M. Hauser, G. Heinzelmann, G. Henri, G. Hermann, J. A. Hinton, W. Hofmann, M. Holleran, D. Horns, O. C. de Jager, I. Jung, B. Khélifi, N. Komin, A. Konopelko, I. J. Latham, R. Le Gallou, M. Lemoine, A. Lemière, N. Leroy, T. Lohse, A. Marcowith, C. Masterson, T. J. L. McComb, M. de Naurois, S. J. Nolan, A. Noutsos, K. J. Orford, J. L. Osborne, M. Ouchrif, M. Panter, G. Pelletier, S. Pita, M. Pohl, G. Pühlhofer, M. Punch, B. C. Raubenheimer, M. Raue, J. Raux, S. M. Rayner, I. Redondo, A. Reimer, O. Reimer, J. Ripken, M. Rivoal, L. Rob, L. Rolland, G. Rowell, V. Sahakian, L. Saugé, S. Schlenker, R. Schlickeiser, C. Schuster, U. Schwanke, M. Siewert, H. Sol, R. Steenkamp, C. Stegmann, J.-P. Tavernet, C. G. Théoret, M. Tluczykont, D. J. van der Walt, G. Vasileiadis, P. Vincent, B. Visser, H. J. Völk, and S. J. Wagner.

Very high energy gamma rays from the direction of Sagittarius A*. *A&A*, 425: L13–L17, October 2004a. doi: 10.1051/0004-6361:200400055.

F. Aharonian, A. G. Akhperjanian, K.-M. Aye, A. R. Bazer-Bachi, M. Beilicke, W. Benbow, D. Berge, P. Berghaus, K. Bernlöhr, C. Boisson, O. Bolz, C. Borgmeier, I. Braun, F. Breitling, A. M. Brown, J. Bussons Gordo, P. M. Chadwick, L.-M. Chounet, R. Cornils, L. Costamante, B. Degrange, A. Djannati-Ataï, L. O'C. Drury, G. Dubus, T. Ergin, P. Espigat, F. Feinstein, P. Fleury, G. Fontaine, S. Funk, Y. A. Gallant, B. Giebels, S. Gillessen, P. Goret, C. Hadjichristidis, M. Hauser, G. Heinzelmann, G. Henri, G. Hermann, J. A. Hinton, W. Hofmann, M. Holleran, D. Horns, O. C. de Jager, I. Jung, B. Khélifi, N. Komin, A. Konopelko, I. J. Latham, R. Le Gallou, A. Lemière, M. Lemoine, N. Leroy, T. Lohse, A. Marcowith, C. Masterson, T. J. L. McComb, M. de Naurois, S. J. Nolan, A. Noutsos, K. J. Orford, J. L. Osborne, M. Ouchrif, M. Panter, G. Pelletier, S. Pita, G. Pühlhofer, M. Punch, B. C. Raubenheimer, M. Raue, J. Raux, S. M. Rayner, I. Redondo, A. Reimer, O. Reimer, J. Ripken, L. Rob, L. Rolland, G. Rowell, V. Sahakian, L. Saugé, S. Schlenker, R. Schlickeiser, C. Schuster, U. Schwanke, M. Siewert, H. Sol, R. Steenkamp, C. Stegmann, J.-P. Tavernet, R. Terrier, C. G. Théoret, M. Tluczykont, G. Vasileiadis, C. Venter, P. Vincent, B. Visser, H. J. Völk, and S. J. Wagner. Very high energy gamma rays from the composite SNR G 0.9+0.1. *A&A*, 432:L25–L29, March 2005a. doi: 10.1051/0004-6361:200500022.

F. Aharonian, A. G. Akhperjanian, K.-M. Aye, A. R. Bazer-Bachi, M. Beilicke, W. Benbow, D. Berge, P. Berghaus, K. Bernlöhr, C. Boisson, O. Bolz, V. Borrel, I. Braun, F. Breitling, A. M. Brown, J. B. Gordo, P. M. Chadwick, L.-M. Chounet, R. Cornils, L. Costamante, B. Degrange, H. J. Dickinson, A. Djannati-Ataï, L. O. Drury, G. Dubus, D. Emmanoulopoulos, P. Espigat, F. Feinstein, P. Fleury, G. Fontaine, Y. Fuchs, S. Funk, Y. A. Gallant, B. Giebels, S. Gillessen, J. F. Glicenstein, P. Goret, C. Hadjichristidis, M. Hauser, G. Heinzelmann, G. Henri, G. Hermann, J. A. Hinton, W. Hofmann, M. Holleran, D. Horns, A. Jacholkowska, O. C. de Jager, B. Khélifi, N. Komin, A. Konopelko, I. J. Latham, R. Le Gallou, A. Lemière, M. Lemoine-Goumard, N. Leroy, T. Lohse, A. Marcowith, J.-M. Martin, O. Martineau-Huynh, C. Masterson, T. J. L. McComb, M. de Naurois, S. J. Nolan, A. Noutsos, K. J. Orford, J. L. Osborne, M. Ouchrif, M. Panter, G. Pelletier, S. Pita, G. Pühlhofer, M. Punch, B. C. Raubenheimer, M. Raue, J. Raux, S. M. Rayner, A. Reimer, O. Reimer, J. Ripken, L. Rob, L. Rolland, G. Rowell, V. Sahakian, L. Saugé, S. Schlenker, R. Schlickeiser, C. Schuster, U. Schwanke, M. Siewert, H. Sol, D. Spangler, R. Steenkamp, C. Stegmann, J.-P. Tavernet, R. Terrier, C. G. Théoret, M. Tluczykont, G. Vasileiadis, C. Venter, P. Vincent, H. J. Völk, and S. J. Wagner. Discovery of Very High Energy Gamma Rays Associated with an X-ray Binary. *Science*, 309:746–749, July 2005b. doi: 10.1126/science.1113764.

F. Aharonian, A. G. Akhperjanian, K.-M. Aye, A. R. Bazer-Bachi, M. Beilicke, W. Benbow, D. Berge, P. Berghaus, K. Bernlöhr, C. Boisson, O. Bolz, I. Braun, F. Breitling, A. M. Brown, J. Bussons Gordo, P. M. Chadwick, L.-M. Chounet, R. Cornils,

L. Costamante, B. Degrange, A. Djannati-Ataï, L. O'C. Drury, G. Dubus, D. Emmanoulopoulos, P. Espigat, F. Feinstein, P. Fleury, G. Fontaine, Y. Fuchs, S. Funk, Y. A. Gallant, B. Giebels, S. Gillessen, J. F. Glicenstein, P. Goret, C. Hadjichristidis, M. Hauser, G. Heinzelmann, G. Henri, G. Hermann, J. A. Hinton, W. Hofmann, M. Holleran, D. Horns, O. C. de Jager, S. Johnston, B. Khélifi, J. G. Kirk, N. Komin, A. Konopelko, I. J. Latham, R. Le Gallou, A. Lemière, M. Lemoine-Goumard, N. Leroy, O. Martineau-Huynh, T. Lohse, A. Marcowith, C. Masterson, T. J. L. McComb, M. de Naurois, S. J. Nolan, A. Noutsos, K. J. Orford, J. L. Osborne, M. Ouchrif, M. Panter, G. Pelletier, S. Pita, G. Pühlhofer, M. Punch, B. C. Raubenheimer, M. Raue, J. Raux, S. M. Rayner, I. Redondo, A. Reimer, O. Reimer, J. Ripken, L. Rob, L. Rolland, G. Rowell, V. Sahakian, L. Saugé, S. Schlenker, R. Schlickeiser, C. Schuster, U. Schwanke, M. Siewert, O. Skjæraasen, H. Sol, R. Steenkamp, C. Stegmann, J.-P. Tavernet, R. Terrier, C. G. Théoret, M. Tluczykont, G. Vasileiadis, C. Venter, P. Vincent, H. J. Völk, and S. J. Wagner. Discovery of the binary pulsar PSR B1259-63 in very-high-energy gamma rays around periastron with HESS. *A&A*, 442:1–10, October 2005c. doi: 10.1051/0004-6361:20052983.

F. Aharonian, A. G. Akhperjanian, K.-M. Aye, A. R. Bazer-Bachi, M. Beilicke, W. Benbow, D. Berge, P. Berghaus, K. Bernlöhr, C. Boisson, O. Bolz, I. Braun, F. Breitling, A. M. Brown, J. Bussons Gordo, P. M. Chadwick, L.-M. Chounet, R. Cornils, L. Costamante, B. Degrange, A. Djannati-Ataï, L. O'C. Drury, G. Dubus, D. Emmanoulopoulos, P. Espigat, F. Feinstein, P. Fleury, G. Fontaine, Y. Fuchs, S. Funk, Y. A. Gallant, B. Giebels, S. Gillessen, J. F. Glicenstein, P. Goret, C. Hadjichristidis, M. Hauser, G. Heinzelmann, G. Henri, G. Hermann, J. A. Hinton, W. Hofmann, M. Holleran, D. Horns, O. C. de Jager, B. Khélifi, N. Komin, A. Konopelko, I. J. Latham, R. Le Gallou, A. Lemière, M. Lemoine-Goumard, N. Leroy, T. Lohse, O. Martineau-Huynh, A. Marcowith, C. Masterson, T. J. L. McComb, M. de Naurois, S. J. Nolan, A. Noutsos, K. J. Orford, J. L. Osborne, M. Ouchrif, M. Panter, G. Pelletier, S. Pita, G. Pühlhofer, M. Punch, B. C. Raubenheimer, M. Raue, J. Raux, S. M. Rayner, I. Redondo, A. Reimer, O. Reimer, J. Ripken, L. Rob, L. Rolland, G. Rowell, V. Sahakian, L. Saugé, S. Schlenker, R. Schlickeiser, C. Schuster, U. Schwanke, M. Siewert, H. Sol, R. Steenkamp, C. Stegmann, J.-P. Tavernet, R. Terrier, C. G. Théoret, M. Tluczykont, D. J. van der Walt, G. Vasileiadis, C. Venter, P. Vincent, H. J. Völk, and S. J. Wagner. Serendipitous discovery of the unidentified extended TeV γ-ray source HESS J1303-631. *A&A*, 439:1013–1021, September 2005d. doi: 10.1051/0004-6361:20053195.

F. Aharonian, A. G. Akhperjanian, A. R. Bazer-Bachi, M. Beilicke, W. Benbow, D. Berge, K. Bernlöhr, C. Boisson, O. Bolz, V. Borrel, I. Braun, F. Breitling, A. M. Brown, P. M. Chadwick, L.-M. Chounet, R. Cornils, L. Costamante, B. Degrange, H. J. Dickinson, A. Djannati-Ataï, L. O'C. Drury, G. Dubus, D. Emmanoulopoulos, P. Espigat, F. Feinstein, G. Fontaine, Y. Fuchs, S. Funk, Y. A. Gallant, B. Giebels, S. Gillessen, J. F. Glicenstein, P. Goret, C. Hadjichristidis, M. Hauser, G. Heinzel-

mann, G. Henri, G. Hermann, J. A. Hinton, W. Hofmann, M. Holleran, D. Horns, A. Jacholkowska, O. C. de Jager, B. Khélifi, N. Komin, A. Konopelko, I. J. Latham, R. Le Gallou, A. Lemière, M. Lemoine-Goumard, N. Leroy, T. Lohse, J. M. Martin, O. Martineau-Huynh, A. Marcowith, C. Masterson, T. J. L. McComb, M. de Naurois, S. J. Nolan, A. Noutsos, K. J. Orford, J. L. Osborne, M. Ouchrif, M. Panter, G. Pelletier, S. Pita, G. Pühlhofer, M. Punch, B. C. Raubenheimer, M. Raue, J. Raux, S. M. Rayner, A. Reimer, O. Reimer, J. Ripken, L. Rob, L. Rolland, G. Rowell, V. Sahakian, L. Saugé, S. Schlenker, R. Schlickeiser, C. Schuster, U. Schwanke, M. Siewert, H. Sol, D. Spangler, R. Steenkamp, C. Stegmann, J.-P. Tavernet, R. Terrier, C. G. Théoret, M. Tluczykont, G. Vasileiadis, C. Venter, P. Vincent, H. J. Völk, and S. J. Wagner. Detection of TeV γ-ray emission from the shell-type supernova remnant RX J0852.0-4622 with HESS. *A&A*, 437:L7–L10, July 2005e. doi: 10.1051/0004-6361:200500130.

F. Aharonian, A. G. Akhperjanian, A. R. Bazer-Bachi, M. Beilicke, W. Benbow, D. Berge, K. Bernlöhr, C. Boisson, O. Bolz, V. Borrel, I. Braun, F. Breitling, A. M. Brown, R. Bühler, I. Büsching, S. Carrigan, P. M. Chadwick, L.-M. Chounet, R. Cornils, L. Costamante, B. Degrange, H. J. Dickinson, A. Djannati-Ataï, L. O'C. Drury, G. Dubus, K. Egberts, D. Emmanoulopoulos, P. Espigat, F. Feinstein, E. Ferrero, A. Fiasson, G. Fontaine, S. Funk, S. Funk, Y. A. Gallant, B. Giebels, J. F. Glicenstein, P. Goret, C. Hadjichristidis, D. Hauser, M. Hauser, G. Heinzelmann, G. Henri, G. Hermann, J. A. Hinton, W. Hofmann, M. Holleran, D. Horns, A. Jacholkowska, O. C. de Jager, B. Khélifi, N. Komin, A. Konopelko, K. Kosack, I. J. Latham, R. Le Gallou, A. Lemière, M. Lemoine-Goumard, T. Lohse, J. M. Martin, O. Martineau-Huynh, A. Marcowith, C. Masterson, T. J. L. McComb, M. de Naurois, D. Nedbal, S. J. Nolan, A. Noutsos, K. J. Orford, J. L. Osborne, M. Ouchrif, M. Panter, G. Pelletier, S. Pita, G. Pühlhofer, M. Punch, B. C. Raubenheimer, M. Raue, S. M. Rayner, A. Reimer, O. Reimer, J. Ripken, L. Rob, L. Rolland, G. Rowell, V. Sahakian, L. Saugé, S. Schlenker, R. Schlickeiser, U. Schwanke, H. Sol, D. Spangler, F. Spanier, R. Steenkamp, C. Stegmann, G. Superina, J.-P. Tavernet, R. Terrier, C. G. Théoret, M. Tluczykont, C. van Eldik, G. Vasileiadis, C. Venter, P. Vincent, H. J. Völk, S. J. Wagner, and M. Ward. Observations of the Crab nebula with HESS. *A&A*, 457:899–915, October 2006a. doi: 10.1051/0004-6361:20065351.

F. Aharonian, A. G. Akhperjanian, A. R. Bazer-Bachi, M. Beilicke, W. Benbow, D. Berge, K. Bernlöhr, C. Boisson, O. Bolz, V. Borrel, I. Braun, F. Breitling, A. M. Brown, P. M. Chadwick, L.-M. Chounet, R. Cornils, L. Costamante, B. Degrange, H. J. Dickinson, A. Djannati-Ataï, L. O'C. Drury, G. Dubus, D. Emmanoulopoulos, P. Espigat, F. Feinstein, G. Fontaine, Y. Fuchs, S. Funk, Y. A. Gallant, B. Giebels, J. F. Glicenstein, P. Goret, C. Hadjichristidis, D. Hauser, M. Hauser, G. Heinzelmann, G. Henri, G. Hermann, J. A. Hinton, W. Hofmann, M. Holleran, D. Horns, A. Jacholkowska, O. C. de Jager, B. Khélifi, S. Klages, N. Komin, A. Konopelko, I. J. Latham, R. Le Gallou, A. Lemière, M. Lemoine-Goumard, T. Lohse, J. M.

Martin, O. Martineau-Huynh, A. Marcowith, C. Masterson, T. J. L. McComb, M. de Naurois, D. Nedbal, S. J. Nolan, A. Noutsos, K. J. Orford, J. L. Osborne, M. Ouchrif, M. Panter, G. Pelletier, S. Pita, G. Pühlhofer, M. Punch, B. C. Raubenheimer, M. Raue, S. M. Rayner, A. Reimer, O. Reimer, J. Ripken, L. Rob, L. Rolland, G. Rowell, V. Sahakian, L. Saugé, S. Schlenker, R. Schlickeiser, C. Schuster, U. Schwanke, M. Siewert, H. Sol, D. Spangler, R. Steenkamp, C. Stegmann, G. Superina, J.-P. Tavernet, R. Terrier, C. G. Théoret, M. Tluczykont, C. van Eldik, G. Vasileiadis, C. Venter, P. Vincent, H. J. Völk, and S. J. Wagner. A detailed spectral and morphological study of the gamma-ray supernova remnant RX J1713.7-3946 with HESS. *A&A*, 449:223–242, 04 2006b.

F. Aharonian, A. G. Akhperjanian, A. R. Bazer-Bachi, M. Beilicke, W. Benbow, D. Berge, K. Bernlöhr, C. Boisson, O. Bolz, V. Borrel, I. Braun, F. Breitling, A. M. Brown, P. M. Chadwick, L.-M. Chounet, R. Cornils, L. Costamante, B. Degrange, H. J. Dickinson, A. Djannati-Ataï, L. O. Drury, G. Dubus, D. Emmanoulopoulos, P. Espigat, F. Feinstein, G. Fontaine, Y. Fuchs, S. Funk, Y. A. Gallant, B. Giebels, S. Gillessen, J. F. Glicenstein, P. Goret, C. Hadjichristidis, M. Hauser, G. Heinzelmann, G. Henri, G. Hermann, J. A. Hinton, W. Hofmann, M. Holleran, D. Horns, A. Jacholkowska, O. C. de Jager, B. Khélifi, N. Komin, A. Konopelko, I. J. Latham, R. Le Gallou, A. Lemière, M. Lemoine-Goumard, N. Leroy, T. Lohse, J. M. Martin, O. Martineau-Huynh, A. Marcowith, C. Masterson, T. J. L. McComb, M. de Naurois, S. J. Nolan, A. Noutsos, K. J. Orford, J. L. Osborne, M. Ouchrif, M. Panter, G. Pelletier, S. Pita, G. Pühlhofer, M. Punch, B. C. Raubenheimer, M. Raue, J. Raux, S. M. Rayner, A. Reimer, O. Reimer, J. Ripken, L. Rob, L. Rolland, G. Rowell, V. Sahakian, L. Saugé, S. Schlenker, R. Schlickeiser, C. Schuster, U. Schwanke, M. Siewert, H. Sol, D. Spangler, R. Steenkamp, C. Stegmann, J.-P. Tavernet, R. Terrier, C. G. Théoret, M. Tluczykont, G. Vasileiadis, C. Venter, P. Vincent, H. J. Völk, and S. J. Wagner. The H.E.S.S. Survey of the Inner Galaxy in Very High Energy Gamma Rays. *ApJ*, 636:777–797, January 2006c. doi: 10.1086/498013.

F. Aharonian, A. G. Akhperjanian, A. R. Bazer-Bachi, M. Beilicke, W. Benbow, D. Berge, K. Bernlöhr, C. Boisson, O. Bolz, V. Borrel, I. Braun, A. M. Brown, R. Bühler, I. Büsching, S. Carrigan, P. M. Chadwick, L.-M. Chounet, R. Cornils, L. Costamante, B. Degrange, H. J. Dickinson, A. Djannati-Ataï, L. O'C. Drury, G. Dubus, K. Egberts, D. Emmanoulopoulos, P. Espigat, F. Feinstein, E. Ferrero, A. Fiasson, G. Fontaine, S. Funk, S. Funk, M. Füßling, Y. A. Gallant, B. Giebels, J. F. Glicenstein, P. Goret, C. Hadjichristidis, D. Hauser, M. Hauser, G. Heinzelmann, G. Henri, G. Hermann, J. A. Hinton, A. Hoffmann, W. Hofmann, M. Holleran, D. Horns, A. Jacholkowska, O. C. de Jager, E. Kendziorra, B. Khélifi, N. Komin, A. Konopelko, K. Kosack, I. J. Latham, R. Le Gallou, A. Lemière, M. Lemoine-Goumard, T. Lohse, J. M. Martin, O. Martineau-Huynh, A. Marcowith, C. Masterson, G. Maurin, T. J. L. McComb, E. Moulin, M. de Naurois, D. Nedbal, S. J. Nolan, A. Noutsos, K. J. Orford, J. L. Osborne, M. Ouchrif, M. Panter, G. Pelletier, S. Pita, G. Pühlhofer, M. Punch, B. C. Raubenheimer, M. Raue, S. M. Rayner, A. Reimer,

O. Reimer, J. Ripken, L. Rob, L. Rolland, G. Rowell, V. Sahakian, A. Santangelo, L. Saugé, S. Schlenker, R. Schlickeiser, R. Schröder, U. Schwanke, S. Schwarzburg, A. Shalchi, H. Sol, D. Spangler, F. Spanier, R. Steenkamp, C. Stegmann, G. Superina, J.-P. Tavernet, R. Terrier, C. G. Théoret, M. Tluczykont, C. van Eldik, G. Vasileiadis, C. Venter, P. Vincent, H. J. Völk, S. J. Wagner, and M. Ward. Energy dependent γ-ray morphology in the pulsar wind nebula HESS J1825-137. *A&A*, 460:365–374, December 2006d. doi: 10.1051/0004-6361:20065546.

F. Aharonian, A. G. Akhperjanian, A. R. Bazer-Bachi, M. Beilicke, W. Benbow, D. Berge, K. Bernlöhr, C. Boisson, O. Bolz, V. Borrel, I. Braun, E. Brion, A. M. Brown, R. Bühler, I. Büsching, S. Carrigan, P. M. Chadwick, L.-M. Chounet, G. Coignet, R. Cornils, L. Costamante, B. Degrange, H. J. Dickinson, A. Djannati-Ataï, L. O'C. Drury, G. Dubus, K. Egberts, D. Emmanoulopoulos, P. Espigat, F. Feinstein, E. Ferrero, A. Fiasson, G. Fontaine, S. Funk, S. Funk, M. Füßling, Y. A. Gallant, B. Giebels, J. F. Glicenstein, B. Glück, P. Goret, C. Hadjichristidis, D. Hauser, M. Hauser, G. Heinzelmann, G. Henri, G. Hermann, J. A. Hinton, A. Hoffmann, W. Hofmann, M. Holleran, S. Hoppe, D. Horns, A. Jacholkowska, O. C. de Jager, E. Kendziorra, M. Kerschhaggl, B. Khélifi, N. Komin, A. Konopelko, K. Kosack, G. Lamanna, I. J. Latham, R. Le Gallou, A. Lemière, M. Lemoine-Goumard, T. Lohse, J. M. Martin, O. Martineau-Huynh, A. Marcowith, C. Masterson, G. Maurin, T. J. L. McComb, E. Moulin, M. de Naurois, D. Nedbal, S. J. Nolan, A. Noutsos, J.-P. Olive, K. J. Orford, J. L. Osborne, M. Panter, G. Pelletier, S. Pita, G. Pühlhofer, M. Punch, S. Ranchon, B. C. Raubenheimer, M. Raue, S. M. Rayner, A. Reimer, O. Reimer, J. Ripken, L. Rob, L. Rolland, S. Rosier-Lees, G. Rowell, V. Sahakian, A. Santangelo, L. Saugé, S. Schlenker, R. Schlickeiser, R. Schröder, U. Schwanke, S. Schwarzburg, S. Schwemmer, A. Shalchi, H. Sol, D. Spangler, F. Spanier, R. Steenkamp, C. Stegmann, G. Superina, P. H. Tam, J.-P. Tavernet, R. Terrier, M. Tluczykont, C. van Eldik, G. Vasileiadis, C. Venter, J. P. Vialle, P. Vincent, H. J. Völk, S. J. Wagner, and M. Ward. Primary particle acceleration above 100 TeV in the shell-type supernova remnant <ASTROBJ>RX J1713.7-3946</ASTROBJ> with deep HESS observations. *A&A*, 464: 235–243, March 2007a. doi: 10.1051/0004-6361:20066381.

F. Aharonian, A. G. Akhperjanian, A. R. Bazer-Bachi, M. Beilicke, W. Benbow, D. Berge, K. Bernlöhr, C. Boisson, O. Bolz, V. Borrel, I. Braun, A. M. Brown, R. Bühler, I. Büsching, S. Carrigan, P. M. Chadwick, L.-M. Chounet, G. Coignet, R. Cornils, L. Costamante, B. Degrange, H. J. Dickinson, A. Djannati-Ataï, L. O. Drury, G. Dubus, K. Egberts, D. Emmanoulopoulos, P. Espigat, F. Feinstein, E. Ferrero, A. Fiasson, M. D. Filipovic, G. Fontaine, Y. Fukui, S. Funk, S. Funk, M. Füßling, Y. A. Gallant, B. Giebels, J. F. Glicenstein, P. Goret, C. Hadjichristidis, D. Hauser, M. Hauser, G. Heinzelmann, G. Henri, G. Hermann, J. A. Hinton, J. S. Hiraga, A. Hoffmann, W. Hofmann, M. Holleran, S. Hoppe, D. Horns, Y. Ishisaki, A. Jacholkowska, O. C. de Jager, E. Kendziorra, M. Kerschhaggl, B. Khélifi, N. Komin, A. Konopelko, K. Kosack, G. Lamanna, I. J. Latham, R. Le

Gallou, A. Lemière, M. Lemoine-Goumard, T. Lohse, J. M. Martin, O. Martineau-Huynh, A. Marcowith, C. Masterson, G. Maurin, T. J. L. McComb, E. Moulin, Y. Moriguchi, M. de Naurois, D. Nedbal, S. J. Nolan, A. Noutsos, K. J. Orford, J. L. Osborne, M. Ouchrif, M. Panter, G. Pelletier, S. Pita, G. Pühlhofer, M. Punch, S. Ranchon, B. C. Raubenheimer, M. Raue, S. M. Rayner, A. Reimer, J. Ripken, L. Rob, L. Rolland, S. Rosier-Lees, G. Rowell, V. Sahakian, A. Santangelo, L. Saugé, S. Schlenker, R. Schlickeiser, R. Schröder, U. Schwanke, S. Schwarzburg, S. Schwemmer, A. Shalchi, H. Sol, D. Spangler, F. Spanier, R. Steenkamp, C. Stegmann, G. Superina, P. H. Tam, J.-P. Tavernet, R. Terrier, M. Tluczykont, C. van Eldik, G. Vasileiadis, C. Venter, J. P. Vialle, P. Vincent, H. J. Völk, S. J. Wagner, and M. Ward. H.E.S.S. Observations of the Supernova Remnant RX J0852.0-4622: Shell-Type Morphology and Spectrum of a Widely Extended Very High Energy Gamma-Ray Source. *ApJ*, 661:236–249, May 2007b. doi: 10.1086/512603.

F. Aharonian, A. G. Akhperjanian, U. Barres de Almeida, A. R. Bazer-Bachi, Y. Becherini, B. Behera, W. Benbow, K. Bernlöhr, C. Boisson, A. Bochow, V. Borrel, I. Braun, E. Brion, J. Brucker, P. Brun, R. Bühler, T. Bulik, I. Büsching, T. Boutelier, S. Carrigan, P. M. Chadwick, A. Charbonnier, R. C. G. Chaves, A. Cheesebrough, L.-M. Chounet, A. C. Clapson, G. Coignet, M. Dalton, B. Degrange, C. Deil, H. J. Dickinson, A. Djannati-Ataï, W. Domainko, L. O'C. Drury, F. Dubois, G. Dubus, J. Dyks, M. Dyrda, K. Egberts, D. Emmanoulopoulos, P. Espigat, C. Farnier, F. Feinstein, A. Fiasson, A. Förster, G. Fontaine, M. Füßling, S. Gabici, Y. A. Gallant, L. Gérard, B. Giebels, J. F. Glicenstein, B. Glück, P. Goret, C. Hadjichristidis, D. Hauser, M. Hauser, S. Heinz, G. Heinzelmann, G. Henri, G. Hermann, J. A. Hinton, A. Hoffmann, W. Hofmann, M. Holleran, S. Hoppe, D. Horns, A. Jacholkowska, O. C. de Jager, I. Jung, K. Katarzyński, S. Kaufmann, E. Kendziorra, M. Kerschhaggl, D. Khangulyan, B. Khélifi, D. Keogh, N. Komin, K. Kosack, G. Lamanna, J.-P. Lenain, T. Lohse, V. Marandon, J. M. Martin, O. Martineau-Huynh, A. Marcowith, D. Maurin, T. J. L. McComb, M. C. Medina, R. Moderski, E. Moulin, M. Naumann-Godo, M. de Naurois, D. Nedbal, D. Nekrassov, J. Niemiec, S. J. Nolan, S. Ohm, J.-F. Olive, E. de Oña Wilhelmi, K. J. Orford, J. L. Osborne, M. Ostrowski, M. Panter, G. Pedaletti, G. Pelletier, P.-O. Petrucci, S. Pita, G. Pühlhofer, M. Punch, A. Quirrenbach, B. C. Raubenheimer, M. Raue, S. M. Rayner, M. Renaud, F. Rieger, J. Ripken, L. Rob, S. Rosier-Lees, G. Rowell, B. Rudak, C. B. Rulten, J. Ruppel, V. Sahakian, A. Santangelo, R. Schlickeiser, F. M. Schöck, R. Schröder, U. Schwanke, S. Schwarzburg, S. Schwemmer, A. Shalchi, J. L. Skilton, H. Sol, D. Spangler, Ł. Stawarz, R. Steenkamp, C. Stegmann, G. Superina, P. H. Tam, J.-P. Tavernet, R. Terrier, O. Tibolla, C. van Eldik, G. Vasileiadis, C. Venter, J. P. Vialle, P. Vincent, M. Vivier, H. J. Völk, F. Volpe, S. J. Wagner, M. Ward, A. A. Zdziarski, and A. Zech. Simultaneous HESS and Chandra observations of Sagitarius A* during an X-ray flare. *A&A*, 492:L25–L28, December 2008a. doi: 10.1051/0004-6361:200810912.

F. Aharonian, J. Buckley, T. Kifune, and G. Sinnis. High energy astrophysics with

ground-based gamma ray detectors. *Reports on Progress in Physics*, 71(9):096901, September 2008b. doi: 10.1088/0034-4885/71/9/096901.

F. Aharonian, A. G. Akhperjanian, G. Anton, U. Barres de Almeida, A. R. Bazer-Bachi, Y. Becherini, B. Behera, K. Bernlöhr, A. Bochow, C. Boisson, J. Bolmont, V. Borrel, J. Brucker, F. Brun, P. Brun, R. Bühler, T. Bulik, I. Büsching, T. Boutelier, P. M. Chadwick, A. Charbonnier, R. C. G. Chaves, A. Cheesebrough, L.-M. Chounet, A. C. Clapson, G. Coignet, M. Dalton, M. K. Daniel, I. D. Davids, B. Degrange, C. Deil, H. J. Dickinson, A. Djannati-Ataï, W. Domainko, L. O'C. Drury, F. Dubois, G. Dubus, J. Dyks, M. Dyrda, K. Egberts, D. Emmanoulopoulos, P. Espigat, C. Farnier, F. Feinstein, A. Fiasson, A. Förster, G. Fontaine, M. Füßling, S. Gabici, Y. A. Gallant, L. Gérard, D. Gerbig, B. Giebels, J. F. Glicenstein, B. Glück, P. Goret, D. Göring, D. Hauser, M. Hauser, S. Heinz, G. Heinzelmann, G. Henri, G. Hermann, J. A. Hinton, A. Hoffmann, W. Hofmann, M. Holleran, S. Hoppe, D. Horns, A. Jacholkowska, O. C. de Jager, C. Jahn, I. Jung, K. Katarzyński, U. Katz, S. Kaufmann, M. Kerschhaggl, D. Khangulyan, B. Khélifi, D. Keogh, D. Klochkov, W. Kluźniak, T. Kneiske, N. Komin, K. Kosack, R. Kossakowski, G. Lamanna, J.-P. Lenain, T. Lohse, V. Marandon, O. Martineau-Huynh, A. Marcowith, J. Masbou, D. Maurin, T. J. L. McComb, M. C. Medina, R. Moderski, E. Moulin, M. Naumann-Godo, M. de Naurois, D. Nedbal, D. Nekrassov, B. Nicholas, J. Niemiec, S. J. Nolan, S. Ohm, J.-F. Olive, E. de Oña Wilhelmi, K. J. Orford, M. Ostrowski, M. Panter, M. Paz Arribas, G. Pedaletti, G. Pelletier, P.-O. Petrucci, S. Pita, G. Pühlhofer, M. Punch, A. Quirrenbach, B. C. Raubenheimer, M. Raue, S. M. Rayner, M. Renaud, F. Rieger, J. Ripken, L. Rob, S. Rosier-Lees, G. Rowell, B. Rudak, C. B. Rulten, J. Ruppel, V. Sahakian, A. Santangelo, R. Schlickeiser, F. M. Schöck, U. Schwanke, S. Schwarzburg, S. Schwemmer, A. Shalchi, M. Sikora, J. L. Skilton, H. Sol, D. Spangler, Ł. Stawarz, R. Steenkamp, C. Stegmann, F. Stinzing, G. Superina, A. Szostek, P. H. Tam, J.-P. Tavernet, R. Terrier, O. Tibolla, M. Tluczykont, C. van Eldik, G. Vasileiadis, C. Venter, L. Venter, J. P. Vialle, P. Vincent, M. Vivier, H. J. Völk, F. Volpe, S. J. Wagner, M. Ward, A. A. Zdziarski, and A. Zech. Very high energy γ-ray observations of the binary PSR B1259-63/SS2883 around the 2007 Periastron. *A&A*, 507:389–396, November 2009a. doi: 10.1051/0004-6361/200912339.

F. Aharonian, A. G. Akhperjanian, G. Anton, U. Barres de Almeida, A. R. Bazer-Bachi, Y. Becherini, B. Behera, K. Bernlöhr, C. Boisson, A. Bochow, V. Borrel, I. Braun, E. Brion, J. Brucker, P. Brun, R. Bühler, T. Bulik, I. Büsching, T. Boutelier, P. M. Chadwick, A. Charbonnier, R. C. G. Chaves, A. Cheesebrough, L.-M. Chounet, A. C. Clapson, G. Coignet, M. Dalton, M. K. Daniel, I. D. Davids, B. Degrange, C. Deil, H. J. Dickinson, A. Djannati-Ataï, W. Domainko, L. O'C. Drury, F. Dubois, G. Dubus, J. Dyks, M. Dyrda, K. Egberts, D. Emmanoulopoulos, P. Espigat, C. Farnier, F. Feinstein, A. Fiasson, A. Förster, G. Fontaine, M. Füßling, S. Gabici, Y. A. Gallant, L. Gérard, B. Giebels, J. F. Glicenstein, B. Glück, P. Goret, D. Hauser, M. Hauser, S. Heinz, G. Heinzelmann, G. Henri, G. Hermann, J. A.

Hinton, A. Hoffmann, W. Hofmann, M. Holleran, S. Hoppe, D. Horns, A. Jacholkowska, O. C. de Jager, I. Jung, K. Katarzyński, U. Katz, S. Kaufmann, E. Kendziorra, M. Kerschhaggl, D. Khangulyan, B. Khélifi, D. Keogh, N. Komin, K. Kosack, G. Lamanna, J.-P. Lenain, T. Lohse, V. Marandon, J. M. Martin, O. Martineau-Huynh, A. Marcowith, D. Maurin, T. J. L. McComb, M. C. Medina, R. Moderski, E. Moulin, M. Naumann-Godo, M. de Naurois, D. Nedbal, D. Nekrassov, J. Niemiec, S. J. Nolan, S. Ohm, J.-F. Olive, E. de Oña Wilhelmi, K. J. Orford, M. Ostrowski, M. Panter, M. Paz Arribas, G. Pedaletti, G. Pelletier, P.-O. Petrucci, S. Pita, G. Pühlhofer, M. Punch, A. Quirrenbach, B. C. Raubenheimer, M. Raue, S. M. Rayner, M. Renaud, F. Rieger, J. Ripken, L. Rob, L. Rolland, S. Rosier-Lees, G. Rowell, B. Rudak, C. B. Rulten, J. Ruppel, V. Sahakian, A. Santangelo, R. Schlickeiser, F. M. Schöck, R. Schröder, U. Schwanke, S. Schwarzburg, S. Schwemmer, A. Shalchi, J. L. Skilton, H. Sol, D. Spangler, Ł. Stawarz, R. Steenkamp, C. Stegmann, G. Superina, A. Szostek, P. H. Tam, J.-P. Tavernet, R. Terrier, O. Tibolla, C. van Eldik, G. Vasileiadis, C. Venter, L. Venter, J. P. Vialle, P. Vincent, M. Vivier, H. J. Völk, F. Volpe, S. J. Wagner, M. Ward, A. A. Zdziarski, and A. Zech. Spectrum and variability of the Galactic center VHE γ-ray source HESS J1745-290. *A&A*, 503:817–825, September 2009b. doi: 10.1051/0004-6361/200811569.

F. A. Aharonian. *Very high energy cosmic gamma radiation : a crucial window on the extreme Universe*. 2004.

F. A. Aharonian, A. G. Akhperjanian, K.-M. Aye, A. R. Bazer-Bachi, M. Beilicke, W. Benbow, D. Berge, P. Berghaus, K. Bernlöhr, O. Bolz, C. Boisson, C. Borgmeier, F. Breitling, A. M. Brown, J. Bussons Gordo, P. M. Chadwick, V. R. Chitnis, L.-M. Chounet, R. Cornils, L. Costamante, B. Degrange, A. Djannati-Ataï, L. O. Drury, T. Ergin, P. Espigat, F. Feinstein, P. Fleury, G. Fontaine, S. Funk, Y. A. Gallant, B. Giebels, S. Gillessen, P. Goret, J. Guy, C. Hadjichristidis, M. Hauser, G. Heinzelmann, G. Henri, G. Hermann, J. A. Hinton, W. Hofmann, M. Holleran, D. Horns, O. C. de Jager, I. Jung, B. Khélifi, N. Komin, A. Konopelko, I. J. Latham, R. Le Gallou, M. Lemoine, A. Lemière, N. Leroy, T. Lohse, A. Marcowith, C. Masterson, T. J. L. McComb, M. de Naurois, S. J. Nolan, A. Noutsos, K. J. Orford, J. L. Osborne, M. Ouchrif, M. Panter, G. Pelletier, S. Pita, M. Pohl, G. Pühlhofer, M. Punch, B. C. Raubenheimer, M. Raue, J. Raux, S. M. Rayner, I. Redondo, A. Reimer, O. Reimer, J. Ripken, M. Rivoal, L. Rob, L. Rolland, G. Rowell, V. Sahakian, L. Saugé, S. Schlenker, R. Schlickeiser, C. Schuster, U. Schwanke, M. Siewert, H. Sol, R. Steenkamp, C. Stegmann, J.-P. Tavernet, C. G. Théoret, M. Tluczykont, D. J. van der Walt, G. Vasileiadis, P. Vincent, B. Visser, H. J. Völk, and S. J. Wagner. High-energy particle acceleration in the shell of a supernova remnant. *Nature*, 432:75–77, November 2004b. doi: 10.1038/nature02960.

F. A. Aharonian, A. G. Akhperjanian, A. R. Bazer-Bachi, B. Behera, M. Beilicke, W. Benbow, D. Berge, K. Bernlöhr, C. Boisson, O. Bolz, V. Borrel, I. Braun, E. Brion, A. M. Brown, R. Bühler, I. Büsching, T. Boutelier, S. Carrigan, P. M.

Chadwick, L.-M. Chounet, G. Coignet, R. Cornils, L. Costamante, B. Degrange, H. J. Dickinson, A. Djannati-Ataï, W. Domainko, L. O'C. Drury, G. Dubus, K. Egberts, D. Emmanoulopoulos, P. Espigat, C. Farnier, F. Feinstein, A. Fiasson, A. Förster, G. Fontaine, S. Funk, S. Funk, M. Füßling, Y. A. Gallant, B. Giebels, J. F. Glicenstein, B. Glück, P. Goret, C. Hadjichristidis, D. Hauser, M. Hauser, G. Heinzelmann, G. Henri, G. Hermann, J. A. Hinton, A. Hoffmann, W. Hofmann, M. Holleran, S. Hoppe, D. Horns, A. Jacholkowska, O. C. de Jager, E. Kendziorra, M. Kerschhaggl, B. Khélifi, N. Komin, K. Kosack, G. Lamanna, I. J. Latham, R. Le Gallou, A. Lemière, M. Lemoine-Goumard, T. Lohse, J. M. Martin, O. Martineau-Huynh, A. Marcowith, C. Masterson, G. Maurin, T. J. L. McComb, E. Moulin, M. de Naurois, D. Nedbal, S. J. Nolan, A. Noutsos, J.-P. Olive, K. J. Orford, J. L. Osborne, M. Panter, G. Pedaletti, G. Pelletier, P.-O. Petrucci, S. Pita, G. Pühlhofer, M. Punch, S. Ranchon, B. C. Raubenheimer, M. Raue, S. M. Rayner, O. Reimer, J. Ripken, L. Rob, L. Rolland, S. Rosier-Lees, G. Rowell, J. Ruppel, V. Sahakian, A. Santangelo, L. Saugé, S. Schlenker, R. Schlickeiser, R. Schröder, U. Schwanke, S. Schwarzburg, S. Schwemmer, A. Shalchi, H. Sol, D. Spangler, R. Steenkamp, C. Stegmann, G. Superina, P. H. Tam, J.-P. Tavernet, R. Terrier, M. Tluczykont, C. van Eldik, G. Vasileiadis, C. Venter, J. P. Vialle, P. Vincent, H. J. Völk, S. J. Wagner, M. Ward, Y. Moriguchi, and Y. Fukui. Discovery of a point-like very-high-energy γ-ray source in Monoceros. *A&A*, 469:L1–L4, July 2007c. doi: 10.1051/0004-6361:20077299.

J. Albert, E. Aliu, H. Anderhub, P. Antoranz, A. Armada, M. Asensio, C. Baixeras, J. A. Barrio, M. Bartelt, H. Bartko, D. Bastieri, S. R. Bavikadi, W. Bednarek, K. Berger, C. Bigongiari, A. Biland, E. Bisesi, R. K. Bock, P. Bordas, V. Bosch-Ramon, T. Bretz, I. Britvitch, M. Camara, E. Carmona, A. Chilingarian, S. Ciprini, J. A. Coarasa, S. Commichau, J. L. Contreras, J. Cortina, V. Curtef, V. Danielyan, F. Dazzi, A. De Angelis, R. de los Reyes, B. De Lotto, E. Domingo-Santamaría, D. Dorner, M. Doro, M. Errando, M. Fagiolini, D. Ferenc, E. Fernández, R. Firpo, J. Flix, M. V. Fonseca, L. Font, M. Fuchs, N. Galante, M. Garczarczyk, M. Gaug, M. Giller, F. Goebel, D. Hakobyan, M. Hayashida, T. Hengstebeck, D. Höhne, J. Hose, C. C. Hsu, P. G. Isar, P. Jacon, O. Kalekin, R. Kosyra, D. Kranich, M. Laatiaoui, A. Laille, T. Lenisa, P. Liebing, E. Lindfors, S. Lombardi, F. Longo, J. López, M. López, E. Lorenz, F. Lucarelli, P. Majumdar, G. Maneva, K. Mannheim, O. Mansutti, M. Mariotti, M. Martínez, K. Mase, D. Mazin, C. Merck, M. Meucci, M. Meyer, J. M. Miranda, R. Mirzoyan, S. Mizobuchi, A. Moralejo, K. Nilsson, E. Oña-Wilhelmi, R. Orduña, N. Otte, I. Oya, D. Paneque, R. Paoletti, J. M. Paredes, M. Pasanen, D. Pascoli, F. Pauss, N. Pavel, R. Pegna, M. Persic, L. Peruzzo, A. Piccioli, M. Poller, G. Pooley, E. Prandini, A. Raymers, W. Rhode, M. Ribó, J. Rico, B. Riegel, M. Rissi, A. Robert, G. E. Romero, S. Rügamer, A. Saggion, A. Sánchez, P. Sartori, V. Scalzotto, V. Scapin, R. Schmitt, T. Schweizer, M. Shayduk, K. Shinozaki, S. N. Shore, N. Sidro, A. Sillanpää, D. Sobczynska, A. Stamerra, L. S. Stark, L. Takalo, P. Temnikov, D. Tescaro, M. Teshima, N. Tonello, A. Torres, D. F. Torres, N. Turini, H. Vankov, V. Vitale, R. M. Wagner, T. Wibig, W. Wit-

tek, R. Zanin, and J. Zapatero. Variable Very-High-Energy Gamma-Ray Emission from the Microquasar LS I +61 303. *Science*, 312:1771–1773, June 2006. doi: 10.1126/science.1128177.

J. Albert, E. Aliu, H. Anderhub, P. Antoranz, A. Armada, C. Baixeras, J. A. Barrio, H. Bartko, D. Bastieri, J. K. Becker, W. Bednarek, K. Berger, C. Bigongiari, A. Biland, R. K. Bock, P. Bordas, V. Bosch-Ramon, T. Bretz, I. Britvitch, M. Camara, E. Carmona, A. Chilingarian, J. A. Coarasa, S. Commichau, J. L. Contreras, J. Cortina, M. T. Costado, V. Curtef, V. Danielyan, F. Dazzi, A. De Angelis, C. Delgado, R. de los Reyes, B. De Lotto, E. Domingo-Santamaría, D. Dorner, M. Doro, M. Errando, M. Fagiolini, D. Ferenc, E. Fernández, R. Firpo, J. Flix, M. V. Fonseca, L. Font, M. Fuchs, N. Galante, R. J. García-López, M. Garczarczyk, M. Gaug, M. Giller, F. Goebel, D. Hakobyan, M. Hayashida, T. Hengstebeck, A. Herrero, D. Höhne, J. Hose, C. C. Hsu, P. Jacon, T. Jogler, R. Kosyra, D. Kranich, R. Kritzer, A. Laille, E. Lindfors, S. Lombardi, F. Longo, J. López, M. López, E. Lorenz, P. Majumdar, G. Maneva, K. Mannheim, O. Mansutti, M. Mariotti, M. Martínez, D. Mazin, C. Merck, M. Meucci, M. Meyer, J. M. Miranda, R. Mirzoyan, S. Mizobuchi, A. Moralejo, D. Nieto, K. Nilsson, J. Ninkovic, E. Oña-Wilhelmi, N. Otte, I. Oya, M. Panniello, R. Paoletti, J. M. Paredes, M. Pasanen, D. Pascoli, F. Pauss, R. Pegna, M. Persic, L. Peruzzo, A. Piccioli, E. Prandini, N. Puchades, A. Raymers, W. Rhode, M. Ribó, J. Rico, M. Rissi, A. Robert, S. Rügamer, A. Saggion, T. Saito, A. Sánchez, P. Sartori, V. Scalzotto, V. Scapin, R. Schmitt, T. Schweizer, M. Shayduk, K. Shinozaki, S. N. Shore, N. Sidro, A. Sillanpää, D. Sobczynska, A. Stamerra, L. S. Stark, L. Takalo, P. Temnikov, D. Tescaro, M. Teshima, D. F. Torres, N. Turini, H. Vankov, V. Vitale, R. M. Wagner, T. Wibig, W. Wittek, F. Zandanel, R. Zanin, and J. Zapatero. Very High Energy Gamma-Ray Radiation from the Stellar Mass Black Hole Binary Cygnus X-1. *ApJL*, 665:L51–L54, August 2007. doi: 10.1086/521145.

R. G. Arendt. An infrared survey of Galactic supernova remnants. *ApJS*, 70:181–212, May 1989. doi: 10.1086/191337.

B. Aschenbach, A. F. Iyudin, and V. Schönfelder. Constraints of age, distance and progenitor of the supernova remnant RX J0852.0-4622/GRO J0852-4642. *A&A*, 350:997–1006, 10 1999.

A. Bamba, R. Yamazaki, and J. S. Hiraga. Chandra Observations of Galactic Supernova Remnant Vela Jr.: A New Sample of Thin Filaments Emitting Synchrotron X-Rays. *ApJ*, 632:294–301, October 2005a. doi: 10.1086/432711.

A. Bamba, R. Yamazaki, T. Yoshida, T. Terasawa, and K. Koyama. A Spatial and Spectral Study of Nonthermal Filaments in Historical Supernova Remnants: Observational Results with Chandra. *ApJ*, 621:793–802, March 2005b. doi: 10.1086/427620.

D. Berge, S. Funk, and J. Hinton. Background modelling in very-high-energy γ-ray astronomy. *A&A*, 466:1219–1229, May 2007. doi: 10.1051/0004-6361:20066674.

K. Bernloehr, O. Carrol, R. Cornils, S. Elfahem, P. Espigat, S. Gillessen, G. Heinzelmann, G. Hermann, W. Hofmann, D. Horns, I. Jung, R. Kankanyan, A. Katona, B. Khelifi, H. Krawczynski, M. Panter, M. Punch, S. Rayner, G. Rowell, M. Tluczykont, and R. van Staa. The optical system of the h.e.s.s. imaging atmospheric cherenkov telescopes, part i: layout and components of the system. *Astropart. Phys.*, 20:111, 1 2003. doi: 10.1051/0004-6361:20053195.

J. M. Blondin, R. A. Chevalier, and D. M. Frierson. Pulsar Wind Nebulae in Evolved Supernova Remnants. *ApJ*, 563:806–815, December 2001. doi: 10.1086/324042.

G. R. Blumenthal and R. J. Gould. Bremsstrahlung, synchrotron radiation, and compton scattering of high-energy electrons traversing dilute gases. *Rev. Mod. Phys.*, 42:237, 1970.

S. V. Bogovalov, D. V. Khangulyan, A. V. Koldoba, G. V. Ustyugova, and F. A. Aharonian. Modelling interaction of relativistic and non-relativistic winds in binary system PSR B1259-63/SS2883 - I. Hydrodynamical limit. *MNRAS*, 387:63–72, June 2008. doi: 10.1111/j.1365-2966.2008.13226.x.

O. Bolz. *Absolute Energiekalibration der abbildenden Cherenkov- Teleskope des H.E.S.S. Experiments und Ergebnisse erster Beobachtungen des Supernova-Uberrests RX J1713.7-3946*. PhD in Physics, Ruprecht-Karls-Universität Heidelberg, 2004.

S. D. Bongiorno, A. D. Falcone, M. Stroh, J. Holder, J. L. Skilton, J. A. Hinton, N. Gehrels, and J. Grube. A New TeV Binary: The Discovery of an Orbital Period in HESS J0632+057. *ApJL*, 737:L11, August 2011. doi: 10.1088/2041-8205/737/1/L11.

K. J. Borkowski, S. P. Reynolds, D. A. Green, Una Hwang, Robert Petre, K. Krishnamurthy, and R. Willett. Radioactive scandium in the youngest galactic supernova remnant g1.9+0.3. *ApJL*, 724:L161–L165, 12 2010.

A. K. Carlton, K. J. Borkowski, S. P. Reynolds, U. Hwang, R. Petre, D. A. Green, K. Krishnamurthy, and R. Willett. Expansion of the Youngest Galactic Supernova Remnant G1.9+0.3. *ApJL*, 737:L22, August 2011. doi: 10.1088/2041-8205/737/1/L22.

S. Carrigan, J. A. Hinton, W. Hofmann, and et al. Establishing a connection between high-power pulsars and very-high-energy gamma-ray sources. In *International Cosmic Ray Conference*, volume 2 of *International Cosmic Ray Conference*, pages 659–662, 2008.

G. Cassam-Chenaï, A. Decourchelle, J. Ballet, J.-L. Sauvageot, G. Dubner, and E. Giacani. XMM-Newton observations of the supernova remnant RX J1713.7-3946 and its central source. *A&A*, 427:199–216, November 2004. doi: 10.1051/0004-6361:20041154.

J. L. Caswell, R. F. Haynes, D. K. Milne, and K. J. Wellington. High-resolution studey of the supernova remnant g330.2+1.0. *MNRAS*, 204:915–920, 1983.

R. C. G. Chaves, E. de Oña Wilhemi, and S. (H.E.S.S. Collaboration) Hoppe. The H.E.S.S. Galactic Plane Survey. In F. A. Aharonian, W. Hofmann, and F. Rieger, editors, *American Institute of Physics Conference Series*, volume 1085 of *American Institute of Physics Conference Series*, pages 219–222, December 2008. doi: 10.1063/1.3076644.

R. C. G. for the H.E.S.S. Collaboration Chaves. Extending the H.E.S.S. Galactic Plane Survey. *ArXiv e-prints*, July 2009.

M. Chernyakova, A. Neronov, A. Lutovinov, J. Rodriguez, and S. Johnston. XMM-Newton observations of PSR B1259-63 near the 2004 periastron passage. *MNRAS*, 367:1201–1208, April 2006. doi: 10.1111/j.1365-2966.2005.10039.x.

M. Chernyakova, A. Neronov, F. Aharonian, Y. Uchiyama, and T. Takahashi. X-ray observations of PSR B1259-63 near the 2007 periastron passage. *MNRAS*, 397: 2123–2132, August 2009. doi: 10.1111/j.1365-2966.2009.15116.x.

R. A. Chevalier. Was SN 1054 A Type II Supernova? In D. N. Schramm, editor, *Supernovae*, volume 66 of *Astrophysics and Space Science Library*, page 53, 1977.

A. E. Chudakov, V. L. Dadykin, G. T. Zatsepin, and N. M. Nestorova. The search of $\sim 10^{13}$ eV photons from local sources of the cosmic radio emission. *"Cosmic rays", Tr. FIAN*, 26:118, 1964. in Russian.

D. F. Cioffi, C. F. McKee, and E. Bertschinger. Dynamics of radiative supernova remnants. *ApJ*, 334:252–265, November 1988. doi: 10.1086/166834.

D. H. Clark, J. L. Caswell, and Anne J. Green. New galactic supernova remnants. *Nature*, 246:27–30, 1973.

D. H. Clark, J. L. Caswell, and A. J. Green. 408 and 5000 mhz observations of 28 new galactic supernova remnants. *Aust. J. Phys. Astrophys. Suppl.*, 37:1–38, 1975.

G. Cocconi. An air shower telescope and the detection of 10^{12} eV photon sources. In *International Cosmic Ray Conference*, volume 2 of *International Cosmic Ray Conference*, page 309, 1960.

L. Cominsky, M. Roberts, and S. Johnston. Detection of X-ray emission from the PSR 1259-63/SS 2883 binary system. *ApJ*, 427:978–983, June 1994. doi: 10.1086/174204.

J. J. Condon, M. R. Griffith, and A. E. Wright. The Parkes-MIT-NRAO surveys. IV - Maps for the Southern Survey covering delta in the range -88 to -37 deg. *Astron. J.*, 106:1095–1100, September 1993. doi: 10.1086/116707.

T. W. Connors, S. Johnston, R. N. Manchester, and D. McConnell. The 2000 periastron passage of PSR B1259-63. *MNRAS*, 336:1201–1208, November 2002. doi: 10.1046/j.1365-8711.2002.05850.x.

J. M. Cordes and D. F. Chernoff. Neutron Star Population Dynamics. II. Three-dimensional Space Velocities of Young Pulsars. *ApJ*, 505:315–338, September 1998. doi: 10.1086/306138.

J. M. Cordes and T. J. W. Lazio. NE2001.I. A New Model for the Galactic Distribution of Free Electrons and its Fluctuations. *ArXiv Astrophysics e-prints*, July 2002.

F. Crawford and C. L. Tiffany. Flux Densities and Radio Polarization Characteristics of Two Vela-like Pulsars. *Astron. J.*, 134:1231–1236, September 2007. doi: 10.1086/521020.

M. L. Dalton. *Identification of the VHE Gamma-ray Source HESS J1303-631 as a Pulsar Wind Nebula Through Multi-wavelength Observations*. PhD thesis, Humboldt Universität zu Berlin, 2011.

A. Daum, G. Hermann, M. Hess, W. Hofmann, H. Lampeitl, G. Pühlhofer, F. Aharonian, A. G. Akhperjanian, J. A. Barrio, A. S. Beglarian, K. Bernlöhr, J. J. G. Beteta, S. M. Bradbury, J. L. Contreras, J. Cortina, T. Deckers, E. Feigl, J. Fernandez, V. Fonseca, A. Frass, B. Funk, J. C. Gonzalez, G. Heinzelmann, M. Hemberger, A. Heusler, I. Holl, D. Horns, R. Kankanyan, O. Kirstein, C. Köhler, A. Konopelko, D. Kranich, H. Krawczynski, H. Kornmayer, A. Lindner, E. Lorenz, N. Magnussen, H. Meyer, R. Mirzoyan, H. Möller, A. Moralejo, L. Padilla, M. Panter, D. Petry, R. Plaga, J. Prahl, C. Prosch, G. Rauterberg, W. Rhode, A. Röhring, V. Sahakian, M. Samorski, J. A. Sanchez, D. Schmele, W. Stamm, M. Ulrich, H. J. Völk, S. Westerhoff, B. Wiebel-Sooth, C. A. Wiedner, M. Willmer, and H. Wirth. First results on the performance of the HEGRA IACT array. *Astroparticle Physics*, 8:1–11, December 1997. doi: 10.1016/S0927-6505(97)00031-5.

O. C. de Jager. Estimating the Birth Period of Pulsars through GLAST LAT Observations of Their Wind Nebulae. *ApJL*, 678:L113–L116, May 2008. doi: 10.1086/588283.

O. C. de Jager and A. Djannati-Ataï. Implications of H.E.S.S. observations of pulsar wind nebulae. *ArXiv e-prints*, March 2008.

O. C. de Jager, S. E. S. Ferreira, and A. Djannati-Ataï. MHD and Radiation Modelling of G21.5-0.9. In F. A. Aharonian, W. Hofmann, and F. Rieger, editors, *American Institute of Physics Conference Series*, volume 1085 of *American Institute of Physics Conference Series*, pages 199–202, December 2008. doi: 10.1063/1.3076638.

O. C. de Jager, S. E. S. Ferreira, A. Djannati-Ataï, M. Dalton, C. Deil, K. Kosack, M. Renaud, U. Schwanke, and O. Tibolla. Unidentified Gamma-Ray Sources as Ancient Pulsar Wind Nebulae. *ArXiv e-prints*, June 2009.

M. de Naurois and L. Rolland. A high performance likelihood reconstruction of γ-rays for imaging atmospheric Cherenkov telescopes. *Astroparticle Physics*, 32: 231–252, December 2009. doi: 10.1016/j.astropartphys.2009.09.001.

L. O.'C. Drury, F. A. Aharonian, and H. J. Völk. The gamma-ray visibility of supernova remnants. a test of cosmic ray origin. *A&A*, 287:959–971, 1994.

G. Dubus. Gamma-ray binaries: pulsars in disguise? *A&A*, 456:801–817, September 2006. doi: 10.1051/0004-6361:20054779.

G. Dubus, B. Cerutti, and G. Henri. Relativistic Doppler-boosted emission in gamma-ray binaries. *A&A*, 516:A18, June 2010. doi: 10.1051/0004-6361/201014023.

Vikram V. Dwarkadas and Roger A. Chevalier. Interaction of type ia supernovae with their surroundings. *ApJ*, 497:807, 4 1998.

Gary J. Feldman and Robert D. Cousins. A unified approach to the classical statistical analysis of small signals. *PHYS.REV.D*, 57:3873, 1998. URL doi:10.1103/PhysRevD.57.3873.

R. S. Fletcher, T. K. Gaisser, P. Lipari, and T. Stanev. sibyll: An event generator for simulation of high energy cosmic ray cascades. *Physical Review D*, 50:5710–5731, November 1994. doi: 10.1103/PhysRevD.50.5710.

Yasuo Fukui, Yoshiaki Moriguchi, Keisuke Tamura, Hiroaki Yamamoto, Yuzuru Tawara, Norikazu Mizuno, Toshikazu Onishi, Akira Mizuno, Yasunobu Uchiyama, Junko Hiraga, Tadayuki Takahashi, Koujin Yamashita, and Satoru Ikeuchi. Discovery of Interacting Molecular Gas toward the TeV Gamma-Ray Peak of the SNR G 347.3–0.5. *PASJ*, 55:L61–L64, 10 2003.

M. S. Fulbright and S. P. Reynolds. Bipolar supernova remnants and the obliquity dependence of shock acceleration. *ApJ*, 357:591–601, July 1990. doi: 10.1086/168947.

S. Funk, G. Hermann, J. Hinton, D. Berge, K. Bernloehr, W. Hofmann, P. Nayman, F. Toussenel, and P. Vincent. The trigger system of the h.e.s.s. telescope array. *Astropart. Phys.*, 22:285, 1 2004. doi: 10.1051/0004-6361:20053195.

S. Funk, J. A. Hinton, O. C. deJager, and for the H. E. S. S. Collaboration. Energy Dependent Morphology in the PWN candidate HESS J1825-137. *ArXiv e-prints*, September 2007.

S. Gabici. Gamma Ray Astronomy and the Origin of Galactic Cosmic Rays. *ArXiv e-prints*, November 2008.

B. M. Gaensler and P. O. Slane. The Evolution and Structure of Pulsar Wind Nebulae. *Annual Review of A&A*, 44:17–47, September 2006. doi: 10.1146/annurev.astro.44.051905.092528.

B. M. Gaensler, N. S. Schulz, V. M. Kaspi, M. J. Pivovaroff, and W. E. Becker. XMM-Newton Observations of PSR B1823-13: An Asymmetric Synchrotron Nebula around a Vela-like Pulsar. *ApJ*, 588:441–451, May 2003. doi: 10.1086/368356.

W. Galbraith and J. V. Jelley. Light Pulses from the Night Sky associated with Cosmic Rays. *Nature*, 171:349–350, February 1953. doi: 10.1038/171349a0.

V. L. Ginzburg and V. V. Zhelezniakov. On the pulsar emission mechanisms. *Annual Review of A&A*, 13:511–535, 1975. doi: 10.1146/annurev.aa.13.090175.002455.

D. A. Green. Galactic supernova remnants: an updated catalogue and some statistics. *BASI*, 32:335–370, 12 2004.

D. A. Green and S. F. Gull. Two new young galactic supernova remnants. *Nature*, 312:527–529, 1984.

D. A. Green, S. P. Reynolds, K. J. Borkowski, U. Hwang, and I. Harrus. The radio expansion and brightening of the very young supernova remnant g1.9+0.3. *MNRAS*, 387:L54–L58, 2008.

H. E. S. S. Collaboration: A. Djannati-Atai, O. C. De Jager, R. Terrier, Y. A. Gallant, and S. Hoppe. New Companions for the lonely Crab? VHE emission from young pulsar wind nebulae revealed by H.E.S.S. *ArXiv e-prints*, October 2007.

HESS Collaboration, A. Abramowski, F. Acero, F. Aharonian, A. G. Akhperjanian, G. Anton, A. Balzer, A. Barnacka, U. Barres de Almeida, Y. Becherini, J. Becker, B. Behera, K. Bernlöhr, E. Birsin, J. Biteau, A. Bochow, C. Boisson, J. Bolmont, P. Bordas, J. Brucker, F. Brun, P. Brun, T. Bulik, I. Büsching, S. Carrigan, S. Casanova, M. Cerruti, P. M. Chadwick, A. Charbonnier, R. C. G. Chaves, A. Cheesebrough, A. C. Clapson, G. Coignet, G. Cologna, J. Conrad, M. Dalton, M. K. Daniel, I. D. Davids, B. Degrange, C. Deil, H. J. Dickinson, A. Djannati-Ataï, W. Domainko, L. O'C. Drury, G. Dubus, K. Dutson, J. Dyks, M. Dyrda, K. Egberts, P. Eger, P. Espigat, L. Fallon, C. Farnier, S. Fegan, F. Feinstein, M. V. Fernandes, A. Fiasson, G. Fontaine, A. Förster, M. Füßling, Y. A. Gallant, H. Gast, L. Gérard, D. Gerbig, B. Giebels, J. F. Glicenstein, B. Glück, P. Goret, D. Göring, S. Häffner, J. D. Hague, D. Hampf, M. Hauser, S. Heinz, G. Heinzelmann, G. Henri, G. Hermann, J. A. Hinton, A. Hoffmann, W. Hofmann, P. Hofverberg, M. Holler, D. Horns, A. Jacholkowska, O. C. de Jager, C. Jahn, M. Jamrozy, I. Jung, M. A. Kastendieck, K. Katarzyński, U. Katz, S. Kaufmann, D. Keogh, D. Khangulyan, B. Khélifi, D. Klochkov, W. Kluźniak, T. Kneiske, N. Komin, K. Kosack, R. Kossakowski, H. Laffon, G. Lamanna, D. Lennarz, T. Lohse, A. Lopatin, C.-C. Lu, V. Marandon, A. Marcowith, J. Masbou, D. Maurin, N. Maxted, M. Mayer, T. J. L. McComb, M. C. Medina, J. Méhault, R. Moderski, E. Moulin, C. L. Naumann, M. Naumann-Godo, M. de Naurois, D. Nedbal, D. Nekrassov, N. Nguyen, B. Nicholas, J. Niemiec, S. J. Nolan, S. Ohm, E. de

Oña Wilhelmi, B. Opitz, M. Ostrowski, I. Oya, M. Panter, M. Paz Arribas, G. Pedaletti1, G. Pelletier, P.-O. Petrucci, S. Pita, G. Pühlhofer, M. Punch, A. Quirrenbach, M. Raue, S. M. Rayner, A. Reimer, O. Reimer, M. Renaud, R. de los Reyes, F. Rieger, J. Ripken, L. Rob, S. Rosier-Lees, G. Rowell, B. Rudak, C. B. Rulten, J. Ruppel, V. Sahakian, D. A. Sanchez, A. Santangelo, R. Schlickeiser, F. M. Schöck, A. Schulz, U. Schwanke, S. Schwarzburg, S. Schwemmer, F. Sheidaei, J. L. Skilton, H. Sol, G. Spengler, Ł. Stawarz, R. Steenkamp, C. Stegmann, F. Stinzing, K. Stycz, I. Sushch, A. Szostek, J.-P. Tavernet, R. Terrier, M. Tluczykont, K. Valerius, C. van Eldik, G. Vasileiadis, C. Venter, J. P. Vialle, A. Viana, P. Vincent, H. J. Völk, F. Volpe, S. Vorobiov, M. Vorster, S. J. Wagner, M. Ward, R. White, A. Wierzcholska, M. Zacharias, A. Zajczyk, A. A. Zdziarski, A. Zech, and H.-S. Zechlin. Discovery of VHE emission towards the Carina arm region with the H.E.S.S. telescope array: HESS J1018-589. *ArXiv e-prints*, March 2012.

A. M. Hillas. Cerenkov light images of EAS produced by primary gamma. In F. C. Jones, editor, *International Cosmic Ray Conference*, volume 3 of *International Cosmic Ray Conference*, pages 445–448, August 1985.

J. S. Hiraga, Y. Uchiyama, T. Takahashi, and F. A. Aharonian. Spectral properties of nonthermal X-ray emission from the shell-type SNR RX J1713.7 3946 as revealed by XMM-Newton. *A&A*, 431:953–961, March 2005. doi: 10.1051/0004-6361:20047015.

M. Hirayama, L. R. Cominsky, V. M. Kaspi, F. Nagase, M. Tavani, N. Kawai, and J. E. Grove. X-Ray/Gamma-Ray Observations of the PSR B1259-63-SS 2883 System near Apastron. *ApJ*, 521:718–722, August 1999. doi: 10.1086/307558.

W. Hofmann, I. Jung, A. Konopelko, H. Krawczynski, H. Lampeitl, and G. Pühlhofer. Comparison of techniques to reconstruct VHE gamma-ray showers from multiple stereoscopic Cherenkov images. *Astroparticle Physics*, 12:135–143, November 1999. doi: 10.1016/S0927-6505(99)00084-5.

S. Hoppe. The H.E.S.S. survey of the inner Galactic plane. In *International Cosmic Ray Conference*, volume 2 of *International Cosmic Ray Conference*, pages 579–582, 2008.

A. F. Iyudin, V. Schönfelder, K. Bennett, H. Bloemen, R. Diehl, W. Hermsen, G. G. Lichti, R. D. van der Meulen, J. Ryan, and C. Winkler. Emission from 44Ti associated with a previously unknown Galactic supernova. *Nature*, 396, 11 1998.

A. F. Iyudin, B. Aschenbach, W. Becker, K. Dennerl, and F. Haberl. XMM-Newton observations of the supernova remnant RX J0852.0-4622/GRO J0852-4642. *A&A*, 429:225–234, January 2005. doi: 10.1051/0004-6361:20041779.

S. Johnston, A. G. Lyne, R. N. Manchester, D. A. Kniffen, N. D'Amico, J. Lim, and M. Ashworth. A high-frequency survey of the southern Galactic plane for pulsars. *MNRAS*, 255:401–411, April 1992a.

S. Johnston, R. N. Manchester, A. G. Lyne, M. Bailes, V. M. Kaspi, G. Qiao, and N. D'Amico. PSR 1259-63 - A binary radio pulsar with a Be star companion. *ApJL*, 387:L37–L41, March 1992b. doi: 10.1086/186300.

S. Johnston, R. N. Manchester, D. McConnell, and D. Campbell-Wilson. Transient radio emission from the PSR B1259-63 system near periastron. *MNRAS*, 302:277–287, January 1999. doi: 10.1046/j.1365-8711.1999.02133.x.

S. Johnston, L. Ball, N. Wang, and R. N. Manchester. Radio observations of PSR B1259-63 through the 2004 periastron passage. *MNRAS*, 358:1069–1075, April 2005a. doi: 10.1111/j.1365-2966.2005.08854.x.

S. Johnston, L. Ball, N. Wang, and R. N. Manchester. Radio observations of PSR B1259-63 through the 2004 periastron passage. *MNRAS*, 358:1069–1075, April 2005b. doi: 10.1111/j.1365-2966.2005.08854.x.

V. M. Kaspi, M. Tavani, F. Nagase, M. Hirayama, M. Hoshino, T. Aoki, N. Kawai, and J. Arons. X-Ray Detection of PSR B1259-63 at Periastron. *ApJ*, 453:424, November 1995. doi: 10.1086/176403.

A. Kawachi, T. Naito, J. R. Patterson, P. G. Edwards, A. Asahara, G. V. Bicknell, R. W. Clay, R. Enomoto, S. Gunji, S. Hara, T. Hara, T. Hattori, S. Hayashi, S. Hayashi, C. Itoh, S. Kabuki, F. Kajino, H. Katagiri, T. Kifune, L. Ksenofontov, H. Kubo, J. Kushida, Y. Matsubara, Y. Mizumoto, M. Mori, H. Moro, H. Muraishi, Y. Muraki, T. Nakase, D. Nishida, K. Nishijima, M. Ohishi, K. Okumura, R. J. Protheroe, K. Sakurazawa, D. L. Swaby, T. Tanimori, F. Tokanai, K. Tsuchiya, H. Tsunoo, T. Uchida, A. Watanabe, S. Watanabe, S. Yanagita, T. Yoshida, and T. Yoshikoshi. A Search for TeV Gamma-Ray Emission from the PSR B1259-63/SS 2883 Binary System with the CANGAROO-II 10 Meter Telescope. *ApJ*, 607:949–958, June 2004. doi: 10.1086/383604.

S. R. Kelner, F. A. Aharonian, and V. V. Bugayov. Energy spectra of gamma rays, electrons, and neutrinos produced at proton-proton interactions in the very high energy regime. *Physical Review D*, 74(3):034018, August 2006. doi: 10.1103/PhysRevD.74.034018.

C. F. Kennel and F. V. Coroniti. Confinement of the Crab pulsar's wind by its supernova remnant. *ApJ*, 283:694–709, August 1984. doi: 10.1086/162356.

M. Kerschhaggl. *The TeV γ-ray Binary PSR B1259-63*. PhD thesis, Humboldt Universität zu Berlin, 2010.

D. Khangulyan, S. Hnatic, F. Aharonian, and S. Bogovalov. TeV light curve of PSR B1259-63/SS2883. *MNRAS*, 380:320–330, September 2007. doi: 10.1111/j.1365-2966.2007.12075.x.

D. Khangulyan, F. A. Aharonian, S. V. Bogovalov, and M. Ribó. Gamma-Ray Signal from the Pulsar Wind in the Binary Pulsar System PSR B1259-63/LS 2883. *ApJ*, 742:98, December 2011. doi: 10.1088/0004-637X/742/2/98.

D. Khangulyan, F. A. Aharonian, S. V. Bogovalov, and M. Ribó. Post-periastron Gamma-Ray Flare from PSR B1259-63/LS 2883 as a Result of Comptonization of the Cold Pulsar Wind. *ApJL*, 752:L17, June 2012. doi: 10.1088/2041-8205/752/1/L17.

J. G. Kirk, L. Ball, and O. Skjaeraasen. Inverse Compton emission of TeV gamma rays from PSR B1259-63. *Astroparticle Physics*, 10:31–45, January 1999. doi: 10.1016/S0927-6505(98)00041-3.

N. Komin. *Detection of Gamma Rays from the Supernova Remnant RX J0852.0-4622 with H.E.S.S.* PhD thesis, Humboldt Universität zu Berlin, 2005.

Katsuji Koyama, Kenzo Kinugasa, Keiichi Matsuzaki, Mamiko Nishiuchi, Mutsumi Sugizaki, Ken'ichi Torii, Shigeo Yamauchi, and Bernd Aschenbach. Discovery of Non-Thermal X-Rays from the Northwest Shell of the New SNR RX J1713.7-3946: The Second SN 1006? *PASJ*, 49:L7–L11, 06 1997.

L. T. Ksenofontov, H. J. Völk, and E. G. Berezhko. Nonthermal properties of supernova remnant g1.9+0.3. *ApJ*, 714:1187–1193, 2010.

H. J. G. L. M. Lamers, F.-J. Zickgraf, D. de Winter, L. Houziaux, and J. Zorec. An improved classification of B[e]-type stars. *A&A*, 340:117–128, December 1998.

T.-P. Li and Y.-Q. Ma. Analysis methods for results in gamma-ray astronomy. *ApJ*, 272:317–324, September 1983. doi: 10.1086/161295.

M. A. Livingstone, V. M. Kaspi, F. P. Gavriil, R. N. Manchester, E. V. G. Gotthelf, and L. Kuiper. New phase-coherent measurements of pulsar braking indices. *Astrophys. Space Sci.*, 308:317–323, April 2007. doi: 10.1007/s10509-007-9320-3.

K. S. Long, S. P. Reynolds, J. C. Raymond, P. F. Winkler, K. K. Dyer, and R. Petre. Chandra CCD Imagery of the Northeast and Northwest Limbs of SN 1006. *ApJ*, 586:1162–1178, April 2003. doi: 10.1086/367832.

M. S. Longair. *High energy astrophysics. Volume 2. Stars, the Galaxy and the interstellar medium.* 1994.

T. A. Lozinskaya. *Supernovae and stellar wind in the interstellar medium*. 1992.

A. G. Lyne, R. S. Pritchard, F. Graham-Smith, and F. Camilo. Very low braking index for the Vela pulsar. *Nature*, 381:497–498, June 1996. doi: 10.1038/381497a0.

MAGIC Collaboration, J. Aleksić, E. A. Alvarez, L. A. Antonelli, P. Antoranz, M. Asensio, M. Backes, J. A. Barrio, D. Bastieri, J. Becerra González, W. Bednarek, A. Berdyugin, K. Berger, E. Bernardini, A. Biland, O. Blanch, R. K. Bock, A. Boller, G. Bonnoli, D. Borla Tridon, I. Braun, T. Bretz, A. Cañellas, E. Carmona, A. Carosi, P. Colin, E. Colombo, J. L. Contreras, J. Cortina, L. Cossio, S. Covino, F. Dazzi, A. De Angelis, G. De Caneva, E. De Cea del Pozo, B. De Lotto, C. Delgado Mendez, A. Diago Ortega, M. Doert, A. Domínguez, D. Dominis Prester, D. Dorner, M. Doro, D. Eisenacher, D. Elsaesser, D. Ferenc, M. V. Fonseca, L. Font, C. Fruck, R. J. García López, M. Garczarczyk, D. Garrido, G. Giavitto, N. Godinović, D. Hadasch, D. Häfner, A. Herrero, D. Hildebrand, D. Höhne-Mönch, J. Hose, D. Hrupec, T. Jogler, H. Kellermann, S. Klepser, T. Krähenbühl, J. Krause, J. Kushida, A. La Barbera, D. Lelas, E. Leonardo, N. Lewandowska, E. Lindfors, S. Lombardi, M. López, A. López-Oramas, E. Lorenz, M. Makariev, G. Maneva, N. Mankuzhiyil, K. Mannheim, L. Maraschi, M. Mariotti, M. Martínez, D. Mazin, M. Meucci, J. M. Miranda, R. Mirzoyan, J. Moldón, A. Moralejo, P. Munar-Adrover, A. Niedzwiecki, D. Nieto, K. Nilsson, N. Nowak, R. Orito, D. Paneque, R. Paoletti, S. Pardo, J. M. Paredes, S. Partini, M. A. Perez-Torres, M. Persic, L. Peruzzo, M. Pilia, J. Pochon, F. Prada, P. G. Prada Moroni, E. Prandini, I. Puerto Gimenez, I. Puljak, I. Reichardt, R. Reinthal, W. Rhode, M. Ribó, J. Rico, S. Rügamer, A. Saggion, K. Saito, T. Y. Saito, M. Salvati, K. Satalecka, V. Scalzotto, V. Scapin, C. Schultz, T. Schweizer, M. Shayduk, S. N. Shore, A. Sillanpää, J. Sitarek, I. Snidaric, D. Sobczynska, F. Spanier, S. Spiro, V. Stamatescu, A. Stamerra, B. Steinke, J. Storz, N. Strah, T. Surić, L. Takalo, H. Takami, F. Tavecchio, P. Temnikov, T. Terzić, D. Tescaro, M. Teshima, O. Tibolla, D. F. Torres, A. Treves, M. Uellenbeck, H. Vankov, P. Vogler, R. M. Wagner, Q. Weitzel, V. Zabalza, F. Zandanel, R. Zanin, and K. Hirotani. Phase-resolved energy spectra of the Crab Pulsar in the range of 50-400 GeV measured with the MAGIC Telescopes. *ArXiv e-prints*, September 2011.

R. N. Manchester, A. G. Lyne, F. Camilo, J. F. Bell, V. M. Kaspi, N. D'Amico, N. P. F. McKay, F. Crawford, I. H. Stairs, A. Possenti, M. Kramer, and D. C. Sheppard. The Parkes multi-beam pulsar survey - I. Observing and data analysis systems, discovery and timing of 100 pulsars. *MNRAS*, 328:17–35, November 2001. doi: 10.1046/j.1365-8711.2001.04751.x.

N. M. McClure-Griffiths, A. J. Green, John M. Dickey, B. M. Gaensler, R. F. Haynes, and M. H. Wieringa. The southern galactic plane survey: The test region. *ApJ*, 551:394–412, 4 2001.

A. Melatos, S. Johnston, and D. B. Melrose. Stellar wind and stellar disc models of dispersion and rotation measure variations in the PSR B1259 - 63/SS2883 binary system. *MNRAS*, 275:381–397, July 1995.

Yoshiaki Moriguchi, Keisuke Tamura, Yuzuru Tawara, H. Sasago, K. Yamaoka, Toshikazu Onishi, and Yasuo Fukui. A Detailed Study of Molecular Clouds to-

ward the TeV Gamma-Ray Supernova Remnant G347.3-0.5. *ApJ*, 631:947–963, 10 2005.

T. Murphy, B. M. Gaensler, and S. Chatterjee. A 20-yr radio light curve for the young supernova remnant g1.9+0.3. *MNRAS*, 389:L23–L27, 2008.

I. Negueruela, M. Ribó, A. Herrero, J. Lorenzo, D. Khangulyan, and F. A. Aharonian. Astrophysical Parameters of LS 2883 and Implications for the PSR B1259-63 Gamma-ray Binary. *ApJL*, 732:L11, May 2011. doi: 10.1088/2041-8205/732/1/L11.

A. Neronov and M. Chernyakova. Radio-to-TeV γ-ray emission from PSR B1259 63. *Astrophys. Space Sci.*, 309:253–259, June 2007. doi: 10.1007/s10509-007-9454-3.

P. L. Nolan, A. A. Abdo, M. Ackermann, M. Ajello, A. Allafort, E. Antolini, W. B. Atwood, M. Axelsson, L. Baldini, J. Ballet, and et al. Fermi Large Area Telescope Second Source Catalog. *ApJS*, 199:31, April 2012. doi: 10.1088/0067-0049/199/2/31.

S. Ohm, C. van Eldik, and K. Egberts. γ/hadron separation in very-high-energy γ-ray astronomy using a multivariate analysis method. *Astroparticle Physics*, 31: 383–391, June 2009. doi: 10.1016/j.astropartphys.2009.04.001.

J. H. Oort. Interaction of Nova and Supernova Shells With the Interstellar Medium. In *Problems of Cosmical Aerodynamics*, page 118, 1951.

T. Padmanabhan. *Theoretical Astrophysics, Volume 2: Stars and Stellar Systems*. April 2001.

Sangwook Park, Koji Mori, Oleg Kargaltsev, Patrick O. Slane, John P. Hughes, David N. Burrows, Gordon P. Garmire, and George G. Pavlov. Discovery of a candidate central compact object in the galactic nonthermal snr g330.2+1.0. *ApJ*, 653:L37–L40, 2006.

Sangwook Park, Oleg Kargaltsev, George G. Pavlov, Koji Mori, Patrick O. Slane, John P. Hughes, David N. Burrows, and Gordon P. Garmire. Nonthermal x-rays from supernova remnant g330.2+1.0 and the characteristics of its central compact object. *ApJ*, 695(1):431–441, 2009.

M. Paz Arribas, U. Schwanke, I. Sushch, N. Komin, F. Acero, S. Ohm, and for the H. E. S. S. Collaboration. H.E.S.S. deeper observations on SNR RX J0852.0-4622. *ArXiv e-prints*, March 2012.

T. A. Porter, I. V. Moskalenko, and A. W. Strong. Inverse Compton Emission from Galactic Supernova Remnants: Effect of the Interstellar Radiation Field. *ApJL*, 648: L29–L32, September 2006. doi: 10.1086/507770.

S. P. Reynolds. Supernova Remnants at High Energy. *Annual Review of A&A*, 46: 89–126, September 2008. doi: 10.1146/annurev.astro.46.060407.145237.

S. P. Reynolds and R. A. Chevalier. Evolution of pulsar-driven supernova remnants. *ApJ*, 278:630–648, March 1984. doi: 10.1086/161831.

S. P. Reynolds and J. W. Keohane. Maximum Energies of Shock-accelerated Electrons in Young Shell Supernova Remnants. *ApJ*, 525:368–374, November 1999. doi: 10.1086/307880.

S. P. Reynolds, K. J. Borkowski, D. A. Green, U. Hwang, I. Harrus, and R. Petre. The youngest galactic supernova remnant g1.9+0.3. *ApJ*, 680:L41–L44, 2008.

S. P. Reynolds, K. J. Borkowski, D. A. Green, U. Hwang, I. Harrus, and R. Petre. X-ray spectral variations in the youngest galactic supernova remnant g1.9+0.3. *ApJ*, 695:L149–L153, 2009.

G. B. Rybicki and A. P. Lightman. *Radiative Processes in Astrophysics*. Wiley, New York, 1979.

S. Schlenker. *Very High Energy Gamma Rays from the Binary Pulsar PSR B1259-63*. PhD thesis, Humboldt Universität zu Berlin, 2005.

L. I. Sedov. *Similarity and Dimensional Methods in Mechanics*. Academic Press, New York, 1959.

S. E. Shaw, M. Chernyakova, J. Rodriguez, R. Walter, P. Kretschmar, and S. Mereghetti. INTEGRAL observations of the PSR B1259-63/SS2883 system after the 2004 periastron passage. *A&A*, 426:L33–L36, November 2004. doi: 10.1051/0004-6361:200400077.

G. Sinnis. Air shower detectors in gamma-ray astronomy. *New Journal of Physics*, 11 (5):055007, May 2009. doi: 10.1088/1367-2630/11/5/055007.

P. Slane, J. P. Hughes, R. J. Edgar, P. P. Plucinsky, E. Miyata, H. Tsunemi, and B. Aschenbach. RX J0852.0-4622: Another Nonthermal Shell-Type Supernova Remnant (G266.2-1.2). *ApJ*, 548:814–819, February 2001. doi: 10.1086/319033.

I. Sushch, E. Birsin, M. Dalton, M. Füßling, M. Paz Arribas, U. Schwanke, and G. Spengler. H.E.S.S. Observation Proposal for the PSR B1259-63 Field of View for 2010/2011. Internal H.E.S.S. observation proposal, 2010.

I. Sushch, B. Hnatyk, and A. Neronov. Modeling of the Vela complex including the Vela supernova remnant, the binary system γ^2 Velorum, and the Gum nebula. *A&A*, 525:A154, January 2011. doi: 10.1051/0004-6361/201015346.

I. Sushch, R. C. G. Chaves, M. Paz Arribas, F. Volpe, N. Komin, M. Kerschhaggl, and for the H. E. S. S. Collaboration. VHE gamma-ray observations of the young synchrotron-dominated SNRs G1.9+0.3 and G330.2+1.0 with H.E.S.S. *ArXiv e-prints*, March 2012.

P. H. T. Tam, R. H. H. Huang, J. Takata, C. Y. Hui, A. K. H. Kong, and K. S. Cheng. Discovery of GeV γ-ray Emission from PSR B1259-63/LS 2883. *ApJL*, 736:L10, July 2011. doi: 10.1088/2041-8205/736/1/L10.

T. Tanaka, A. Allafort, J. Ballet, S. Funk, F. Giordano, J. Hewitt, M. Lemoine-Goumard, H. Tajima, O. Tibolla, and Y. Uchiyama. Gamma-Ray Observations of the Supernova Remnant RX J0852.0-4622 with the Fermi Large Area Telescope. *ApJL*, 740:L51, October 2011. doi: 10.1088/2041-8205/740/2/L51.

Y. Tanaka, H. Inoue, and S.S. Holt. The x-ray satellite asca. *PASJ*, 46:L37, 1994.

M. Tavani and J. Arons. Theory of High-Energy Emission from the Pulsar/Be Star System PSR 1259-63. I. Radiation Mechanisms and Interaction Geometry. *ApJ*, 477:439, March 1997. doi: 10.1086/303676.

J. H. Taylor and J. M. Cordes. Pulsar distances and the galactic distribution of free electrons. *ApJ*, 411:674–684, July 1993. doi: 10.1086/172870.

The H.E.S.S. Collaboration: Abramowski, A., Acero, F., Aharonian, F., Akhperjanian, A. G., Anton, G., Balenderan, S., Balzer, A., Barnacka, A., Becherini, Y., Becker, J., Bernlöhr, K., Birsin, E., Biteau, J., Bochow, A., Boisson, C., Bolmont, J., Bordas, P., Brucker, J., Brun, F., Brun, P., Bulik, T., Büsching, I., Carrigan, S., Casanova, S., Cerruti, M., Chadwick, P. M., Charbonnier, A., Chaves, R. C. G., Cheesebrough, A., Cologna, G., Conrad, J., Couturier, C., Dalton, M., Daniel, M. K., Davids, I. D., Degrange, B., Deil, C., Dickinson, H. J., Djannati-Ataï, A., Domainko, W., Drury, L. O´C., Dubus, G., Dutson, K., Dyks, J., Dyrda, M., Egberts, K., Eger, P., Espigat, P., Fallon, L., Farnier, C., Fegan, S., Feinstein, F., Fernandes, M. V., Fiasson, A., Fontaine, G., Förster, A., Füßling, M., Gajdus, M., Gallant, Y. A., Garrigoux, T., Gast, H., Gérard, L., Giebels, B., Glicenstein, J. F., Glück, B., Göring, D., Grondin, M.-H., Häffner, S., Hague, J. D., Hahn, J., Hampf, D., Harris, J., Hauser, M., Heinz, S., Heinzelmann, G., Henri, G., Hermann, G., Hillert, A., Hinton, J. A., Hofmann, W., Hofverberg, P., Holler, M., Horns, D., Jacholkowska, A., Jahn, C., Jamrozy, M., Jung, I., Kastendieck, M. A., Katarzy´nski, K., Katz, U., Kaufmann, S., Khélifi, B., Klochkov, D., Klu´zniak, W., Kneiske, T., Komin, Nu., Kosack, K., Kossakowski, R., Krayzel, F., Laffon, H., Lamanna, G., Lenain, J.-P., Lennarz, D., Lohse, T., Lopatin, A., Lu, C.-C., Marandon, V., Marcowith, A., Masbou, J., Maurin, G., Maxted, N., Mayer, M., McComb, T. J. L., Medina, M. C., Méhault, J., Menzler, U., Moderski, R., Mohamed, M., Moulin, E., Naumann, C. L., Naumann-Godo, M., de Naurois, M., Nedbal, D., Nekrassov, D., Nguyen, N., Nicholas, B., Niemiec, J., Nolan, S. J., Ohm, S., de Oña Wilhelmi, E., Opitz, B., Ostrowski, M., Oya, I., Panter, M., Paz Arribas, M., Pekeur, N. W., Pelletier, G., Perez, J., Petrucci, P.-O., Peyaud, B., Pita, S., Pühlhofer, G., Punch, M., Quirrenbach, A., Raue, M., Reimer, A., Reimer, O., Renaud, M., de los Reyes, R., Rieger, F., Ripken, J., Rob, L., Rosier-Lees, S., Rowell, G., Rudak, B., Rulten, C. B., Sahakian, V., Sanchez, D. A., Santangelo, A., Schlickeiser, R., Schulz, A.,

Schwanke, U., Schwarzburg, S., Schwemmer, S., Sheidaei, F., Skilton, J. L., Sol, H., Spengler, G., Stawarz, L., Steenkamp, R., Stegmann, C., Stinzing, F., Stycz, K., Sushch, I., Szostek, A., Tavernet, J.-P., Terrier, R., Tluczykont, M., Valerius, K., van Eldik, C., Vasileiadis, G., Venter, C., Viana, A., Vincent, P., Völk, H. J., Volpe, F., Vorobiov, S., Vorster, M., Wagner, S. J., Ward, M., White, R., Wierzcholska, A., Zacharias, M., Zajczyk, A., Zdziarski, A. A., Zech, A., and Zechlin, H.-S. Identification of hess j1303-631 as a pulsar wind nebula through , x-ray, and radio observations. *A&A*, 548:A46, 2012. doi: 10.1051/0004-6361/201219814. URL `http://dx.doi.org/10.1051/0004-6361/201219814`.

K. Torii, H. Uchida, K. Hasuike, and H. Tsunemi. Discovery of a featureless x-ray spectrum in the supernova remnant shell of g330.2+1.0. *PASJ*, 58:L11–L14, 2006.

Hiroshi Tsunemi, Emi Miyata, Bernd Aschenbach, Junko Hiraga, and Daisuke Akutso. Overabundance of Calcium in the Young SNR RX J0852-4622: Evidence of Over-Production of 44Ti. *PASJ*, 52:887–893, 10 2000.

E. van der Swaluw and Y. Wu. Inferring Initial Spin Periods for Neutron Stars in Composite Remnants. *ApJL*, 555:L49–L53, July 2001. doi: 10.1086/321733.

VERITAS Collaboration, E. Aliu, T. Arlen, T. Aune, M. Beilicke, W. Benbow, A. Bouvier, S. M. Bradbury, J. H. Buckley, V. Bugaev, K. Byrum, A. Cannon, A. Cesarini, J. L. Christiansen, L. Ciupik, E. Collins-Hughes, M. P. Connolly, W. Cui, R. Dickherber, C. Duke, M. Errando, A. Falcone, J. P. Finley, G. Finnegan, L. Fortson, A. Furniss, N. Galante, D. Gall, K. Gibbs, G. H. Gillanders, S. Godambe, S. Griffin, J. Grube, R. Guenette, G. Gyuk, D. Hanna, J. Holder, H. Huan, G. Hughes, C. M. Hui, T. B. Humensky, A. Imran, P. Kaaret, N. Karlsson, M. Kertzman, D. Kieda, H. Krawczynski, F. Krennrich, M. J. Lang, M. Lyutikov, A. S. Madhavan, G. Maier, P. Majumdar, S. McArthur, A. McCann, M. McCutcheon, P. Moriarty, R. Mukherjee, P. Nuñez, R. A. Ong, M. Orr, A. N. Otte, N. Park, J. S. Perkins, F. Pizlo, M. Pohl, H. Prokoph, J. Quinn, K. Ragan, L. C. Reyes, P. T. Reynolds, E. Roache, H. J. Rose, J. Ruppel, D. B. Saxon, M. Schroedter, G. H. Sembroski, G. D. Şentürk, A. W. Smith, D. Staszak, G. Tešić, M. Theiling, S. Thibadeau, K. Tsurusaki, J. Tyler, A. Varlotta, V. V. Vassiliev, S. Vincent, M. Vivier, S. P. Wakely, J. E. Ward, T. C. Weekes, A. Weinstein, T. Weisgarber, D. A. Williams, and B. Zitzer. Detection of Pulsed Gamma Rays Above 100 GeV from the Crab Pulsar. *Science*, 334:69–, October 2011. doi: 10.1126/science.1208192.

J. Vink. Supernova Remnants: An Introductory Review. In F. Camilo & B. M. Gaensler, editor, *Young Neutron Stars and Their Environments*, volume 218 of *IAU Symposium*, pages 57–+, 2004.

Z. R. Wang, Q.-Y. Qu, and Y. Chen. Is RX J1713.7-3946 the remnant of the AD393 guest star? *A&A*, 318:L59–L61, February 1997.

L. B. F. M. Waters, E. P. J. van den Heuvel, A. R. Taylor, G. M. H. J. Habets, and P. Persi. Evidence for low-velocity winds in Be/X-ray binaries. *A&A*, 198:200–210, June 1988.

M. G. Watson, A. C. Schröder, D. Fyfe, C. G. Page, G. Lamer, S. Mateos, J. Pye, M. Sakano, S. Rosen, J. Ballet, X. Barcons, D. Barret, T. Boller, H. Brunner, M. Brusa, A. Caccianiga, F. J. Carrera, M. Ceballos, R. Della Ceca, M. Denby, G. Denkinson, S. Dupuy, S. Farrell, F. Fraschetti, M. J. Freyberg, P. Guillout, V. Hambaryan, T. Maccacaro, B. Mathiesen, R. McMahon, L. Michel, C. Motch, J. P. Osborne, M. Page, M. W. Pakull, W. Pietsch, R. Saxton, A. Schwope, P. Severgnini, M. Simpson, G. Sironi, G. Stewart, I. M. Stewart, A.-M. Stobbart, J. Tedds, R. Warwick, N. Webb, R. West, D. Worrall, and W. Yuan. The XMM-Newton serendipitous survey. V. The Second XMM-Newton serendipitous source catalogue. *A&A*, 493:339–373, January 2009. doi: 10.1051/0004-6361:200810534.

T. C. Weekes. Revealing the Dark Tev Sky:. the Atmospheric Cherenkov Imaging Technique for Very High Energy Gamma-Ray Astronomy. In K. Sato and J. Hisano, editors, *Energy Budget in the High Energy Universe*, pages 282–302, March 2007. doi: 10.1142/9789812708342_0030.

R. L. White and K. S. Long. Supernova remnant evolution in an interstellar medium with evaporating clouds. *ApJ*, 373:543–555, June 1991. doi: 10.1086/170073.

J. B. Z. Whiteoak and A. J. Green. The most supernova remnant catalogue. *A&AS*, 118:329–380, 1996.

E. D. O. Wilhelmi. Cherenkov Telescopes Results on Pulsar Wind Nebulae and Pulsars. In D. F. Torres and N. Rea, editors, *High-Energy Emission from Pulsars and their Systems*, page 435, 2011. doi: 10.1007/978-3-642-17251-9_37.

B. Woermann, M. J. Gaylard, and R. Otrupcek. Kinematics of the Gum nebula region. *MNRAS*, 325:1213–1227, August 2001. doi: 10.1046/j.1365-8711.2001.04558.x.

J. H. K. Wu, E. M. H. Wu, C. Y. Hui, P. H. T. Tam, R. H. H. Huang, A. K. H. Kong, and K. S. Cheng. Discovery of Gamma-Ray Emission from the Supernova Remnant Kes 17 with Fermi Large Area Telescope. *ApJL*, 740:L12, October 2011. doi: 10.1088/2041-8205/740/1/L12.

Q. Yuan, S. Liu, Z. Fan, X. Bi, and C. L. Fryer. Modeling the Multi-Wavelength Emission of the Shell-type Supernova Remnant RX J1713.7-3946. *ApJ*, 735:120, July 2011. doi: 10.1088/0004-637X/735/2/120.

G. T. Zatsepin and A. E. Chudakov. On the methods of searching for local sources of high energy photons. *J. Exp. Theor. Phys.*, 41:655, 1961. in Russian.

List of Figures

List of Tables

Selbständigkeitserklärung

Ich erkläre, dass ich die vorliegende Arbeit selbständig und nur unter Verwendung der angegebenen Literatur und Hilfsmittel angefertigt habe.

Berlin, den 31.05.2012 Iurii Sushch